Nº d'ordre: 635873

THÈSE EN COTUTELLE PRÉSENTÉE

POUR OBTENIR LE GRADE DE

DOCTEUR DE L'UNIVERSITÉ DE BORDEAUX

ET DE L'INSTITUTO SUPERIOR TÉCNICO DE

L'UNIVERSITÉ DE LISBONNE

ÉCOLE DOCTORALE DES SCIENCES CHIMIQUES

ÉCOLE DOCTORALE DE INGÉNIERIE DES MATÉRIAUX

SPÉCIALITÉ PHYSICO-CHIMIE DE LA MATIÈRE CONDENSÉE

Par Alexandre CUNHA

MULTISCALE FEMTOSECOND LASER SURFACE TEXTURING OF TITANIUM AND TITANIUM ALLOYS FOR DENTAL AND ORTHOPAEDIC IMPLANTS

Sous la direction de Marie-Christine DURRIEU et de Rui VILAR

Soutenue le 9 Janvier 2015

Membres du jury:

M. ALMEIDA, Rui Manuel Amaral de	Professeur, Instituto Superior Técnico, Universidade de Lisboa, Portugal	Président
Mme DURRIEU, Marie-Christine	Dr., Université de Bordeaux, France	Promoteur
M. VILAR, Rui Mário Correia da Silva	Professeur, Instituto Superior Técnico, Universidade de Lisboa, Portugal	Co-Promoteur
M. MONTEIRO, Fernando Jorge Mendes	Professeur, Universidade do Porto, Portugal	Rapporteur
M. OLIVEIRA, Victor Manuel Barbas	Professeur, Instituto Superior de Engenharia de Lisboa, Portugal	Rapporteur
Mme CONDE, Olinda Maria Quelhas Fernandes	Professeur, Faculdade de Ciências, Universidade de Lisboa, Portugal	Examinateur
M. PLAWINSKI, Laurent	Dr., Université de Bordeaux, France	Examinateur

This thesis was carried out in the scope of the International Doctoral School in Functional Materials (IDS-FunMat) for Energy, Information Technology and Health in a collaboration between:

Université de Bordeaux

CNRS, Chimie et Biologie des Membranes et des Nanoobjets UMR 5248

Institut Européen de Chimie et Biologie

2 Rue Robert Escarpit

33607 Pessac, France

Under the supervision of

Doctor Marie-Christine DURRIEU

and

Instituto Superior Técnico, Universidade de Lisboa

Instituto de Ciência e Engenharia de Materiais e Superfícies

1 Av. Rovisco Pais

1049-001 Lisboa, Portugal

Under the co-supervision of

Professor Rui VILAR

Titre: Texturation multi-échelle de titane au moyen d'un laser femtoseconde pour la conception d'implants dentaires et orthopédiques

Résumé: Dans ce travail de thèse, la texturation de surface d'alliages de titane a été étudiée en utilisant un procédé d'écriture directe par laser femtoseconde dans le but d'améliorer la mouillabilité d'implants dentaires et orthopédiques par les fluides biologiques et la minéralisation de la matrice (formation osseuse) tout en réduisant l'adhésion bactérienne et la formation de biofilmes. Des surfaces de titane (Ti-6Al-4V et cp Ti) ont été micro-, nano-texturées par laser femtoseconde et une biofonctionnalisation de ces surfaces a été ajoutée ou non par greffage de peptides d'adhésion cellulaire (peptides RGD) en surface de ces différents matériaux. Les textures de surface peuvent être classées comme suit: (a) structures périodiques de surface induites par laser (LIPSS); (b) étalage de nanopiliers (NP); (c) étalage de micro-colonnes recouvertes de LIPSS (MC-LIPSS) formant une distribution bimodale de rugosité. Nous avons montré que la texturation de surface par laser améliore la mouillabilité des surfaces avec de l'eau ainsi qu'une solution saline tamponnée Hank's (HBSS) et amène une anisotropie de mouillage. Une minéralisation cellulaire est observée pour toutes les surfaces des deux alliages de titane lorsque des Cellules Souches Mésenchymateuses humaines (hMSC) sont cultivées dans un milieu ostéogénique. La minéralisation de la matrice et la formation de nodules osseux sont considérablement améliorées sur les surfaces texturées LIPSS et NP. Parallèlement, l'adhésion de *Staphylococcus aureus* et la formation de biofilmes sont considérablement réduites pour les surfaces texturées LIPSS et NP. La biofonctionnalisation des différentes surfaces texturées (cp Ti) par laser a été réalisée et caractérisée par spectroscopie de photoélectrons (XPS) et par microscopie à fluorescence en utilisant des peptides fluorescents. L'ensemble des résultats obtenus suggèrent que la texturation de surface d'alliages de titane (Ti-6Al-4V et cp Ti) en utilisant une technique d'écriture directe par laser femtoseconde est un procédé prometteur pour l'amélioration de la mouillabilité de la surface d'implants dentaires et orthopédiques par les fluides biologiques et leur ostéointégration (différenciation ostéoblastique et minéralisation de la matrice), tout en réduisant l'adhésion de *Staphylococcus aureus* et la formation de biofilmes. Enfin, la combinaison de la texturation par laser et du greffage covalent d'un principe actif (ici un peptide d'adhésion cellulaire comme le peptide RGD) amènera

indéniablement une bioactivité utile pour favoriser l'adhésion des hMSC et faciliter la formation osseuse.

Mots clés*:* Lasers femtosecondes; Texturation de surface; Alliages de titane; Implants dentaires et orthopédiques; Mouillabilité; Cellules Souches Mésenchymateuses; ostéointégration; bactéries; *Staphylococcus aureus*; Biofilme; Biofonctionnalisation.

Title: Multiscale femtosecond laser surface texturing of titanium and titanium alloys for dental and orthopaedic implants

Abstract: In the present thesis the surface texturing of Ti alloys using femtosecond laser direct writing method is explored as a potential technique to enhance the wettability of dental and orthopaedic implants by biological fluids and matrix mineralisation (bone formation), while reducing bacteria adhesion and biofilm formation. The surface texture was combined with biofunctionalisation by covalent grafting of a RGD peptide sequence as well. The surface textures can be classified as follows: (a) Laser-Induced Periodic Surface Structures-LIPSS; (b) nanopillars arrays (NP); (c) arrays of microcolumns covered with LIPSS (MC-LIPSS), forming a bimodal roughness distribution. Laser texturing enhances surface wettability by water and Hank's balanced salt solution (HBSS) and introduces wetting anisotropy, crucial in controlling the wetting behaviour. Matrix mineralisation is observed for all surfaces of both Ti alloys when human mesenchymal stem cells (hMSCs) are cultured in osteogenic medium. Matrix mineralisation and formation of bone-like nodules are significantly enhanced on LIPSS and NP textured surfaces. On the contrary, *Staphylococcus aureus* adhesion and biofilm formation are significantly reduced for LIPSS and NP textured surfaces. The biofunctionalisation of the laser textured surfaces of cp Ti is sucessfully achieved. In general, these results suggest that surface texturing of Ti alloys using femtosecond laser direct writing is a promising method for enhancing surface wettability of dental and orthopaedic implants by biological fluids and their osseointegration (osteoblastic differentiation and matrix mineralisation), while reducing *Staphylococcus aureus* adhesion and biofilm formation. Finally, the combination of

laser texturing and covalent grafting of a RGD peptide sequence may be potentially useful for increasing cell adhesion and facilitating bone formation.

Keywords*:* Femtosecond lasers; Surface texturing; Titanium alloys; Dental and orthopaedic implants; Wettability; Mesenchymal Stem Cells; Osseointegration; Bacteria; *Staphylococcus aureus*; Biofilm; Biofunctionalisation.

Unité de recherche

CNRS, CBMN UMR 5248 Institut Européen de Chimie et Biologie 2 Rue Robert Escarpit 33607 Pessac, France

N° d'ordre: 635873

RÉSUMÉ

THÈSE PRÉSENTÉE

POUR OBTENIR LE GRADE DE

DOCTEUR DE L'UNIVERSITÉ DE BORDEAUX ET DE L'INSTITUTO SUPERIOR TÉCNICO DE L'UNIVERSITÉ DE LISBONNE

ÉCOLE DOCTORALE DES SCIENCES CHIMIQUES

ÉCOLE DOCTORALE D'INGÉNIERIE DES MATÉRIAUX

SPÉCIALITÉ PHYSICO-CHIMIE DE LA MATIÈRE CONDENSÉE

Par Alexandre CUNHA

TEXTURATION MULTI-ÉCHELLE DE TITANE AU MOYEN D'UN LASER FEMTOSECONDE POUR LA CONCEPTION D'IMPLANTS DENTAIRES ET ORTHOPÉDIQUES

Sous la direction de Marie-Christine DURRIEU et de Rui VILAR

2015

1. INTRODUCTION

Le marché global d'implants dentaires et orthopédiques augmente considérablement ces dernières années, compte tenu du vieillissement de la population et de la nécessité de traiter des patients de plus en plus jeunes. En dépit des progrès considérables déjà réalisés, les implants dentaires et orthopédiques ont toujours une durée de vie limitée dans le corps (10-15 ans), et des échecs dus à l'inflammation, infection, corrosion, usage, rupture, et le manque d'osseointegration se produisent toujours. Parmi eux, le manque d'ostéointégration et les infections associées sont les questions critiques. L'ostéointégration est définie comme un contact étroit entre l'os et le biomatériau lors de l'interprétation des sections histologiques. L'incapacité d'une surface d'implant à s'intégrer avec l'os adjacent et aux autres tissus entrainent le descellement des implants. Les infections osseuses sont principalement provoquées par des bactéries comme les *Staphylococcus aureus* représentant de loin le microbe pathogène le plus commun rencontré. Ces infections critiques empêchent l'intégration appropriée de l'implant dans les tissus environnants, et entrainent la destruction des joints et de l'os suite à cette inflammation.

La demande de nouveaux implants dentaire et orthopédique intelligents avec une réponse biologique améliorée est permanent. Il est aujourd'hui accepté que des améliorations significatives de la réponse biologique des implants exigent les doter d'une fonctionnalité de surface plus élevée. La nano et micro structuration de surface d'implants est l'une des méthodes prometteuses. L'objectif visé est de placer les cellules dans un environnement nano structuré qui mime l'environnement constitué par la matrice extracellulaire in vivo. La topographie et la composition chimique d'un implant définissent les propriétés telles que la rugosité, l'anisotropie, la mouillabilité et l'énergie libre de surface, qui jouent un rôle essentiel dans le contrôle des interactions entre l'implant et le milieu biologique (adsorption protéique, adhésion, prolifération et différentiation cellulaire), qui sont essentielles pour la formation d'une interface étroite os-implant et d'un risque d'infection limité.

Au cours des années plusieurs des méthodes physique, chimiques et mécaniques ont été étudiées pour la modification de surface des alliages titane, qui sont employés couramment comme implants dentaire et

orthopédique, dus à leur faible module d'élasticité, leur biocompatibilité nettement supérieure et leur résistance à la corrosion élevée, par rapport à l'acier inoxydable et aux alliages composés de cobalt. Certaines de ces méthodes (« Plasma-spraying », « Grit-blasting », « Acid-etching », et « Anodisation ») ont rencontré un succès commercial mais bon nombre d'entre elles tendent à polluer la surface, à changer fondamentalement la structure et les propriétés du matériau, à renforcer la colonisation bactérienne, et ne permettent de produire ces différents types de textures de façon reproductible. Des méthodes plus avancées, telles que la photolithographie, la lithographie par faisceau d'électrons, et le « nanoimprint », permettent la création des surfaces micro et nano structurées bien définies avec des géométries prédéfinies. Ces méthodes permettent de surmonter plusieurs des limitations précédemment décrites mais ont un inconvénient majeur puisqu'elles ne peuvent traiter des petites surfaces ainsi que des matériaux avec des géométries complexes. Réciproquement, la texturation de surface par les lasers ultra-rapide en utilisant les méthodes d'écriture directe diffère d'autres méthodes de modification de surface acompte tenu de leur flexibilité, simplicité, et leur reproductibilité élevée dans la fabrication de différents types de nano et de micro structures. Aussi, le traitement de laser n'entraine pas de contamination de surface du matériau, et les lasers autorisent le traitement de matériaux avec des géométries complexes, telles que celles des implants dentaires et orthopédiques. Récemment, notre équipe de recherche a prouvé que les lasers ultra-rapides permettent de fabriquer des surfaces titane présentant une variété de textures avec des caractéristiques extrêmement prometteuses pour l'application biomédicale. Les nanostructures ainsi que les textures micro-échelles peuvent être produites de façon reproductible en utilisant une méthode d'écriture directe de laser de femtoseconde. Par conséquent, l'objectif principal de cette thèse était d'explorer le potentiel de cette nouvelle méthode de modification de surface par laser pour augmenter la mouillabilité et l'ostéointégration d'implants titane, tout en réduisant l'adhésion de *Staphylococcus aureus* et la formation de biofilms. Deux types d'implants titane ont été utilisés: le grade 2 Ti (cp-commercial pur) et le grade 5 Ti-6Al-4V alliage. L'adhésion de cellules souches mésenchymateuses et leur différentiation vers un lignage particulier a été également étudié. Dans le but de conférer une bioactivité à ces matériaux titane, ceux-ci ont parallèlement

été rendus bioactifs par leur fonctionnalisation par des peptides d'adhésion cellulaire connus pour favoriser l'adhésion cellulaire. Notre groupe de recherche a déjà mis en évidence l'intérêt d'une fonctionnalisation de surface par des principes actifs (peptides RGD, facteurs de croissance) afin de contrôler l'adhésion, la prolifération, et la différenciation cellulaire.

2. PROCÉDURE EXPÉRIMENTALE

2.1. PREPARATION DES ALLIAGES DE TITANE

Des disques du titane de grade 2 (cp-commercial pur) et d'alliage de grade 5 Ti-6Al-4V avec des dimensions de 150 x 150 mm^2, et 1.0 et 1.2 mm d'épaisseur, respectivement, ont été coupés en spécimens carrés avec des aires de 10 x 10 et 20 x 20 mm^2, selon le type d'analyse à exécuter. Les spécimens ont été polis avec un ordre de la granulation 600-4000 des papiers de SiC. Après le meulage, les spécimens ont été polis miroir en utilisant des particules d'alumine abrasives (6.0 et 3.0 μm) et de la silice colloïdale (50 nm), suspendus dans de l'eau distillée. Le polissage a été exécuté pour assurer à la fois l'homogénéité des propriétés optiques de surface et une reproductibilité de la texturisation de surface par laser. Finalement, les spécimens ont été nettoyés par ultrasons dans une solution de détergent et à l'acétone pendant 10 minutes pour dégraisser et retirer les résidus de polissage.

2.2. TRAITEMENT DE LA SURFACE AU LASER

La texturisation de surface a été effectuée par une technique d'écriture directe au laser, à l'aide d'un laser de femtoseconde. Un système laser (Yb: KYW, HP S-PULSE, Amplitude Systèmes, France) avec une longueur d'onde centrale de 1030 nm et une durée d'impulsions laser de 500 fs a été employé pour les traitements laser. La texturisation au laser de grandes surfaces a été effectuée en utilisant une méthode d'écriture directe. Par cette méthode, les spécimens ont été constamment déplacés sous le rayon laser stationnaire avec différentes vitesses de balayage avec l'aide d'une table XYZ commandée par un ordinateur. En modulant et contrôlant les paramètres du laser tels que la fluence moyenne, la polarisation du rayon laser, le nombre d'impulsions, la vitesse de balayage, et le déplacement latéral du rayon laser, trois différents

types de textures de surface ont pu être produits sur les alliages titane. Ces textures se composent sont appelées : (a) « Laser-Induced Periodic Surface Structures » (LIPSS), (b) étalage de nanopiliers (NP); (c) étalage de micro-colonnes recouvertes de LIPSS (MC-LIPSS) formant une distribution bimodale de rugosité.

2.3. CARACTÉRISATION DE LA SURFACE

La topographie, la composition chimique, et la structure cristallographique des surfaces texturées par laser ont été caractérisées par microscopie optique binoculaire, microscopie électronique de balayage (MEB), reconstruction tridimensionnelle de la surface, microscopie à force atomique (MFA), spectroscopie de photoélectron de rayon X (XPS), spectroscopie de micro-Raman (μ-Raman), et diffraction des rayons X (XRD).

2.4. MESURES DE MOUILLABILITÉ ET ÉTUDES IN VITRO

La mouillabilité a été évaluée par la méthode « sessile drop », en utilisant de l'eau déionisée et une solution saline « Hank's Balanced Salt Solution » (HBSS). La réponse biologique des surfaces texturisées par laser a été évaluée *in vitro*, en utilisant des Cellules Souches Mésenchymateuses humaines (hMSCs) et des *Staphylococcus aureus* (*S. aureus*). Nous avons étudié les hMSCs (adhésion, prolifération, engagement et différentiation) et le comportement de *S. aureus* (adhésion et formation de biofilm) par microscopie à fluorescence et observations par MEB.

2.5. BIOFUNCTIONNALISATION DE LA SURFACE

Le biofunctionalisation des surfaces titane a été réalisée dans une boite à gants sous atmosphère contrôlée (Argon) afin d'éviter la contamination de surface et assurer un greffage reproductible des peptides en surface ainsi que leur stabilité. Le peptide KRGDSPC a été greffé de manière covalente en surface des matériaux titane. La stratégie pour l'immobilisation de peptide a impliqué trois étapes principales comme suit : (i) greffe d'une molécule silane (aminopropyltriéthoxysilane) (APTES)) sur les groupements OH présents en surface du titane ; (ii) greffage d'un agent intermédiaire hétérobifonctionnels (succinimidyl maléimidopropionate (SMP)) sur les groupements NH_2 présents; (iii) greffage du peptide KRGDSPC par réaction de la fonction thiol de la

Cystéine sur le groupement maléimide. Toutes les étapes de cette fonctionnalisation de surface ont été validées par XPS. L'intensité de distribution et de fluorescence des peptides greffés après conjugaison avec du fluorochrome d'isothiocyanate de fluorescéine (FITC-KRGDSPC) ont été évaluées par microscopie de fluorescence.

3. RÉSULTATS ET DISCUSSION

3.1. SURFACES TEXTURÉES AU LASER

Trois différents types de textures de surface peuvent être produits, selon la fluence et le nombre d'impulsions. Le premier type de texture se compose des « Laser-Induced Periodic Surface Structures » (LIPSS). On les observe sur des surfaces traitées avec 0.20 J/cm^2 et 192 impulsions. La périodicité du LIPSS semble équivalente quel que soit le titane utilisé (cp ou Ti-6Al-4V) (708 ± 59 et 715 ± 86 nm pour le cp Ti et Ti-6Al-4V alliage, respectivement), et la hauteur maximale est 251 ± 77 et 296 ± 58 nm, respectivement. Les textures laser LIPSS sont observées dans un éventail large de matériaux texturés par laser et existent dans deux catégories différenciées par leur périodicité par rapport à la longueur d'onde de rayonnement. La « Low Spatial Frequency LIPSS » (LSFLs) ont une période du même ordre de grandeur de la longueur d'onde de rayonnement (en général légèrement inférieure), alors que la « High Spatial Frequency LIPSS » (HSFLs) ont des périodes de quelques centaines de nanomètres. La formation de LSFLs a été expliquée par l'interférence entre le rayon laser incident et les ondes électromagnétiques dispersées de surface (Sipe *et al.* ont proposé les premiers principes d'une théorie pour expliquer ce phénomène). Actuellement, ces ondes électromagnétiques sont connues pour être des « Surface Plasmons Polaritons » (SPPs). En revanche, les mécanismes de la formation des HSFLs sont toujours en discussion. On a proposé plusieurs mécanismes pour expliquer leur formation tels que la self-organisation, la génération de second harmonique, et la dispersion de Mie.

Le deuxième type de texture se compose d'un étalage de nanopiliers (NP). On observe ces structures sur des surfaces soumises à un traitement en deux étapes avec traitement des paramètres dans la gamme de formation de LIPSS. Dans la première étape, les surfaces ont été traitées avec 0.3 J/cm^2 and 192

impulsions, tandis que la deuxième étape a été exécutée avec la fluence et un nombre inférieur d'impulsions (0.10 J/cm^2 et 47, respectivement). En tenant compte de l'influence de la polarisation du rayon laser sur de la direction de LIPSS, dans la deuxième étape, la direction de la polarisation a été tournée de 90° par rapport à la direction de la polarisation utilisée dans la première étape du traitement. Dans ces conditions, les *LIPSS* formés dans le premier traitement ont été partiellement réduits en fragments, provoquant les nanopiliers. Le diamètre inférieur des nanopiliers était 747 ± 132 et 696 ± 88 nm pour le cp Ti et Ti-6Al-4V alliage, respectivement, et leur hauteur maximale 174 ± 41 et 228 ± 63 nm. Le troisième type de texture se compose d'un étalage de micro-colonnes avec une section transversale rudement elliptique, fréquemment couverte de LIPSS (MC-LIPSS). On observe ces micro-colonnes sur des surfaces traitées avec 0.80 J/cm^2 et 1069 impulsions. La longueur de l'axe principal et de l'axe mineur des colonnes était 11 ± 2 et 8 ± 2 µm, et 10 ± 2 et 6 ± 1 µm pour le cp Ti et le Ti-6Al-4V alliage, respectivement. Leur hauteur maximale était de 3 ± 1 et 4 ± 1 µm. Ces colonnes sont couvertes par des textures LIPSS de périodicité semblable et de même orientation que ceux précédemment décrites, formant une distribution bimodale de rugosité. On a observé ces structures (colonnes, cônes, piliers, etc.) depuis un certain nombre d'années en utilisant le traitement laser sur des surfaces. Leurs mécanismes de formation ont fait l'objet de nombreuses polémiques, attribuées au rayonnement ombrageant des impuretés, à l'ablation différentielle, aux effets hydrodynamiques, ou à l'influence de la distribution de phase du matériel sur l'absorption de rayonnement, ce dernier mécanisme menant aux textures en colonnes qui sont proportionnées à la microstructure du matériau. Très récemment, il a été démontré que le développement de ces structures de surface sur le nickel (Ni) est caractérisé par un équilibre des mécanismes de croissance, tels que la dispersion des structures de surface et des effets géométriques causant l'ablation préférentielle dans les vallées, l'écoulement du matériel fondu, et le redéposition du matériel enlevé.

3.2. TOPOGRAPHIE, COMPOSITION CHIMIQUE ET STRUCTURE CRISTALLOGRAPHIQUE

Les paramètres de rugosité R_a et R_z ont été mesurés. Le R_a et R_z indiquent la taille de moyenne arithmétique et la hauteur maximale (distance entre les crêtes les plus élevées et les plus basses vallées), respectivement. Les Ra et Rz sont plus grands pour des surfaces texturées avec MC-LIPSS (1.1-1.2 et 5.3-5.4 µm, respectivement) par rapport aux surfaces texturées avec LIPSS (0.3 et 1.4-1.5 µm, respectivement) et NP (0.3 et 1.3-1.6 µm, respectivement), mais les différences ne sont pas statistiquement significatives quand nous comparons les mêmes textures des 2 alliages. Le traitement au laser, effectué sous air, oxyde la surface du matériel. Les analyses de XPS prouvent que l'oxyde le plus abondant actuel dans les surfaces est titania (TiO_2), mais une quantité significative d'alumine (Al_2O_3) est également présente sur les surfaces texturées par laser de Ti-6Al-4V alliage. La spectroscopie Raman et les XRD indiquent que le TiO_2 est composé d'anatase et de rutile. La présence de l'oxyde sur les surfaces titane était attendue, puisque c'est un métal fortement réactif qui réagit avec l'oxygène après quelques microsecondes d'exposition à l'air. L'oxydation induite par laser peut être expliquée par les températures atteintes en surfaces des surfaces métalliques pendant le traitement de laser. La présence d'une couche d'oxyde de titane permet l'obtention d'une surface biocompatible et plus résistante à la corrosion, acompte tenu de sa faible conductivité électronique et d'une nature thermodynamiquement stable aux valeurs du pH physiologique. La couche d'oxyde incorpore également facilement des ions minéraux (calcium-phosphates), de l'eau, et d'autres constituants une fois en contact avec l'environnement biologique favorisant ainsi la minéralisation.

3.3. MOUILLABILITÉ

Pendant les premières étapes de la formation osseuse, l'adsorption de fluides biologiques, tels que l'eau, le sang, les solutions salines et les protéines en surface d'implants joue un rôle crucial sur l'adhésion et la différentiation de cellules. En particulier, les cellules interagissent directement avec les protéines adsorbées sur les surfaces des implants, et par conséquent cette couche de protéines adsorbées joue un rôle essentiel sur le comportement de cellules. Par conséquent, le contrôle de la mouillabilité d'implants est une question essentielle pour assurer la biocompatibilité d'un implant. Le traitement laser de titane augmente la mouillabilité de ces matériaux avec

l'eau et les solutions salines par rapport aux surfaces polies, principalement pour les surfaces de cp Ti. Les surfaces texturées par LIPSS induisent une anisotropie de mouillage. Le traitement de laser augmente de manière significative l'énergie libre de surface, principalement pour les surfaces de cp Ti. Ces résultats sont relativement en accord avec l'augmentation du caractère hydrophile des surfaces texturées par laser du cp Ti en comparaison de celui de l'alliage de Ti-6Al-4V. Une augmentation de la quantité de protéines favorisant l'adhésion cellulaire telles que la fibronectine et la vitronectine sur des surfaces hydrophiles a été rapportée. Réciproquement, l'albumine, qui empêche l'adhésion de cellules, est connue pour avoir une affinité élevée sur les surfaces hydrophobes. Ainsi, l 'augmentation du caractère hydrophile des surfaces texturées par laser pourrait faciliter l'adsorption des protéines favorisant l'adhésion de cellules tout en réduisant l'adsorption de l'albumine.

3.4. ETALEMENT, FORME ET ADHÉSION CELLULAIRE (24 H APRÈS L'ENSEMENCEMENT CELLULAIRE)

La croissance des cellules Souches Mésenchymateuses humaines (hMSCs) est sensiblement plus grande sur Ti-6Al-4V alliage que sur des surfaces de cp Ti. L'étalement des hMSCs est fortement diminué par les textures de surface sur les deux alliages de Ti, par rapport aux surfaces polies. La topographie de surface affecte de manière significative la forme de hMSCs. Des fibres d'étirage et d'effort de cellules sont induites par des textures de LIPSS et de MC-LIPSS, alors que la formation significative de filopodia semble être induite par les textures de NP. Le nombre de cellules adhérentes semble indépendant de la texture et est semblable pour les deux alliages de Ti, mais la taille des ponts focaux d'adhésion est fortement réduite dans le cas des surfaces texturées par laser par rapport aux surfaces polies. L'adhésion est un facteur essentiel pour la viabilité de cellules et le développement de fonctions cellulaires. En revanche, le manque d'adhésion de cellules mène à la mort programmée de cellules. *In vivo*, les cellules adhèrent à la matrice extracellulaire, à d'autres cellules, et à la surface d'implants. Par conséquent, cytocompatibilité d'un implant peut être directement liée à l'adhérence de cellules. Dans ce travail, l'adhésion de hMSCs a été évaluée après 24 h de culture. L'étalement de cellules sur toutes les surfaces des alliages de Ti a été démontré. L'interaction entre les cellules et les surfaces texturées par laser a été confirmée par des

images obtenues par MEB. Celles-ci prouvent que le cytosquelette de cellules se déforme en fonction de la texture de surface, indiquant un contact fort du cytosquelette avec les surfaces. Des études antérieures ont également démontré l'impact de la nanotopographie de surface sur le comportement de cellules. Par ailleurs, nos travaux montrent que l'étalement du noyau de cellules est sensiblement diminué dans le cadre des surfaces texturées par laser des deux alliages de titane par rapport aux surfaces polies. Le noyau de cellules est par ailleurs légèrement déformé, mais ce phénomène semble indépendant de la topographie et de l'alliage de titane.

3.5. PROLIFÉRATION ET ENGAGEMENT OSTÉOBLASTIQUE (2 SEMAINES APRÈS L'ENSEMENCEMENT CELLULAIRE)

La prolifération des hMSCs change en fonction du matériau utilisé. La prolifération de cellules semble augmentée sur des surfaces de cp Ti par rapport à Ti-6Al-4V alliage. D'une part, la prolifération de cellules semble moins apparente sur les surfaces texturées par laser de Ti-6Al-4V par rapport aux surfaces polies. Les *hMSCs* s'engagent vers un lignage ostéoblastique, comme indiqué par l'expression des marqueurs tels qu'ostérix (OSX) et ostéopontine (OPN). Par ailleurs, l'intensité du signal des marqueurs ostéoblastiques est augmentée dans le cadre des surfaces de Ti-6Al-4V par rapport au cp Ti, mais pour leur expression semble indépendante du type de texture de surface.

3.6. DIFFÉRENCIATION OSTÉOBLASTIQUE (4 SEMAINES APRÈS L'ENSEMENCEMENT CELLULAIRE)

Aucune minéralisation cellulaire n'est observée lorsque les cellules sont cultivées dans un milieu non ostéogénique. On observe une minéralisation cellulaire avec toutes les surfaces et alliages de Ti lorsque les cellules sont cultivées dans un milieu ostéogénique. La minéralisation de la matrice est fortement augmentée avec les surfaces texturées avec LIPSS et NP, principalement pour l'alliage Ti-6Al-4V. Une organisation cellulaire concentrique est clairement observée. Nos résultats montrent également le rôle important des facteurs solubles, à savoir β- glycérophosphate, acide ascorbique, et dexaméthasone sur la minéralisation osseuse. Après 4 semaines de culture, il n'y a aucune trace de minéralisation de matrice pour

des cellules cultivées dans le milieu non ostéogénique tandis que l'opposé se produit quand les cellules sont cultivées dans un milieu ostéogénique. D'une manière plus importante, nous avons constaté que les textures de LIPSS et de NP augmentent considérablement l'effet des facteurs ostéogéniques utilisé.

3.7. ADHESION DES BACTERIES ET FORMATION DE BIOFILMS (48 H APRÈS L'ENSEMENCEMENT CELLULAIRE)

L'adhésion de *Staphylococcus aureus* et la formation de biofilms semblent sensiblement réduites lorsque les surfaces texturées LIPSS et NP sont utilisées par rapport aux surfaces polies et les surfaces texturées MC-LIPSS. La couche d'« Extracellular Polymeric Substance » (EPS) n'est pas continue sur les surfaces LIPSS et les surfaces texturées par NP. Au contraire, les bactéries sont couvertes par une couche continue d'EPS sur les surfaces polies et texturées MC-LIPSS. La formation des biofilms pathogènes de bactéries sur la surface des implants est l'une des causes principales d'échec ayant pour conséquence le retrait chirurgical de l'implant. La croissance du biofilm dépend de l'adhésion de bactéries sur la surface et de leur agrégation. La diminution de l'adhésion des bactéries et de la formation de biofilm sur les matériaux texturés LIPSS et NP peuvent réduire la croissance de biofilm et empêcher l'infection des tissus voisins.

3.8. SURFACES BIOFONCTIONNALISÉES

Deux approches différentes sont utilisées généralement dans la modification de surface des implants osseux. La première approche est basée sur la modification de la topographie. Dans le travail actuel, un traitement par laser de femtoseconde a été appliqué. La deuxième approche s'inscrit dans la fonctionnalisation de surface de matériaux par des principes actifs susceptibles d'orienter la réponse cellulaire. Dans le cadre de substituts osseux, des principes actifs pouvant favorisés l'adhésion et la différenciation cellulaire sont utilisés. L'objectif ici est de mimer l'environnement cellulaire composé par la matrice extracellulaire. Notre groupe de recherche a d'ores et déjà validé la fonctionnalisation de surface de titane par des peptides favorisant l'adhésion cellulaire (des peptides qui contiennent une séquence minimale reconnue pour favoriser cette adhésion cellulaire et notamment de

cellules osseuses : la séquence RGD). Dans la thèse, nous avons démontré la faisabilité de fonctionnalisation des surfaces texturées par laser. Les analyses de XPS (compositions atomiques et spectres haute résolution) prouvent que le peptide KRGDSPC est greffé sur des surfaces de cp Ti. Les analyses XPS et par microscopie à fluorescence (en utilisant des peptides KRGDSPC-FITC) indiquent que les surfaces greffées sont tout à fait homogènes et reproductibles. Une densité plus importante de peptides immobilisés en surface des matériaux LIPSS a été observée, alors qu'aucune différence statistiquement significative n'a été observée entre les surfaces MC-LIPSS et les surfaces NP.

4. CONCLUSIONS

Dans ce travail de recherche, une texturisation de surface d'alliages de Ti employant une écriture directe par le biais d'un système laser femtoseconde a été explorée comme méthode potentielle pour augmenter la mouillabilité et l'ostéointégration d'implants titane, tout en réduisant l'adhésion de *Staphylococcus aureus* et la formation de biofilm dans le cadre de la synthèse d'implants dentaires et orthopédiques intelligents (pouvant être rendus bioactifs par leur fonctionnalisation par des peptides favorisant l'adhésion cellulaire). En contrôlant les paramètres laser, tels que la fluence et le nombre d'impulsions, différentes textures de surface ont été produites. Deux types de titane ont été utilisés : un titane de grade 2 (cp-Ti) et un titane de grade 5 (l'alliage Ti-6Al-4V). Ces textures ont été nommées : (a) « Laser-Induced Periodic Surface Structures »; (b) étalage de nanopiliers; (c) étalage de micro-colonnes recouvertes de LIPSS formant une distribution bimodale de rugosité. Compte tenu que le traitement de laser est effectué à l'air, la surface du matériau est oxydée. TiO_2 est l'oxyde principal des deux alliages (anatase et rutile), mais une quantité significative d'alumine (Al_2O_3) est également présente en surface de l'alliage Ti-6Al-4V. Le traitement de laser augmente aussi la mouillabilité des surfaces avec l'eau et une solution saline en utilisant les deux alliages de titane texturés par rapport aux surfaces polies. Nos résultats montrent que toutes nos surfaces induisent un engagement des hMSCs vers un lignage ostéoblastique, comme indiqué par la présence des marqueurs ostérix et de l'ostéopontine. L'intensité de ces marqueurs

osteóblastiques est augmentée dans le cas de l'alliage Ti-6Al-4V par rapport au cp Ti, indépendamment de la texture de surface. La minéralisation cellulaire ne se produit pas quand des cellules sont cultivées dans un milieu non ostéogénique, mais celle-ci est observée lorsque les cellules sont cultivées dans un milieu ostéogénique. Dans un milieu ostéogénique, la minéralisation de la matrice est fortement augmentée avec les textures LIPSS et NP. Cet effet est encore plus marqué avec l'alliage, plus ainsi pour Ti-6Al-4V avec lequel des nodules osseux sont clairement formés. L'adhésion des bactéries *Staphylococcus aureus* et la formation de biofilm sont sensiblement réduites avec les textures LIPSS et NP par rapport aux surfaces polies et aux textures MC-LIPSS. La fonctionnalisation des surfaces titane texturées avec le peptide KRGDSPC a été réalisée avec succès. Les surfaces greffées bioactives sont tout à fait homogènes. Une grande densité de peptides greffés a été observée avec les surfaces texturées LIPSS.

L'écriture directe par le biais d'un laser femtoseconde est une méthode potentiellement utile pour la nano structuration de la surface d'implants dentaires et orthopédiques en titane. Le traitement de laser augmente la mouillabilité de surface par les fluides biologiques et la minéralisation de la matrice (formation d'os), tandis que l'adhésion de bactéries et la formation de biofilm semblent largement réduites. En conclusion, la combinaison du traitement par laser d'alliage de titane ainsi que leur biofonctionnalisation devrait permettre de favoriser à la fois l'adhésion cellulaire et l'ostéointégration d'alliages de titane.

RÉFÉRENCES

Toutes les références peuvent être trouvées dans la thèse

Acknowledgements

I would like to acknowledge the Fundação para a Ciência e a Tecnologia (FCT) for the doctoral grant SFRH/BD/61002/2009;

I acknowledge the *Programme d'Actions Universitaires Intégrées Luso-Françaises* (PAUILF) for financial support in the scope of the International Doctorate School in Functional Materials for Energy, Information Technology and Health (IDS-FunMat);

I also thank the extra grant *Aide à la mobilité cotutelle de thèse de l'Université Bordeaux* provided by the *Université de Bordeaux* for lodging and food;

A special thanks to my supervisor, Rui Mário Correia da Silva Vilar, of Instituto Superior Técnico-Universidade de Lisboa, and my co-supervisors Marie-Christine Durrieu and Maria Amélia Martins de Almeida, of *Université de Bordeaux* and Instituto Superior Técnico-Universidade de Lisboa, respectively, for supporting and guiding me during my PhD thesis;

A special thanks to Reiko Oda for receiving me in her research group in the facilities of the *Institut Européen de Chimie et Biologie* (IECB), Pessac-France;

I thank Doctor Vitor Oliveira for teaching me how to use the laser system as well as for the implementation of the software used for controlling it;

A great thanks to Doctor Ana Paula Serro for the fruitful collaboration in the wettability measurements and interpretation of the respective results;

I would like to thank Doctors Ana Maria Rego and Christine Labrugère for the collaboration in the X-ray photoelectron spectroscopy (XPS) analysis and interpretation of the respective results;

I thank Engineer Isabel Nogueira for her help in the preparation of the samples for scanning electron microscopy (SEM) analysis as well as in the operation of the microscopes;

I thank Doctor Rogério Colaço for allowing me to use the atomic force microscope of his research group. A special thanks to my PhD colleague and friend Bruno Nunes for helping me in the AFM analysis;

I thank Doctor Luis Santos for allowing me to use the micro-Raman microscope. A special thanks to my PhD colleague and friend Liliana Cangueiro for helping me in the micro-Raman analysis and for fruitful discussions regarding laser processing of materials;

A great thanks to Doctors Omar Farouk Zouani and Laurent Plawinski for helping me in the cell culture experiments and for fruitful discussions regarding cell biology;

I thank Doctor Maria C. Urdaci for allowing me to work in her microbiology laboratory, in the facilities of the *Ecole Nationale d'Ingénieurs des Travaux Agricoles de Bordeaux* (ENITAB), *Université de Bordeaux*, and Doctor Anne-Marie Elie for helping me in the bacteria culture experiments;

I thank Mr. Daniel Pomiel de Jesus for helping me in the preparation of metallographic specimens;

A huge thanks to all my Portuguese, Polish, Malayan, French, Chinese, Japanese, and Indian colleagues and friends, for sharing with me their personal and scientific experiences during these last four years. In particular, I would like to deeply thanks my friends Bruno Nunes, Liliana Cangueiro, Sahendra Sharma, Omar F. Zouani, Annie Cheng, Guillaume Le Saux, Dmytro Dedovets, Alla Malinenko, Jiaji Cheng, Yutaka Okazaki, Rajat Kumar Das, Filipa Curado, Tomin Liu and Yifeng Lei;

A special thanks to my beloved family for supporting me during these years, in particular, my mother Iara Cunha and my younger brother André Cunha. I know we are far away from each other at the moment, but you are all always in my heart;

A special thanks to my beloved girlfriend Catarina Fernandes for supporting and helping me in these last years. Thank you so much for sharing your life with me, you are an essential person in my life;

Finally, last but not least, a special thanks and hugs to all the people that somehow helped me during this phase of my life.

Abbreviations

	A
AAOS	American Academy of Orthopaedic Surgeons
ADSA-P	Axisymmetric Drop Shape Analysis Profile Method
AES	Auger Electron Spectroscopy
ALP	Alkaline Phosphatase
ANOVA	Analysis of Variance
APS	Atmospheric Plasma Spraying
APTES	Three-aminopropyltriethoxysilane
ASG	Above-Surface-Growth
ASTM	American Society for Testing and Materials
ATCC	American Type Culture Collection
	B
BCC	Body Centrered Cubic
BE	Binding Energy
BGP	Beta-Glycerolphosphate
BIC	Bone-to-Implant Contact
BMP	Bone Morphogenetic Protein
BSA	Bovine Serum Albumin
BSG	Below-Surface-Growth
	C
C	Cystein
CA	Contact Angle
CAM	Cell Adhesion Molecule
CBMN	*Chimie et Biologie des Membranes et Nanoobjets*
CFSE	Carboxyfluorescein Succinimidyl Ester
CFU	Colony-Forming Unit
CNRS	*Centre National de la Reserche Scientifique*
CW	Continuous Wave
cp	Commercially Pure
CP	Supersaturated Calcium Phosphate
CPS	Calcium Phosphate Supersaturated Solution
	D
DAPI	4',6-diamidino-2-phenylindole
DD	Distilled-Deionised
DEM	Digital Elevation Mode
DMF	Dimethylformamide
DNA	Deoxyribonucleic Acid
DPBS	Dulbecco's Phosphate Buffered Saline
	E
EBL	Electron Beam Lithography
ECAP	Equal Channel Angular Pressing
ECM	Extracellular Matrix
EDTA	Ethylenediaminetetraacetic Acid
ELI	Extra Low Interstitial
ENITAB	*Ecole Nationale d'Ingénieurs des Travaux Agricoles de Bordeaux*
EPS	Extracellular Polymeric Substance
	F
FAK	Focal Adhesion Kinase
FAs	Focal Adhesions
FAT	Fixed Analyser Transmission
FBS	Foetal Bovine Serum

FCC	Face Centrered Cubic
FEG-SEM	Field Emission Gun-Scanning Electron Microscopy
FHRRIKA	Phenylalanine-Histidine-Arginine-Arginine-Isoleucine-Lysine-Alanine
FI	Fluorescence Intensity
FITC	Fluorescein Isothiocyanate
FTIRRAS	Fourier Transform Infrared Reflection Absorption Spectroscopy
FWHM	Full Width at Half Maximum
	G
GI-XRD	Glancing Incidence X-ray Diffraction
	H
HA	Hydroxyapatite
HBSS	Hank's Balanced Salt Solution
HCP	Hexagonal Closely-Packed
HFOB	Human Foetal Osteoblastic Cells
HMDS	Hexamethyl-Disilazane
hMSCs	Human Mesenchymal Stem Cells
HOS	Human Osteosarcoma
HSCs	Hematopoietic Stem Cells
HSFLs	High Spatial Frequency LIPSS
	I
ICDD	International Centre for Diffraction Data
ID	Integrated Density
IECB	*Institut Européen de Chimie et Biologie*
IR	Infrared
ISO	International Organization for Standardization
	K
K	Lysin
KRSR	Lysine-Arginine-Serine-Arginine
	L
LIPSS	Laser-Induced Periodic Surface Structures
LSFLs	Low Spatial Frequency LIPSS
	M
M	Molar
MAP	Mitogen-Activated Protein Kinase
MAP2	Microtubule Associated Protein 2
MEM	Minimal Essential Medium
μ–Raman	Micro-Raman Spectroscopy
MSCGM™	Mesenchymal Stem Cell Growth Medium
MSCRAMMs	Microbial Surface Components Recognising Adhesive Matrix Molecules
	N
NA	Numerical Aperture
NCP	Non-Collagenic Proteins
NI	Nosocomial Infection
NIH	National Institutes of Health
NIL	Nanoimprint Lithography
NIR	Near Infrared
NIST	National Institute of Standards and Technology
	O
OCN	Osteocalcin
OD	Optical Density
OI	OsteoImage™
OPN	Osteopontin
OSX	Osterix
	P
P	Prolin

PBS	Phosphate Buffered Saline
PCR	Polymerase Chain Reaction
PDF	Powder Diffraction Files
PDMS	Polydimethylsiloxane
PE	Polyethylene
PFA	Paraformaldehyde
PGA	Polyglycolic Acid
PIA	Polysaccharide Intercellular Adhesin
PLA	Polylactic Acid
PLACAMAT	*Plataforme Aquitaine de Caractérisation des Matériaux*
PMMA	Poly(Methyl Methacrylate)
PNAG	Poly-N-Acetylglucosamine
PTFE	Polytetrafluoroethylene
PSMs	Phenol-Soluble Modulins
PUU	Poly(Urethane Urea)
PVA	Preferential Valley Ablation
	R
RGD	Arginin-Glycin-Aspartic Acid
RIE	Reactive Ion Etching
ROI	Region Of Interest
	S
S	Serin
SBF	Simulated Body Fluid
SCP	Supersaturated Calcium Phosphate Solution
SCS	Supersaturated Calcifying Solutions
SEM	Scanning Electron Microscopy
SMP	3-Succinimidyl-3-MaleimidoPropionate
SSI	Surgical Site Infection
SPPs	Surface Plasmons Polaritons
	T
TCPS	Tissue Culture Polystyrene
TE	Transverse-Electric
TM	Transverse-Magnetic
TOA	Take-Off Angle
TGF	Transforming Growth Factor
Triton-X-100	4-(1,1,3,3-Tetramethylbutyl)phenyl-polyethylene glycol
TSB	Tryptic Soy Broth
Tween 20	Polyoxyrthylenesorbitan Monolaurate
	U
UMR	*Unité Mixtes de Recherche*
UV	Ultraviolet
	V
VIS	Visible
VPS	Vacuum Plasma Spraying
	W
WD	Working Distance
	X
XO	Xylenol Orange
XPS	X-ray Photoelectron Spectroscopy
XRD	X-ray Diffraction

List of Figures

Figure I-1. Market forecasting of the worldwide expenditure with joint replacement, implant, regenerative products, bone repair, cartilage, and soft tissues (adapted from [2]). 8
Figure I-2. Growth of human bone (osseointegration) on a plasma-sprayed titanium porous coating at 45 days after implantation (Courtesy of Hospital de Clínicas de Porto Alegre, POA, RS, Brazil). 12
Figure I-3. Scheme of the various causes of implant failure that may lead to revision surgery (adpted from [4]). 14
Figure I-4. Alpha (a) and beta (b) crystal structures of titanium and the different categories of titanium phase diagrams depending on the alloying elements (adapted from [39]). 17
Figure I-5. Applications of titanium and its alloys on the manufacturing of hip joints (a), knee (b), dental implants (c), vascular stents (d), and screws and plates for bone fixation (e) (adapted from [13]). 22
Figure I-6. Low and high magnifications SEM micrographs of plasma-sprayed titanium (a-b) and hydroxyapatite (c-d) coatings (adapted from [54]). The scale bar is 100 μm (a and c) and 10 μm (b and d)..... 25
Figure I-7. Low and high magnifications SEM micrographs of a titanium surface blasted with TiO_2 particles (adapted from [54]). The scale bar is 100 μm (left) and 2 μm (right). 26
Figure I-8. Low and high magnifications SEM micrographs of a titanium surface treated with a fluoride solution (a-b) and SLA (c-d) (adapted from [54]). The scale bar is 100 μm (a and c), 2 μm (b), and 1 μm (d). 27
Figure I-9. Schematic setup for anodisation of titanium in fluoride containing electrolytes (a). SEM micrographs of TiO_2 micropores (b) and nanotubes (c) (adapted from [5, 11]). The scale bar is 20 μm (b) and 1 μm (c). 28
Figure I-10. Scheme of a photolithographic process performed on SiO_2. 29
Figure I-11. Scheme of electron beam lithography (a) and SEM micrographs of different nanopitted silicon surfaces with different pit sizes produced by high-resolution e-beam (b) (adapted from [59]). The scale bar is 1 μm. 30
Figure I-12. Scheme of a nanoimprint lithographic process (adapted from [61]). 32

Figure I-13. Schematic drawing of the physical adsorption method. The implants are soaked in a solution containing the bioactive molecules of interest. Generally, proteins are used as the target biomolecules (adapted from [20]). 33
Figure I-14. Covalent immobilisation of a RGD peptide sequence on a Ti-6Al-4V surface using an intermediary aminoalkylsilane spacer molecule to the oxidised titanium surface, followed by the covalent bounding of the peptide sequence to the free terminal NH_2 groups using 3-succinimidyl-3-maleimidopropionate (SMP) as a coupling agent (adapted from [21]). 35
Figure I-15. Schematic drawing of the biomimetic incorporation of bioactive molecules on the bone-like mineral part produced onto implant surfaces (adpted from [20]). 36
Figure I-16. Typical experimental setup for direct femtosecond laser surface texturing. (1) femtosecond laser; (2) focusing lens; (3) computer-controlled XYZ-translation stage; (4) beam splitter; (5) joulemeter; (6) electro-mechanical shutter; (7) variable attenuator; and (8) polarisation control device (adapted from [15]). 38
Figure I-17. LIPSS and periodic patterns in nature. Ripples in sand dunes (a) and in the bottom of a river (b). SEM micrographs of LIPSS produced on a titanium surface using direct femtosecond laser surface texturing (c-d). Despite the similarity in morphology, ripples in nature are produced at a macroscale level, while LIPSS are nanoscaled structures with periodicities and heights at the sub-micrometre level. 40
Figure I-18. Columnar microstructures produced on titanium (a), stainless steel (b), and silicon (c) surfaces by femtosecond laser irradiation (adapted from [124-126]). 44
Figure I-19. Scheme of the growth mechanisms of columnar microstructures produced by femtosecond laser irradiation. Below-surface-growth (BSG) and above-surface-growth (ASG) features (adapted from [131]). 45
Figure I-20. Femtosecond laser irradiation of a Ti-6Al-4V surface under both stationary and non-stationary conditions. Low magnification SEM micrograph of a single spot showing the columnar microstructures at the centre and LIPSS at the periphery of the spot (a). High magnification SEM micrograph of the columnar microstructures formed on a large textured area (b) and LIPSS overlapping the columnar microstructures (c). 48
Figure I-21. Forward (a) and backward (d) scanning modes of the cut fs-laser beam. SEM micrographs of the titanium surface after its scanning by femtosecond laser pulses in the forward “positive” direction (b-c) and in the backward “negative” direction (e-f) [133]. 49

Figure I-22. Time evolution of adsorption of body fluids and proteins and cell adhesion on the implant surface during the early stages of bone formation, in which wettability plays a crucial role [4]. 50
Figure I-23. Representation of two opposite wetting behaviours when a liquid droplet is brought into contact with a solid surface. Complete drying (a) and complete wetting (b). The balance between the surface tensions ($\boldsymbol{\gamma}$) of the three phases involved defines the contact angle ($\boldsymbol{\theta c}$) of the liquid droplet (c). 51
Figure I-24. Representation of the Wenzel and Cassie-Baxter models developed to describe the different states of a liquid droplet into contact with a solid rough surface. 53
Figure I-25. Superhydrophobic and superhydrophilic surfaces in nature. Low and high magnification SEM micrographs of a lotus leaf (1), red rose petal (2), gecko foot (3), butterfly wing (4), wings of cicada (5), and desert beetle *Stenocara sp* (6) (adapted from [139]). 56
Figure I-26. Representation of the bone tissue and its components at different scale levels (adapted from [156]). 60
Figure I-27. Representation of the major proteins involved in cell-biomaterial and cell-cell adhesion processes (adapted from [62]). The RGD present on the extracellular matrix proteins binds to the integrins. 63
Figure I-28. Different types of stress fibres observed on fibroblasts according to their subcellular location. 68
Figure I-29. Representation of the common protocol used for isolation and expansion of MSCs from bone marrow. Bone marrow is collected, and a density gradient centrifugation with Ficoll-Paque is performed to separate nonnucleated red blood cells from nucleated cells. Then, the mononuclear cell fraction is transferred to plastic T-tubes, in which MSCs adhere. Finally, monocytes are separated from MSCs by trypsinisation (adaptation from [172]). 72
Figure I-30. Cell division by invariant and populational asymmetry. S denotes stem cell and P denotes progenitor cell. (A) In invariant asymmetric cell division, a mother cell gives rise to two daughter cells, one of which stays stem while the other becomes a progenitor cell that becomes a fully differentiated cell. (B) In populational asymmetric cell division, each daughter cell has a finite probability of staying as a stem cell or becoming a progenitor cell. The daughter cells can go down different routes and become different types of progenitor cells (P1, P2, P3) and ultimate become fully differentiated cells [195]. 73

Figure I-31. The MSCs differentiation process. MSCs are able to differentiate into many different types of mature, end-stage cells. Throughout the differentiation process, MSCs are capable of producing cells with distinct phenotypes at intermediate stages [197]... 74
Figure I-32. Representation of the differentiation sequence during osteogenesis and the relation with the self-renewal capacity of the cells. 75
Figure I-33. Culture-expanded hMSCs exhibit a spindle-shaped fibroblastic morphology following *ex vivo* culture expansion (top panel). Under appropriate inducing conditions, the culture will demonstrate osteogenic, adipogenic, and chondrogenic differentiation (adapted from [200])..... 76
Figure I-34. Low and high magnification SEM micrographs of a *Staphylococcus* biofilm. Bacteria are covered with a polysaccharide matrix (adapted from [6]). The scale bar is 1 μm. 79
Figure I-35. Representation of the cycle of biofilm formation. Bacteria attach and adhere to the surfaces (1) followed by proliferation (2), production of the extracellular polymeric substance (EPS) and biofilm maturation (3), and detachment of single cells or cell clusters (4) (adapted from [208]). 80
Figure I-36. SEM micrograph of *S. aureus* forming grape-like clusters [6]. The scale bar is 1 μm. 82
Figure II-1. Flow-chart describing the procedures to obtain mirror-polished titanium surfaces. 98
Figure II-2. Representative scheme of the experiment performed on a Ti-6Al-4V alloy surface for the determination of ω_0. (A) Several single craters were produced with increasing average pulse energy and number of laser pulses. (B) Four diameters were measured in different directions for each crater produced and an average diameter determined. 102
Figure II-3. Direct writing femtosecond laser surface texturing setup. 102
Figure II-4. Laser surface texturing strategies. 104
Figure II-5. Non-textured (polished) and laser textured surfaces of both titanium alloys. The reproducible colour modification of the surfaces is used as a complementary control of the production of each type of texture. 105
Figure II-6. Scheme of the experimental setup for the measurement of the contact angles (adapted from [253])..... 108
Figure II-7. Representative images of droplets of the two liquids on the same material, acquired with the video microscope. 109

Figure II-8. Demonstration of how quantifications were performed using Image J freeware. The original images of F-actin fibers, nucleus, and vinculin are first converted into 8-bits images followed by optimisation of contrast and brightness. Then, threshold is applied and the parameters are measured with the "Analyse Particles" tool..... 115
Figure II-9. Demonstration of how quantifications were performed using Image J freeware. The original images of OSX, OPN, calcium-rich and hydroxyapatite-rich zones are first converted into 8-bits images. The regions of interest are selected by using the polygon tool and the area of the region of interest, mean grey value, and the integrated density are measured. Image background is subtracted by performing at least three measurements of the mean grey value around the regions of interest..... 116
Figure II-10. Molecular structure and chemical formula of APTES, hexane, DMF, and SMP compounds used in the biofunctionalisation of the titanium surfaces..... 120
Figure II-11. Molecular structure of the KRGDSPC peptide sequence conjugated with fluorescein isothiocyanate (FITC) fluorochrome. 121
Figure II-12. Scheme of the purified Ar atmosphere chamber used for the biofunctionalisation of the titanium surfaces. Introduction chamber, main chamber, outgassing chamber, humidity (H_2O) gauge, oxygen (O_2) content gauge, heating system, vacuum system, and Argon tubes. G represents the gloves of the main and outgassing chambers..... 122
Figure II-13. Covalent immobilisation of the KRGDSPC peptide sequence on the titanium surfaces..... 123
Figure III-1. SEM micrographs of different laser-induced craters produced on a cp Ti surface with average pulse energies of (a) 44, (b) 86, (c) 176, (d) 262, (e) 340, and (f) 518 μJ, and 200 laser pulses at a repetition rate of 10 Hz. (a1) and (b1) High magnification SEM micrographs of the centre of the craters in (a) and (b), respectively. The scale bar is 100 μm (a-f), 5 μm (a1), and 10 μm (b1)..... 128
Figure III-2. SEM micrographs of the centre of the craters produced on a cp Ti surface, showing the LIPSS evolution with the number of pulses (N) and repetition rate in the ranges 2-100 and 1-10 Hz, respectively. The radiation fluence was ~ 0.2 J/cm^2. The yellow arrow indicates the polarisation direction of the linearly p-polarised laser beam. The yellow arrow-heads indicate the resolidified material between the LIPSS. The scale bar is 1 μm..... 130

Figure III-3. SEM micrographs of the centre of the craters produced on a cp Ti surface, showing the LIPSS evolution with the number of pulses (N) and repetition rate in the ranges 5-100 and 1-10 Hz, respectively. The radiation fluence was ~ 0.2 J/cm^2. The yellow arrow indicates the polarisation direction of the laser beam (45° towards the p-polarisation). The yellow arrow-heads indicate the resolidified material between the LIPSS. The scale bar is 1 μm. 131
Figure III-4. SEM micrographs of the centre of the craters produced on a cp Ti surface, showing LIPSS evolution with the number of pulses (N) and repetition rate in the ranges 5-100 and 1-10 Hz, respectively. The radiation fluence was ~ 0.2 J/cm^2. LIPSS were produced with a circularly polarised laser beam. The scale bar is 1 μm. 132
Figure III-5. SEM micrographs of the centre of the craters produced on a cp Ti surface, showing the microcolumns evolution with the number of pulses (N) and repetition rate in the ranges 2-100 and 1-10 Hz, respectively. The radiation fluence was ~ 0.6 J/cm^2. The yellow arrow indicates the polarisation direction of the linearly p-polarised laser beam. The scale bar is 1 μm (N = 2-50) and 10 μm (N = 100). 133
Figure III-6. SEM micrographs of the centre of the craters produced on a cp Ti surface, showing the microcolumns evolution with the number of pulses (N) and repetition rate in the ranges 5-100 and 1-10 Hz, respectively. The radiation fluence was 0.6 J/cm^2. Microcolumns were produced with a circularly polarised laser beam. The scale bar is 1 μm (N = 2-10) and 10 μm (N = 50-100). 134
Figure III-7. Laser-induced craters produced on a Ti-6Al-4V alloy surface in stationary conditions. The average pulse energy (E_p) and the number of pulses (N) were in the ranges 240-640 μJ and 20-1000, respectively. The scale bar is 100 μm. 136
Figure III-8. Plots of the square of the average crater diameter (D^2) versus the logarithm of the average pulse energy ($\ln E_p$) for number of pulses (N) in the range 20-1000. ... 137
Figure III-9. Optical micrographs of the laser textured surfaces of cp Ti and Ti-6Al-4V alloy specimens. The inset pictures in (a-c) show the characteristic colours of the different laser textured surfaces. The radiation fluence and the repetition rate were in the ranges 0.2-0.8 J/cm^2 and 50-1000 Hz, respectively. The scale bar is 100 μm. The laser-induced surfaces structures produced in (a-f) are depicted in Figure III-10. 138
Figure III-10. High magnification SEM micrographs of the laser textured surfaces of Ti-6Al-4V alloy. Surface textures consist of LIPSS (a-b), NP (c-d), and MC-LIPSS (e-f). The inset micrograph in (f) shows LIPSS covering the top of microcolumns. The SEM

micrographs in (b, d, and f) were acquired at 45° tilting. The yellow arrows indicate the polarisation direction of the linearly polarised laser beam. The radiation fluence and the repetition rate were in the ranges 0.2-0.8 J/cm^2 and 50-1000 Hz, respectively. The scale bar is 1 μm (a-d) and 10 μm (e-f). 140
Figure III-11. Representative three-dimensional (3D) reconstruction (Digital Elevation Mode-DEM) and the corresponding 2D roughness profiles of the laser textured surfaces of both Ti alloys obtained from Alicona-MeX© software 2.0. The roughness profiles were taken in a direction perpendicular to the laser beam scanning direction indicated in Figure III-10. 141
Figure III-12. XPS survey spectra for cp Ti (a) and Ti-6Al-4V alloy (b) surfaces. 143
Figure III-13. Expanded views of the XPS spectra of the Ti 2p and O 1s regions for cp Ti surfaces..... 144
Figure III-14. Expanded views of the XPS spectra of the Al 2p region for Ti-6Al-4V alloy surfaces. 145
Figure III-15. μ-Raman spectra for cp Ti surfaces. A and R denote the TiO_2 polymorphs anatase and rutile, respectively. The assigned active modes are presented in parentheses. 147
Figure III-16. μ-Raman spectra for Ti-6Al-4V alloy surfaces. A and R denote the TiO_2 polymorphs anatase and rutile, respectively. The assigned active modes are presented in parentheses. The inset graphic shows the spectrum of the polished surface. 148
Figure III-17. X-ray diffractograms for cp Ti surfaces obtained by Bragg-Brentano geometry. A and R denote the TiO_2 polymorphs anatase and rutile, respectively. 149
Figure III-18. X-ray diffractograms for cp Ti surfaces obtained by glancing incidence. A and R denotes the TiO_2 polymorphs anatase and rutile, respectively. 150
Figure III-19. Time evolution of the contact angle for DD water (a) and HBSS (b) droplets on polished and laser textured surfaces of Ti-6Al-4V alloy. The presented values were measured based on the droplet profiles taken in a direction perpendicular to the laser beam scanning direction (Figure III-10). 151
Figure III-20. Anisotropic wetting of DD water and HBSS droplets on LIPSS textured surfaces. Contact angle values measured for both testing liquids viewed perpendicularly and parallelly to LIPSS orientation (a). Representative droplet profiles for both liquids when viewed perpendicularly (b) and parallelly (c) to LIPSS orientation. 153

Figure III-21. Time evolution of the contact angle for DD water droplets on polished and laser textured surfaces of cp Ti. The presented values were measured based on the droplet profiles taken in a direction perpendicular to the laser beam scanning direction (Figure III-10). 154
Figure III-22. (A) Representative low magnification fluorescence images of MSCs on the surfaces of both Ti alloys at 24 h after cell seeding. Polished (a and e), LIPSS (b and f), NP (c and g), and MC-LIPSS (d and h) surfaces. F-actin fibres (Alexa Fluor® 488 *phalloidin*) and cell nucleus (DAPI) were stained green and blue, respectively. The scale bar is 200 μm. (B) SEM micrographs of the corresponding surface textures are also showed (see Figure III-10). The scale bar is 1 μm (LIPSS and NP) and 10 μm (MC-LIPSS). 158
Figure III-23. Quantification of MSCs spreading by analysing the average cell area on the cp Ti (a) and Ti-6Al-4V alloy (b) surfaces at 24 h after cell seeding. Statistical analysis was performed using ANOVA and Tukey's test. ∗ indicates statistically significant differences between the average values ($p < 0.05$). At least 50 cells were analysed for each type of surface. 159
Figure III-24. Representative high magnification fluorescence images of MSCs shape on cp Ti surfaces at 24 h cell seeding. Polished (a-c), LIPSS (d-f), NP (g-i), and MC-LIPSS (j-l) surfaces. F-actin fibres and cell nucleus were stained green and blue, respectively. The yellow arrows and arrow-heads (d and j, and g) indicate the cell stretching direction and filopodia structures, respectively. Similar MSCs shapes were observed for Ti-6Al-4V alloy surfaces. The scale bar is 50 μm. The corresponding surface textures are presented in Figure III-10. 160
Figure III-25. Quantification of the average MSCs stretching by analysing the cell elongation factor on the cp Ti (a) and Ti-6Al-4V alloy (b) surfaces at 24 h after cell seeding. Statistical analysis was performed using ANOVA and Tukey's test. ∗ indicates statistically significant differences between the average values ($p < 0.05$). At least 20 cells were analysed for each type of surface. 161
Figure III-26. Representative high magnification fluorescence images showing the F-actin fibres filaments organisation on the Ti-6Al-4V alloy surfaces at 24 h after cell seeding. Polished (a), LIPSS (b), NP (c), and MC-LIPSS (d) surfaces. F-actin fibres filaments were stained green. Similar organisation of the F-actin fibres filaments was

observed for the cp Ti surfaces. The scale bar is 50 μm. The corresponding surface textures are presented in Figure III-10. 161
Figure III-27. Quantification of MSCs adhesion by analysing the average cell density on cp Ti (a) and Ti-6Al-4V alloy (b) surfaces at 24 h after cell seeding. Statistical analysis was performed using ANOVA and Tukey's test. There is no statistically significant differences among the average values. At least 10 low magnification images were used for estimation of the cell density. 162
Figure III-28. Representative high magnification fluorescence images of vinculin showing the FAs (white squares) for both Ti alloys surfaces at 24 h after cell seeding. Polished (a-b), LIPSS (c-d), NP (e-f), and MC-LIPSS (g-h) surfaces. Vinculin and nucleus were stained red and blue, respectively. The yellow arrow-heads indicate the shape of the FAs. A representative image of the negative control (secondary antibody Alexa Fluor® 568) is shown on the top. The corresponding surface textures are presented in Figure III-10. 164
Figure III-29. Quantification of focal adhesions (FAs) area on cp Ti (a) and Ti-6Al-4V alloy (b) surfaces at 24 h after cell seeding. Statistical analysis was performed using ANOVA and Tukey's test. ∗ indicates statistically significant differences between the average values ($p < 0.05$). At least 50 cells were taken for estimation of the FAs area. 165
Figure III-30. Representative SEM micrographs of the MSCs on the laser textured surfaces of cp Ti at 24 h after cell seeding. LIPSS (a), NP (b), and MC-LIPSS (c) surfaces. The red lines were drawed to highlight the cell edges. The scale bar is 5 μm (a-b) and 10 μm (c). Similar cytoskeleton deformation was observed for cells cultured on Ti-6Al-4V alloy surfaces. 165
Figure III-31. (A) Quantification of cell nucleus spreading and deformation by analysing the average cell nucleus area and circularity on cp Ti (a and c) and Ti-6Al-4V alloy (b and d) surfaces, respectively, at 24 h after cell seeding. Statistical analysis was performed using ANOVA and Tukey's test. ∗ indicates statistically significant differences between the average values ($p < 0.05$) in (a) and (b). There is no statistically significant differences among the average values in (c) and (d). At least 100 cells were analysed for each type of surface. (B) Representative high magnification fluorescence images of cell nucleus are also presented. The scale bar is 50 μm. The corresponding surface textures are presented in Figure III-10. 167

Figure III-32. Representative SEM micrographs of MSCs partially aligned (cell contact guidance) on LIPSS textured surfaces at 24 h after cell seeding. Histograms presenting the relative frequency of the cell alignment angle on the cp Ti (a) and Ti-6Al-4V alloy (b) surfaces. At least 20 cells were analysed for each type of Ti alloy. The scale bar is 10 μm. 168
Figure III-33. (A) Representative fluorescence images of the collective cytoskeleton organisation on cp Ti and Ti-6Al-4V alloy surfaces at 2 weeks after cell seeding. Polished (a and e), LIPSS (b and f), NP (c and g), and MC-LIPSS (d and h) surfaces. F-actin fibres and cell nucleus were stained green and blue, respectively. The white arrows (b, f, d, and h) indicate the preferential stretching direction of cells. The white arrow-heads (c and g) indicate less filopodia structures in comparison with those observed at 24 h after cell seeding. The scale bar is 100 μm (a, b, d, e, f, and h) and 50 μm (c and g). (B) SEM micrographs of the corresponding surface textures are also presented. The scale bar is 1 μm (LIPSS and NP) and 10 μm (MC-LIPSS). 170
Figure III-34. Representative low magnification fluorescence images of cell nucleus on cp Ti (a-h) and Ti-6Al-4V alloy (i-p) surfaces at 24 h and 2 weeks after cell seeding. Polished (a, b, i, and j), LIPSS (c, d, k, and l), NP (e, f, m, and n), and MC-LIPSS (g, h, o, and p) surfaces. The scale bar is 200 μm. Quantification of cell proliferation at 2 weeks after cell seeding on cp Ti (q) and Ti-6Al-4V alloy (r) surfaces. Statistical analysis was performed using ANOVA and Tukey's test. ∗ indicates statistically significant differences between the average values ($p < 0.05$) in (r). There is no statistically significant differences among the average values in (q). At least 10 images were taken for counting the number of cell nucleus in the total area of the images. The corresponding surface textures are presented in Figure III-10. 172
Figure III-35. Representative high magnification fluorescence images of cell nucleus, Osterix (OSX) and Osteopontin (OPN) osteoblast markers on polished and laser textured surfaces of Ti-6Al-4V alloy at 2 weeks after cell seeding. Cell nucleus, OSX and OPN were stained blue and red, respectively. The scale bar is 50 μm. Quantification of the expression levels (fluorescence intensity) of OSX and OPN on cp Ti (a and c) and Ti-6Al-4Valloy (b and d) surfaces, respectively. Statistical analysis was performed using ANOVA and Tukey's test. ∗ indicates statistically significant differences between the average values ($p < 0.05$) in (a) and (c). There is no statistically significant differences among the average values in (b) and (d). At least 50 cells were analysed for

each type of surface. The corresponding surface textures are presented in Figure III-10. 173
Figure III-36. Representative high magnification fluorescence images of F-actin fibres (green), cell nucleus (blue), and Xylenol orange (XO; red) on cells cultured on tissue culture polystyrene (TCPS) at 4 weeks after cell seeding. Cells were cultured in non-osteogenic (Alpha-MEM) and osteogenic (Lonza Poietics™) media. TCPS was used as a control to confirm if the osteogenic medium was able to promote Mesenchymal Stem Cells osteogenesis. The scale bar is 50 μm. 175
Figure III-37. Two representative fluorescence images of cells cultured on cp Ti surfaces at 4 weeks after cell seeding. Cells were cultured in non-osteogenic (Alpha-MEM) and osteogenic (Lonza Poietics™) media. F-actin fibres and cell nucleus were stained green and blue, respectively. The scale bar is 100 μm. The corresponding surface textures are presented in Figure III-10. 176
Figure III-38. Two representative fluorescence images of cells cultured on Ti-6Al-4V alloy surfaces at 4 weeks after cell seeding. Cells were cultured in non-osteogenic (Alpha-MEM) and osteogenic (Lonza Poietics™) media. F-actin fibres and cell nucleus were stained green and blue, respectively. The scale bar is 100 μm. The corresponding surface textures are presented in Figure III-10. 177
Figure III-39. Representative high magnification fluorescence images of cells cultured on cp Ti surfaces at 4 weeks after cell seeding. Cells were cultured in osteogenic medium (Lonza Poietics™). Cell nucleus, Xylenol orange (XO), and OsteoImage™ (OI) were stained blue, red, and green, respectively. The scale bar is 50 μm for all the images. The corresponding surface textures are presented in Figure III-10. 178
Figure III-40. Representative high magnification fluorescence images of cells cultured on Ti-6Al-4V alloy surfaces at 4 weeks after cell seeding. Cells were cultured in osteogenic medium (Lonza Poietics™). Cell nucleus, Xylenol orange (XO), and OsteoImage™ (OI) were stained blue, red, and green, respectively. The scale bar is 50 μm for all the images. The corresponding surface textures are presented in Figure III-10. 179
Figure III-41. Quantification of the expression levels (fluorescence intensity) of Xylenol orange (XO) and OsteoImage™ (OI) markers of matrix mineralisation on cells cultured on cp Ti (a and c) and Ti-6Al-4V alloy (b and d) surfaces. Cells were cultured in osteogenic medium (Lonza Poietics™). Statistical analysis was performed using

ANOVA and Tukey's test. ∗ indicates statistically significant differences between the average values ($p < 0.05$). At least 25 images were analysed for each type of surface. 180
Figure III-42. Representative high magnification fluorescence images of cells cultured on cp Ti surfaces at 4 weeks after the initial cell seeding. Cells were cultured in non-osteogenic medium (Alpha-MEM). Cell nucleus, Xylenol orange (XO), and OsteoImage™ (OI) were stained blue, red, and green, respectively. The scale bar is 50 μm for all the images. The corresponding surface textures are presented in Figure III-10. 181
Figure III-43. Representative high magnification fluorescence images of cells cultured on Ti-6Al-4V alloy surfaces at 4 weeks after the initial cell seeding. Cells were cultured in non-osteogenic medium (Alpha-MEM). Cell nucleus, Xylenol orange (XO), and OsteoImage™ (OI) were stained blue, red, and green, respectively. The scale bar is 50 μm for all the images. The corresponding surface textures are presented in Figure III-10. 182
Figure III-44. Representative fluorescence images of *Staphylococcus aureus* (ATCC 25923) on cp Ti surfaces at 48 h after bacteria seeding. TCPS (a-b), polished (c-d), LIPSS (e-f), NP (g-h), and MC-LIPSS (i-j) surfaces. TCPS was used as a positive control for bacteria growth. Bacteria were immunostained with carboxyfluorescein succinimidyl ester (CFSE), which provides a green fluorescence signal. The scale bar is 50 μm for all the images. SEM micrographs of the corresponding surface textures are also presented. The scale bar is 1 μm (LIPSS and NP) and 10 μm (MC-LIPSS). Similar bacteria adhesion was observed for Ti-6Al-4V alloy surfaces. 184
Figure III-45. Quantification of the fluorescence intensity of *Staphylococcus aureus* (ATCC 25923) on cp Ti (a) and Ti-6Al-4V alloy (b) surfaces at 48 h after bacteria seeding. TCPS was used as a positive control for bacteria growth. Statistical analysis was performed using ANOVA and Tukey's test. ∗ indicates statistically significant differences between the average values ($p < 0.05$). At least 15 images were analysed for each type of surface. 185
Figure III-46. Representative photographs of the solubilised Crystal Violet dye collected from the TCPS (a), cp Ti and Ti-6Al-4V alloy surfaces (b), and the bacteria adhered on the TCPS used for the culture of the Ti specimens (c). Optical density (OD_{550nm}) at a

wavelength of 550 nm of the solubilised crystal violet dye collected from the cp Ti (d) and Ti-6Al-4V alloy (e) surfaces. 186
Figure III-47. Representative high magnification SEM micrographs of *Staphylococcus aureus* (ATCC 25923) biofilm on cp Ti surfaces at 48 h after bacteria seeding. Polished (a-b), LIPSS (c-d), NP (e-f), and MC-LIPSS (g-h). SEM micrographs (b, d, f, and h) were acquired at 45° tilting. The dashed white lines (a, c, e and g) were drawed to highlight the bacterial colonies. The scale bar is 1 μm for all images. Similar bacterial biofilm formation was observed for Ti-6Al-4V alloy surfaces. 187
Figure III-48. Expanded views of Ti 2p and Si 2p regions. The average spectra are presented after each reaction step, since similar peak components were observed for all surfaces. Peak fitting for polished surfaces of cp Ti after silanization (APTES), reaction with the cross-linker (SMP), and peptide grafting (KRGDSPC). 191
Figure III-49. Expanded views of O 1s region. The average spectra are presented after each reaction step, since similar peak components were observed for all surfaces. Peak fitting for polished surfaces of cp Ti after silanization (APTES), reaction with the cross-linker (SMP), and peptide grafting (KRGDSPC). 192
Figure III-50. Expanded views of N 1s. The average spectra are presented after each reaction step, since similar peak components were observed for all surfaces. Peak fitting for LIPSS textured surfaces of cp Ti after outgassing, silanization (APTES), reaction with the cross-linker (SMP), and peptide grafting (KRGDSPC). 193
Figure III-51. Expanded views of C 1s. The average spectra are presented after each reaction step, since similar peak components were observed for all surfaces. Peak fitting for LIPSS textured surfaces of cp Ti after outgassing, silanization (APTES), reaction with the cross-linker (SMP), and peptide grafting (KRGDSPC). 195
Figure III-52. Representative fluorescence images of the FITC-KRGDSPC peptide sequence (green fluorescence) covalently grafted on LIPSS (a), NP (b), and MC-LIPSS (c) textured surfaces of cp Ti. Fluorescence intensity of the grafted peptides (d). Statistical analysis was performed using ANOVA and Tukey's test. ∗ indicates statistically significant differences between the average values ($p < 0.05$). At least 10 images were analysed for each type of surface. The scale bar is 100 μm for all images. The corresponding surface textures are presented in Figure III-10. 196

List of Tables

Table I-1. Terms and definitions in biomaterials science established by the European Society for Biomaterials (adapted from [11]). 6
Table I-2. General classification of biomaterials according to their interaction with the surrounding tissues (adapted from [4]). 9
Table I-3. Physical properties of unalloyed titanium (adapted from [13]). 16
Table I-4. Biomedical grade titanium alloys (adapted from [4]). 18
Table I-5. Mechanical properties of titanium alloys developed for biomedical applications (adapted from [32, 34]). 19
Table I-6. Classification of the surfaces according to the contact angle (CA) of a water droplet. 52
Table I-7 Organic phase components of the bone matrix (adapted from [157]). 61
Table I-8 Bone cell types and their respective functions 61
Table I-9. Ligand-binding specificities of human integrins [159] 65
Table I-10. Characteristic features of cell-matrix and cell-biomaterial adhesion. 66
Table I-11. Different types of human stem cells. 70
Table II-1. Nominal chemical composition of cp Ti (Grade 2) and Ti-6Al-4V alloy (Grade 5). 98
Table II-2. Specifications of the s-Pulse HP model femtosecond laser system used for the surface texturing of the titanium specimens. 99
Table II-3. Laser processing parameters and conditions used for the production of the laser textured surfaces. 103
Table II-4. Ionic composition (mM) and pH of HBSS and human blood plasma. 108
Table II-5. List of primary antibodies and stainings used for fluorescence imaging of cells cytoskeleton, cells nuclei, FAs, osteoblast markers, and matrix mineralisation. . 113
Table II-6. List of the excitation and emission wavelengths of the fluorochromes used for labeling different cellular structures and osteoblast markers. 114
Table III-1. 2D Roughness parameters of the laser textured surfaces obtained from the three-dimensional (3D) surface reconstruction (Digital Elevation Mode-DEM) using Alicona-MeX© software 2.0. The roughness parameters were calculated from surface profiles taken in a direction perpendicular to the laser beam scanning direction indicated in Figure III-10. 142
Table III-2. XPS atomic ratios. 146

Table III-3. Spreading coefficient (n) calculated by fitting of the experimental data with a power function θ_{static} (t) = kt^n. The presented values were measured from droplet profiles taken in a direction perpendicular to the laser beam scanning direction (Figure III-10). 152
Table III-4. Surface free energy (γ_{SV}) of the surfaces of both Ti alloys calculated by using the geometric mean approach combined with the method of Owens and Wendt. The polar (γ_{SV}^{p}) and dispersive (γ_{SV}^{d}) components are also given. 155
Table III-5. Equilibrium contact angles of water and diiodomethane measured experimentally, and the surface tension (γ_{LV}) of both liquids and their polar (γ_{LV}^{p}) and dispersive (γ_{LV}^{d}) components [253]. 155
Table III-6. XPS atomic composition (at %) of cp Ti surfaces (Polished, LIPSS, NP, and MC-LIPSS) after outgassing, silanization (APTES), reaction with the cross-linker (SMP), and peptide grafting (KRGDSPC). 189

Table of Contents

Acknowledgements v

Abbreviations vii

List of Figures x

List of Tables xxiii

Outline xxx

Research Motivation xxx

Introduction 1

Chapter I. Literature Review 5

1. Biomaterials 5

1.1. What Are Biomaterials? 5

1.2. The Biomaterials Market 7

1.3. Essential Requirements of Endosseous Implants 8

1.3.1. Biocompatibility 8

1.3.2. Mechanical Properties 10

1.3.3. Corrosion and Wear Resistance 10

1.3.4. Osseointegration 11

2. Metallic Biomaterials and Their Limitations 12

3. Titanium and Its Alloys 15

3.1. Titanium Oxides 19

3.2. Biomedical Applications of Titanium and Its Alloys 21

4. Surface Modification of Titanium Implants 22

4.1. Pioneering Methods for Topography Modification 23

4.1.1. Plasma-Spraying 24

4.1.2. Grit-Blasting 25

4.1.3. Acid-Etching 26

4.1.4. Anodisation 27

4.2. Advanced Methods for Topography Modification 28

4.2.1. Photolithography 29

4.2.2. Electron Beam Lithography 30

4.2.3. Nanoimprint Lithography 31
4.3. Bioactive Titanium Surfaces 32
5. Laser Surface Texturing 36
5.1. Laser Ablation 37
5.2. Direct Femtosecond Laser Surface Texturing 37
5.2.1. Laser-Induced Periodic Surface Structures 38
5.2.2. Columnar Surface Structures 44
6. Wettability 50
6.1. Contact Angle and Surface Tension 51
6.2. Wetting Models for Rough Surfaces 53
6.3. Contac Angle Hysteresis 54
6.4. Bio-Inspired Wettability 54
6.5. Wettability Control Using Ultrafast Lasers 56
7. Bone Tissue 59
8. Dynamics of Cell Adhesion 62
8.1. Extracellular Matrix Proteins 63
8.2. Integrins and Cadherins as Adhesion Molecules 64
8.3. Adhesion sites 65
8.4. Signal Transduction and Cell Shape 67
9. Mesenchymal Stem Cells 69
9.1. Identification and Isolation of MSCs 70
9.2. Self-Renewal 72
9.3. MSCs Differentiation 73
10. Bacteria, The Agents of Infection 77
10.1. What Are Bacteria? 78
10.2. Biofilm and Its Formation 78
10.3. Staphylococci 81
10.4. Bacteria Adhesion on Bone 82
10.5. Bacteria Adhesion on Biomaterial Surfaces 83
11. On The Control of Tissue and Bacterial Cells Behaviour 83
11.1. Impact of Surface Topography on Tissue Cell Behaviour 84
11.2. Impact of Chemical Composition on Tissue Cell Behaviour 89
11.3. Impact of Surface Topography on Bacterial Cell Behaviour 91

Chapter II. Experimental 97
1. Laser Textured Surfaces 97
1.1. Preparation of the Titanium Alloys 97
1.2. Laser Surface Texturing 99
1.3. Surface Characterisation 105
1.4. Wettability Measurements 107
1.5. Human Mesenchymal Stem Cells Studies 111
1.5.1. Cell Culture 111
1.5.2. Cell Immunostaining and Staining 112
1.5.3. Epifluorescence Microscopy 114
1.5.4. Scanning Electron Microscopy 117
1.6. Bacteria Studies 117
1.6.1. Bacteria Culture 118
1.6.2. Immunostaining 118
1.6.3. Epifluorescence Microscopy 118
1.6.4. Crystal Violet Binding Assay 119
1.6.5. Scanning Electron Microscopy 119
2. Surface Biofunctionalisation 119
2.1. Molecular Structures 120
2.2. Peptide Grafting 121
2.3. X-ray Photoelectron Spectroscopy 124
2.4. Fluorescence Microscopy 125
3. Statistical Analysis 125
Chapter III. Results 127
1. Experiments in Stationary Conditions 127
1.1. Influence of the Radiation Fluence 127
1.2. Influence of the Number of Pulses and Laser Beam Polarisation 129
1.3. Summary 135
2. Experiments in Non-stationary Conditions 135
2.1. Determination of the Laser Beam Radius 135
2.2. Surface Morphology and Topography 138
2.3. Surface Chemical Composition 143
2.4. Crystallographic Structure 148

2.5. Wettability 150
2.6. Summary 156
2.7. Human Mesenchymal Stem Cells Behaviour 156
2.7.1. Cell Spreading and Shape (after 24 h of cell culture) 157
2.7.2. Cell Adhesion (after 24 h of cell culture) 162
2.7.3. Nucleus Spreading and Deformation (after 24 h of cell culture) 166
2.7.4. Cell Contact Guidance (after 24 h of cell culture) 168
2.7.5. Summary of the Results After 24 h of Cell Culture 169
2.7.6. Collective Cytoskeleton Organisation (after 2 weeks of cell culture) 169
2.7.7. Cell Proliferation and Commitment (after 2 weeks of cell culture) 171
2.7.8. Summary of the Results After 2 Weeks of Cell Culture 174
2.7.9. Cell Differentiation (after 4 weeks of cell culture) 174
2.7.10. Summary of the Results After 4 weeks of Cell Culture 182
2.8. Bacteria Behaviour 183
2.8.1. *Staphylococcus Aureus* Adhesion (after 48 h of cell culture) 183
2.8.2. Biofilm Formation (after 48 h of cell culture) 185
2.8.3. Summary of the Results After 48 h of Cell Culture 188
3. Biofunctionalised surfaces 188
3.1. Confirmation of RGD Peptide Grafting 189
3.2. Distribution and Fluorescence Intensity of RGD Peptides 195
3.3. Summary 197
Chapter IV. Discussion 199
1. Surface Modification of Titanium Implants vs Biological Response 199
2. Laser-Induced Surface Textures 200
3. Surface Topography, Chemical Composition and Crystallographic Structure of Titanium Implants 202
4. Wettability of Titanium Implants 204
5. MSCs Adhesion, Spreading and Shape 207
6. MSCs Proliferation, Commitment and Differentiation 210
7. Implant-Associated Infections 212
8. Biofunctionalisation of Titanium Implants 215

Chapter V. Conclusions and Suggestions for Future Work . 217
References 223
Appendices 247
A.1. Comissão de Acompanhamento de Tese (CAT) 247
A.2. IDS-FunMat Deliverables 247
A.3. Scientific Communications 247
A.4. Awards 249

Outline

Research Motivation

Cutting edge technologies and research have enabled the design and development of better or longer-lasting biomedical devices, which improve the patients quality of life. Despite the considerable progress already achieved in recent years, dental and orthopaedic implants still have a limited lifespan in the body (10-15 years), and failures due to inflammation, infection, corrosion, wear, fracture, and lack of osseointegration occur frequently. Among them, the lack of osseointegration and implant-associated infections are critical issues, which make surface engineering of implants an extremely active research field.

It is widely accepted that further improvements in biomaterials can only be achieved by endowing them with higher surface functionality. Both the topography and the chemical composition of an implant surface play an important role in controlling cell behaviour. Among the several methods commercially available for the surface modification of endosseous implants, ultrafast laser technology appears as highly promising, due to its flexibility, simplicity, controllability and high reproducibility in creating different types of surface textures on a wide range of materials such as metals, polymers, and ceramics. Moreover, laser processing allows texturing surfaces from the micro to the nano scale without the need of a clean room.

Recently, our research team showed that ultrafast lasers allow texturing titanium surfaces with a variety of textures with extremely promising characteristics for biomedical applications. Nano- and microscale textures, as well as complex bimodal distribution surface topographies can be reproducibly produced using femtosecond laser direct writing methods. The major goal of this research project was to explore the potential of these new surface modification methods to enhance the wettability and osseointegration of dental and orthopaedic implant surfaces, while reducing bacteria colonisation and biofilm formation. The investigation was performed on Grade 2 Ti (cp-commercially pure) and Grade 5 Ti-6Al-4V alloys.

Introduction

The dental and orthopaedic implants global market is undoubtedly expanding in the last few years, due to the continuous trend for population ageing and the need to treat younger patients. The American Academy of Orthopaedic Surgeons (AAOS) estimated that over 713,000 arthroplasties were performed in the US in 2000, including 150,000 hip and 299,000 knee replacements [1]. In 2010, the orthopaedic biomaterial market recorded revenues of $12 billion or 37.5% of the total global biomaterial market. In 2013, orthopaedic implants made up the bulk of all implanted devices (~ $1.5 million per annum worldwide [2]. Currently, the number of oral surgeries is also enormous and continuously increasing due to the rising concerns about oral health and aesthetics, mainly in Europe, which has the largest global market (~ 42 %) for dental implants and prosthetics [3].

Despite the economic impact of this field and the considerable progress already achieved, dental and orthopaedic implants still have a limited lifespan in the body (10-15 years), and failures due to inflammation, infection, corrosion, wear, fracture, and lack of osseointegration still occur [4]. Among them, lack of osseointegration and implant-associated infections are critical issues. Osseointegration is defined experimentally as the close contact between bone and implant material in histological sections and, in clinical terms, as the stability and ankylosis (fusion of a joint) of an implant in bone [5]. The inability of an implant surface to integrate with the adjacent bone and other tissues leads to micromotion, resulting eventually in implant loosening. Infections are primarily caused by bacteria, with *Staphylococcus aureus* representing by far the most common pathogen found in surgical wounds (50-60 % of the cases worldwide) [6]. Critical infections prevent proper integration of the implant into the surrounding tissues, and lead to inflammatory destruction of joints and bone [7].

The demand for dental and orthopaedic implants with improved biological response is permanent. It is widely accepted that significant improvements of the biological response of implants require endowing them with higher surface functionality, and using nano- and microstructured implant surfaces are one of the most promising methods to do so [8, 9]. Cells are expected to respond to nano- and microstructured surfaces because *in vivo* they live in an nanostructured environment and their own

machinery is composed of nano- and microstructures. The surface topography and chemical composition of an implant define properties such as surface roughness, anisotropy, wettability and surface free energy, which play an essential role in controlling implant-host interactions upon implantation (water shell formation, proteins absorption, cell adhesion, proliferation and differentiation), which are essential for the formation of a solid implant-bone interface and low infection risk [10].

Over the years several physical, chemical and mechanical methods have been investigated for the surface modification of titanium alloys, which are widely used as dental and orthopaedic implants, due to their low Young modulus, superior biocompatibility and high corrosion resistance, as compared to stainless steel and cobalt-based alloys [11, 12]. Some of these methods (plasma-spraying, grit-blasting, acid-etching, and anodisation) were successful commercially but many of them tend to contaminate the surface, change the structure and properties of the underlying material, potentiate bacteria colonisation, and do not allow different types of textures to be reproducibly produced [13]. More advanced methods, such as photolithography, electron beam lithography, and nanoimprint lithography, allow the creation of well-defined patterned surfaces with ordered or random nano- and microscale features, without altering the surface chemical composition [14]. These methods allow overcoming many of the limitations of the methods previously described, but due to their high cost and limitations on the shape of the parts whose surfaces are to be treated, these methods are more suited for the surface patterning of semiconductors and not titanium implants. In addition, they only allow patterning small areas. Conversely, surface texturing by ultrafast laser direct writing methods differ from other surface modification methods due to their flexibility, simplicity, and high reproducibility in the fabrication of different types of nano- and microtextures [15]. Moreover, the laser treatment does not lead to material surface contamination, and lasers allow texturing large areas of parts with complex geometry, such as dental and orthopaedic implants. Recently, our research team showed that ultrafast lasers allow texturing titanium surfaces with a variety of textures with extremely promising characteristics for biomedical application [16, 17]. Nano- and microscale textures, as well as complex bimodal distribution surface topographies can be produced in a highly reproducible manner using a femtosecond laser direct writing method. Therefore, the primary goal of the present thesis was to explore the potential of this new laser surface modification

method to enhance the wettability and osseointegration, while reducing bacteria colonisation of Grade 2 Ti (cp-commercially pure) and Grade 5 Ti-6Al-4V alloy surfaces. Cell adhesion and differentiation towards a particular lineage may also be achieved by biochemical surface modification, which consists in the incorporation of a thin layer of organic molecules such as proteins, enzymes or peptides at the surface [18]. Currently, the immobilisation of RGD peptide sequences is a common strategy for improving cell adhesion and bone formation on titanium surfaces [19, 20], and a previous study by the present group showed that the peptide layer promoted the adhesion of osteoprogenitor cells [21]. A secondary goal of the present thesis was to investigate the suitability of this method for the biofunctionalisation of laser textured surfaces.

The textured surfaces were characterised by binocular optical microscopy, scanning electron microscopy (SEM), three-dimensional (3D) surface reconstruction, atomic force microscopy (AFM), X-ray photoelectron spectroscopy (XPS), micro-Raman spectroscopy (μ-Raman), and X-ray diffraction (XRD). The surface wettability was evaluated by the sessile drop method, using distilled-deionized (DD) water and Hank's balanced salt solution (HBSS) as testing media. The biological response of the laser textured surfaces was assessed *in vitro*, using human mesenchymal stem cells (hMSCs) and *Staphylococcus aureus* (*S. aureus*) as the testing cells. The biofunctionalisation of the titanium surfaces was carried out by covalent grafting of a KRGDSPC peptide sequence. The peptide grafting was evaluated by XPS analysis. The distribution and fluorescence intensity of the grafted peptides after conjugation with fluorescein isothiocyanate fluorochrome (FITC-KRGDSPC) were evaluated by fluorescence microscopy.

Chapter I. Literature Review

In this section the reader will become acquainted with the essential scientific knowledge behind this PhD thesis. The major concepts forming the basis of this thesis are listed below:

- Biomaterials and their applications as endosseous implants;
- Titanium and titanium alloys as the base materials for the manufacturing of endosseous implants;
- Surface modification of endosseous implants;
- Ultrafast laser technology as a potential tool for surface texturing of endosseous implants;
- Surface wettability as a key factor influencing the adsorption of biological fluids and proteins;
- Bone tissue;
- Dynamics of cell adhesion;
- Mesenchymal Stem Cells (MSCs) for the regeneration of bone;
- Bacteria as the agents of bone and implant-associated infections;
- The impact of topographical and chemical cues on the response of tissue and bacterial cells.

1. Biomaterials

1.1. What Are Biomaterials?

Historically, the damage or loss of tissues or organs due to disease, accidents, and ageing have been a critical problem for Mankind. Archeological findings in Europe, Middle East, as well as in Central America show that men had tried to replace lost teeth using various materials, such as human teeth, teeth from animal origin, carved bone, pieces of ivory and mother of pearl, by attaching them to the remaining teeth [22-24]. However, the purpose was merely aesthetic. In terms of mastication they were worthless [25]. Similar evidence was also reported in what concerns orthopaedic implants. Hegetor (100 B.C.) was the first to describe in detail the anatomy and functioning of the hip joint. Hippocrates (460-370 B.C.), known as “the father of medicine” presented the first rational description of bone fractures. Furthermore, artificial prostheses such as

wooden legs, iron hands, and artificial feet were also reported during the Roman era. Unfortunately, a high level of critical infections and failure of these implantable devices existed due to the lack of suitable sterilisation techniques. All these evidences clearly prove that ancients contributed with considerable knowledge for the current state of the art in biomaterials science.

Biomaterials are materials used to construct artificial organs, rehabilitation devices, or implants that may be close or in direct contact with the body to augment or replace faulty tissues [11]. In general, biomaterials can be classified into living or once living materials, which fit into the description of tissue engineering, as well as synthetic materials. This concept is extended to the materials used in drug-delivery systems, biosensors or devices operating outside the body but in communication with it, such as artificial heart systems. Recently, progress in many different fields has paved the way to creating innovative biomaterials to improve existing treatments and develop new ones for a higher quality of life.

In 1987 the European Society for Biomaterials established some important terms and definitions in biomaterials science. These terms and definitions are given in **Table I-1**.

Table I-1. Terms and definitions in biomaterials science established by the European Society for Biomaterials (adapted from [11]).

TERMS	DEFINITIONS
Biomaterial	A non viable material used in a medical device, intended to interact with biological systems
Implant	Any medical device made from one or more materials that is intentionally placed within the body, either totally or partially buried beneath an epithelial surface
Prosthesis	A device that replaces a limb, organ or tissue of the body
Artificial organ	A medical device that replaces, in part or in whole, the function of one of the organs of the body

The definition of biomaterial was debated at a further conference held few years later, in which the reference to non viability was deleted [26]. The situation was posteriorly discussed by the current author in a contextual dictionary of biomaterials science published in 1999 [27]. The postulated definition at that time was “a material intended to interface with biological systems to evaluate, treat, augment or replace any

tissue, organ or function of the body". Recently, the meaning of biomaterial itself was revisited and discussed in a leading opinion published by David F. Williams (Editor-in-Chief of Biomaterials Journal), since the situations in which biomaterials are currently used are vastly different to those of just a decade ago [28]. After considering some of the more significant literature that reflect the changing emphasis on the character of biomaterials, the biomaterial paradigm was refined and the word "biomaterial" was redefined as:

"*A biomaterial is a substance that has been engineered to take a form which, alone or as part of a complex system, is used to direct, by control of interactions with components of living systems, the course of any therapeutic or diagnostic procedure, in human or veterinary medicine.*"

1.2. The Biomaterials Market

Very recently, Holzapfel *et al* [29] have discussed how smart the biomaterials need to be from a scientific and clinical point of view in order to fulfil the increasing expedinture worldwide. As a population ages, there is a growing need to replace and repair hard and soft tissues such as bones, cartilage, blood vessels or even entire organs. The biomaterials industry was worth ca. $28 billion in 2013, with an annual growth rate of 15 % expected for the next few years. This year the global market for biomaterials is expected to be worth $64.7 billion (www.marketsandmarkets.com).

In 2010, the orthopaedic biomaterial market recorded revenues of $12 billion or 37.5% of the total global biomaterial market. In 2013, orthopaedic implants made up the bulk of all devices implanted (around $10 billion). Nevertheless, the orthopaedic biomaterials market is estimated to grow slowly (2010-2015) because the market is relatively mature compared to other product markets. The market forecasting performed by BCC Research [2] with concern to the worldwide expenditure with joint replacement, implant, regeneraitve products, bone repair, cartilage, and soft tissues is showed in **Figure I-1**.

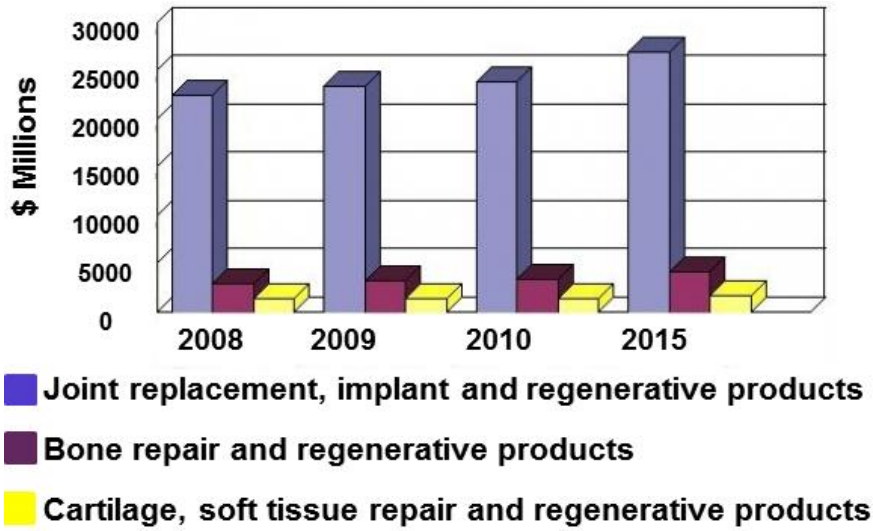

Figure I-1. Market forecasting of the worldwide expenditure with joint replacement, implant, regenerative products, bone repair, cartilage, and soft tissues (adapted from [2]).

In fact, the biomaterials market definitely holds a significant opportunity for innovators, but extensive research is required to develop new and improved products at competitive prices. In addition, it is worth noting that while metals, polymers and ceramics are currently the major players on the biomaterials market, significant changes are envisioned with tissue engineering constructs anticipated to become major contenders.

1.3. Essential Requirements of Endosseous Implants

The design and selection of biomaterials depend on the intended medical application. In order to serve for longer periods without rejection, an endosseous implant should possess major attributes regarding biocompatibility, mechanical properties, high corrosion and wear resistance, and osseointegration [11]. These essential requirements are described in the following sections.

1.3.1. Biocompatibility

Materials used as endosseous implants are expected to be highly nontoxic, noncarcinogenic and should not cause any inflammatory or allergic reactions in the body that may lead to cell death or impairment of cellular or tissue functions [30]. The success of a biomaterial is mainly dependent on the reaction of the body to the implant, which defines the biocompatibility of a material [31]. Biocompatibility has been defined as “the ability of a material to perform with an appropriate host response in a specific

application" [32]. In general, biomaterials are classified as biotolerant, bioactive and bioreabsorbable according to their interaction with the surrounding tissues, **Table I-2**.

Table I-2. General classification of biomaterials according to their interaction with the surrounding tissues (adapted from [4]).

CLASSIFICATION	RESPONSE	MATERIALS
Biotolerant	Formation of thin connective tissue capsules (0.1-10 μm) not adherent to the implant surface	▪ PTFE ▪ PMMA ▪ Ti and its alloys ▪ Co-Cr ▪ Stainless steel
Bioactive	Formation of bony tissue around the implant material displaying a strong integration with the implant surface	▪ Bioglass ▪ Synthetic calcium phosphates, including hydroxyapatite (HA)
Bioreabsorbable	Replaced by the autologous tissue	▪ PLA ▪ PGA ▪ Processed bone grafts ▪ Composites of all tissue extracts ▪ Proteins

Bioactive materials are often preferred for orthopaedic applications as they give rise to high integration with surrounding bone, stimulating osseoconduction and/or osseoinduction. Biotolerant materials are also accepted for implant manufacturing. As aforementioned, when implants are exposed to human tissues and fluids, several reactions take place between the host and the implant material, dictating the acceptability of these materials by the biological system. The issues with regard to biocompatibility are thrombosis, which involves blood coagulation and adhesion of blood platelets to biomaterial surface, and the fibrous tissue encapsulation of biomaterials that are implanted in soft tissues. Bioreabsorbable materials are intended to dissolve in the body once their purpose has been served. By dissolving in the body after fulfilling their function, implants engineered from bioreabsorbable materials could eliminate the need for risky explantation surgery for a plethora of implants and, consequently, enhance patient care. Polymeric materials such as PLA and PGA have proven successful in such applications as sutures, anchors, and screws. In recent years, however, the potential for bioreabsorbable materials beyond orthopaedic fixation

devices has become increasingly evident. Not only have they been instrumental in driving progress in drug-eluting devices development, but bioreabsorbable materials are also playing an important role in the revolutionary next-generation of resorbable implants, including stents, vascular grafts, scaffolds, and tissue engineering applications. It is noteworthy that the words bioreabsorbable and biodegradable are often considered as synonymous. However, while bioreabsorbable materials degradate and further resorb *in vivo* followed by elimination through natural pathways, biodegradable materials degradate and are further dispersed *in vivo* but may not be eliminated from the body [33].

1.3.2. Mechanical Properties

Hardness, tensile strength, Young modulus and elongation of endosseous implants are of prime importance [34]. The response of the material to the repeated cyclic loads or strains is determined by its fatigue strength, which determines the long-term success of the implant subjected to cyclic loading, for instance, during mastication, walking or running. If an implant fractures due to insufficient strength or mechanical properties mismatch between the bone and implant, then this phenomenon is referred to as biomechanical incompatibility. The materials replacing bone are expected to have an Young modulus similar to that of bone. The bone Young modulus varies in the range 4-30 GPa depending on the type of the bone and direction of measurement. However, the current implant materials have higher stiffness than bone, preventing the needed stress being transferred to adjacent bone. It results in bone resorption around the implant and consequently to implant loosening. This biomechanical incompatibility that leads to bone resorption is known as stress shielding effect. Therefore, materials with excellent combination of high strength and low Young modulus, closer to that of bone, has to be used for implantation in order to avoid loosening of implants.

1.3.3. Corrosion and Wear Resistance

The service lifetime of an implant is often determined by the corrosion and wear resistance of the material. Low wear and corrosion resistance of implant materials interacting with the body fluids results most of the times in the release of metal ions or metallic fragments by the implant into the body, which are found to cause allergic or toxic reactions. Therefore, the development of implant materials with high corrosion

and wear resistance is of prime importance for the longevity of the implant in the organism.

1.3.4. Osseointegration

Currently, osseointegration is defined experimentally as the close contact between bone and implant material in histological sections and, in clinical terms, as the stability and ankylosis of an implant in bone [5]. Following the studies carried out by P.I. Branemark and colleagues, implantologoy could reach a high level of the scientific recognition and the indexes of success reported nowadays [35, 36]. Early in the 1950s, Branemark discovered, unintentionally, an alternative mechanism of bone fixation during an experimental study on bone microcirculation and problems related to wound healing. These studies were carried out using what is known as "vital microscope", method in which a thin layer of live tissue is prepared and examined with a microscope. In his experiments, optical cameras made of tantalum (Ta) or titanium (Ti) were built and surgically introduced in the animal's bone during the *in vivo* studies. The technique used was not new, but what caught his attention was the fact of the metal titanium being adhered perfectly to bone.

Bone formation at the endosseous implant surface was considered as a positive outcome compared to fibrous encapsulation, which is a much less interesting result. From a physico-chemical point of view, osseointegration is considered as the result of the response to the foreign body, in which the surgical trauma arising from implantation induces a severe oxidative stress, resulting in the overproduction of free radicals and oxygenated derivatives at the titanium surface, which leads to the thickening of the titanium dioxide (TiO_2) layer [37]. Calcium and phosphorus ions from the bone matrix are then incorporated within the TiO_2 matrix, making the bone-implant interface highly dynamic. Conversely, the contamination or destruction of the TiO_2 layer leads to the pathological loss of osseointegration, known as peri-implantitis. Therefore, the inability of an implant surface to integrate with the adjacent bone and other tissues due to micromotion, results in implant loosening. Precisely how much of the implant surface contacts directly with bone, how rapidly the bone accrual occurs, and the mechanical nature and properties of the bone-implant interface is influenced by the nature of the implant surface itself. Surface topography, chemical composition, and wettability play a major role in the development of adequate osseointegration [13]. Hence, materials with

an appropriate surface are essential for the implant to integrate well with the adjacent bone. Currently, the term osseointegration is also used with non-metal surfaces, although the underlying biochemical mechanisms are different, because they are not related to titanium oxidation. An example of osseointegration observed in a human body is depicted in **Figure I-2**. A significant mass of human bone formed on a plasma-sprayed titanium porous coating 45 days after implantation is clearly observed. Nevertheless, the osseointegration of implants is a complex phenomenon and still deserves further investigation.

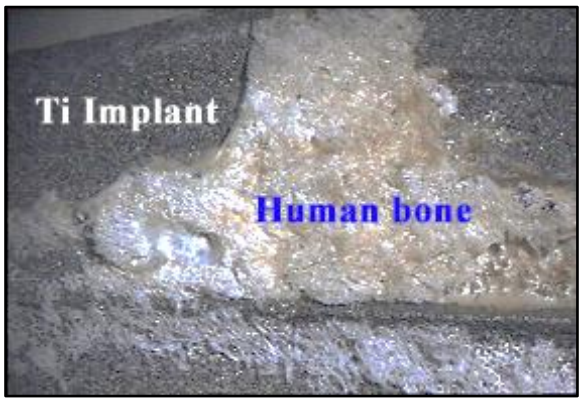

Figure I-2. Growth of human bone (osseointegration) on a plasma-sprayed titanium porous coating at 45 days after implantation (Courtesy of Hospital de Clínicas de Porto Alegre, POA, RS, Brazil).

2. Metallic Biomaterials and Their Limitations

The first metal alloy developed specifically for the human body environment was the "vanadium steel", used to manufacture bone fracture plates (Sherman plates) and screws. Most metals are used in the manufacturing of implants, such as iron (Fe), chromium (Cr), cobalt (Co), nickel (Ni), titanium (Ti), tantalum (Ta), niobium (Nb), molybdenum (Mo), and tungsten (W). However, these metals can only be tolerated by the body in minute amounts. Some of these metallic elements, in naturally occuring form, are essential in red blood cell functions (Fe) or in the systhesis of a vitamin B12 (Co), among others, but cannot be tolerated in large amounts in the body [32]. Metallic biomaterials found extensive use in partial or total joint replacement as well as in dental implants, in which requirements for mechanical stability are coupled with a demand for high strength and wear resistance tribological performance. The metallic materials commonly used as endosseous implants include 316L stainless steel (316LSS), cobalt

chromium (Co-Cr) alloys, and titanium and its alloys. It is noteworthy that none of the currently metallic alloys can completely fulfil all the necessary requirements for implants and, consequently, some limitations arise.

Elements such as Ni, Cr and Co are released from stainless steel and cobalt-chromium alloys due to corrosion in the body environment, inducing toxic effects. Skin related diseases such as dermatitis due to Ni toxicity have been reported and numerous animal studies have shown the carcinogenicity of Co [10]. In addition, both 316LSS and Cr-Co alloys possess much higher elastic modulus than bone, leading to insufficient stress transfer to bone and promoting bone resorption and loosening of the implant after some years of implantation. High cycle fatigue failure in hip prostheses is also observed as these implants are subjected to cyclic loading over many years. A scheme of the various causes of implant failure that may lead to revision surgery is shown in **Figure I-3**.

Amongst the materials available for endosseous implants, titanium alloys present outstanding characteristics, due to their combination of high strength, low density (high specific strength), high corrosion resistance, suitable inertness to body environment, high biocompatibility, low Young modulus and high osseointegration capacity [38, 39]. Their Young modulus (55-110 GPa) is lower than those of 316 L stainless steel (210 GPa) and cobalt-chromium alloys (240 GPa). Commercially pure (cp) Ti and Ti-6Al-4V ELI (Ti64, Extra Low interstitial) are the most commonly used titanium alloys for endosseous implant applications. Although titanium and its alloys have an excellent reputation for corrosion resistance and biocompatibility, the long-term performance of these alloys has raised some concerns, due to release of aluminum and vanadium from Ti-6Al-4V alloy. Both Al and V ions were found to be associated with long-term health problems, such as Alzheimer desease, neuropathy and ostemomalacia. Vanadium is also toxic both in the elemental state and an oxide (V_2O_5), which are present at the implant surface. Commercially pure titanium has poor shear strength, making it unsuitable for bone screws, plates and similar applications. It also tends to undergo severe wear in mated pairs or when sliding against other metals. Finally, wear of Ti and its alloys presenting high coefficient of friction can leads to the formation of wear debris that result in inflammatory reaction, causing pain and loosening of the implants due to osteolysis.

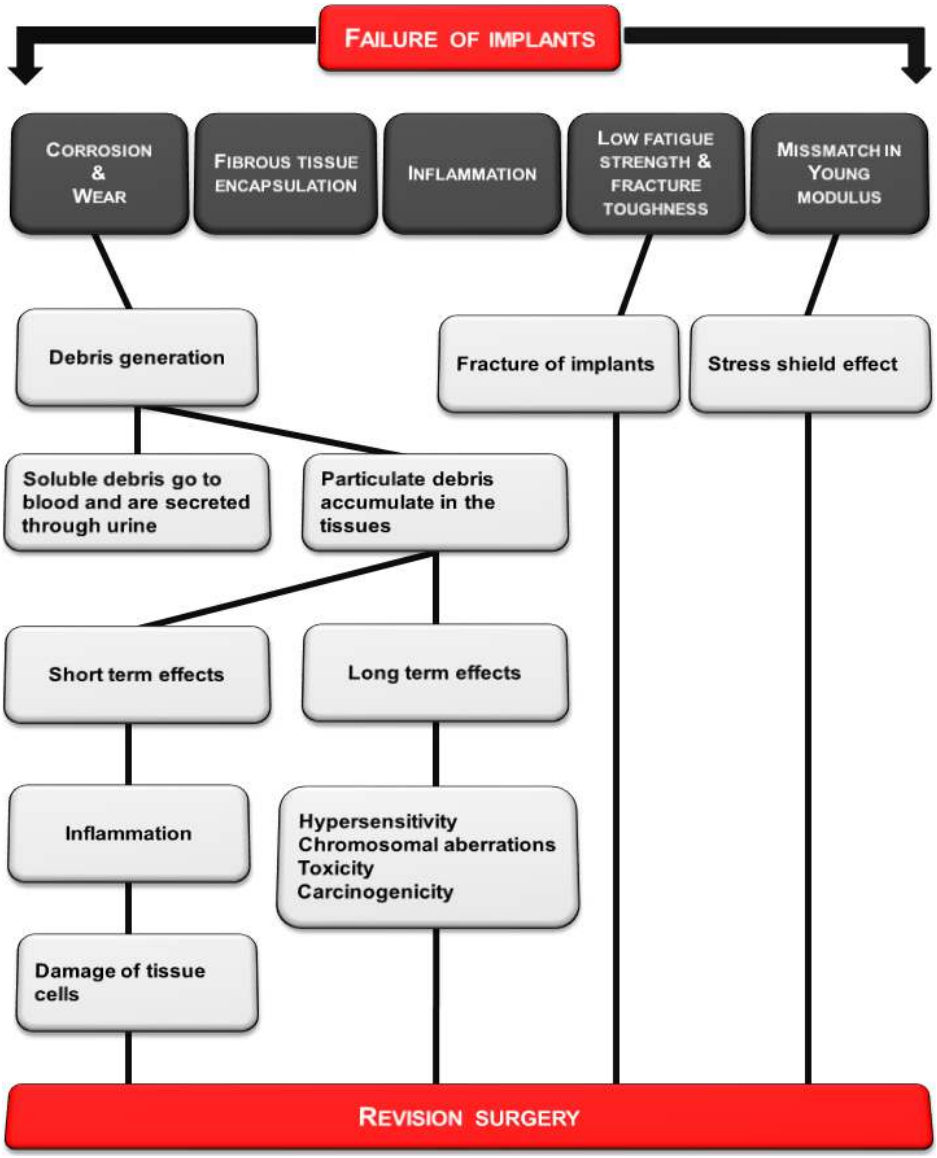

Figure I-3. Scheme of the various causes of implant failure that may lead to revision surgery (adpted from [4]).

Due to the limitations of these so-called first generation biomaterials, the service lifetime of implants made out of these materials is restricted to about 10-15 years. This fact has stimulated materials engineers and biomedical researchers to develop and optimise implants that may mimic human bone. For instance, the development of low Young modulus β-titanium alloys based on biocompatible alloying elements is one of the significant advances in this field [40, 41].

3. Titanium and Its Alloys

Since its discovery, titanium has been considered one of the most important metallic material both in the industrial and the biomedical fields. Over the past 20 years, the production methods of titanium and its alloys have maturated more rapidly than perhaps any other structural material in the history of metallurgy [39]. The following statement was given in the preface of the Proceedings of an International Conference on the Science, Technology and Applications of Titanium in 1968:

"*Never has there been, as in the case of titanium, the concentration of scientific and technical devotion to a single metal, with so much money, over such diversified areas, both technical and geographical. Never has a metal invited and received such attention, not only from the technical viewpoint, but also from the political arena and the world of finance. Never has metal, normally considered so mundane, been so extravagantly described as the wonder metal, the glamour metal and the metal of promise.*"

Titanium was discovered in 1791 by William Gregor in England [37]. During his accurate chemical analysis of Cornish minerals, W. Gregor could isolate a residual substance containing an unknown metal while studying ilmenite (iron titanium oxide, $FeTiO_3$) from the Manaccan valley. On that time, this metallic substance was named manaccanite. It received its current name in 1795, when Martin Heinrich Klaproth discovered the same metallic substance in the mineral rutile. The name "Titanium" comes from the mythological first sons of the Earth, the Titans in Greek mythology. Chemically, titanium is one of the transition elements in the group IV and period 4 of Mendeleev's periodic table. It has an atomic number of 22 and an atomic weight of 47.9 [13]. Being a transition element, titanium has an incompletely filled shell in its electronic structure, which enables titanium to form solid solutions with most substitutional elements. The physical properties of unalloyed titanium are summarised in **Table I-3**.

Table I-3. Physical properties of unalloyed titanium (adapted from [13]).

PROPERTIES	VALUES
Atomic number	22
Atomic weight [g/mol]	47.9
Crystal structure	
α (HCP)	
c [Å]	4.6832 ± 0.0004
a [Å]	2.9504 ± 0.0004
β (BCC)	
a [Å]	3.28 ± 0.003
Density [g/cm^3]	4.54
Coefficient of thermal expansion [K^{-1}], α-phase at 20 ºC	8.4x10^{-6}
Thermal conductivity [W/mK]	19.2
Melting temperature [ºC]	1668
Estimated boiling temperature [ºC]	3260
Transformation temperature [ºC]	882.5
Electrical resistivity	
High purity [μΩcm]	42
Commercial purity [μΩcm]	55
Elastic modulus, α, (GPa)	105
Yield strength, α, (MPa)	692
Ultimate strength, α, (MPa)	785

Titanium and its alloys have been used as an implantable biomaterial since the 1950's. Its alloys are constantly being improved with respect to their composition and bulk and surface properties in order to meet the need for improved function and longer lifetime in the human body. Titanium exists in two allotropic forms. At low temperatures it has a closed packed hexagonal crystal structure (HCP), commonly known as α-phase, which at 882.5 ºC transforms into another allotropic form with a body centrered cubic (BCC) crystal structure designated by β-phase, **Figure I-4 a-b**. The α to β transformation temperature varies when alloying elements are added to Ti, depending on the nature of these elements and their concentration. Alloying elements such as Al, O, N, and C tend to stabilise the α-phase and are known as α stabilisers. The

addition of these elements increases the beta transus temperature. The elements, such as V, Mo, Nb, Ta, Fe, and Cr, stabilise the β-phase and are known as β stabilisers. The addition of these elements decreases the β transus temperature, **Figure I-4 c**.

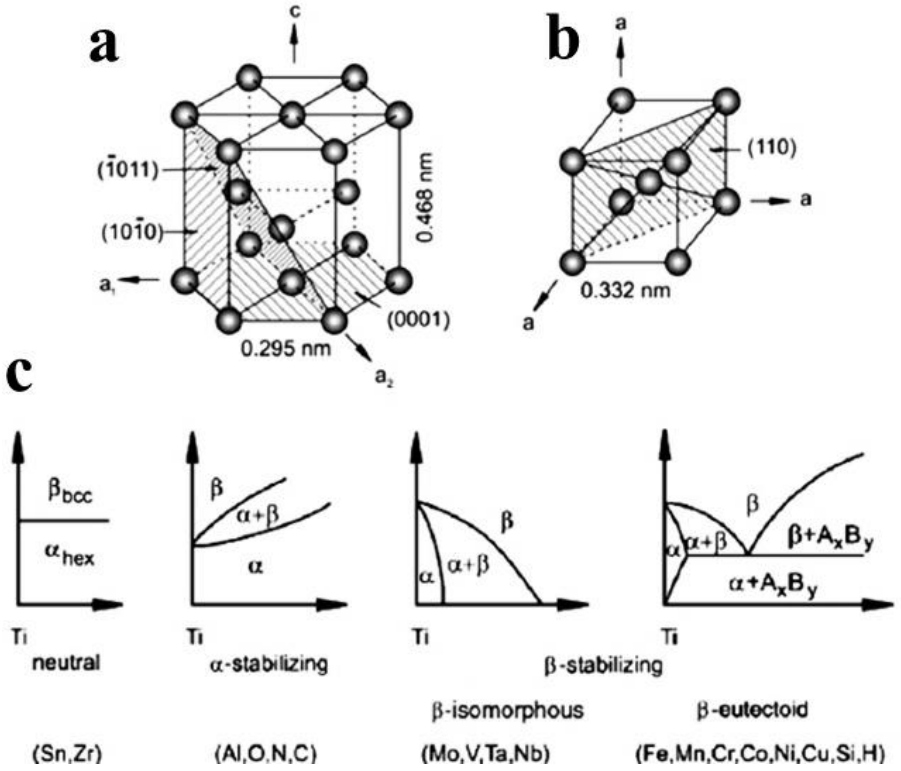

Figure I-4. Alpha (a) and beta (b) crystal structures of titanium and the different categories of titanium phase diagrams depending on the alloying elements (adapted from [39]).

The predominant phase in the microstructure of Ti alloys forms the basis for the most widely accepted classification of titanium alloys, according to the American Society for Testing and Materials (ASTM) standard. Alloys containing only α stabilisers and consisting entirely of α phase are known as α alloys. Alloys containing 1-2 % of β stabilisers and about 5-10 % of β phase are designated by near-α alloys. Alloys containing higher amounts of β stabilisers, resulting in 10-30 % of β-phase in the microstructure are known as α + β alloys. Alloys with even higher amounts of β stabilisers, where the β-phase can be retained at room temperature by fast cooling, are known as metastable β alloys. These alloys tend to decompose into an α + β mixture on aging. Most biomedical grade titanium alloys belong to α + β or metastable β class. The major biomedical grade titanium alloys are presented in **Table I-4**.

Table I-4. Biomedical grade titanium alloys (adapted from [4]).

TITANIUM ALLOYS	STANDARD	ALLOY TYPE
First generation (1950-1990)		
Commercially pure Ti (cp Grade 1-4)	ASTM 1341	α
Ti-6Al-4V ELI wrought	ASTM F136	α+β
Ti-6Al-4V ELI Standard grade	ASTM F1472	α+β
Ti-6Al-7Nb wrought	ASTM F1295	α+β
Ti-5Al-2.5Fe	-	α+β
Second generation (1990-till date)		
Ti-13Nb-13Zr wrought	ASTM F1713	Metastable β
Ti-12Mo-6Zr-2Fe (TMZF)	ASTM F1813	β
Ti-35Nb-7Zr-5Ta (TNZT)	-	β
Ti-29Nb-13Ta-4.6Zr	-	β
Ti-35Nb-5Ta-7Zr-0.4O (TNZTO)	-	β
Ti-15Mo-5Zr-3Al	-	β
Ti-Mo	ASTM F2066	β

Despite the predominance of commercially pure (cp) titanium and Ti-6Al-4V, specially Ti-6Al-4V ELI as orthopaedic and dental materials, new titanium alloys like Ti-6Al-7Nb and Ti-5Al-2.5Fe were developed in order to overcome the problem of potential toxicity of elements in Ti-6Al-4V alloy. In addition, biomedical titanium alloys with greater biocompatibility were also developed. These alloys are mainly β type, and contain only non-toxic elements such as Nb, Zr, Ta, etc. The β alloys enhance the biomechanical compatibility because their Young modulus is closer to bone's as compared to α+β alloys. Furthermore, they also exhibit higher strength and toughness. The mechanical properties of the different types of titanium alloys developed for biomedical applications are presented in **Table I-5**.

Table I-5. Mechanical properties of titanium alloys developed for biomedical applications (adapted from [32, 34]).

MATERIALS	TENSILE STRENGTH [MPa]	YIELD STRENGTH [MPa]	YOUNG MODULUS [GPa]
α alloys			
cp Ti Grade 1	240	170	102.7
cp Ti Grade 2	345	275	102.7
cp Ti Grade 3	450	380	103.4
cp Ti Grade 4	550	485	104.1
α+β alloys			
Ti-6Al-4V	895-930	825-869	110-114
Ti-6Al-4V ELI	860-965	795-875	101-110
Ti-6Al-7Nb	900-1050	880-950	114
Ti-5Al-2.5Fe	1020	895	112
β alloys			
Ti-13Nb-13Zr	973-1037	836-908	79-84
Ti-12Mo-6Zr-2Fe	1060-100	1000-1060	74-85
Ti-15Mo	874	544	78
Ti-15Mo-5Zr-3Al	852-1100	838-1060	80
Ti-15Mo-2.8Nb-0.2Si	979-999	945-987	83
Ti-35.3Nb-5.1Ta-7.1Zr	596.7	547.1	55
Ti-29Nb-13Ta-4.6Zr	911	864	80

3.1. Titanium Oxides

The metal oxides present on the surface of biomedical metallic alloys play an important role in determining their biocompatibility [42, 43]. Except for inert materials, such as Au and Pt, the response of the body to metallic implants is mediated by the oxide layer, which depends on the chemical composition of the bulk material. This oxide layer plays an important role in controlling the corrosion and wear resistance of the metal. Titanium spontaneously forms a layer of titanium oxide (~ 6-10 nm thick) within microseconds when exposed to ambient atmosphere [38]. Moreover, these alloys exhibit repassivation capability, i.e., when the oxide film is disrupted mechanically, the underlying metal reacts rapidly with the atmospheric oxygen to reform the oxide film [44]. Titanium dioxide (TiO_2) spontaneously form at the surface of titanium and Ti alloys. In the case of alloys, the natural oxide film can also contain oxides of the alloying elements. For instance, alumina (Al_2O_3) and vanadium III, IV, and V oxides may be present on the surface of Ti-6Al-4V alloys [45].

Chapter I. Literature Review

Understanding the composition, microstructure and physicochemical properties of titanium oxides is a central point to explain the interactions between the biological environment and Ti and Ti alloys implants. As previously mentioned, the oxide layer that naturally covers titanium alloys consists generally of the more thermodinamically stable Ti oxide, TiO_2. However, titanium can assume a wide range of valencies in its oxides and other oxides with different Ti/O ratio exist, namely Ti_3O, Ti_3O_2, TiO, Ti_2O_3, Ti_3O_5, and Ti_2O_2. Titania (TiO_2) exhibits three polymorphs: rutile, anatase, and brookite, but can also be amorphous [43]. While rutile is the stable phase, both anatase and brookite are metastable. The latter is difficult to synthesise and so is seldom studied. The formation of the TiO_2 phases depends significantly on the synthesis parameters. The kinetics of these processes typically are considered in terms of temperature and time. In air, pure bulk anatase begins to transform irreversibly to rutile at about 600 ºC, but transitions temperatures may vary in the range 400-1200 ºC.

An important point is the alteration of the oxide layer when Ti implants interact with the biological environment. Sundgren *et al.* [46] and McQueen *et al*. [47], using Auger Electron Spectroscopy (AES) to study the change in the composition of the titanium surface during implantation in human bone, observed that the oxide formed on titanium implants grows and takes up minerals during the implantation. The growth and uptake occur even though the adsorbed layer of protein is present on the oxide, indicating that mineral ions pass through the adsorbed protein. Liedberg *et al*. [48], using Fourier Transform Infrared Reflection Absorption Spectroscopy (FTIRRAS), showed that phosphate ions are adsorbed by the titanium surface after protein adsorption. Using X-ray Photoelectron Spectroscopy (XPS), Hanawa [45] demonstrated that oxides on titanium and Ti-6Al-4V alloy change into complex phosphates of titanium and calcium containing hydroxyl groups, which bind water on immersion in artificial saliva (pH 5.2). All these studies indicate that the surface oxide on titanium reacts with mineral ions, water, and other constituents of biological fluids, and that these reactions in turn cause a remodeling of the surface. The main reasons for this are still largely unknown, but it may be related the high dielectric constant of TiO_2, which should result in considerably stronger van der Waals bonds on TiO_2 than other oxides. In addition, TiO_2 may be catalytically active for a number of organic and inorganic chemical interactions influencing biological processes at the implant interface. Properties of the oxide such as stoichiometry, defect density, crystal structure and orientation, surface defects, and

impurities were suggested as factors determining biological performance of the implants [37].

3.2. Biomedical Applications of Titanium and Its Alloys

Earlier applications of titanium in medical, surgical, and dental devices were based on post-World War II advances in manufacturing processes as a result of the more stringent requirements demanded by the aerospace and military industry [13]. Despite the large scale application in the industrial and military sectors, the success of application of titanium and its alloys in the biomedical field is truly astonishing. Increased use of titanium and its alloys as biomaterials stems is due to their lower Young modulus, superior biocompatibility and better corrosion resistance when compared to stainless steel and cobalt-based alloys. These attractive properties were the driving force for the early introduction of α and $\alpha + \beta$ alloys as well as the more recent development of modern Ti-based alloys. In spite of the fact that Ti-6Al-4V alloy was originally developed for aerospace applications, its high corrosion resistance and excellent biocompatibility led its introduction in the biomedical field. Typical applications are dental implants and parts for orthodontic surgery, joint replacement parts for hip, knee, shoulder, spine, elbow and wrist, bone fixation materials like nails, screws, nuts and plates, housings for pacemakers and artificial heart valves, vascular stents, surgical instruments, and components in high-speed blood centrifuges [12]. Some examples of dental implants, orthopaedic joint replacement parts, vascular stents, and screws and plates for bone fixation are depicted in **Figure I-5**.

One of the most common application of titanium and its alloys is in artificial hip joints that consist of an articulating bearing (femoral head and cup) and a stem [30]. The articulating bearing must be positioned in such a way that they can reproduce the natural movement inside the hip joints whereas secure positioning of the femoral head in relation to the intramedullary canal of the femur. The cup, which is the articulating partner of the femoral head, is used for fixation by reaming out the natural acetabulum to fit the design. Titanium alloys are also often used in knee joint replacements, which consist of a femoral component, a tibial component, and a patella. These alloys are also used as dental implants, which can be classified as subperiosteal, transosteal and endosseous according to their position and shape [49]. Subperiosteal implants consist of a custom-cast framework resting on the bone surface beneath the mucoperiosteum. The

implant is secured on posts or abutments that penetrate the mucosa into the oral cavity. Transosteal implants can only be placed in the frontal lower jaw while endosseous implants can be placed in both the upper and lower jaws via a mucoperiosteal incision. This is the most commonly used type of implants and can be applied in almost any situation as single implants to replace one missing tooth as well as in cases of partial and total edentulism. The most commonly used endosseous implant are root-forming analogs.

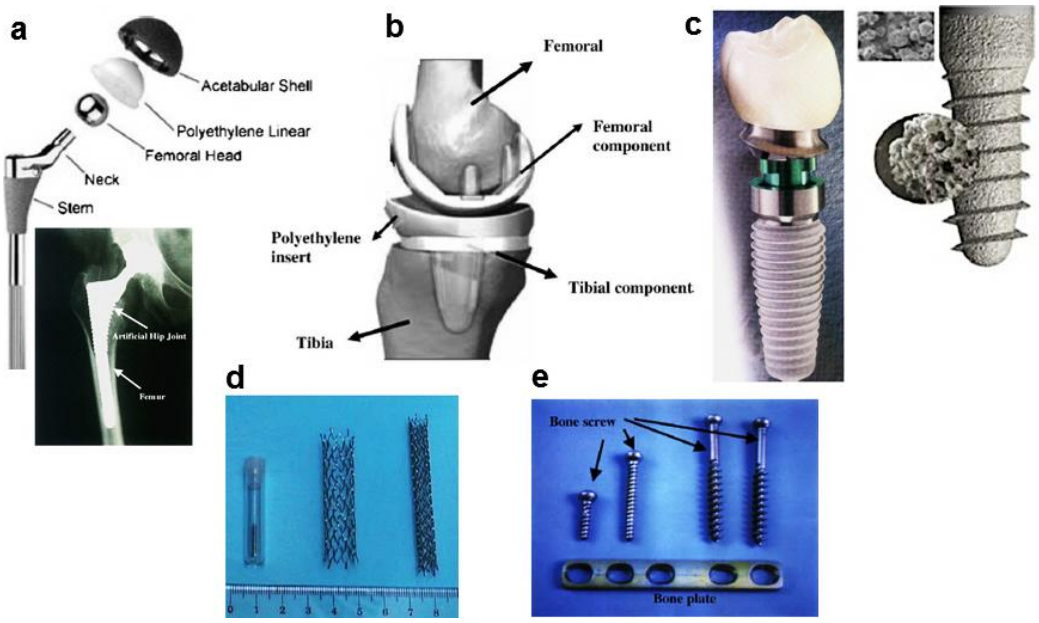

Figure I-5. Applications of titanium and its alloys on the manufacturing of hip joints (a), knee (b), dental implants (c), vascular stents (d), and screws and plates for bone fixation (e) (adapted from [13]).

4. Surface Modification of Titanium Implants

As aforementioned, the bulk properties of biomaterials, such as non-toxicity, corrosion resistance, Young modulus, and fatigue strength have been recognised to be highly relevant in terms of the properly selection of a biomaterial for a specific biomedical application. The events after implantation include interactions between the biological environment and the artificial material surfaces, onset of biological reactions, as well as the particular response paths chosen by the organism [12, 50].

It is well accepted that the material surface has an upmost importance in the response of the biological environment to the artificial medical devices. Various surface parameters such as roughness, chemical composition, wettability, electrical charge, and

crystallinity influence the response of the host tissue [51]. In titanium implants, the common manufacturing steps usually lead to an oxidised and contaminated surface layer, which is often stressed and plastically deformed, non-uniform and rather poorly defined. Such "native" surfaces are not appropriate for biomedical applications and some surface treatments must be performed. Furthermore, specific surface properties that are different from those of the bulk are often required. Positive modulation of the host-implant tissues response by an optimised surface, that may improve the quality of osseointegration by accelerating bone healing and increasing bone anchorage to the implants, is the main goal of this research field. The concept that titanium biocompatibility supported clinical osseointegration success has dominated the clinical thinking, and experiments with surface topography encouraged new considerations of improvements in bone formation at the implant surface [5]. In addition, many efforts have been made in the development of surface treatments capable of reducing or preventing bacteria colonisation on the implant surfaces [52, 53].

Basically, two different approaches are used in the surface modification of implants. In the first, the bone-implant interface is improved physically by the surface topography modification [54]. The rational for this approach is that at the micrometre level, a rough surface presents a higher specific area than a smooth surface, and thus facilitates bone anchorage and reinforces the bone-implant mechanical interlocking, at least up to a certain level of roughness. At the nanometre level, roughness increases the surface energy, and thus potentially improves extracellular matrix protein adsorption and bone cell migration and proliferation, and consequently osseointegration. In the second approach the interface is improved by coating the implant material with compounds such as calcium phosphates, which might stimulate bone regeneration. Biochemical surface modification is a variant of this second approach, which incorporates organic molecules such as proteins, enzymes or peptides at the surface, to induce specific cell and tissue responses [19, 21, 55]. In the following sections the major surface modification methods applied for physically or chemically altering the titanium implants are described.

4.1. Pioneering Methods for Topography Modification

In this section the first developed methods for surface modification, referred here as "pioneering methods", commercially applied on dental and orthopaedic titanium

implants are described. Among them, plasma-spraying, grit-blasting, acid-etching, and anodisation stant out [54]. Nevertheless, several other physical and chemical methods exist [13]. These surface modification methods are used by dental implant manufacturers such as Straumann AG (Bern, Switzerland), Astra Tech (Astra Zeneca, Rueil-Malmaison, France), Nobel Biocare (Sweden), and Cam Implants BV (Leiden, The Netherlands) [5]. They are basically used for promote a micrometre roughening of the implant surfaces in order to increase the bone-to-implant contact (BIC) [50]. At least three different lines of thinking have evolved to better interpret or explain how surface topography at the microscale can improve osseointegration. The first is the biomechanical theory of Hansson and Norton [56], the second is the concept of contact osteogenesis [57], and the third is a surface signaling hypothesis supported by many cell culture investigations [35, 58]. It is noteworthy that for an optimal and true ingrowth of bone into porous structures of implants, a macro porosity with the size in the range 100-500 μm is typically required. Therefore, the surface modification methods described here (with smaller scale ranges) are more directed towards the development of a proper interlocking of the host tissue with the implant surface rather than an ingrowth of bone.

4.1.1. Plasma-Spraying

Plasma-spraying uses a plasma to melt and spray materials onto the implant surfaces [13]. The coating deposition can be performed in ambient atmosphere (atmospheric plasma spraying-APS) or in inert gas or in vacuum (vacuum plasma spraying-VPS). The powder of the coating material is injected through a plasma torch and the material molten in contact with the high temperature plasma is projected towards the surface of the implant where the droplets solidify and fuse together, forming a coating up to 500 μm thick. The thickness must reach 40-50 μm to be uniform. The density, temperature of the plasma beam and the velocity of the carrier gas are essential to the formation of the coating. The high temperature of the plasma in plasma torches makes plasma spraying one of the successful thermal spraying techniques. Plasma spraying has some advantages as compared to alternative thermal spraying methods such as high deposition rate (80 $g.min^{-1}$), thick deposits (5 mm in some materials), and high quality of the coatings. However, plasma spraying coatings tend to present low adhesion to the substrate. To overcome this drawback the implant surfaces are usually roughened before thermal spraying in order to increase adhesion.

Plasma spraying is often used to deposited ceramic coatings such as Al_2O_3, ZrO_2, TiO_2, and hydroxyapatite (HA) on the surface of titanium implants, **Figure I-6**. The TiO_2 coatings are used clinically due to their excellent wear and corrosion resistance conjugated with an adequate osseointegration. The HA coatings are widely used due to their osseoinduction properties. However, Al_2O_3 and ZrO_2 coatings cannot bond directly to human bone due to its bioinertness, thereby limiting their applications in orthopaedic and dental implants. The resulting plasma sprayed porous coatings have an average roughness (R_a) of approximately 7 μm.

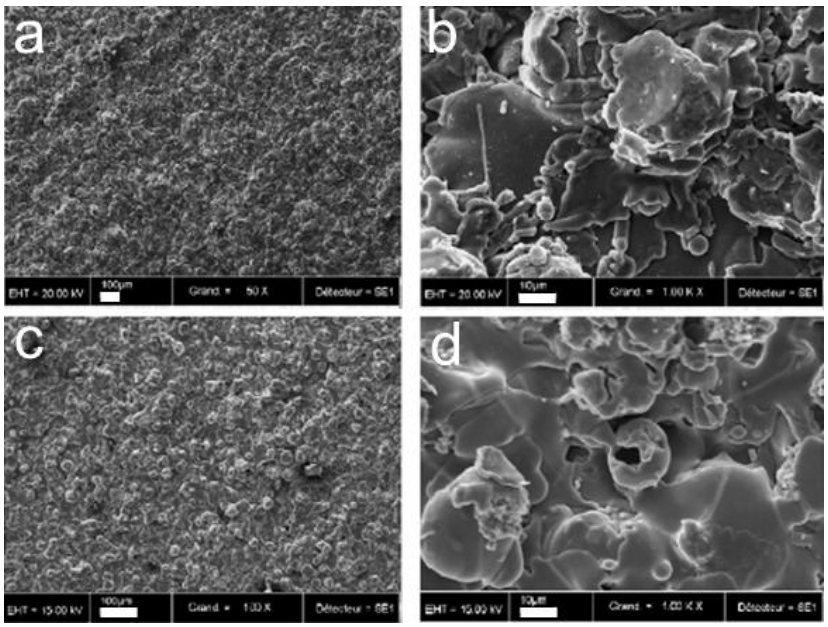

Figure I-6. Low and high magnifications SEM micrographs of plasma-sprayed titanium (a-b) and hydroxyapatite (c-d) coatings (adapted from [54]). The scale bar is 100 μm (a and c) and 10 μm (b and d).

4.1.2. Grit-Blasting

This technique consists in blasting the implant surface with hard ceramic particles such as Al_2O_3 and TiO_2, with sizes in the range 25-75 μm, carried by a fast gas flow. The ceramic particles are projected through a nozzle at high velocity by means of compressed air. The particle kinectic energy transferred during the impact with the implant causes a plastic deformation of the surface, **Figure I-7**. Depending on the size of the ceramic particles, different surface roughnesses (R_a) can be achieved. TiO_2 particles with an average size of 25 μm produce a moderately rough surface in the 1-2 μm range. Blasting with Al_2O_3 often results in incrustation of the particles into the

implant surface and residues remain even after ultrasonic cleaning, acid passivation and sterilisation. Biocompatible, osseoconductive and resorbable calcium phosphates materials such as HA, beta tricalcium phosphate and phosphates mixtures have been considered useful blasting materials. These materials are resorbable, leading to a clean, textured, pure titanium surface.

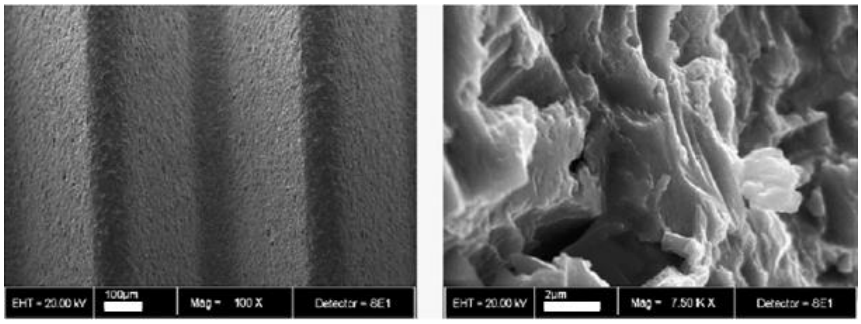

Figure I-7. Low and high magnifications SEM micrographs of a titanium surface blasted with TiO_2 particles (adapted from [54]). The scale bar is 100 µm (left) and 2 µm (right).

4.1.3. Acid-Etching

Acid-etching consists in the immersion of titanium implants in strong acids such as HCl, H_2SO_4, HNO_3 or HF for roughening the implant surfaces, **Figure I-8 a-b**. The acid removes the "native" oxide layer and some of the underlying material. The extent of material removed depends on the acid concentration, temperature and treatment time. This treatment provides homogeneous roughness and increases surface area. High temperature acid-etching produces a homogeneous microporous surface with pit diameters in the range 0.5-2 µm. Dual acid-etching is a variation of this method, in which titanium implants are immersed for several minutes in a mixture of concentrated HCl and H_2SO_4 heated above 100 °C. A combination of sandblasting and acid-etching (SLA treatment) may also be performed. This treatment uses 250-500 µm particles blasting process followed by etching with a mixture of HCl-H_2SO_4 acid, **Figure I-8 c-d**. Chemical treatments might reduce the mechanical properties of titanium implants due to hydrogen embrittlement. The creation of micro cracks on the surface may reduce the fatigue resistance of the implants.

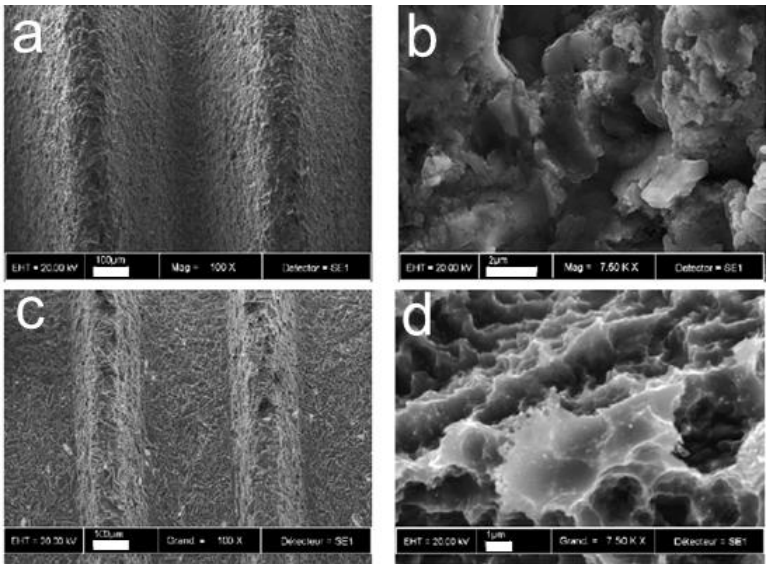

Figure I-8. Low and high magnifications SEM micrographs of a titanium surface treated with a fluoride solution (a-b) and SLA (c-d) (adapted from [54]). The scale bar is 100 μm (a and c), 2 μm (b), and 1 μm (d).

4.1.4. Anodisation

Potentiostatic or galvanostatic anodisation of titanium implants in strong acids such as H_2SO_4, H_3PO_4, HNO_3 or HF at high current density (200 $A.m^{-2}$) or potential (100 V) is applied to produce micro- or nanoporous surfaces and TiO_2 nanotubes, **Figure I-9**. This method depends on various parameters such as current density, concentration of acids, composition and electrolyte temperature. Anodisation provides oxide layers with more than 1 μm in thickness. When strong acids are used as electrolytes, the oxide layer dissolves in the regions where the current density is higher and is thickened in other regions. The dissolution of the oxide layer leads to the formation of micro and nanopores on the titanium surfaces. Modifications in the microstructure and the crystallinity of the titanium oxide layer also occur.

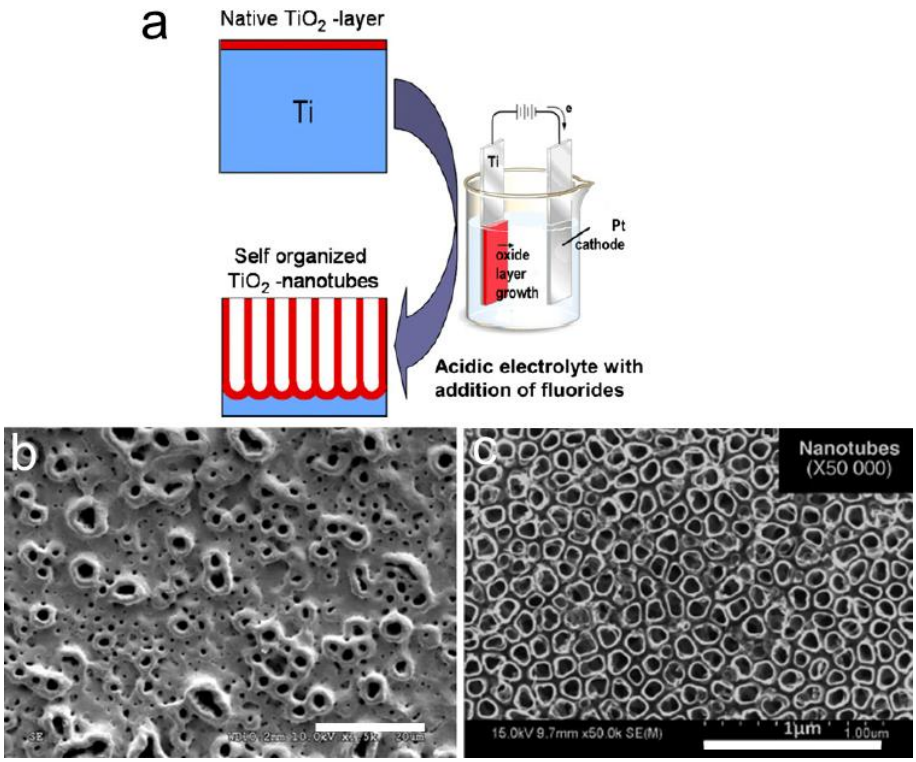

Figure I-9. Schematic setup for anodisation of titanium in fluoride containing electrolytes (a). SEM micrographs of TiO_2 micropores (b) and nanotubes (c) (adapted from [5, 11]). The scale bar is 20 µm (b) and 1 µm (c).

4.2. Advanced Methods for Topography Modification

Among the current surface modification methods, photolithography, electron beam lithography, and nanoimprint lithography are described in this section [11, 14, 59, 60]. While the precedent methods showed significant clinical success in terms of osseointegration, these advanced methods are not commercialy employed yet. Nevertheless, they allow the creation of well-defined patterned surfaces, with ordered or random micro- and nanotopographies, in a highly reproducible fashion and with a precise control of the surface chemistry. These characteristics allow overcoming the poor control of topography organisation and chemical composition of the methods previously described. Micro- and nanopatterned surfaces have been widely tested for the cell response by using *in vitro* studies. The possibility of producing surfaces with grooves with different aspect ratios as well as arrays of pillars, pits and islands with different patterns allows studying the influence of nanotopography on cell behaviour. However, while the methods described in the previous section were established for surface modification of titanium implants, the advanced methods are usually applied for surface patterning of "model materials" such as semiconductors and polymers.

4.2.1. Photolithography

Photolithography is commonly used for patterning of semiconductor devices used in the microelectronic industry. It allows fabricating well-defined surface features, with extremely high lateral resolutions, in materials ranging from silicon and quartz to polystyrene and silicone elastomer. Photolithography involves the use of a mask as a template for pattern transfer. A light sensitive photoresist is first deposited onto the surface, generally by spin coating. A mask with predefined patterns is then placed over the resist-covered substrate and the surface is exposed to UV light. Finally, the substrate is immersed in a developer solution, where the outcome depends on wheter positive or negative photoresist is used, **Figure I-10**.

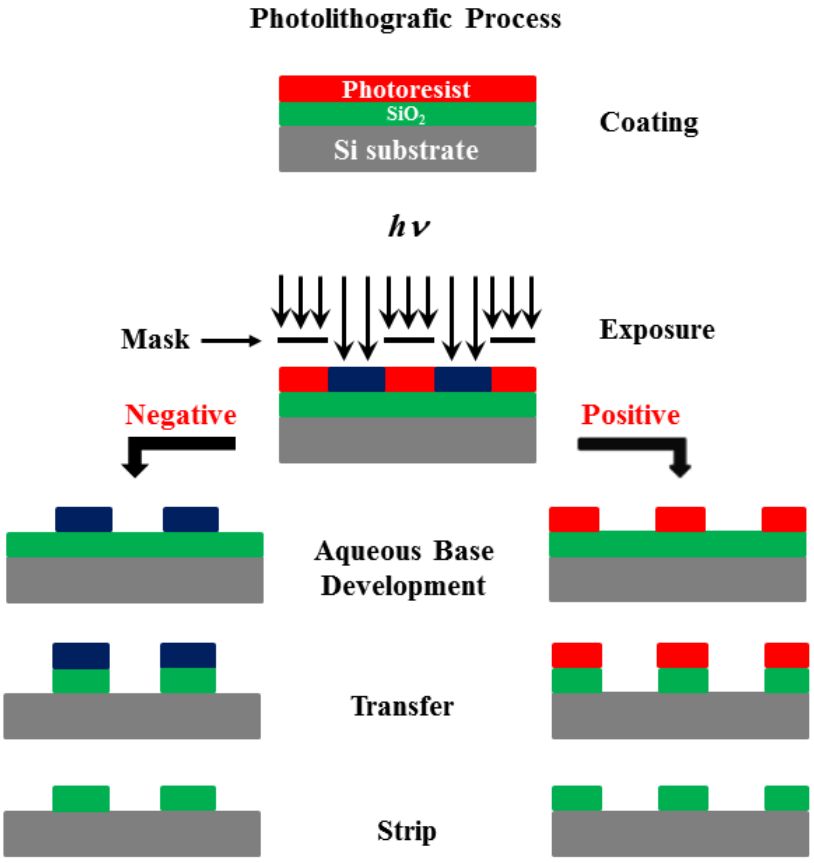

Figure I-10. Scheme of a photolithographic process performed on SiO_2.

In both cases, exposure to light changes the structure of the resist. If the photoresist is positive, the light makes it soluble in the developer solution, and thus the regions exposed by the mask dissolve and are washed away. In contrast, negative photoresist is further polymerised by light and exposures becomes more difficult to dissolve. As a

result, only the areas that were initially protected by the mask are washed away. In any case, the process results in the transfer of the pattern to the surface. In semiconductors microfabrication a further etching step is applied, but in bioengineering the surface is often subjected to surface modification with biomolecules. The final step consists in the removal of the remaining photoresist after the functionalisation steps by washing with an organic solvent. Photolithography does have its drawbacks. First, it is unsuitable for patterning non-planar surfaces. Second, due to the diffraction limit of light, the resolution of photolithography is limited to a value close to the wavelength of light. Therefore, its adequacy to nanopatterning is very limited and higher resolution methods have been introduced to allow producing ordered surface topographies with resolution at the nanometre level.

4.2.2. Electron Beam Lithography

To overcome the resolution limit due to the diffraction of light, Electron Beam Lithography (EBL) has been developed. It allows reaching 3-5 nm in resolution, not achievable by photolithography. Its resolution depends on the electron scattering on the resist and on the substrate nature.

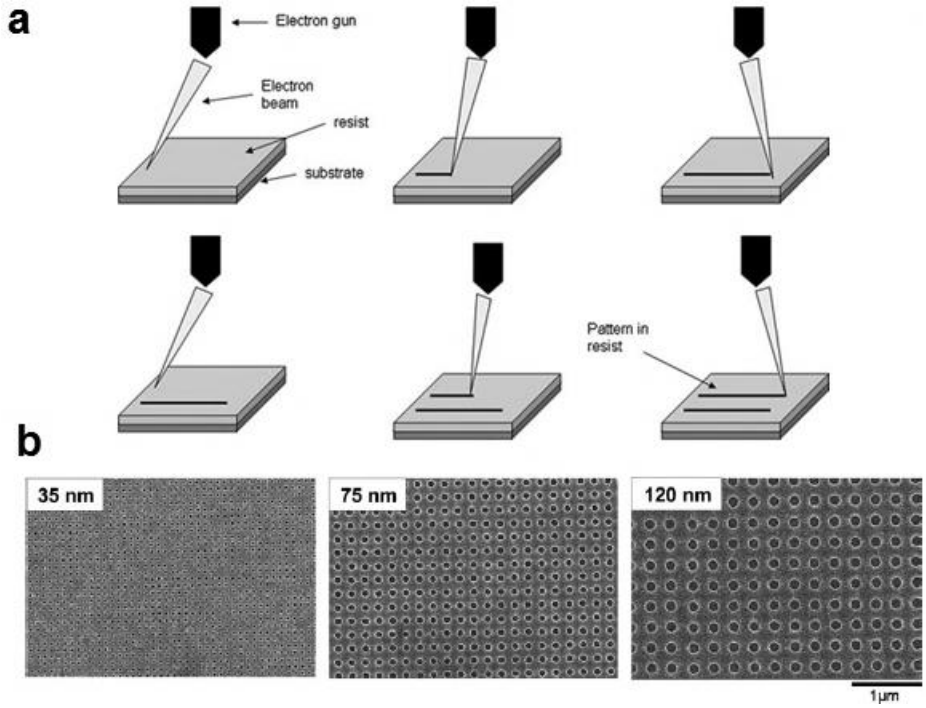

Figure I-11. Scheme of electron beam lithography (a) and SEM micrographs of different nanopitted silicon surfaces with different pit sizes produced by high-resolution e-beam (b) (adapted from [59]). The scale bar is 1 µm.

The principle of EBL is similar to that of photolithography, but it presents two main differences. First, the resist is exposed to an electron beam instead of light, and second, the process is maskless, i.e., the pattern is produced by direct writing, **Figure I-11**. The direct writing ability makes EBL a flexible tool for fabricating patterns with arbitrary shapes and sizes. The resist used in EBL is electron-sensitive and is either positive or negative, but negative resist tend to yield lower resolution. Despite the possibility of fabricating nanopatterns down to 3-5 nm, EBL is a high cost and time-consuming process, in which only small areas can be patterned.

4.2.3. Nanoimprint Lithography

Nanoimprint Lithography (NIL) is a high-throughput low-cost technique for fabricating surface patterns with a resolution down to 50 nm. Due to its resolution range, NIL has become increasingly popular in the microelectronics industry, particularly in the manufacturing of integrated ciscuits, and magnetic and optoelectronic devices. Basically, NIL consists of compression molding and pattern transfer. A polymer resist, preferably a thermoplastic, is first deposited onto the substrate surface. A solid mold with predefined nanometre scale features is then pressed onto the resist as the system is heated to above the glass transition temperature of the polymer. At this stage, the polymer behaves as a liquid and can therefore conform to the shape of the mold. Then, the mold is removed following the imprint process and a Reactive Ion Etching (RIE) step is performed to remove the resist remaining on the patterned regions, exposing the underlying substrate and completing the pattern transfer process [61], **Figure I-12**. Because NIL functions by direct deformation of the resist material, it can overcome the limits of resolution posed by light diffraction and electron beam scattering in photolithography and electron beam lithography, respectively.

Aside from thermal NIL, UV-assisted NIL and step-and-flash imprint lithography (SFIL) are also applied. Both techniques use UV light instead of heating the system. In UV-based NIL, the resist is a low viscosity UV-curable precursor material. Photo-initiators are added so that the resist can be polymerised and hardened when exposed to UV light through a mask. Transparent materials, such as quartz are used to create the mask as UV light penetrates through the transparent regions to interact with the resist. An advantage of UV-based NIL over the thermal system is that it can be performed at room temperature, avoiding repeated heating and cooling cycles imposed by the thermal

process, which can decrease throughput and cause improper overlay of device layers and features in multilayer fabrication.

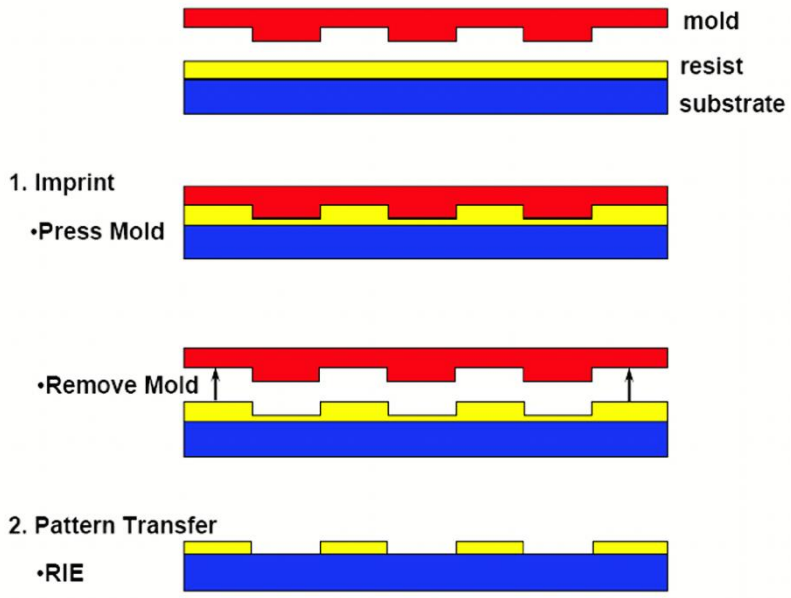

Figure I-12. Scheme of a nanoimprint lithographic process (adapted from [61]).

4.3. Bioactive Titanium Surfaces

Implant surfaces often need to be chemically modified in order to facilitate cell attachment and growth. A common strategy is coating the implant surfaces with biomolecules that enhance cell adhesion and/or differentiation towards a particular lineage [55]. Bioactive modification of implants offers the advantage of improving the surface bioactivity by an ultrathin layer of bioactive molecules without adversely affecting the bulk properties. Biomolecules present in the extracellular matrix (ECM), such as collagenous and non-collagenous glycoproteins, hyaluronan, and proteoglycan, are usually employed [20]. The ECM does not only act as a scaffold for the cells, but it also serves as a reservoir for growth factors and cytokines responsible for modulating cell activation status and turnover. Depending on the cell type different matrix molecules are secreted, and the nature and amount of these molecules change with developmental age. Consequently, ECM composition, immobilisation, and spatial arrangement vary for each type of tissue. Bone ECM consists mostly of collagen I mineral and non-collagenous growth factors and proteins such as osteocalcin, fibronectin, and vitronectin [62]. RGD (arginine [R], glycine [G], and aspartic acid [D])

is a peptide sequence present in most of the extracellular matrix proteins known to be involved in cell adhesion. Currently, immobilisation of RGD peptide sequences on titanium surfaces is a common strategy for enhancing cell adhesion and bone formation [55]. In this section, some of the methods used to immobilise bioactive molecules on implant surfaces are described. These methods include physical adsorption, chemically covalent bonding and biomimetic incorporation of the biomolecules [18, 20].

The physical adsorption method involves soaking the implants in a solution containing the bioactive molecules of interest, where spontaneous adsorption takes place, making this method fast and convenient, **Figure I-13**. Proteins such as albumin, fibronectin, and BMP 2 can be adsorbed on the implant surfaces by this method. However, this method does not allow controlling the amount and density of the adsorbed bioactive molecules accurately. The adsorption process depends mainly on the surface chemistry, topography, hydrophilicity, the solution properties, as well as the chemical interactions between the bioactive molecules and the implant surface. Changes in surface properties can alter the way a protein is adsorbed onto the implants, for example by conformational alteration. The relatively weak bounding forces that maintain the biomolecules adherent to the implant surface depend on factors, such as the solution pH, ionic strength, and protein concentration. Therefore, changes in these conditions may lead to the desorption of the molecules making the process unreliable.

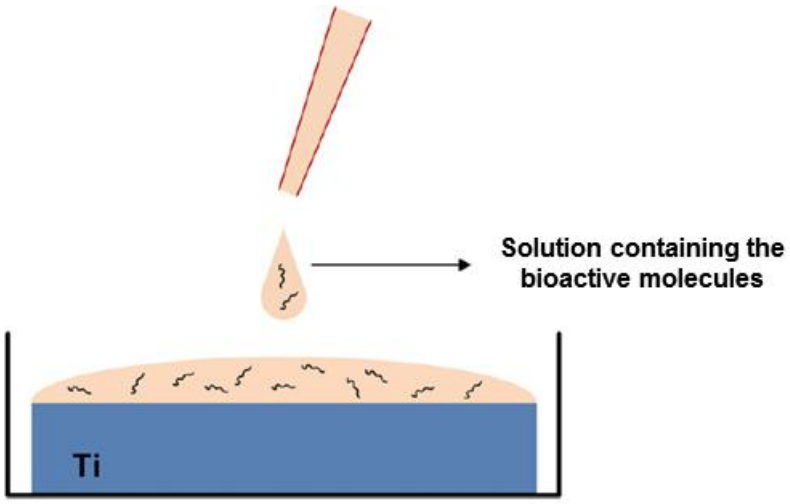

Figure I-13. Schematic drawing of the physical adsorption method. The implants are soaked in a solution containing the bioactive molecules of interest. Generally, proteins are used as the target biomolecules (adapted from [20]).

In contrast, covalent immobilisation of biomolecules to implant surfaces is less dependent on the external conditions. Covalent bonding allows immobilising controlled densities of bioactive molecules and controlling their orientation on the implant surface. However, this method involves many steps and requires the use of different types of chemicals and cross-linking agents. Briefly, it is based on the functionalisation of an implant surface with reactive groups, such as amino or carboxylic groups, which can react with the acidic or basic functions of bioactive molecules, respectively. Therefore, stable amide bonds could form between the surface and bioactive molecules. Usually, a bifunctional molecule is further used to introduce a longer spacer to immobilise the bioactive molecule on the implant surface, preserving its conformation in biological environments. Different strategies have been devised for the immobilisation of bioactive molecules on titanium surfaces: (i) covalently bounding of an intermediary aminoalkylsilane spacer molecule to oxidised titanium surfaces, followed by the covalent bounding of bioactive molecules to the free terminal NH_2 groups using glutaraldehyde or 3-succinimidyl-3-maleimidopropionate (SMP) as coupling agents, **Figure I-14**; (ii) introduction of functional groups by plasma polymerisation of allyl alcohol or allyl amine, which can yield hydroxyl or amino groups, respectively, to readily participate in the immobilisation of bioactive molecules on the titanium surfaces; and (iii) treatment of a titanium surface with a biomimetic anchor such as dopamine, and then covalently grafting with glucopyranosylamine (CS) or oxidised dextran using glutaraldehyde as a coupling agent. Consequently, the CS or dextran are employed to covalently bond the bioactive molecules of interest. The strategy (i) used in the present work for the covalent immobilisation of a RGD peptide sequence on the laser textured titanium surfaces was developed by our group [21] and is depicted in **Figure I-14**.

Finally, the third method for obtaining bioactive surfaces consists in the precipitation of inorganic minerals from simulated body fluid (SBF) with ion concentrations similar to human blood plasma, at mild temperature and pressure. The immersion of titanium implants in a metastable solution of calcium phosphate allows producing biomimetic coatings consisting of bone-like apatite layers [18].

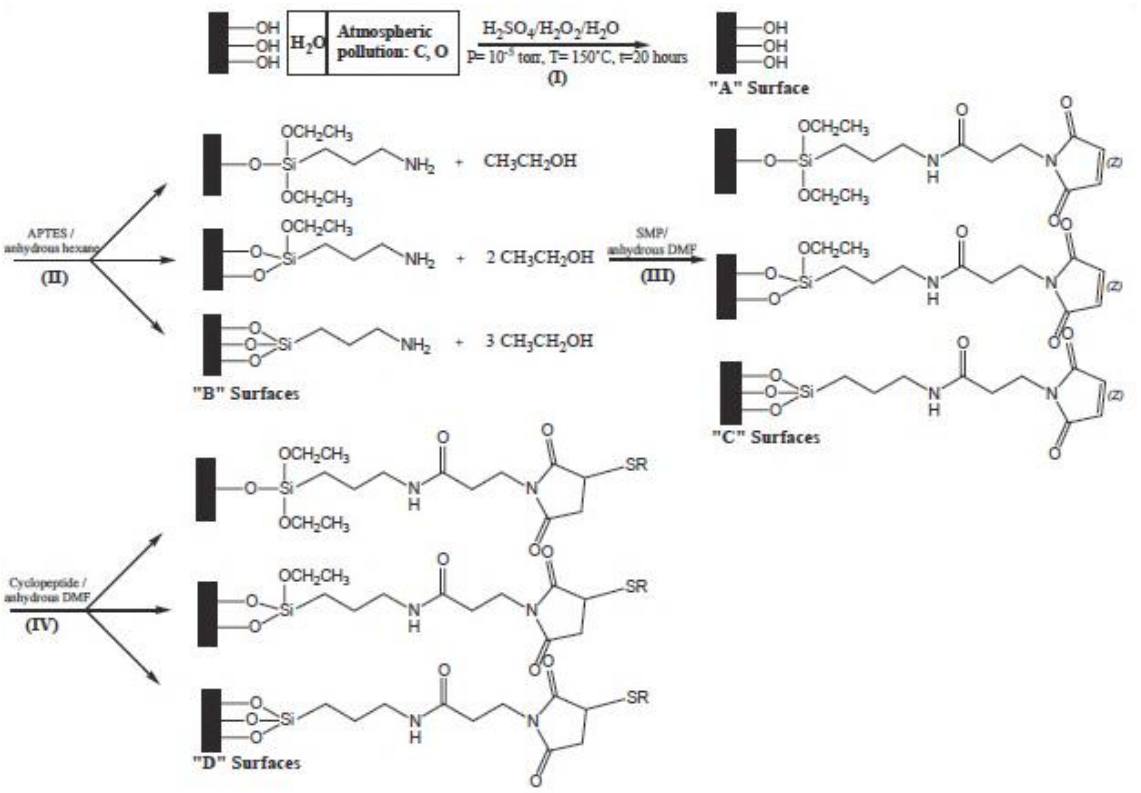

Figure I-14. Covalent immobilisation of a RGD peptide sequence on a Ti-6Al-4V surface using an intermediary aminoalkylsilane spacer molecule to the oxidised titanium surface, followed by the covalent bounding of the peptide sequence to the free terminal NH_2 groups using 3-succinimidyl-3-maleimidopropionate (SMP) as a coupling agent (adapted from [21]).

In this approach the minerals being bioabsorbable, porous, and microcrystalline, have the ability to load bioactive molecules onto titanium, **Figure I-15**. Among these solutions, simulated body fluid (SBF), Hank's balanced salt solution (HBSS), Dulbecco's phosphate buffered saline (DPBS), supersaturated calcium phosphate solution (SCP), supersaturated calcium phosphate (CP), calcium phosphate supersaturated solution (CPS), and supersaturated calcifying solutions (SCS) are commonly used. The thickness of the mineral layer is contolled by altering the temperature or ion concentration of the solutions. The higher the initial calcium and phosphate ion concentration the higher the initial supersaturation level, and the precipitation of the minerals. Remarkably, these biomimetic coatings can even grow on three-dimensional scaffolds.

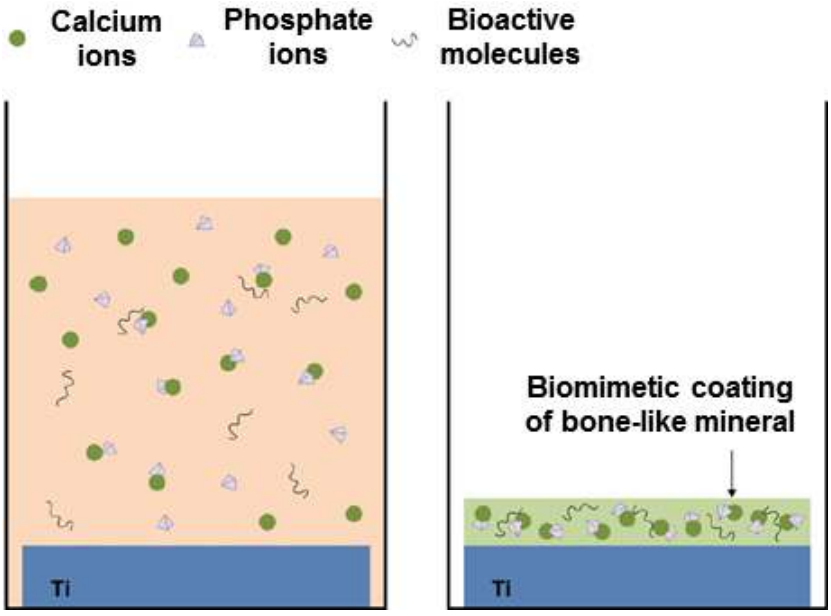

Figure I-15. Schematic drawing of the biomimetic incorporation of bioactive molecules on the bone-like mineral part produced onto implant surfaces (adpted from [20]).

5. Laser Surface Texturing

Laser processing of materials is widely employed in different technological applications due to its versatility and simplicity. Lasers are often used for the heat treatment of metals [63], cladding [64], surface cleaning [65], treatment of biological tissues [66], cell nanosurgery [67], and surface texturing of industrial materials and biomaterials [68]. Among these applications, special attention is given in this monograph to laser surface texturing of materials, since this is the surface modification method used in the present work. In the biomedical field, laser surface texturing allows fabricating implants with enhanced biological response surfaces, in which laser-induced surface textures are employed to control protein adsorption and cell adhesion [69, 70]. By properly selecting the laser processing parameters, the topography and chemistry of the implant surfaces can be optimised for the desired biomedical application. In this section, the basic concepts concerning to laser ablation, direct femtosecond laser surface texturing method, as well as the specific laser-induced surface structures produced by this surface modification method are described.

5.1. Laser Ablation

Laser ablation may be defined as a sputtering process leading to the ejection of atoms, ions, molecules, and even clusters from a surface as a result of the conversion of an initial electronic or vibrational photoexcitation into kinetic energy of nuclear motion [71, 72]. This is frequently characterised by a threshold fluence F_{th} (J/cm^2) or energy density – ablation threshold – above which modification of the material occurs. This threshold depends on the material properties and laser processing parameters such as radiation wavelength, pulse duration, etc [73]. Usually, several ablation mechanisms occur simultaneously, or one of them may dominate, depending on the processing conditions and materials properties. The major laser ablation mechanisms are described in detail in previous work [73, 74-76].

5.2. Direct Femtosecond Laser Surface Texturing

The availability of femtosecond lasers stimulated the development of several laser surface structuring techniques, among them, the mask projection technique [77], near-field ablation [78], laser-assisted chemical etching [79], laser PVD [80], thin films nanostructuring by laser-induced melting [81], plasmonic nanoablation [82], direct ablation [16, 17, 83], and interferometric ablation [84]. In recent years, direct writing methods were the most widely investigated for material surface micro- and nanotexturing due to their flexibility, simplicity, and controllability [15]. These methods can be applied to a wide range of materials (metals, ceramics, polymers, semiconductors, and glasses), allow texturing non-planar surfaces, and creating a variety of textures. They are maskless single-step processes capable of processing material in normal environment, without needing vacuum or a controlled atmosphere.

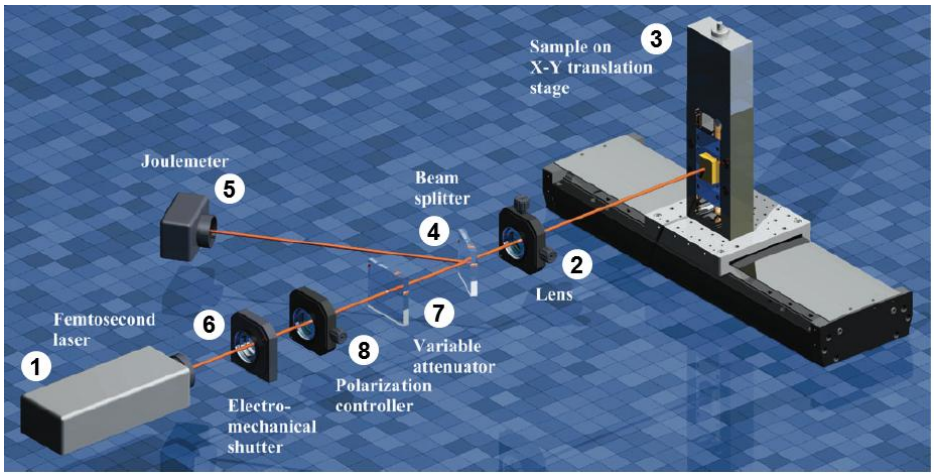

Figure I-16. Typical experimental setup for direct femtosecond laser surface texturing. (1) femtosecond laser; (2) focusing lens; (3) computer-controlled XYZ-translation stage; (4) beam splitter; (5) joulemeter; (6) electro-mechanical shutter; (7) variable attenuator; and (8) polarisation control device (adapted from [15]).

A typical setup for direct femtosecond laser surface texturing is shown in **Figure I-16**. Pulses from a femtosecond laser are focused by a lens at the surface of a sample mounted on a computer-controlled XYZ-translation stage. A beam splitter and a joulemeter are used for monitoring the pulse energy while an electromechanical shutter controls the number of laser pulses applied to the sample. A variable attenuator is used to vary the laser pulse energy incident on the material surface, while $\frac{\lambda}{2}$ or $\frac{\lambda}{4}$ plates allow controlling the beam polarisation when producing polarisation-sensitive surface structures. This setup is suitable for texturing spot, lines, or areas. By varying processing parameters such as the pulse energy, beam polarisation and number of pulses incident at each point of the material surface, a large variety of surface structures can be reproducibly produced. Micro- and nanoscale surface structures, such as laser-induced periodic structures, nanoholes and nanohole arrays and various irregular structures (nanocavities, nanospheres, nanoprotrusions, nanowires), can be produced by this direct writing method. In the following sections special attention is given to laser-induced periodic surface structures (LIPSS), columnar structures and combinations of these, which are the basis of the titanium textures investigated in the present work.

5.2.1. Laser-Induced Periodic Surface Structures

Laser-induced periodic surface structures (LIPSS) are parallel ripples or waves. These ripples can be produced by continuous wave (CW) or pulsed laser irradiation on

various types of materials, such as metals, ceramics, polymers, and semiconductors under specific laser processing conditions [16, 85-87]. LIPSS resemble periodic patterns often found in nature such as those in Aeolian sand dunes as well as in the bottom of oceans, lakes, and rivers [88], **Figure I-17**. Nevertheless, while the ripples formed on nature are large scale features, LIPSS are micro- or nanoscale structures with periodicity and height in the micrometre or submicrometre ranges.

The periodicity and orientation of LIPSS depend on processing parameters such as radiation wavelength, angle of incidence of the laser beam, number of incident laser pulses, radiation fluence, laser beam polarisation, ambient conditions, as well as on the material's properties [89-95]. LIPSS can be classified into two different types: (i) Low Spatial Frequency LIPSS (LSFLs); and (ii) High Spatial Frequency LIPSS (HSFLs). LSFLs have been observed for more than 50 years at the surface of materials melted with CW or pulsed (μs-fs) linearly polarised laser beams at normal incidence. Their period is close or slightly lower than the radiation wavelength, and they are perpendicular to the laser beam polarisation vector. Generally, LSFLs are produced with radiation fluences slightly above the material damage-threshold.

HSFLs were discovered more recently, mainly on semiconductor and metal surfaces. They appear only on surfaces irradiated with ultrashort laser pulses. Their period is significantly smaller than the radiation wavelength ($\sim \lambda_{laser}/10$ to $\lambda_{laser}/4$), and they are orientated either perpendicularly or parallelly to the polarisation direction. HSFLs are solely observed in lower fluence areas of the laser spot, often at its periphery and after hundreds to thousands of laser pulses. Surfaces textured with LIPSS have been tested for different applications [96] such as friction reduction [97], wettability [98, 99] and cell growth direction control [100], structural colour [101], control of surface reflectivity [102] and SERS (Surface-Enhanced Raman Spectroscopy) [103].

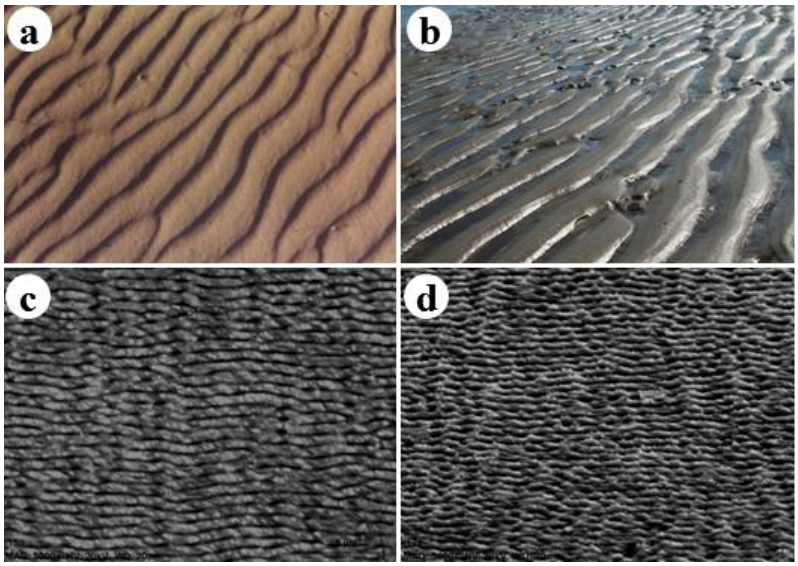

Figure I-17. LIPSS and periodic patterns in nature. Ripples in sand dunes (a) and in the bottom of a river (b). SEM micrographs of LIPSS produced on a titanium surface using direct femtosecond laser surface texturing (c-d). Despite the similarity in morphology, ripples in nature are produced at a macroscale level, while LIPSS are nanoscaled structures with periodicities and heights at the sub-micrometre level.

In 1965, Birnbaum was the first to observe periodic patterns on polished surfaces of semiconductors such as Ge, Si, GaAs, GaSb, InSb, and InAs irradiated with a focused ruby laser beam incident at the pseudo-Brewster angle (≈ 75º) [104]. The damaged surfaces presented a regular pattern of parallel straight grooves, parallelly oriented to the projection of the laser light onto the material surface. The direction of the grooves was not affected by rotating the sample around an axis perpendicular to its surface. The grooves were observed for power levels lower than the ones required to produce cracking, spallation and melting. Their spacing for Ge was approximately 2 μm. The formation of these grooves was explained by diffraction effects produced at the focus point of the lens. For the lens used in the experiments, the spacing of maxima or minima, calculated on the basis of diffraction theory was 1.4 μm, in fairly good agreement with the experimental results. Birnbaum considered that the grooves were produced by the material removal at the maxima of the electric field. He also analysed the influence of the laser beam incidence angle and concluded that the groove spacing was not dependent on this angle but, for angles of incidence lower than roughly 50º, slightly damaged areas presented patches of arbitrarily oriented parallel arcs with a spacing close to the observed on parallel grooves. The transition between parallel grooves and parallel arcs was gradual.

A few years later (1973), Emmony *et al.* [105] observed parallel lines with a periodicity of 10.6 μm, the same of the laser radiation wavelength, in the damaged area of the output Ge mirror of a built TEA CO_2 laser. The authors provided an explanation based on the fact that, in the laser cavity, radiation only propagates perpendicularly to the laser output mirror. For damage to occur with a periodicity corresponding to the radiation wavelength a mechanism must be invoked in which radiation propagates along the surface and hence normal to the laser beam. One such mechanism could be scattering from particles or surface defects on the mirror surface. In their laser the mirror was 10 cm from the discharge region and therefore liable to be contaminated by metal particles generated when an occasional arc was formed. These particles act as scattering centres leading to light scattering and radial propagation. Interference between the scattered radiation and the laser beam can originates interference fringes with a spacing corresponding to the 10.6 μm wavelength. Based on this hypothesis, the authors performed preliminary experiments outside the laser cavity, on glass substrates coated with 0.1 μm thick thin films of Ge and observed the parallel lines. They also noticed that the damage was more conspicuous if the film was scored and damaged, with fringes appearing paralell to scratches. Further proof of surface scattering and interference was obtained by tilting the samples around the axis of the scratches in the film and the axis of the laser beam. Interference occurred in the forward and backward scattering directions with a spacing of the fringes (d) given by $d = \frac{\lambda}{(1 \pm \sin\theta)}$, where the signal corresponds to the cases where the scattered radiation has a component of velocity towards or away from the incident laser beam. The sample tilted by an angle of 30º from the normal to the laser beam showed lines on both sides of the scratches with spacings of 7.3 and 19.9 μm, in good agreement with this equation. The most interesting feature in the surface damage was the predominantely parallel nature of the damage lines with a spacing which could be explained by the interference mechanism, also known as “surface-scattered wave” concept. Later work showed that permanent ripples (LIPSS) could be created on the surface of various metals, semiconductors, and insulators with linearly polarised laser pulses. It was generally considered that these patterns resulted from an inhomogeneous energy deposition associated with the interference of the incident beam with surface scattered waves, but the nature of this waves remained the subject of controversy [106].

Keilmann *et al.* [107] introduced another important concept about the mechanisms of LIPSS formation. The authors showed for the first time the influence of surface polaritons on the formation of laser-induced periodic surface structures. Kielmann and his co-workers agreed with the common idea that the ripple pattern formation is due to interference of the incident and a scattered field (surface-scattered wave concept), the latter arising from disturbances at the material surface, such as scratches and dust particles. But they proposed that the scattered field leading to ripple formation was essentialy due to surface polaritons, i.e., electromagnetic modes bound to and propagating along the material surface and proposed a theory explaining the surface polariton-incident wave interference and the mechanisms of ripple formation due to surface polaritons. In order to confirm their hypothesis, ripples were produced on quartz samples using a TEA CO_2 laser (λ = 10.6 μm; τ = 80 ns) and the influence of the laser radiation wavelength, beam polarisation and angle of incidence and the number of laser pulses studied. Among their findings, they concluded that ripples did not form under irradiation with a circularly polarised laser beam, and that surface roughness strongly influenced the resulting ripple patterns due to the alteration of the phase velocity of the surface polaritons. Interestingly, the surface roughness was the central component studied in the Sipe´s theory published a few months later.

In 1983, Sipe *et al.* [108] established a first-principles analyses of low frequency LIPSS (LSFLs) formation. The theory of Sipe and co-workers is currently known as the "efficacy factor theory" or "η theory". This theory is based on the effect of surface roughness on the electromagnetic field. It predicts an inhomogeneous energy absorption of linearly polarised electromagnetic plane waves on rough material surfaces and that ripples form where the absorbed energy is the largest [109]. As Clark *et al.* [110] stated in 1989, Sipe's theory is "the most rigorous, comprehensive, and indeed the only theory that, to our knowledge, can accurately explain all of the observed features of LIPSS formation". This theory overcame the physical inconsistencies of the surface-scattered wave concept, namely: (i) since the damage patterns were presumably produced by the absorption of energy within the material, it was not clear why the surface-scattered wave which induced them should propagate with a wavelength of λ instead of $\frac{\lambda}{n}$, where n is the refractive index of the material; and (ii) at normal incidence, the scattered wave should be longitudinally polarised, but such waves do not satisfy Maxwell's equations.

Recently, further studies on the role of surface polaritons on LIPSS formation were carried out by Bonse *et al.* [111], who investigated LIPSS formation on silicon surfaces due to intense femtosecond laser radiation. The optical properties of silicon after non-linear excitation by an intense ultrashort pulse duration laser beam was modelled by the Drude model, which was combined with Sipe's theory. This approach allowed to explain the LIPSS orientation, periodicity, and the dependence on the laser radiation intensity, which is responsible for defining the level of excitation of the material. Their findings suggest that the early stage of LIPSS formation is dominated by the excitation of surface plasmon polaritons (SPPs), once enough electrons are transferred to the conduction band by non-linear excitation processes, such as multiphoton absorption, due to intense laser excitation. Experimental evidence showed that this mechanism operates even for single laser pulses, and that the surface plasmons created act as a seed for a subsequent growth phase, which leads to the formation of LIPSS. Surface defects also mediate excitation of the SPPs and are essential for the multipulse feedback phase in the LIPSS formation, as previously observed by Keilmann and his co-workers.

These theories for the formation of LSFLs are generally accepted, but some inconsistences still exist. Recently, Reif *et al.* [112] highlighted that these models [94, 113, 114] do not account for the observed variation of ripple period across the diameter of the irradiated spot, the fluence dependence of ripples period [93, 115], ripples bifurcation [116], and the transition from ripples to cones or columns in a single spot [117]. These authors considered that LIPSS resembles the structures observed in surfaces submitted to ion sputtering [118], and suggested that LIPSS can be explained by surface self-organisation following a laser-induced surface instability. This concept is well established for the explanation of the surface structures formed due to ion sputtering, based on Sigmund's ion sputtering theory [119]. The mechanism suggested by Reif *et al*. relies on self-organised structure formation upon femtosecond laser ablation, based on the asymmetry of the initial electron kinetic energy distribution due to the laser electric field and the related variation in excitation transfer probability. This model is capable of explaining the different structure shapes and sizes found in the production of LIPSS.

The mechanisms of formation of HSFLs is still under debate. Several mechanisms were proposed to explain their formation such as self-organisation [116, 117], second-harmonic generation [92, 120], a modified η theory incorporating the alteration of the

optical properties of the material during multishot irradiation [121, 122], and Mie scattering [96]. Despite all the progress already achieved in the study of LIPSS formation mechanisms as well as on the study of the influence of the laser processing parameters on their characteristics, this is still an active research field and further investigations are necessary.

5.2.2. Columnar Surface Structures

Columns, cones, pillars, spikes, and mounds are another common type of laser-induced structures observed on various types of materials such as metals, polymers, semiconductors, and biological hard tissues due to irradiation with both short and ultrashort laser pulses in the ns-fs ranges, **Figure I-18**. Due to the biomedical potential and optical applications of these particular type of strucutres, ultrafast laser fabrication of these columnar microstructures on metals has been extensively studied [123, 124]. Generally, these structures consist of tightly packed self-organised features with an aspect ratio of 2:1 or higher that develop over a series of tens to hundreds of laser shots with radiation fluences significantly higher than the material-damage threshold. These features may have different shapes such as cylinders and sharp or rounded cones, with dimensions of up to tens of microns in both height and diameter. In addition, they are typically covered by a layer of nanoparticles.

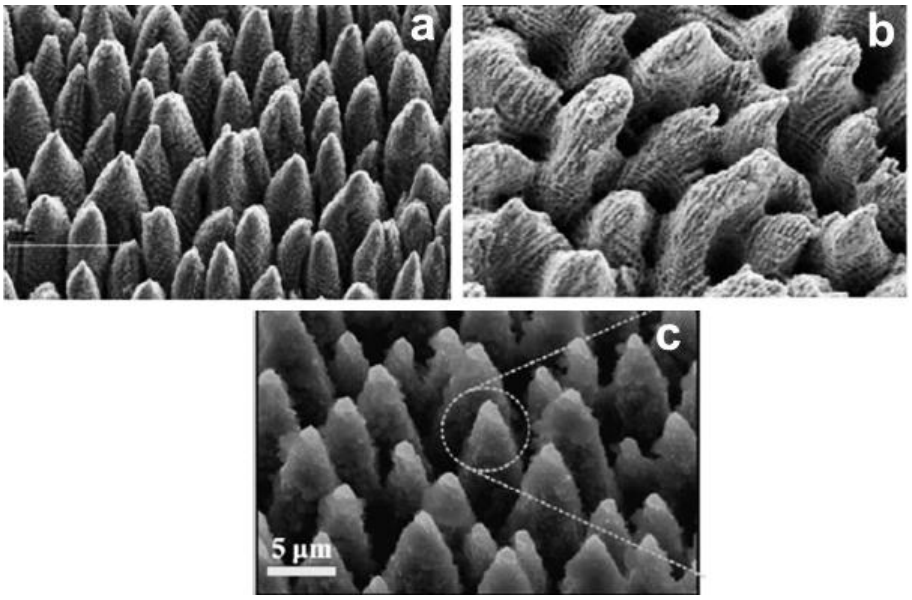

Figure I-18. Columnar microstructures produced on titanium (a), stainless steel (b), and silicon (c) surfaces by femtosecond laser irradiation (adapted from [124-126]).

The physical mechanisms explaining the formation of these surface structures are highly dependent on the properties of the material as well as on the specific laser processing parameters and conditions, including the radiation fluence, number of incident laser pulses, radiation wavelength, laser pulse duration, and atmospheric conditions. A comprehensive model capable of accurately describing the formation of these surface structures has yet to be developed. Their formation mechanisms were the object of intense controversy, being attributed to radiation shadowing by impurities [127], differential ablation [128], hydrodynamic effects [129], or to the influence of the material phase distribution on radiation absorption [130], the latter mechanism leading to columnar textures which are commensurate with the material microstructure. Generally, these structures may growth below (below-surface-growth, BSG) or above (above-surface-growth, ASG) the original surface of metallic materials, depending on the fluence and the number of pulses, **Figure I-19**. As aforementioned, these surface structures are produced with fluences significantly higher than the material-damage threshold. When surfaces are irradiated with low fluences, the columnar features lie at or below (BSG) the original surface. Contrarily, when surfaces are irradiated with high fluences the columnar features rise above (ASG) the original surface.

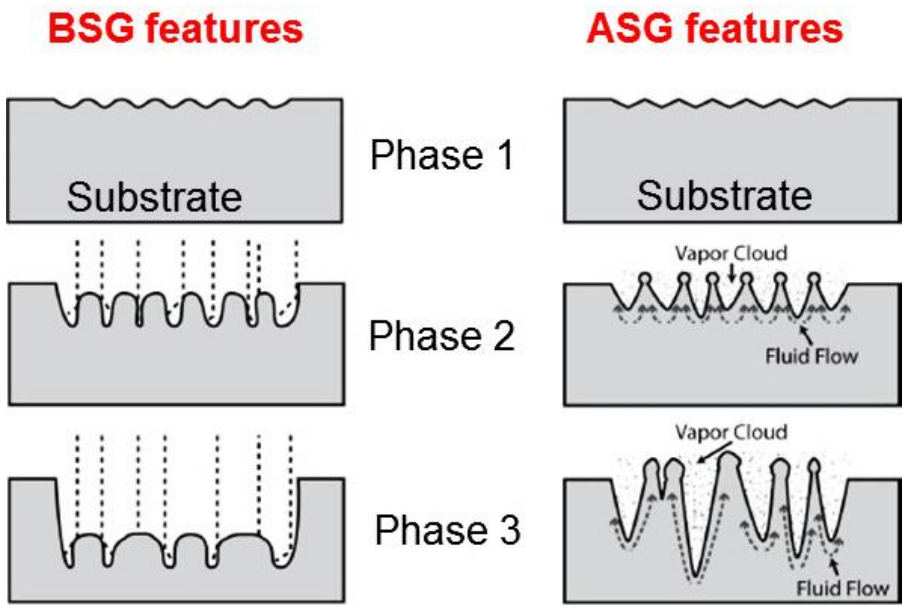

Figure I-19. Scheme of the growth mechanisms of columnar microstructures produced by femtosecond laser irradiation. Below-surface-growth (BSG) and above-surface-growth (ASG) features (adapted from [131]).

Very recently, Zuhlke *et al.* [131] have performed a detailed stepped growth experiments on nickel substrates. It was demonstrated that the development of these surface structures is characterised by a balance of growth mechanisms, including scattering from surface structures and geometric effects causing preferential ablation in the valleys, flow of the molten material, and redeposition of ablated material. The growth of these columnar features via femtosecond laser irradiation can be divided into three phases. The first phase is the creation of roughness at the nanometre and micrometre scales, leading to the onset of precursor sites that affect the distribution of the laser energy of subsequent laser pulses on the surface. In this phase, the surface is covered by random nanostructures. After each laser shot, the random nanostructure is destroyed and a new random nanostructure created, without preserving the surface features of the previous laser shot. With increasing number of laser shots, the surface structures become larger and denser. This evolution is attributed to increased radiation absorption by nanoparticles on the surface produced by previous laser pulses as well as by geometric effects caused by scattering of radiation due to increasingly rough surface. This random nanostructure develops through hydrodynamical fluid flow driven by surface tension gradients, as well as by the formation of nanocavities due to cavitation bubbles. Finally, further irradiation of the random nanostructure with femtosecond laser pulses results in the evolution to microscale self-organised features, also konwn as precursor sites. The precursor sites formation takes place in two ways. The first is the formation of microripples, which are periodic ripples that form parallel to the incident laser beam polarisation with a fluence dependent period ranging from 2.5-5 μm. Along the peaks of these microripples, domes form with a diameter similar to the microripple size. In principle, these structures are the only form of precursor sites observed for the formation of below-surface-growth features. In the case of above-surface-growth features, a second type of precursor sites appears in some cases consisting of pitting of the surface. With increased number of pulses, the pits grow deeper and rims of displaced material form. Along these rims, domes form, which act as precursors. Usually, pit formation starts at the microscale defects present on the surfaces before processing, but in some cases the pits form from nanoscale surface defects as well.

The second phase of growth is the development of the precursor sites to form larger self-organised features, while the third phase represents the evolution of these self-organised structures upon further irradiation. The transition between the first and second

phases occurs when the presence of precursor sites significantly alters the distribution of energy of subsequent laser pulses. The laser fluence has a significant impact during this second phase on the dominant growth mechanism and final surface morphology. For below-surface-growth features, the peaks remain below the original surface level regardless of the number of laser pulses, suggesting that the precursor sites induce preferential valley ablation (PVA). PVA is a surface geometry driven process in which incoming laser light is scattered off the precursor sites, resulting in increased laser radiation fluence and a corresponding increase in ablation at the valleys between precursor sites. The precursor sites then evolve into conical structures. Once these structures are formed, the laser radiation fluence on the sidewalls is decreased relative to the valleys due to increased subtended area as described by Hwang and Guo [132]. The conical structures grow in height and width. The third phase of below-surface-growth features development is characterised by the merging of the conical structures as they grow. Conical structures will merge when their growth reduces the width of the valleys and thus the effects of PVA between them. In the case of above-surface-growth features development, as the number of laser pulses incident on the surface increases, PVA causes the valleys to deepen. However, a combination of fluid flow and redeposition of ablated material cause the peaks to rise above the surface. The fluid flow is likely driven by the same processes that lead to PVA. The inhomogeneous energy distribution induces thermal gradients in the surface molten layer, which drive fluid flow away from the valleys between structures and up the structures themselves. Another growth mechanism of the surface structures is the redeposition of material ablated at the valleys onto the tops of the structures. This mechanism has been described as vapour-liquid-solid (VLS) growth. During VLS growth, each pulse liquefies the tops of the structures, while PVA also takes place. This results in a vapour cloud of the material around the structures, which then reacts with the melted tops, causing them to grow taller.

Another important point is the production of columnar structures covered with LIPSS. In stationary conditions, where the sample and the laser beam are stationary, the columnar structures form at the centre of the laser spot (high fluence) while LIPSS appear at the periphery (low fluence). However, in non-stationary conditions, textures consisting of LIPSS overlapping microcolumns are produced, leading to a surface texture with a bimodal roughness distribution, **Figure I-20**.

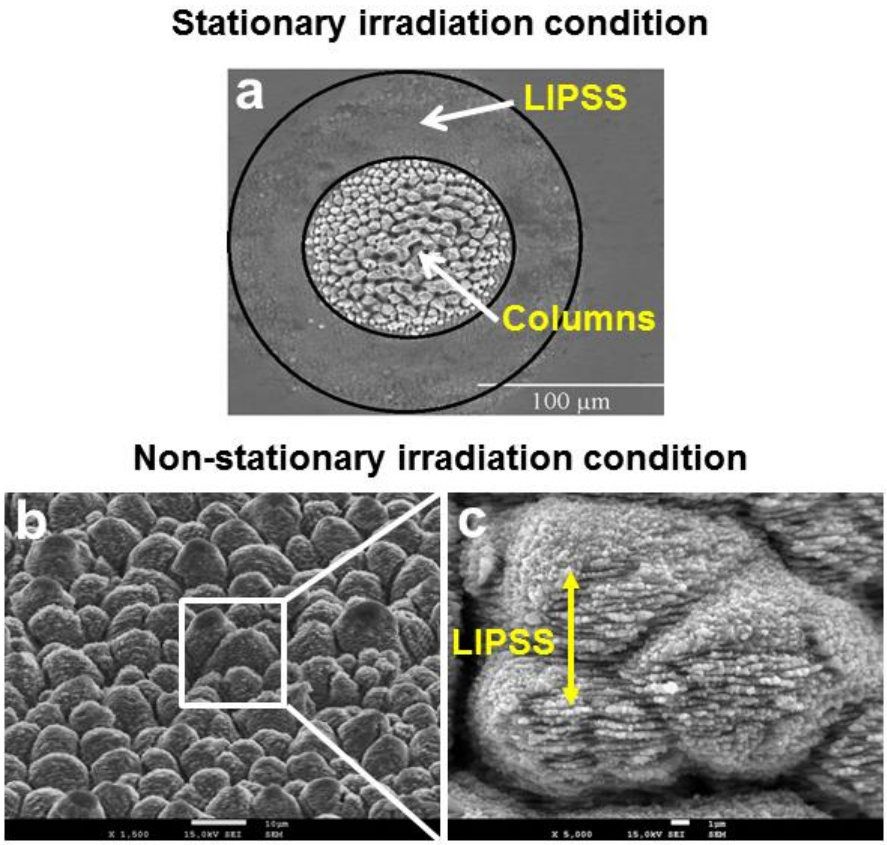

Figure I-20. Femtosecond laser irradiation of a Ti-6Al-4V surface under both stationary and non-stationary conditions. Low magnification SEM micrograph of a single spot showing the columnar microstructures at the centre and LIPSS at the periphery of the spot (a). High magnification SEM micrograph of the columnar microstructures formed on a large textured area (b) and LIPSS overlapping the columnar microstructures (c).

Nayak et al. [124] were the first to observe this bimodal texture on titanium surfaces after femtosecond laser irradiation under non-stationary conditions. They proposed that contrarily to microcolumns formation mechanism where LIPSS formed initially were thougth to evolve into columns, thus disappearing, LIPSS on titanium microcolumns remained on their surfaces. Recently, the formation of this bimodal texture was better elucidated by Oliveira *et al.* [16] in a detailed study on the formation of microcolumns and LIPSS on titanium surfaces treated by femtosecond laser irradiation under both irradiation conditions. They concluded that LIPSS formation does not precede columns formation but follows it. Since the spatial profile of the laser beam is Gaussian, each point of the material surface is subjected to varying fluences when the sample moves linearly under the stationary laser beam. When the fluence corresponding to the maximum radiation intensity in the transverse cross-section of the laser beam is considerably higher than the material damage-threshold columns form. As the laser

beam moves away the same area is irradiated by lower fluences, at the periphery of the laser spot and LIPSS form. Since all points of the surface are consecutively submitted to high fluences, then to low fluences, LIPSS always overlap microcolumns.

Very recently, Ionin *et al.* [133] developed a new method for manipulating the nanotopography of these columnar microstructures. The columnar structures can be produced with or without LIPSS covering their tops under non-stationary femtosecond laser irradiation regime. This method involves femtosecond laser beam shaping, e.g., by breaking the symmetry of the Gaussian spatial profile of the laser beam by simply cutting a half of the laser beam using an oblique knife-edge screen before the laser beam impinges on the sample surface, **Figure I-21**. The cut laser beam is scanned over the material surface in two opposite directions, **Figure I-21 a** and **d**.

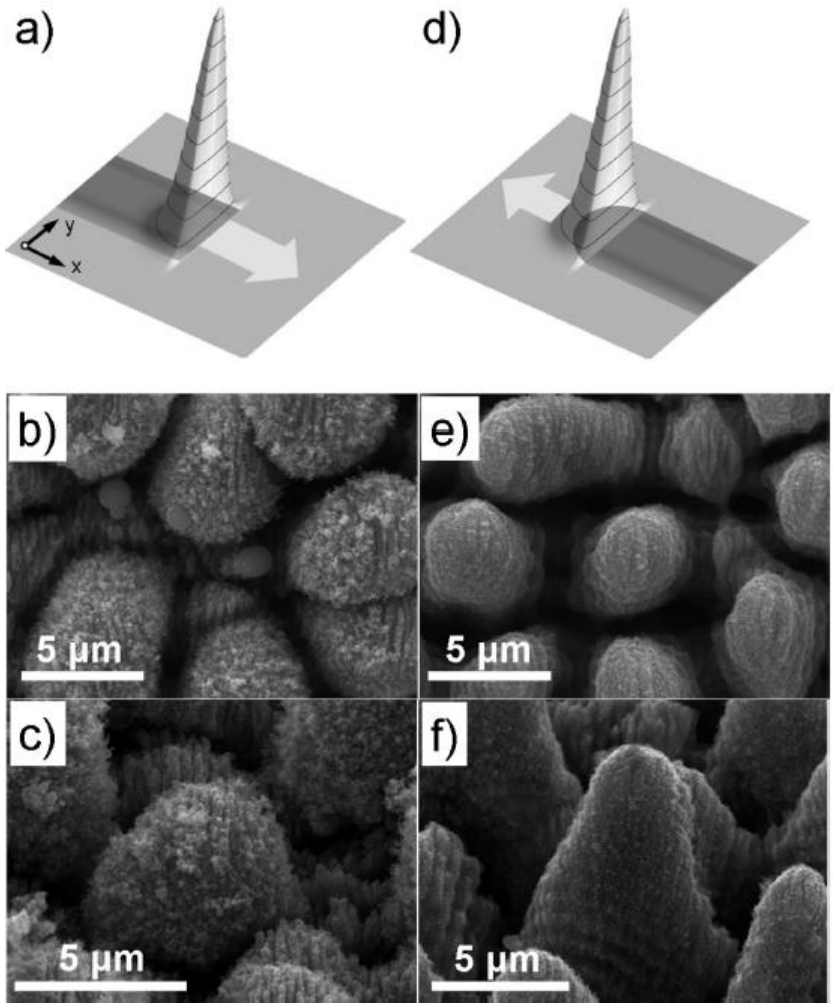

Figure I-21. Forward (a) and backward (d) scanning modes of the cut fs-laser beam. SEM micrographs of the titanium surface after its scanning by femtosecond laser pulses in the forward "positive" direction (b-c) and in the backward "negative" direction (e-f) [133].

In the case of the forward scanning (positive x-direction) the microcolumns emerge first, then LIPSS overlap them. The final surface morphology presents both nano- and microstructures, **Figure I-21 b** and **c**. In the case of a backward scanning (negative x-direction) LIPSS emerge first and then the microcolumns totally replaced them, **Figure I-21 e** and **f**. The final surface morphology consists of microcolumns with no LIPSS, resembling the columns produced under stationary conditions with a symmetrical laser beam.

6. Wettability

Controlling the wettability of an implant surface is a key issue in ensuring its success. The wettability of a solid surface depends on its chemical composition and topography, indicated by the surface roughness and surface organisation (isotropy and anisotropy) [134]. The wettability of implants affects the spreading of biological fluids, and the adsorption of important molecules during the early stages of bone formation [135]. Since cells do not interact directly with the implant surface, but with the protein layers previously adsorbed onto it, the way in which extracellular matrix proteins, for instance fibronectin and vitronectin, adsorb on the implant surface affects cell adhesion, and consequently cell fate (commitment and differentiation), **Figure I-22**.

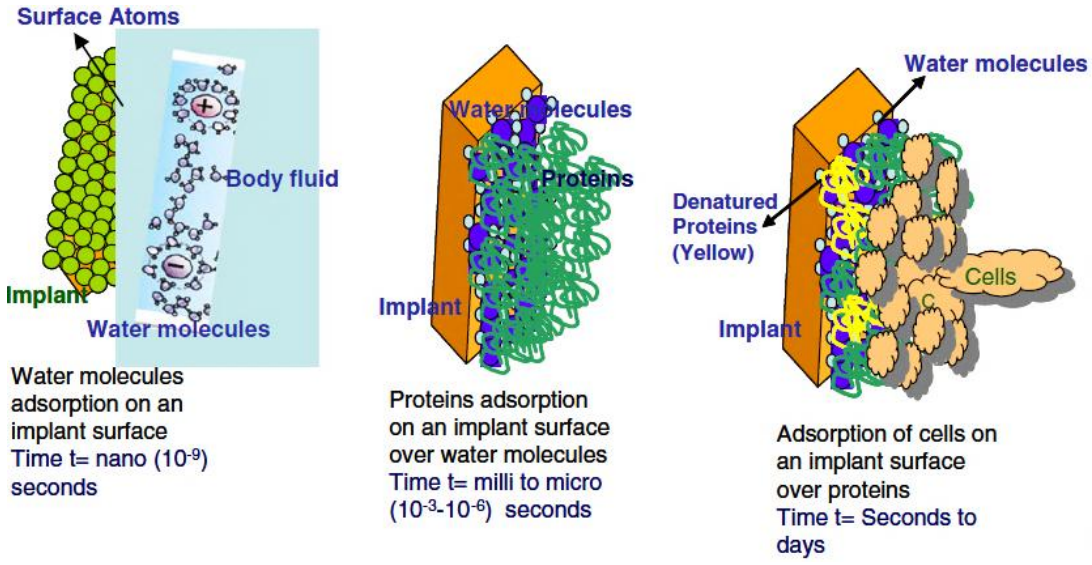

Figure I-22. Time evolution of adsorption of body fluids and proteins and cell adhesion on the implant surface during the early stages of bone formation, in which wettability plays a crucial role [4].

Thus, the development of materials with optimised wettability may be relevant to applications in the biomedical field. In this section the basic concepts with respect to wettability, bio-inspired wetting properties, and the recent work on the control of the wettting properties of metals, polymers, semiconductors, and biological tissues textured by ultrafast lasers are briefly described.

6.1. Contact Angle and Surface Tension

Generally, two opposite wetting behaviours are desired, depending on the application intended [136, 137]. The first behaviour is defined by complete drying, in which a liquid droplet brought into contact with a solid surface remains spherical without developing any significant contact with it, **Figure I-23 a**. The second behaviour is defined by complete wetting, in which a droplet brought into contact with a solid surface spontaneously spreads and forms a film on it (superwetting), **Figure I-23 b**. Intermediary behaviours can also occur, in which the droplet partially wets the solid surface.

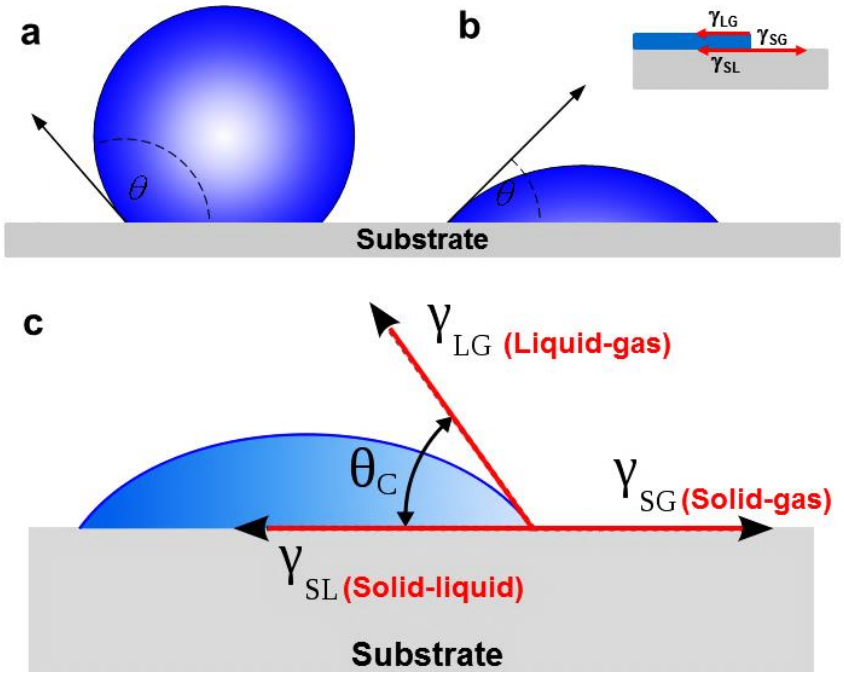

Figure I-23. Representation of two opposite wetting behaviours when a liquid droplet is brought into contact with a solid surface. Complete drying (a) and complete wetting (b). The balance between the surface tensions (γ) of the three phases involved defines the contact angle (θ_c) of the liquid droplet (c).

Therefore, it is of obvious interest to determine which surface parameters favour these different wetting behaviours. The degree of wetting may be distinguished through the

contact angle (CA) of a liquid droplet into contact with a solid surface. The contact angle is defined as the angle between the tangent to the liquid surface and the solid surface in a point of the contact line or threephasic line (where the three phases involved meet each other), as shown in **Figure I-23 c**. The surfaces can be classified into four different types depending on the contact angle developed by a water droplet, as shown in **Table I-6**. Hydrophobic surfaces yield a water contact angle larger than 90°, while a superhydrophobic surface exhibits a water contact angle larger than at least 150°. In contrast, hydrophilic surfaces present contact angles lower than 90°, while a superhydrophilic surface shows a water contact angle equals or near to 0°. For liquids other than water, the terms lyophobic and lyophilic are used for high and low contact angle surfaces, respectively. Similarly, the terms omniphobic and omniphilic are applied to both polar and apolar liquids.

Table I-6. Classification of the surfaces according to the contact angle (CA) of a water droplet.

CLASSIFICATION	CONTACT ANGLES [°]
Hydrophobic	> 90°
Superhydrophobic	> 150°
Hydrophilic	< 90°
Superhydrophilic	≈ 0°

It is known that surfaces carry a specific energy, the so-called surface tension, which reflects the cohesion of the underlying condensed phase (either solid or liquid). Surface tension is defined as an energy per unit area ($J.cm^{-2}$) or a force per unit length ($N.m^{-1}$) [134, 138]. This force applies along a αβ surface to minimise the corresponding positive surface energy, and is usually denoted as $\gamma_{\alpha\beta}$ for an interface between the α and β phases. The indices S, L, and G represent the solid, liquid and gas phases, respectively, **Figure I-23 c**. Briefly, let us consider a situation in which a liquid droplet is deposited on a solid surface, the solid-gas surface tension is higher than the sum of the solid-liquid and liquid-gas surface tensions. The sign of the spreading parameter $S = \gamma_{SG} - \gamma_{SL} - \gamma_{LG}$ determines the behaviour of the liquid droplet on the surface. For $S > 0$, it spreads, while in the opposite case, $S < 0$, it forms a cap. Thus, the droplet meets the surface with a well-defined contact angle. The contact angle value is then given by a force balance exisisting between the surface tensions acting on the contact line, provided that the system is in equilibrium. This balance is mathematically described by $\gamma_{SG} = \gamma_{SL} +$

$\gamma_{LG}\cos\theta$, which is known as Young's equation. In this case, the contact angle is thus determined univocally by the phases involved and the atmosphere.

6.2. Wetting Models for Rough Surfaces

Young's equation is valid for flat and homogeneous surfaces. Nevertheless, the wetting behaviour of a liquid droplet is affected by the surface roughness, present in all solid surfaces. For example in the case of implant surfaces surface roughness is created by the manufacturing processes. Two new approaches were developed to describe the effect of surface roughness on the wetting behaviour. They are Wenzel and Cassie-Baxter models [125], **Figure I-24**.

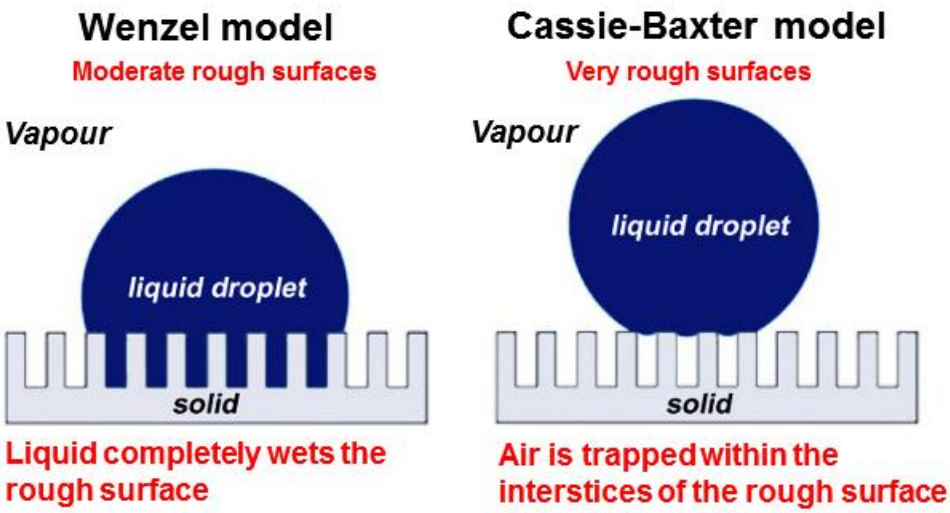

Figure I-24. Representation of the Wenzel and Cassie-Baxter models developed to describe the different states of a liquid droplet into contact with a solid rough surface.

In the Wenzel model, the liquid is assumed to be in contact with the whole area of the rough surface. The apparent CA (θ_r^W) on the rough surface is given by $\cos\theta_r^W = r\cos\theta_c$, where r is the ratio between the actual and the projected surface areas and θ_c is the intrinsic contact angle of a liquid droplet on a flat surface. Because r is greater than 1, for hydrophilic flat surfaces ($\theta_c < 90^\circ$) roughness decreases the contact angle, while for hydrophobic flat surfaces ($\theta_c > 90^\circ$) roughness increases the contact angle. Surface roughness leads to an amplification of the wetting behaviour of flat material surfaces. However, for surfaces with high roughness or porous structures the Wenzel model is not valid, and the Cassie-Baxter model is used. This model assumes that the liquid does not wet completely the surface, and the contact of a droplet with the surface should be a

contact with substrate material and air trapped in the roughness. The apparent contact angle is given by $\cos\theta_r^C = f(\cos\theta_c + 1) - 1$, where f represents the fraction of the solid-liquid contact in the total contact area. The larger the fraction of air trapped within the interstices of the surface the smaller the value of f, and consequently the higher the value θ_r^C, independent of the value of θ_c. In addition, both models can be combined by $\cos\theta_r^C = f(r\cos\theta_c + 1) - 1$, in order to obtain a general form to describe the contact angle of liquid droplet on a solid rough surface [139].

6.3. Contac Angle Hysteresis

Contact angle hysteresis, also referred as sliding angle, occurs when a liquid droplet is brought into contact with a solid rough surface, where defects can act as pinning sites for the contact line. Both chemical heterogeneities and asperities can act as pinning sites [134]. As a consequence, droplets can display two different apparent contact angles, in nonwetting defects and wetting defects, respectively. The resulting asymmetry in contact angles creates a Laplace pressure difference between the high curvature and the low curvature regions. Quantification of the contact angle hysteresis consists of slowly increasing the volume of a droplet so that, the contact line first remains stuck before it suddenly jumps above a critical volume, for which the line depins and moves toward a next series of pinning defects. The maximum observed angle is the so-called advancing contact angle θ_a. Conversely, decreasing the volume of the droplet lead it to flatten until it depins and retracts to the next pinning sites. The minimum corresponding angle is the so-called receding contact angle θ_r. The contact angle hysteresis $\Delta\theta = \theta_a - \theta_r$ may vary dramatically on a rough surface from nearly zero to a value of the order of θ_a itself. Sliding angles $< 10°$ represent strong pinning, while sliding angles $> 10°$ represent weak pinning of the droplet.

6.4. Bio-Inspired Wettability

Nature provides a model for the development of functional surfaces with special wetting behaviour. Recently, bio-inspired surfaces have attracted the scientific attention for fundamental and practical reasons and became a hot research topic [140-142]. The laser-induced surface structures investigated in the present work resemble some of these bio-inspired structures.

Chapter I. Literature Review

A great variety of artificial superhydrophobic surfaces with self-cleaning behaviour have been fabricated by using chemical compositions and a surface topography inspired by lotus leaves and cicada wings, which exhibit contact angles above 150° and small sliding angles of about 2°, **Figure I-25-1 and 5**. Raindrops roll easily on these surfaces, carrying away dirt and particles. The self-cleaning characteristics of the lotus leaves can be attributed to the epicuticular wax and the multiscale hierarchical architectures where nanostructures superimpose on micrometre scale papillae. The self-cleaning effect observed on the cicada wings is attributed to its texture consisting of hexagonally ordered nipple-shaped protusions. In contrast, superhydrophobic surfaces with high adhesive force, where droplets balls up and do not slide off have been fabricated inspired by the red rose petal and the gecko's feet, **Figure I-25-2 and 3**. Micropapillae and nanofolds on the rose petals'surfaces provide sufficient roughness for superhydrophobicity and a high adhesive force to water. These structures are larger than those of the lotus leaves. Water droplets can enter the larger scale grooves, wetting out and clinging to the petal surface. The gecko foot is made up of well-aligned microscopic keratinous hairs called setae, which are 30 to 130 μm in length and 5 μm in diameter, split into hundreds of nanoscale ends with 0.2-0.5 μm diameter, called spatulae. Anisotropic wetting surfaces have also been fabricated inspired on the superhydrophobic wings of the butterfly Morpho aega, **Figure I-25-4**. Water droplets present a directional adhesion, in which they roll easily away along the radial outward direction of the central axis of the body, but are pinned strongly against movement in the opposite direction. These special abilities of butterfly wings resulted from the anisotropic arrangement of flexible nanotips on ridging nanostripes and microscales overlapped on its wings at the one dimensional level. Two distinct contact modes of a droplet with orientation-tuneable microstructures occur and thus produce different adhesive forces. Finally, surfaces have been also inspired on the water-collecting surface of the tenebrionid beetle (Stenocara sp.), **Figure I-25-6**. The Stenocara beetle's back is covered by a near-random array of bumps, 0.5 mm in diameter and arranged 0.5-1.5 mm apart. The peak of each bump is smooth and hydrophilic whereas the slopes of each bump and the troughs in between are covered by special microstructures coated with wax. The microstructure consists of flattened hemispheres, 10 μm in diameter, arranged in a regular hexagonal array, resulting in a superhydrophobic background. Therefore, in a foggy dawn the water in the fog accumulates on the hydrophilic seeding

peaks of Stenocara's bumps and coalesces. When the water droplets become large and heavy enough to overcome the binding forces of the hydrophilic region, they detach and roll down from the top of the peaks and are channeled to a spot on the beetle's back that leads straight to its mouth.

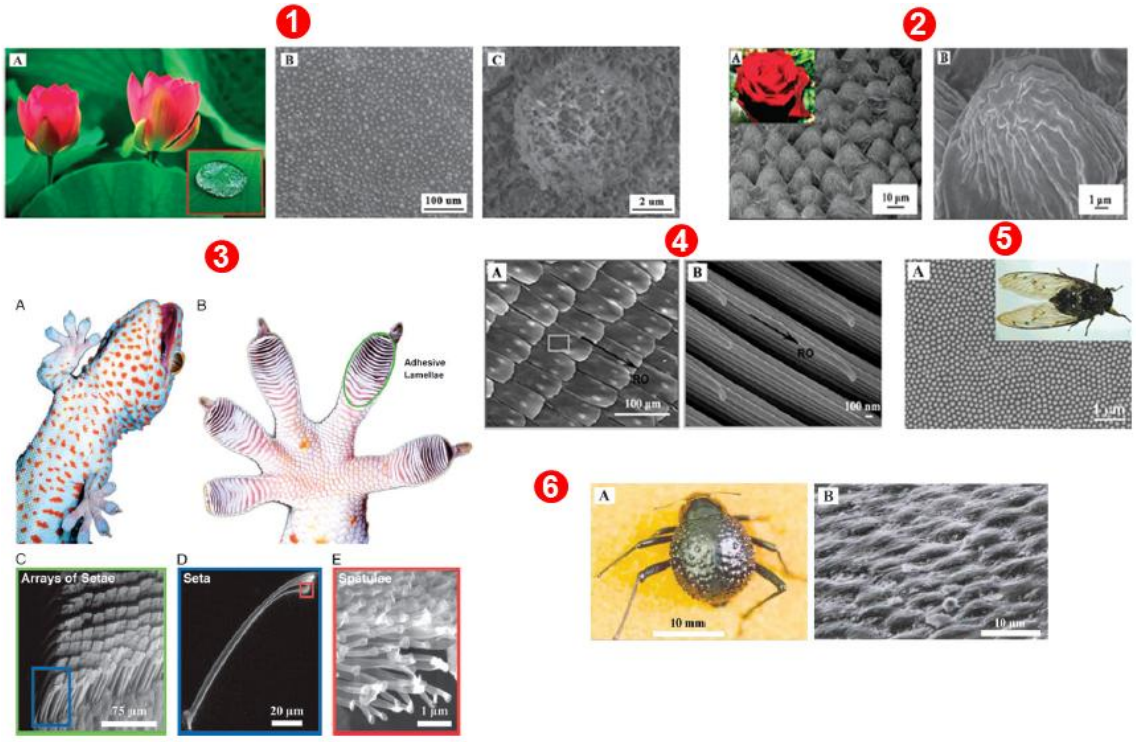

Figure I-25. Superhydrophobic and superhydrophilic surfaces in nature. Low and high magnification SEM micrographs of a lotus leaf (1), red rose petal (2), gecko foot (3), butterfly wing (4), wings of cicada (5), and desert beetle *Stenocara sp* (6) (adapted from [139]).

6.5. Wettability Control Using Ultrafast Lasers

Different surface modification methods have been used to fabricate artificial surfaces capable of controlling wettability [141]. In the last years, modification of the wetting properties of metals, polymers, semiconductors, and biological tissues using femtosecond laser surface texturing has been an actively studied area due to a range of promising applications in microfluidics, biomedicine and biochemical sensors [143]. In this section some of these recent studies are described.

Zorba *et al*. [126] prepared artificial silicon surfaces in a reactive gas atmosphere, possessing hierarchical structures consisting of protusions with conical and pyramidal

asperities that mimic the structure and the wetting behaviour of the natural Lotus leaf. The laser textured surfaces lead to contact angles of 154 ± 1° and small contact angle hysteresis of 5 ± 2°. In another study on silicon surfaces, Zorba *et al.* [144] simultaneously structured the surfaces on the micrometre- and nanometre scale. By varying the laser fluence the wetting properties and the surface roughness were reproducibly controlled. The water contact angle could be increased from 66° to more than 130°. The authors also showed that by creating surface structures with wettability gradients, the droplet centre can be driven in a desired direction, even upwards.

Baldacchini *et al.* [143] also fabricated superhydrophobic silicon surfaces by femtosecond laser treatment followed by coating with a layer of fluoroalkylsilane. By varying the fluence, different surface morphologies are fabricated, tunning the wetting behaviour of water and hexadecane. For water, the laser textured surfaces yield contact angles higher than 160° and negligible hysteresis, while for hexadecane a transition from non-wetting to wetting regime occured.

Wu *et al.* [125] fabricated superhydrophobic surfaces by microstructuring and silanising stainless steel. Laser-induced periodic surface structures (LIPSS) were produced with low laser fluence, providing contact angles of about 150.3°. By increasing the fluence, periodic ripples and cone-shaped spikes at the micrometre scale, both covered with LIPSS, were produced. These surfaces presented contact and sliding angles of about 166.3° and 4.2°, respectively. Jagdheesh *et al.* [145] observed the same wetting behaviour of AISI 304L stainless steel and Ti-6Al-4V alloy, which had their surface energies reduced via application of a layer of perfluorinated octyltrichlorosilane after laser texturing. By increasing the number of laser pulses, nanoscale structures evolved to microscale structures. The top surface of these structures was covered with nanoscale protrusions, which were most pronounced on the Ti-6Al-4V surface. The laser textured surfaces of Ti-6Al-4V attained superhydrophobicity, presenting an improvement in the contact angle higher than 27 % in comparison with the nontextured surfaces.

Zhao *et al.* [146] observed an anisotropic wetting on submicrometre scale periodic structures consisting of parallel grooves fabricated on azobenzene-containing multiarm star polymer films by laser interference. Macroscopic distortion of water drops was found on such small scale surface structures. The contact angles measured from the

direction parallel to the grooves were larger than those measured from the perpendicular direction. By increasing the groove depth, the degree of wetting anisotropy and the contact angle hysteresis perpendicular to the grooves increased as a result of the increase in the energy barrier. Chen *et al.* [147] also reported an anisotropic wetting on silicon surfaces. The anisotropic wetting was induced by restricting a droplet on a unstructured Si hydrophobic domain between two superhydrophobic strips fabricated by femtosecond laser treatment. The anisotropic wetting of water droplets on the small Si domain was attributed to the adhesive force of the structured regions. Vorobyev and Guo [148, 149] reported superhydrophilicity and even superwicking effect on silicon and glass surfaces fabricated with an array of parallel nanotextured microgrooves. Water droplets spread highly anisotropically on the textured areas and moved preferentially along the microgrooves with a contact angle nearly 0°. When droplets are dropped on the bottom of the textured area vertically positioned, the water immediately sprints vertically uphill against the gravity. In addition, the same approach was used for the improvement of the wettability of biological tissues such as human enamel and dentin [150].

Kietzig *et al.* [137] fabricated dual scale roughness structures on metal alloys such as stainless steel (AISI 304L and AISI 630), low-alloy steel (AISI 4140), high speed tool steel (AISI M2), mold steel (AISI P20) coated with Armoloy thin dense chromium (TDC) coating, and Ti-6Al-4V alloy. Interestingly, it was found that initially all the surfaces showed superhydrophilic behaviour with complete wetting of the laser textured surfaces. However, the surfaces became superhydrophobic over time, with contact angles above 150°, while the contact angle hysteresis was in the range 2-6°. The change in wetting behaviour was correlated with the increasing amount of carbon on the laser textured surface over time. These results showed the time dependency of the surface wettability under a combined effect of surface topography and chemical composition. Conversely, Nunes *et al.* [151] reported an ageing effect on silicon surfaces fabricated by femtosecond laser texturing and posteriorly acid cleaned. Highly hydrophobic silicon surfaces with contact angles higher than 120° were obtained immediately after the laser treatment and cleaning with the acid solution. Nevertheless, these surfaces presented contact angles of about 80° over time. This change in wetting behaviour was attributed to a SiO_2 oxide layer spontaneously formed with time. Wang *et al.* [152] investigated the change in the wetting properties of polymethyl methacrylate (PMMA) textured by

femtosecond laser pulses with different laser fluences. Both hydrophilic and hydrophobic surfaces were produced depending on the laser fluence. The change in wetting behaviour was attributed to laser-induced modification of chemical bonds and not to the laser-induced surface textures.

These studies clearly show that micro- and nanotextures fabricated by femtosecond lasers on various types of materials are capable of producing both superhydrophobic and superhydrophilic surfaces, by mimicking hierarchical morphologies found in nature. Anisotropic liquid spreading is also achieved by creating anisotropic surface textures. Further, it is clear that changes in the wetting behaviour may occur over time, depending on the type of material and surface treatment conditions.

7. Bone Tissue

Bone is a hard, dynamic, anisotropic, and highly vascularised tissue with an unique capacity to heal and remodel without leaving scars. It is the component of the skeletal system, involved in the protection, support (load bearing), mineral resorvoir, and motion of the human body [153]. Bones from the rib cage protect heart, lungs, and other organs responsible for motion, expansion and contraction due to their flexibility and elasticity. In addition, bone structurally supports the mechanical action of soft tissues such as contraction of muscles or expansion of lungs thanks to its high stiffness. Bone also acts as a production site for specialised tissues as well as a mineral reservoir of calcium and phosphate.

Bone can be structurally described at different scale levels , as shown in **Figure I-26**. It consists of two different structures, namely: (i) an external layer, known as cortical or compact bone (~ 80% of the total skeleton), which is hard, smooth, continuous, dense (~ 1.80 $g.cm^{-3}$), and 10 % porous. The cortical bone can be either classified as primary or secondary, where the former is made up of highly organised lamellar sheets, while the latter consists of sheets disrupted by the tunnelling of osteons centred around a Haversian canal; and (ii) an internal part, known as trabecular or cancellous bone, which is highly porous (50-90 %) and less dense (0.2 $g.cm^{-3}$) in comparison with the cortical bone [154, 155].

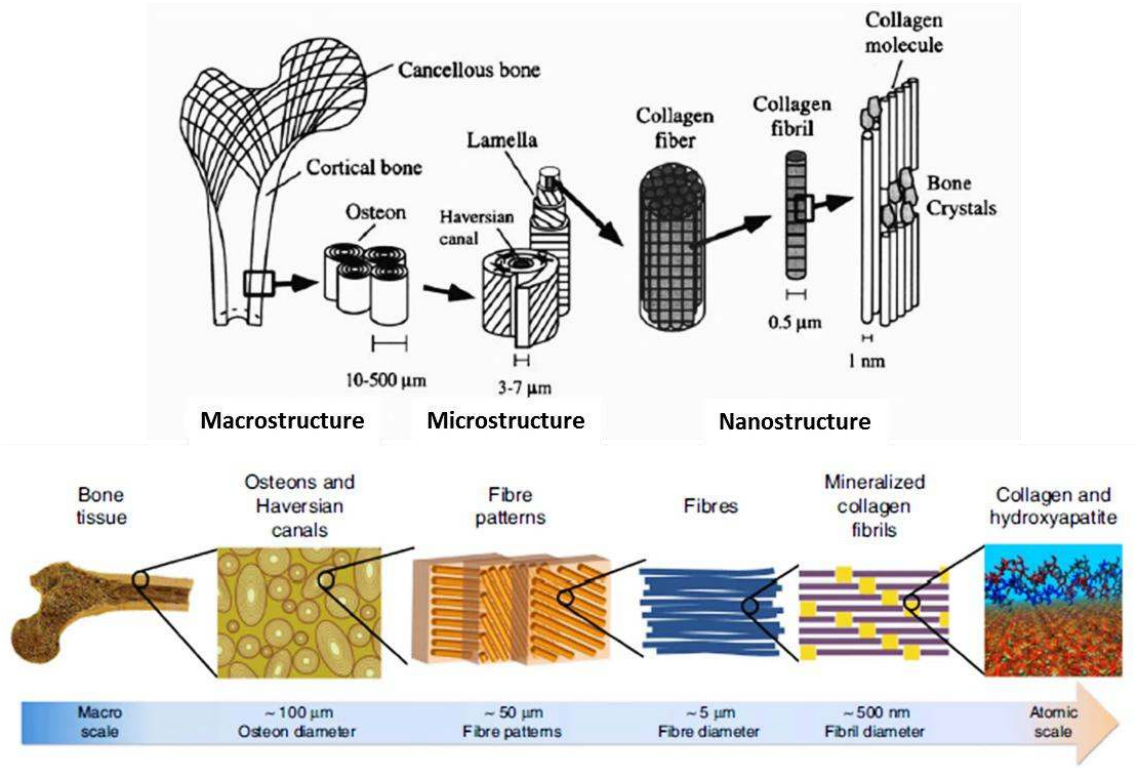

Figure I-26. Representation of the bone tissue and its components at different scale levels (adapted from [156]).

Furthermore, bone consists of a mineral part formed by hydroxyapatite (65-70 % of the matrix) and an organic part consisting of glycoproteins, proteoglycans, sialoproteins, and bone "gla" proteins (30-35 % of the total matrix), **Table I-7**. The mineral part of the bone is approximately 60 % mineral, 10 % water and about 30 % organic matrix (90 % type I collagen and 10 % proteoglycans and other non collagenous proteins). Bone apatites nucleate into the nanopores of the collagen fibrils as the extracellular fluids are supersaturated in calcium and phosphates ions. Crystallisation takes place along these fibrils, interconnecting the whole collagen network. These apatitic crystals form as thin plates of irregular shapes, with sizes varying in the range 2-110 nm, increasing the surface area facing extracellular fluids. The combination of a high surface area and crystallographic vacancies of bone crystals are responsible for the ionic exchanges.

Table I-7 Organic phase components of the bone matrix (adapted from [157]).

BONE ECM	FUNCTIONS AND PROPERTIES
Type I collagen	▪ Provides a framework for skeletal structure ▪ Matrix calcification
Biglycan	▪ Proteoglycan ▪ Affect collagen fiber growth and diameter ▪ Involved in the process of matrix mineralisation
Osteonectin	▪ Glycoprotein ▪ Binds Ca^{+2} and collagen ▪ Nucleates hydroxyapatite
Thrombospondin	▪ Glycoprotein ▪ Binds calcium, hydroxyapatite, osteonectin and other cell surface proteins ▪ Mediates cell adhesion in a RGD-independent fashion
Fibronectin	▪ Osteoblast attachment to the biomaterial surface
Osteopontin	▪ Bone Sialoprotein ▪ Constituent of cement line ▪ Involved in bone remodelling
Bone Sialoprotein	▪ Sialoprotein ▪ Constituent of cement line
Osteocalcin	▪ Skeletal gla protein ▪ Late marker of osteogenic phenotype ▪ Involved in bone remodelling

Three different cell types with very well defined functions (osteoblasts, osteocytes and osteoclasts) are responsible for the maintenance and resorption of bone, as shown in **Table I-8**.

Table I-8 Bone cell types and their respective functions.

CELL TYPE	MORPHOLOGICAL CHARACTERISTICS	FUNCTIONS
Osteoblasts	▪ Cuboidal in shape ▪ Polarised ▪ Located at the bone surface ▪ Form a tight layer of cells	▪ Synthesis and regulation of bone ECM deposition and mineralisation
Osteocytes	▪ Stellate shaped ▪ Possess fewer organelles than the osteoblasts	▪ Respond to mechanical stimuli ▪ Calcification of the osteoid matrix ▪ Blood-calcium homeostasis ▪ Mechanosensor cells of the bone
Osteoclasts	▪ Polarised ▪ Multinucleated	▪ Bone resorption

In terms of mechanical properties, the cortical bone has a tensile strength and Young modulus in the range 78.8-151.0 MPa and 17.0-20.0 GPa in the longitudinal direction, and 51.0-56.0 MPa and 6.0-13.0 GPa in the transversal direction, respectively, reflecting its anisotropy. The mechanical properties of the trabecular bone are about 20 times inferior than those of cortical bone, reflecting its high porosity. The anisotropic character is due to the combination an organic matrix with mineral crystals (calcium phosphate apatite) usually oriented in the longitudinal direction of bone, giving higher strength and stiffness in this direction.

8. Dynamics of Cell Adhesion

Cell adhesion is involved in various natural phenomena such as embryogenesis, maintenance of tissue structure, wound healing, immune response, metastasis as well as tissue integration on a biomaterial surface [62]. The majority of cell types derived from tissues (except blood cells) must adhere to other cells or to the extracellular matrix (ECM) in order to survive, which makes cell adhesion a critical factor determining cell survival. The onset of cell signaling occurs upon initial cell contact with its surrounding environment, whether it is the extracellular matrix (ECM), another cell, or a biomaterial [62]. A cell must be able to anchor efficiently on a surface in order to proliferate and undergo normal cellular functions. The term “adhesion” in the biomaterial domain covers different phenomena. The attachment phase occurs rapidly and involves short-term events like physicochemical linkages between cells and materials (ionic forces, van der Walls forces). The adhesion phase occurs in the longer term and involves various biomolecules such as extracellular matrix proteins, cell membrane proteins, and cytoskeleton proteins which interact together to induce signal transduction. As a result, transcription factors are activated and regulation of gene expression occurs determining the cell fate. Therefore, a myriad of complex reactions are initiated at sites of cell adhesion, involving receptor activation, actin cytoskeletal reorganisation, mechanosensing, and responsive signaling. In this section, the formation of adhesion sites as well as the major proteins involved in cell adhesion and signal transduction such as extracellular matrix proteins, adhesion molecules, and cytoskeleton proteins are described. A representation of both cell-biomaterial and cell-cell adhesion as well as the major proteins involved in the process is showed in **Figure I-27.**

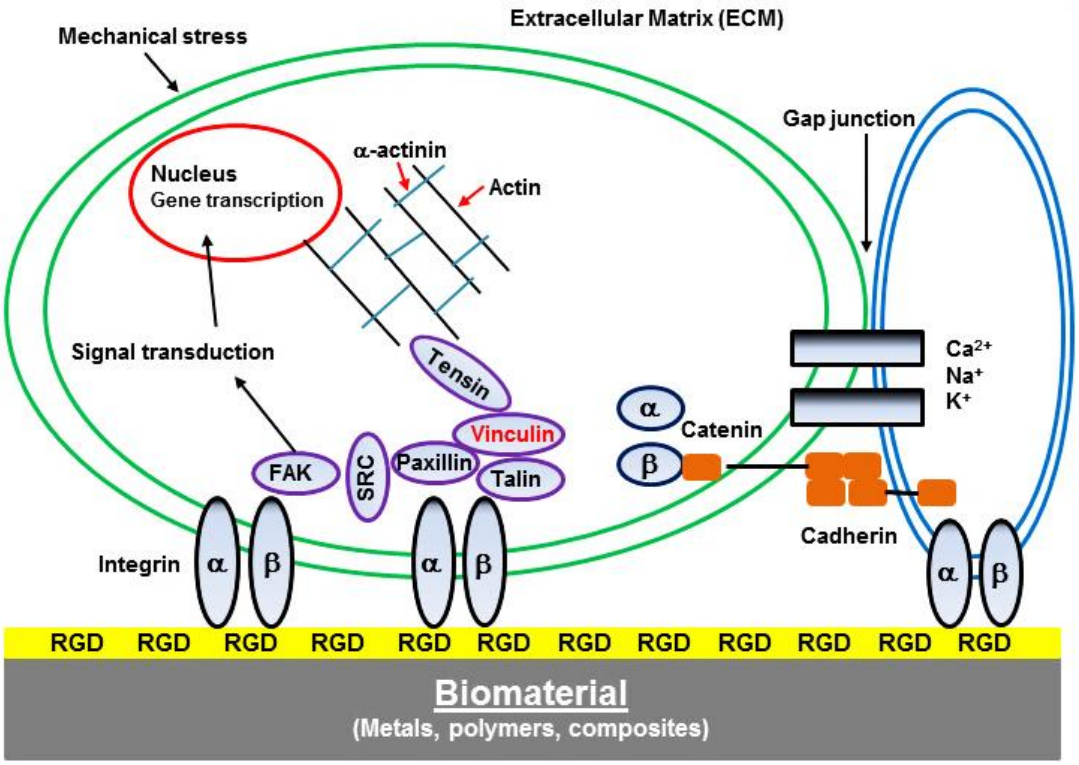

Figure I-27. Representation of the major proteins involved in cell-biomaterial and cell-cell adhesion processes (adapted from [62]). The RGD present on the extracellular matrix proteins binds to the integrins.

8.1. Extracellular Matrix Proteins

The extracellular matrix of bone is composed of 90 % collagenic proteins (97 % type I collagen and 3 % type V collagen) and of 10 % non-collagenic proteins (20 % osteocalcin, 20 % osteonectin, 12 % bone sialoproteins, 10 % proteoglycans, osteopontin, fibronectin, growth factors, bone morphogenetic proteins, etc.). All these proteins are synthesised by osteoblasts and most of them are intimally involved in the process of cell adhesion. Some bone proteins such as fibronectin, osteopontin, bone sialoprotein, thrombospondin, type I collagen, and vitronectin possess chemotactic or adhesive properties, notably because they contain Arginine-Glycine-Aspartic acid (RGD) sequences which specifically bind to some transmembrane receptors such as integrins.

8.2. Integrins and Cadherins as Adhesion Molecules

Adhesion molecules are characterised by their capacity to interact with a specific ligand. These ligands may be located on the membrane of neighbouring cells or in the extracellular matrix proteins. They belong to different families, in which the four main classes are selectins, immunoglobulin superfamily, integrins and cadherins. Integrins and cadherins have been described in osteoblastic cells during the adhesion process.

Integrins are transmembrane receptors that mediate the connection between a cell and its surroundings. The integrin family is structurally composed of 22 heterodimers with two types of sub-units α and β (16 α and 8 β sub-units have been discovered). Each sub-unit is made up of a large extracellular domain, a transmembrane domain and a short cytoplasmic domain. Different α/β subunit combinations give rise to an integrin with a different configuration and specificity for different binding proteins [158]. The human integrins and their binding specificities are given in **Table I-9**. The integrin spanning the cell membrane acts as an interface between the intra- and extracellular compartments and can translate the attachment of external ligands to internal information which induces cell adhesion, spreading, migration and consequently regulates cell growth and differentiation.

In contrast, cadherins are responsible for cell-cell adhesion in the adherens junctions (cell adhesion molecule-CAM). Cadherins are transmembrane glycoproteins acting with intracellular partners known as catenins. The later are responsible for interacting with intracellular proteins. The cadherin family is composed of numerous types of calcium-dependent molecules (E, P, N, L, R, 6B, 7, 11, 4). Association with α, β or γ-catenin is a prerequisite for the adhesive function of cadherins. They associate in a zipper homophilic model of interactions between cadherin molecules exposed on the plasma membrane of adjacent cells. Cell recognition and adhesion precede and control cell-cell communication via gap junctions. The gap junctions are constituted by homohexamus derived from a family of proteins called connexins. When the connexin of one cell, composed of six connexin molecules, is in register with a similar structure on a neighbouring cell, a transcellular channel is formed. Adherens junctions provide anchorage to surrounding cells and allow intercellular communications which occur through direct exchange of ions via gap junctions or through signals produced by the action of adherens junction containing cadherins.

Table I-9. Ligand-binding specificities of human integrins [159].

INTEGRINS	LIGANDS
α1β1	Laminin, collagen
α2β1	Laminin, collagen, thrombospondin, E-cadherin, tenascin
α3β1	Laminin, thrombospondin, uPAR
α4β1	Thrombospondin, MAdCAM-1, VCAM-1, fibronectin, osteopontin, ADAM, ICAM-4
α5β1	Fibronectin, osteopontin, fibrillin, thrombospondin, ADAM, COMP, L1
α6β1	Laminin, thrombospondin, ADAM, Cyr61
α7β1	Laminin
α8β1	Tenascin, fibronectin, osteopontin, vitronectin, LAP-TGF-β, nephronectin
α9β1	Tenascin, VCAM-1, osteopontin, uPAR, plasmin, angiostatin, ADAM, VEGF-C, VEGF-D
α10β1	Laminin, collagen
α11β1	Collagen
αVβ1	LAP-TGF-β, fibronectin, osteopontin, L1
αLβ2	ICAM, ICAM-4
αMβ2	ICAM, iC3b, factor X, fibrinogen, ICAM-4, heparin
αXβ2	ICAM, iC3b, fibrinogen, ICAM-4, heparin, collagen
αDβ2	ICAM, VCAM-1, fibrinogen, fibronectin, vitronectin, Cyr61, plasminogen
αIIbβ3	Fibrinogen, thrombospondin, , fibronectin, vitronectin, vWF, Cyr61, ICAM-4, L1, CD40 ligand
αVβ3	Fibrinogen, vitronectin, vWF, thrombospondin, fibrillin, tenascin, PECAM-1, fibronectin, osteopontin, BSP, MFG-E8, ADAM-15, COMP, Cyr61, ICAM-4, MMP, FGF-2, uPA, uPAR, L1, angiostatin, plasmin, cardiotoxin, LAP-TGF-β, Del-1
α6β4	Laminin
αVβ5	Osteopontin, BSP, vitronectin, CCN3, LAP-TGF-β
αVβ6	LAP-TGF-β, fibronectin, osteopontin, ADAM
α4β7	MAdCAM-1, VCAM-1, fibronectin, osteopontin
αEβ7	E-cadherin
αVβ8	LAP-TGF-β

8.3. Adhesion sites

Cells are able to modify their adhesive behaviour in response to changes in the molecular composition and physical forces present in their surrounding environment. Cell-ECM or cell-biomaterial contact occur through sites where cell adhesion receptors anchor a cell's cytoskeleton to a surface [160]. As aforementioned cells are able to recognise the characteristics of the environment through integrin-based signaling

pathways. The specific way through which a cell binds to a surface is via the formation of adhesion complexes. Adhesion complexes are closed junctions where the distance between the biomaterial surface and the cell membrane is about 10-15 nm. The external face of a adhesion complex present specific transmembrane receptor proteins such as integrins. On the internal face, some cytoskeleton proteins such as talin, paxillin, vinculin, focal adhesion kinase (FAK), and tensin mediate interactions between actin filaments and integrins. The exact composition of a given adhesion complex will in turn regulate cellular adhesion, migration, proliferation, and differentiation. The stability and further maturation of these adhesion complexes are mediated by a variety of factors such as applied force, spatial and temporal interactions between the actin cytoskeleton and integrin-based molecules [161]. The formation of adhesion complexes occurs in several stages, evolving in terms of size, structure, composition, and stability. The different types of cell-matrix and cell-biomaterial adhesion are summarised in **Table I-10**.

Table I-10. Characteristic features of cell-matrix and cell-biomaterial adhesion.

PROPERTY / STRUCTURE	FOCAL COMPLEXES	FOCAL ADHESIONS	FIBRILLAR ADHESIONS
Cell region	▪ Edge of lamellipodium	▪ Periphery	▪ Central region
Morphology	▪ Dot-like	▪ Elongated ▪ Oval	▪ Fibrillar
Size (long axis)	▪ 1 µm	▪ 3-10 µm	▪ 1-10 µm
Composition	▪ Paxillin ▪ Vinculin ▪ Tyrosine-phosphorylated proteins	▪ α_v integrin ▪ Paxillin ▪ Vinculin ▪ α-actinin ▪ Talin ▪ FAK ▪ Tyrosine-phosphorylated proteins	▪ α_5 integrin ▪ Tensin

Integrin assemblies first develop into nascent focal complexes, which are small dot-like compositions with approximately 1 µm in diameter. Focal complexes are formed under the cell lamellipodia, which are structures found at the periphery of a spreading cell in the shape of flat protrusions, containing branched networks of actin filaments [162-164]. These focal complexes are transient and unstable, and will therefore either

dissolve or develop into more mature structures depending on the cellular mobility. Further rearrangement of elementary nanocomplexes and reinforcement of the integrin-cytoskeleton bond will lead to the stabilisation of focal complexes, resulting in their development into larger focal contacts, which further mature into focal adhesions (FAs). FAs are typically elongated structures of about 2 μm wide and 3-10 μm in length, comprising integrins assembled in a cluster. They essentially serve as the points of contact between the ECM-biomaterial and the contractile actomyosin stress fibres inside the cytoskeleton, transferring chemical signals within and between cells [165]. Further maturation of FAs is marked by the presence of fibrillar adhesion, which are biochemically and structurally distinct from FAs and located more centrally in cells [166, 167]. They are rich in the protein tensin and are thin, elongated structures formed in alignment with the actin stress fibres, associating with fibronectin matrix deposition [166-168]. As the formation of fibrillar adhesions is driven by an actomyosin-dependent mechanism that affects cell contractility, it is expected that the dynamics of fibrillar adhesions will have a direct impact on stem cell phenotype, which is in part regulated by intracellular tension [167].

8.4. Signal Transduction and Cell Shape

As aforementioned Integrins, CAM molecules and gap junctions regulate gene expression by a signal transduction induced by cell-biomaterial or cell-cell adhesion processes. Integrins and cadherins have direct interactions with the cytoskeleton (F-actin fibre filaments) via α-actinin, talin and catenins. Integrin clustering and occupancy provoke the recruitment of tensin and FAK, their phosphorylation and subsequently the recruitment of talin, vinculin, and α-actinin. Some other molecules like FAK may play a mechanical role in binding a number of signalling and cytoskeletal molecules in parallel with its kinase activity. Talin, vinculin and α-actinin are responsible for linking the F-actin fibres to the plasma membrane. Various other intracellular signalling pathways are activated by cell adhesion. Among them, protein tyrosine phosphorylations, mitogen-activated protein kinase (MAP) activation, Ca^{2+} influx, pH alterations and inositol lipid turnover stand out. β-catenin molecules can interact with the cadherin system but also with fascin, which is involved in the formation of F-actin fibre filament bundles and with transcription factors.

The architecture of the actin cytoskeleton is essential to the maintenance of cell shape and adhesion. The rearrangement of F-actin fibre filament bundles induces changes in cell shape observed by finger-like (filopodia) or sheet-like (lamellipodia) protrusions. If assembled in long bundles, F-actin fibre filaments support filopodia formation. Conversely, if assembled in a mesh form, it supports lamellipodia formation. Furthermore, if present in bundles coupled with adhesion plaques, actin "stress fibres" may transmit forces to the ECM or biomaterial surfaces [169]. Many specialised contractile cell types use stress fibres to remodel tissues and extracellular matrix. The term "stress fibres" was coined to fit with the idea that these structures arise from the effects of tension on protoplasm. However, subsequent studies showed that in fact it is the stress fibres themselves that are contractile. Stress fibres are composed of bundles of approximately 10-30 actin filaments. These bundles are held together by the actin-crosslinking protein α-actinin, although other actin crosslinking proteins such as fascin, espin and filamin have also been detected in these structures. Different categories of stress fibres exist, and some of these structures are less suited for cell motility and more suited to static contraction. The stress fibres observed in fibroblasts have been divided into three classes on the basis of their subcellular location, i.e., ventral stress fibres, dorsal stress fibres and transverse arcs. An scheme showing the different types of stress fibres is presented in **Figure I-28**.

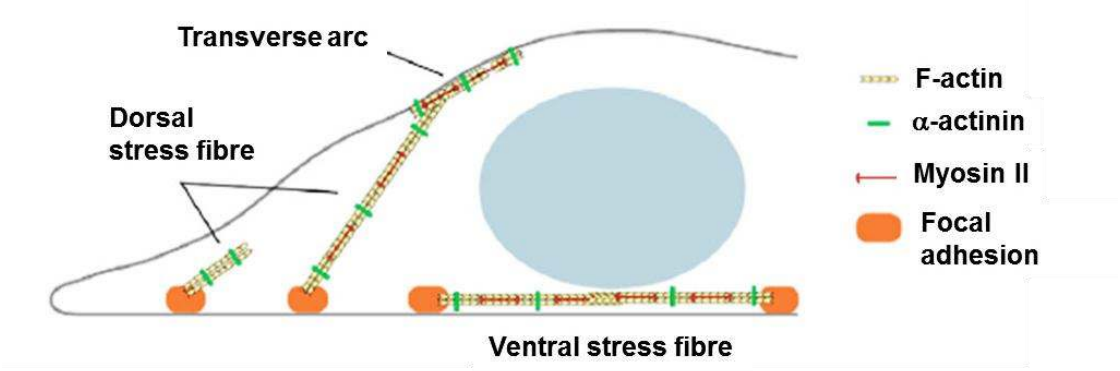

Figure I-28. Different types of stress fibres observed on fibroblasts according to their subcellular location.

Ventral stress fibres are the most commonly observed structures and lie along the base of the cell, attached to integrin-rich focal adhesions at each end. Dorsal stress fibres are attached to a focal adhesion at one end only, which tethers them to the base of the cell.

The rest of the structures rises towards the dorsal surface, terminating in a loose matrix of actin filaments. Transverse arcs are bundles of actin usually observed beneath the dorsal surface of migrating cells, just behind the protrusive lamella.

Finally, the signals mediated by alteration of cell shape may be processed by the nuclear matrix, which is physically linked to the cytoskeleton via the nuclear lamins. The latter are nuclear structural proteins involved in the regulation of gene transcription. ECM-mediated changes in cell shape can modify the nuclear matrix and therefore alter gene expression. Consequently, alteration of cell shape is able to initiate a switch between the proliferative and differentiative state of cells. Two main hypotheses exist to explain direct mechanotransduction, that is, percolation and tensegrity. The percolation hypothesis involves a network of fibres which transfers a mechanical signal from one side to the other of the cell. According to this, the network extends from the ECM, which is connected by focal adhesions to actin fibres, which are then connected by intermediate filaments to lamins in the nucleus. In this way the plasma membrane is connected with the nuclear region [170]. The second hypothesis, known as tensegrity or tensional integrity, is based on continuous alternating compression and tension of cytoskeleton filaments [171]. The actin microfilaments and the intermediate filaments act as tensile elements, while the microtubules act as compressive elements. When the mechanical signal, transferred by the tensegrity elements, is transmitted to lamins in the nucleus it can influence the transcription of specific genes.

9. Mesenchymal Stem Cells

Historically, in 1970s, Friedenstein and colleagues [172, 173] demonstrated that bone marrow contains a population of Hematopoietic Stem Cells (HSCs) and a rare population of plastic adherent stromal cells (0.001-0.01 % of total nucleated cells) [174]. These plastic adherent cells, initially referred to as stromal cells, and now commonly called Mesenchymal Stem Cells (MSCs), were capable of forming single-cell colonies. As the plastic-adherent bone marrow cells were expanded in culture, round colonies resembling fibroblastoid cells formed and were given the name colony forming unit-fibroblasts.

MSCs have been significantly contributed to advances in the fields of tissue engineering and orthopaedics due to their unique characteristics (self-renewal and

multipotency). Therefore, in the present work human Mesenchymal Stem Cells (hMSCs) were selected to study the impact of topographical and chemical cues present on the laser textured titanium surfaces. In this section concepts as the identification and isolation of MSCs, self-renewal and differentiation capacities are described.

9.1. Identification and Isolation of MSCs

The defined microenvironments in which stem cells dwell are called niches. Different types of stem cells dwell in different natural habitats where they undergo growth and transition. The different types of human stem cells are summarized in **Table I-11**.

Table I-11. Different types of human stem cells.

STEM CELL	SOURCE	CELLS PRODUCED	REFS
Hematopoietic	▪ Bone marrow	▪ Blood ▪ Endothelial ▪ Hepatic ▪ Muscle cells	[175, 176]
Neural	▪ Brain	▪ Neurons ▪ Astrocytes ▪ Oligodendrocytes ▪ Blood cells	[177, 178]
Epithelial	▪ Gut ▪ Epidermis	▪ All cells in epithelium crypts ▪ All cells in epidermal layers	[179, 180]
Mesenchymal	▪ Bone marrow ▪ Adipose tissue ▪ Epithelial tissue ▪ Umbilical cord matrix	▪ Bone ▪ Cartilage ▪ Tendon ▪ Adipose ▪ Muscle ▪ Marrow stroma ▪ Neural	[181, 182]
Embryonic	▪ Blastocyst inner cell ▪ Mass primordial germ cells	▪ All cells	[183-185]

No unique cell surface marker unequivocally distinguishes MSCs from other HSCs, which makes a uniform definition difficult. However, The International Society for Cell

Therapy proposed a minimum criteria for defining multipotent mesenchymal stroma cells [186] that comprise: (i) adherence to plastic in standard culture conditions; (ii) expression of the surface molecules CD73, CD90, and CD105 in the absence of CD34, CD45, HLA-DR, CD14 or CD11b, CD79a, or CD19 surface molecules as assessed by fluorescence-activated cell sorter analysis; and (iii) a capacity for differentiation to osteoblasts, adipocytes, and chondroblasts *in vitro*. These criteria were established to standardise hMSCs isolation but may not apply uniformly to other species such as murine MSCs, for instance.

MSCs isolated from bone marrow [187], adipose tissue [188], synovial tissue [189], lung tissue [190], umbilical cord blood [191], and peripheral blood [192] are heterogeneous, with variable growth potential, but all have similar surface markers and mesodermal differentiation potential [193]. Furthermore, MSCs have been isolated from nearly every tissue type (brain, spleen, liver, kidney, lung, bone marrow, muscle, thymus, aorta, vena cava, pancreas) of adult mice, which suggests that MSCs may reside in all postnatal organs. They have been isolated from numerous species and the three critical steps that allow MSCs to be isolated from other bone marrow cells are as follows: (i) the use of density gradient centrifugation (Ficoll-Paque; hydrophilic polysaccharide reagent) to separate nonnucleated red blood cells from nucleated cells; (ii) the ability of MSCs to adhere to plastic; and (iii) the ability of monocytes to be separated from MSCs by trypsinisation. Protocols for isolation and expansion are similar among various species. Expansion of plastic adherence MSCs is the most widely used method for obtaining these cells and represents the most commonly used source of MSCs for different applications. A scheme of MSCs isolation and expansion is given in **Figure I-29**.

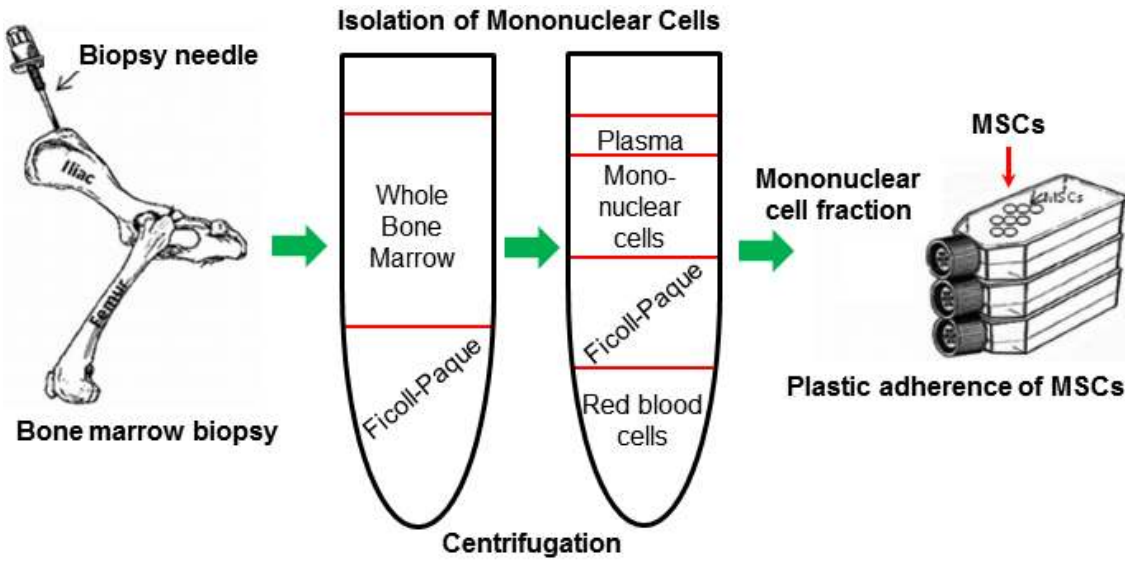

Figure I-29. Representation of the common protocol used for isolation and expansion of MSCs from bone marrow. Bone marrow is collected, and a density gradient centrifugation with Ficoll-Paque is performed to separate nonnucleated red blood cells from nucleated cells. Then, the mononuclear cell fraction is transferred to plastic T-tubes, in which MSCs adhere. Finally, monocytes are separated from MSCs by trypsinisation (adaptation from [172]).

9.2. Self-Renewal

Self-renewal is the process through which stem cells proliferate and divide while retaining their undifferentiated stem state [194]. Due to the unique ability of adult stem cells to both self-renew and differentiate, a well-balanced tissue homeostasis must be maintained in order to regulate these two processes. If self-renewal overwhelmed differentiation, an unnecessarily large stem cell population may be present, but if differentiation is uncontrolled, the stem cell population will exhaust quickly. The stem cell niche plays an important role in keeping the balance between self-renewal and differentiation through several mechanisms. Stem cells divide through a process known as asymmetric division [194]. The two established asymmetrical models of stem cell division are known as invariant asymmetry and populational asymmetry [195], **Figure I-30**. In invariant asymmetric cell division, an adult stem cell gives rise to two daughter cells, one of which stays a stem cell while the other undergoes differentiation. This route of stem cell division is most prevalent in unicellular organisms and invertebrates. In contrast, mammalian stem cells generally follow the route of populational asymmetric division, which is highly regulated. In this mechanism, each adult stem cell divides to give rise to daughter cells that each has a finite probability of staying as a

stem cell or becoming a committed progenitor that will undergo differentiation. Statistically, one stem cell results in one stem daughter and one committed progenitor. However, it is also possible for both daughter cells to be stem or committed progenitors. The fate of the daughter cells is dependent on a variety of extrinsic cues that are exposed in the ECM. Thus, a complex combination of niche factors works together to dictate the outcome of each cell division, thereby upholding a precise balance between stem cell self-renewal and differentiation [195].

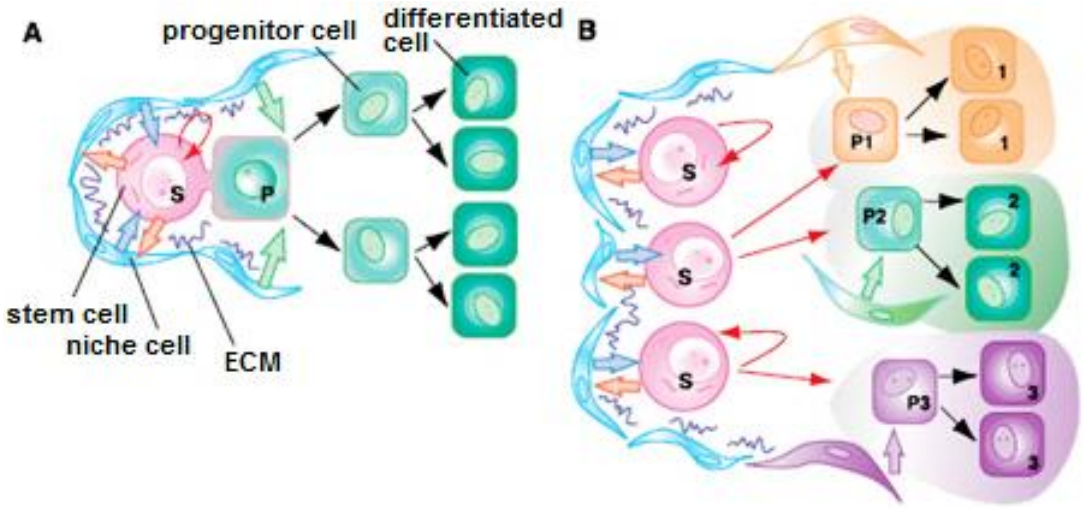

Figure I-30. Cell division by invariant and populational asymmetry. S denotes stem cell and P denotes progenitor cell. (A) In invariant asymmetric cell division, a mother cell gives rise to two daughter cells, one of which stays stem while the other becomes a progenitor cell that becomes a fully differentiated cell. (B) In populational asymmetric cell division, each daughter cell has a finite probability of staying as a stem cell or becoming a progenitor cell. The daughter cells can go down different routes and become different types of progenitor cells (P1, P2, P3) and ultimate become fully differentiated cells [195].

9.3. MSCs Differentiation

MSCs are a unique type of stem cells derived from the bone marrow capable of undergo differentiation into distinctive end-stage cell type [196, 197]. These cells include but are not limited to osteoblasts (bone), chondrocytes (cartilage), adipocytes (fat), myoblasts (muscle), and fibroblasts (tendon), **Figure I-31**. The differentiation process follows a strict route whereby the MSCs first undergoes a highly proliferative stage, then enters commitment and gradually becomes a differentiated cell type through lineage progression.

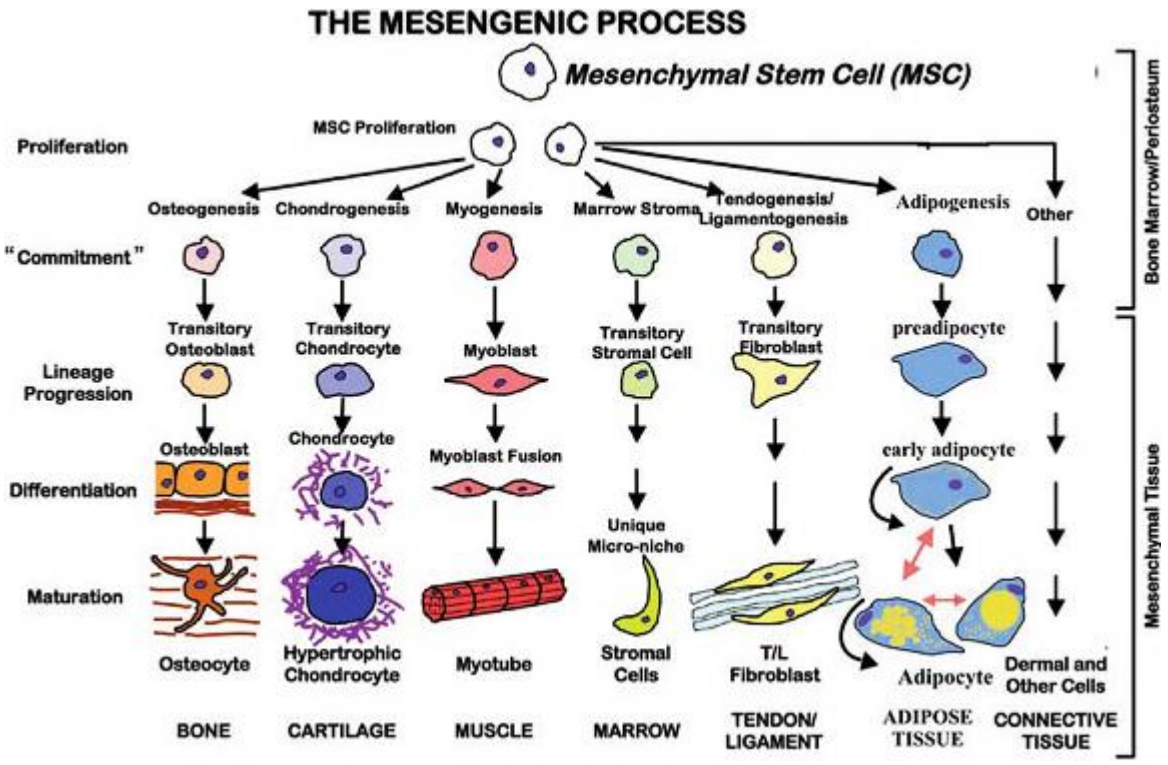

Figure I-31. The MSCs differentiation process. MSCs are able to differentiate into many different types of mature, end-stage cells. Throughout the differentiation process, MSCs are capable of producing cells with distinct phenotypes at intermediate stages [197].

The detection of molecular and cellular markers at various stages of MSCs differentiation characterises the cell lineage development. A detailed summary of these markers can be found in a review article published by Minguell *et al.* [198]. In particular, bone cells can be identified by markers such as osterix (OSX), osteopontin (OPN), osteocalcin (OCN), alkaline phosphatase (ALP) activity, among others. Matrix mineralisation can also be observed through the use of calcium and hydroxyapatite binding fluorescent dyes such as xylenol orange and OsteoImage^{TM}. It is noteworthy that some of the aforementioned bone markers were used in the present work for the assessment of MSCs differentiation.

In the case of an osteogenic lineage, the cascade of differentiation is shown in **Figure I-32**. The later the differentiation stage the lower the capacity for self-renewal and cell proliferation. Osteoprogenitor cells are characterised by the expression of several bone matrix macromolecules. Mature osteoblasts are non-migratory and highly differentiated cells that can differ substantially in their properties depending on their stage of development. Depending on their function and phenotype mature osteoblasts

are divided into four categories, namely: (i) active osteoblasts, which are cuboidal in shape, mononuclear and rich in alkaline phosphatase activity. They synthesise and secrete collagen type I and glycoproteins (osteopontin and osteocalcin), cytokines and growth factors into a region of unmineralised matrix, and produce calcium phosphates minerals extra- and intracellularlly within vesicles; (ii) osteocytes, mature osteoblasts which have been trapped within bone matrix and are responsible for bone maintenance and homeostasis; (iii) bone lining cells, found along the bone surfaces that undergo neither *de novo* bone formation nor resorption; and (iv) inactive osteoblasts, which are elongated cells, undistinguishable morphologically from the bone lining cells.

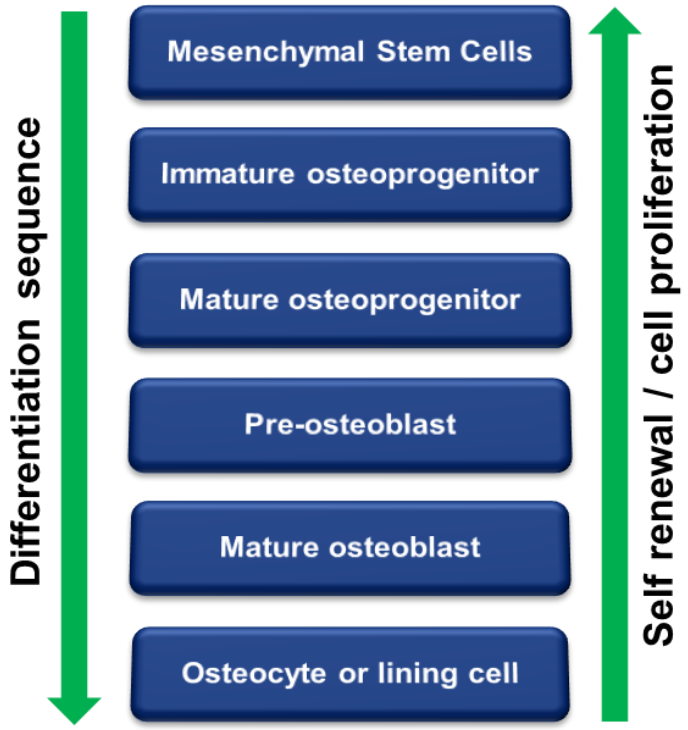

Figure I-32. Representation of the differentiation sequence during osteogenesis and the relation with the self-renewal capacity of the cells.

Furthermore, chemical signals are directly implicated in the differentiation of stem cells. The differentiation of MSCs into a particular lineage can be stimulated by the presence of growth factors and specific chemicals that activate the differentiation pathway, **Figure I-33**. *In vitro* observations have been showed that MSCs in the presence of dexamethasone (~ 10 nM), β-glycerolphosphate (BGP; 5-10 mM), and ascorbic acid (50-500 μM) express alkaline phosphatase and calcium accumulation, a morphology consistent with osteogenic differentiation [199].

These osteogenic cells reacts with antiosteogenic antibodies and form a mineralised extracellular matrix. Dexamethasone is a synthetic glucocorticoid tha stimulates MSCs proliferation. Organic phosphate released after enzymatic hydrolisis of β-glicerolphosphate plays an important role in matrix mineralisation. Ascorbic acid is a co-factor in hydroxilation of prolins and lysine moiety of collagen molecules and is an abundant protein in the ECM [174].

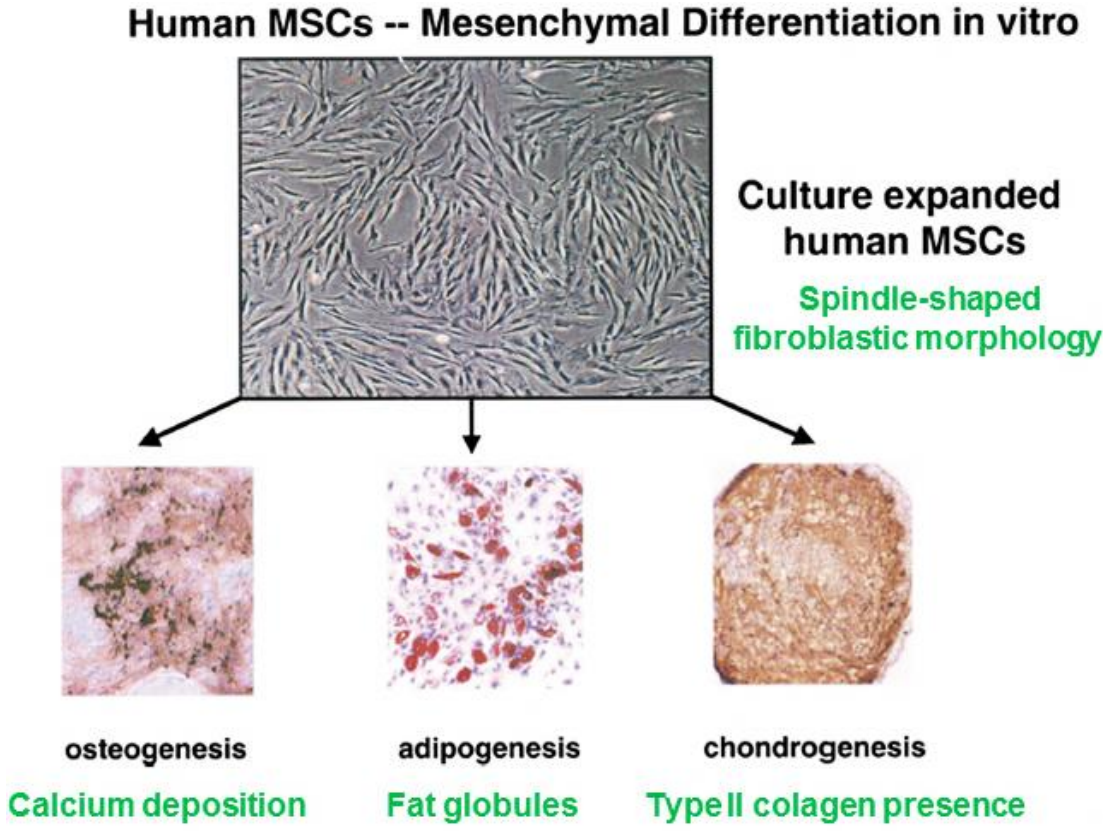

Figure I-33. Culture-expanded hMSCs exhibit a spindle-shaped fibroblastic morphology following *ex vivo* culture expansion (top panel). Under appropriate inducing conditions, the culture will demonstrate osteogenic, adipogenic, and chondrogenic differentiation (adapted from [200]).

In addition to these osteogenic supplements, there are other osteogenic factors, including BMP-2 and bFGF. Chondrocyte differentiation has been commonly observed on MSCs cultured in the presence of dexamethasone and TGF-β3 [201]. Subsequently, the cells begin secreting an extracellular matrix, which includes type II collagen, aggrecan, and anionic proteoglycans, consistent with articular cartilage formation. Glucocorticoids play an important role in the differentiation of MSCs into chondrocyte lineage by promoting TGF-β-mediated upregulation of collagen type II and inducing the

matrix components aggrecan, dermatopontin, and collagen type XI. Adipogenic differentiation of MSCs have been reported in the presence of dexamethasone, insulin, indomethacin, and 1-methyl-3 isobutylxanthine [187]. Cells express markers consistent with adipocytes, such as peroxisome proliferation-activated receptor-γ2, lipoprotein lipase, and fatty acid binding protein aP2. These adipocytes accumulate lipid-rich vacuoles and eventually coalesce.

In addition, the phenotype of terminally differentiated cells can be distinguished by their morphology and chemical properties. The shape of cells and their specific interaction with the surroundings may provide clues that define their identity. Mature cells with high tension morphologies, such as osteoblasts, will present a distinct appearance characterised by a well-spread cytoplasm, highly organised actin stress fibres, and stable and mature focal adhesions to support intracellular tension. In contrast, low tension morphologies are present in adipocytes which tend to present a rounded shape with sparse and undeveloped focal complexes.

10. Bacteria, The Agents of Infection

The number of surgical procedures being performed has increased during the last 30 years due to advances in surgical techniques, the increasing importance given to healthcare priorities by the general public and longer life-time expectancy [202]. Given that the overall number of surgical procedures is increasing, the burden of Surgical Site Infections (SSIs) could be more significant. SSIs comprise the third most frequently reported Nosocomial Infection (NI), representing 14-16% of all hospital nosocomial infections [203]. It has been reported that about 2-5% of patients undergoing surgery will develop SSIs [204]. In addition to the increase of postoperative morbidity and mortality in surgical patients, SSIs are also the cause of increased hospitalisation costs by lengthening the mean postoperative hospitalisation stay.

Surgical site infections are primarily caused by bacteria, with *Staphylococcus aureus* representing by far the most common pathogen found in surgical wounds. *Staphylococcus* strain have been reported to be responsible for about 50-60 % of the bone and implant-associated infections cases worldwide [6]. Surveillance data from the Health Protection Agency on surgical site infections in the U.K. between 1997 and 2005 found *S. aureus* to be the causative agent in 41.4 % of hip prosthesis, 33.5 % of knee prosthesis, 53 % of bone fracture and 59.1 % of hip hemiarthroplasty infections.

Therefore, the concepts concerning to bacteria (*Staphylococcus*), bacteria adhesion on bone and biomaterial surfaces and biofilm formation are described.

10.1. What Are Bacteria?

Briefly, bacteria constitute a large domain of prokaryotic microorganisms, i.e., unlike cells of animals and other eukaryotes, bacterial cells do not contain a nucleus and rarely harbour membrane-bound organelles. Their cell wall is composed of phospholipids, like eukaryotic cells, but they are much more rigid. This is in part due to an external layer of peptidoglycan, which is thicker in Gram-positive bacteria than that of Gram-negative bacteria. In the latter, the peptidoglycan layer is covered by an additional polysaccharide outer layer. Typically, these microorganisms are few micrometres in length (1μm to several tens of microns), and have a number of shapes, ranging from spherical to rod-shaped and twisted. Bacteria also vary in the structures present on their surface. Some bacteria can express flagella transiently, which renders them very motile. Bacteria may also have fimbriae, also called pili or curli depending on species and strain, which aid in attachment to the surfaces. Whereas single cells can adhere to surfaces independently of each other, bacteria live on surfaces as a community within a species- and strain-specific Extracellular Polymeric Substance (EPS) [9, 205].

Bacteria inhabit soil, water, acidic hot springs, radioactive waste, and the deep portions of Earth's crust. They also live in symbiotic and parasitic relationships with plants and animals. The vast majority of the bacteria in the human body are rendered harmless by the protective effects of the immune system, and some are beneficial. However, several species of bacteria are pathogenic and can cause infectious diseases, which can strongly affect the human health and even lead to death.

10.2. Biofilm and Its Formation

Bacterial biofilms are sticky agglomeration of bacteria embedded in an EPS [206, 207], **Figure I-34**. Biofilms are particularly durable and persistent, and their formation is a critical step in both bone and implant-associated infections. Owing to their high resistance to mechanical interference, mechanisms of innate and acquired host defenses, and antibiotic treatment, they cause enormous problems in the environment as well as in human and animal infections.

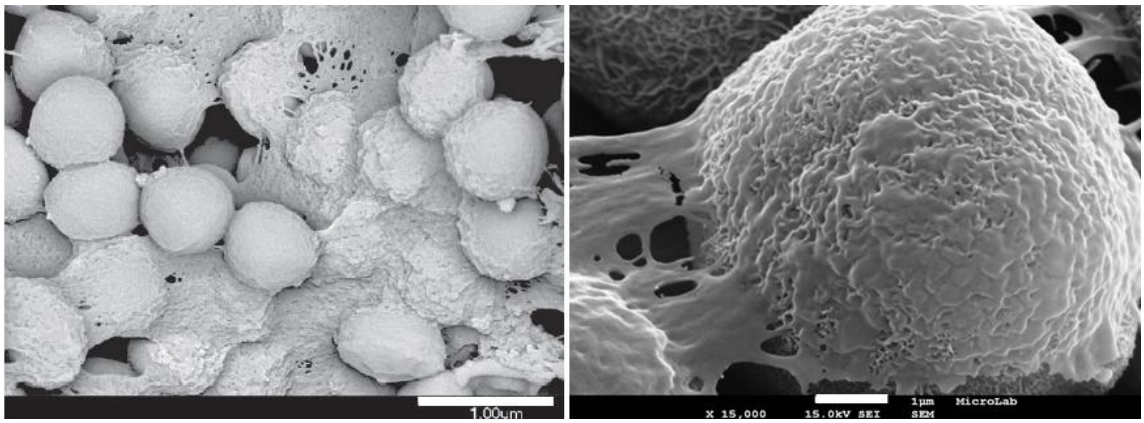

Figure I-34. Low and high magnification SEM micrographs of a *Staphylococcus* biofilm. Bacteria are covered with a polysaccharide matrix (adapted from [6]). The scale bar is 1 µm.

The formation and development of a biofilm follow steps that may vary depending on the biological characteristics of the bacteria. The presence of appendages and specific membrane receptors and the quantity and nature of the exopolymeric substances synthesised by the bacteria are examples of factors that are highly dependent on bacterial species and are able to strongly influence bacterial adhesion and biofilm development. Nevertheless, four common steps are usually distinguished in the biofilm formation, that is, attachment, adhesion, proliferation, and detachment, **Figure I-35**.

In the first step a bacterium is brought into contact with the surface of implant due to gravitational forces, Brownian motion or hydrodynamic forces. In addition, flagella can induce motion in some bacterial species, which is not the case of *Staphylococcal* cells. The second step of biofilm formation consists of adhesion of the bacteria to a surface, which may occur onto any biotic or abiotic surface. In particular, *S. aureus* has an extraordinary capacity to attach to indwelling medical devices through direct interaction with the device's polymer or metal surface or by establishing connections to human matrix proteins after those proteins have covered the device surface. Both physico-chemical and chemical interactions are thought to be involved at this stage. These interactions are highly dependent on the properties of the material surface on which the biofilm may develop. This is the step most influenced by topographical and chemical features of the surfaces.

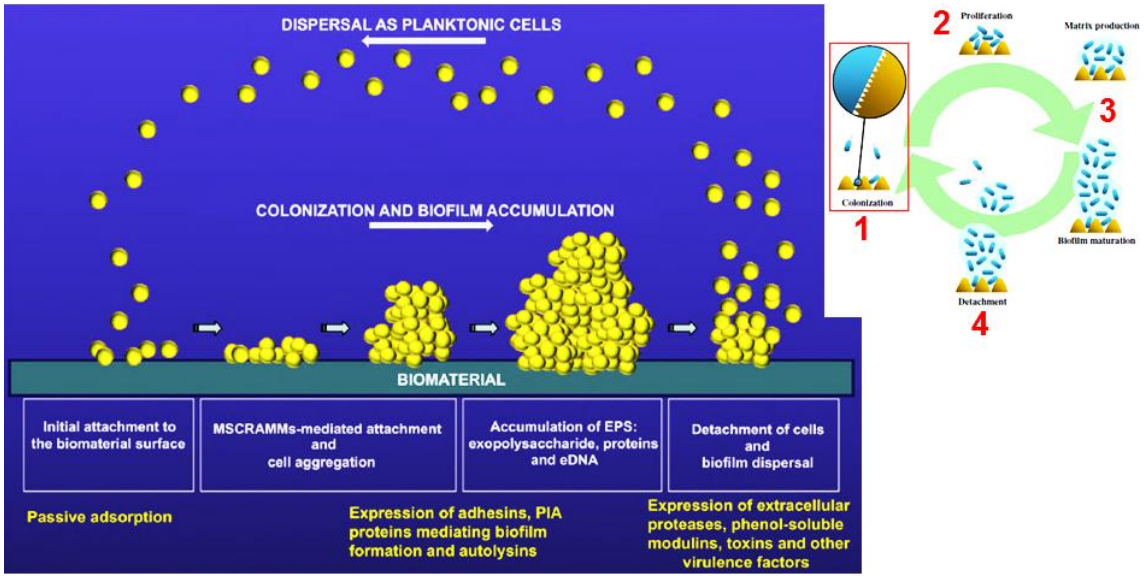

Figure I-35. Representation of the cycle of biofilm formation. Bacteria attach and adhere to the surfaces (1) followed by proliferation (2), production of the extracellular polymeric substance (EPS) and biofilm maturation (3), and detachment of single cells or cell clusters (4) (adapted from [208]).

The third step of biofilm formation cosists of proliferation of the adherent bacteria and, in most cases, synthesis of the biofilm matrix, which contributes to intercellular aggregation. In *Staphylococcal* cells, the matrix consists of several secreted polymers such as exopolysaccharide, teichoic acids, and specific proteins as well as DNA originating from lysed cells. Further, the biofilm becomes mature and is associated with a specific bacterial metabolism and physiology. The phase of biofilm maturation is characterised by intercellular aggregation, that can be accomplished by a variety of molecules such as adhesive proteins or- usually polysaccharide-based-exopolymers, and biofilm structuring forces that lead to the typical three-dimensional appearance of mature biofilms with its mushroom-like cell towers surrounding fluid-filled channels. The main molecule responsible for intercellular adhesion is the Polysaccharide Intercellular Adhesin (PIA), which is also called Poly-N-Acetylglucosamine (PNAG) [208]. The de-acetylation of N-acetylglucosamine residues in PIA introduces a positively charged character in the otherwise neutral molecule by liberating free amino groups that become charged at neutral or acid pH. As the bacterial cell surface is negatively charged, PIA supposedly works like a glue that sticks the cells together by electrostatic interaction. In the spaces between the “towers” or “mushrooms” of a three-dimensional biofilm structure there are fluid-filled channels that are believed to have a

vital function in delivering nutrients to cells in deeper biofilm layers. *Staphylococcal* cells use quorum-sensing controlled surfactant peptides to structure biofilms. Phenol-soluble modulins (PSMs) are a class of peptides that have first been described as pro-inflammatory agents in *Staphylococcus epidermidis*. PSM homologs also occur in *S. aureus* but it is not known if they have the same role in biofilm development such those in *S. epidermidis* [206].

Within this community bacteria interact with each other through membrane organelles and biochemical signals. As aforementioned, the creation of a viable biofilm requires channels through which nutrients can penetrate into deeper biofilm layers and thus, additional factors that disrupt cell-cell interactions. These factors can, ultimately, also lead to the detachment of cells and cell clusters from the biofilm (fourth step) and therefore control biofilm thickness and expansion. Biofilm detachment plays a critical role during biofilm-associated infection, because it enables cells to spread through the blood and other body fluids to new infection sites. In *staphylococcal* cells, this mechanism is controlled by the quorum-sensing system *agr*.

10.3. Staphylococci

The genus *Staphylococci* currently contains 48 species, all of which are part of the normal skin and mucous membrane flora of humans and animals [209]. As aforementioned, the common causes of both bone and implant-associated infections are *S. aureus* and *S. epidermidis*. The former is a common cause of metal-biomaterial, bone-joint, and soft-tissue infections, while the latter is common found in polymer-associated implant infections. *Staphylococci* are Gram-positive bacteria with diameters in the range 1-2 μm, nonmotile, and nonspore forming facultative anaerobes that grow by aerobic respiration or fermentation. They are characterised by individual cocci, which divide in more than one plane to form grape-like clusters, **Figure I-36**. Their cell wall is composed of peptidoglycan and teichoic acids, and attached to them are adhesins and exotoxins. Many *Staphylococci* strains, particularly *S. epidermidis* and some *S. aureus* strains have the capability of producing biofilm. Usually, biofilm-associated infections involving *S. aureus* usually requires more intensive care. Often, their biofilm-associated infections are difficult to treat with antibiotics and devices need to be replaced more frequently than those infected with *S. epidermidis*.

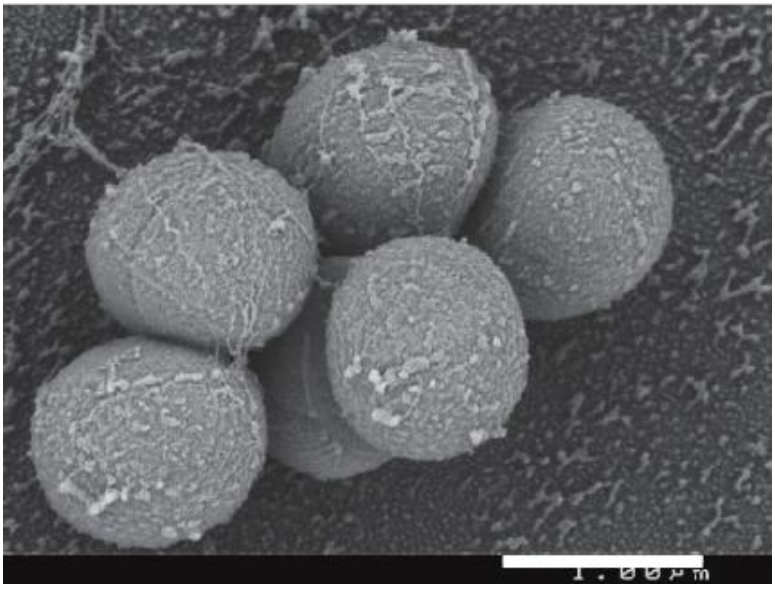

Figure I-36. SEM micrograph of *S. aureus* forming grape-like clusters [6]. The scale bar is 1 μm.

10.4. Bacteria Adhesion on Bone

Bacteria of the genus *Staphylococcus* are the principal causative agents of two major types of infection affecting bone-septic arthritis and osteomyelitis, which involve the inflammatory destruction of joint and bone, respectively. These infections cause serious morbidity and are often difficult to manage. The principal routes of infection for both osteomyelitis and septic arthritis are either haematogenous, resulting from bacteremia; contiguous, when the infection is transmitted from local tissue; or direct, resulting from infiltration of bone, often following injury, surgery or implantation of a foreign body, such as joint replacement [7].

It is known that the balance of activity between osteoblasts and osteoclasts is crucial to maintaning the homeostasis of bone turnover, and any shift in the relative levels of osteoblast and osteoclast activity can result in bone pathology. Infection with a pathogen such as *S. aureus* is capable of stimulating such a shift mediated in part by induction of an inflammatory response. A number of host cytokines play a significant role in the pathogenesis of osteomyelitis, and there is strong evidence that the production of these cytokines is induced by *Staphyloccoccal* infection of bone, contributing directly to bone destruction. *S. aureus* infection of bone initiates local and systemic production of TNFα, IL-1 and IL-6, among others cytokines. Elevated levels

of these cytokines tend to increase the osteoclast differentiation and bone resorption and decrease osteoblast-mediated bone matrix production and mineralisation. In addition to *Staphylococcal* induction of inflammatory mediators, bacteria of this genus are involved in more direct interactions with bone cells. Invasion and persistence of *S. aureus* in host cells *in vitro* has been decribed for many different cell types, including epithelial cells, endothelial cells and keratinocytes. Therefore, the internalisation of *S. aureus* by bone cells *in vivo* provides a protective niche for the bacterium, where it is shielded from immune effector mechanisms and antibiotics, may explain the persistent cases of osteomyelitis. The physical contact between the bacteria and osteoblasts induces the expression of specific cytokines that bind to proteins associated with death domain and activate the commitment of cells towards an apoptotic pathway.

10.5. Bacteria Adhesion on Biomaterial Surfaces

Biomaterial science has greatly progressed in the achievement of a safe biocompatibility, free from damage to neighbouring tissues. Unfortunately, a major drawback to implanted devices remains in the possibility of bacterial adhesion to biomaterials, which causes biomaterial-centrered infection. Therefore, the search for biomaterials that are able to provide the optimal resistance to infection can be based only on the deep understanding of the interactions between bacteria and biomaterial surfaces. Bacteria are able to attach to human extracellular matrix proteins, which exist as an adsorbed layer in the implant surfaces soon after insertion in the human body. *S. epidermidis* and *S. aureus* express dozens of so-called MSCRAMMs (Microbial Surface Components Recognising Adhesive Matrix Molecules) that have the capacity to bind to human matrix proteins such as fibrinogen or fibronectin, and often combine binding capacity for several different matrix proteins. MSCRAMMs have a common structure that includes an exposed binding domain, a cell-wall spanning domain, which often has a repeat structure, and a domain that is responsible for the covalent or non-covalent attachment to the bacterial surface.

11. On The Control of Tissue and Bacterial Cells Behaviour

While implants have achieved high success rates, two major complications may be encountered, that is, the lack of bone tissue integration and implant-associated infections. The interaction of proteins, tissue cells, and bacteria with the implant

surface, plays a determining role in the success or failure of the implant. Therefore, to enhance the success of implants, their surfaces should inhibit bacterial colonisation and concomitantly promote tissue cell (MSCs and osteoblast) functions. Thus, the precise control of the biomaterial surface properties is of upmost importance to induce preferred cell responses. In this section some previous works dealing with some common ways with which tissue cell and bacteria response may be controlled by exploring the biomaterial's surface properties are revisited.

11.1. Impact of Surface Topography on Tissue Cell Behaviour

There is a plethora of literature describing the effect of nanotopography on tissue cells. However, the type of topography studied has been dictated more by the type of substrate available than biological motivation. A multitude of factors may affect the behaviour of cells in response to surface topography. These include the height, width and shape, but also the organisation of the nanofeatures, the chemistry and rigidity of the surfaces and the type of cell used in the study.

As early as the 1950s, researchers have investigated the changes in cell morphology and cell movement towards different substrate parameters [210]. Due to their motility and dinamics, their shapes constantly change as they undergo to environmental stimulli. The cascade of cell signaling determining a cell's fate lies within the conformations of its cytoskeleton structures, responsible for guiding the cell's transduction and reception of signals and cues. In turn, changes in cell shape and spreading plays an expressive role in directing the multitude of cell response pathways. Chen *et al*. [211] demonstrated that cell shape and morphology affects the conformation of integrin binding, which induced changes in the apopitotic behaviour of endothelial cells. In this study, fibronectin beads of various sizes were deposited on the substrate surface, and changes in cell shape and spreading were assessed after cellular culture. The authors found that cells adhered and spread on larger beads (25 μm in diameter) with a flattened morphology. Conversely, cells adopted a more rounded shape as the bead size decreased (10 μm in diameter), resulting in more apparent apoptosis. In the same study it was showed that the correlation between cell shape and focal adhesions (FAs) was directly proportional to cell spreading. Changes in cell shape and symmetry induced alterations in the internal cytoskeleton architecture, thereby affecting FAs assembly which ultimately leads to signal transduction for driving cell function.

McBeath *et al.* [212] showed the influence of cell morphology on their fate using patterned fibronectin islands of varying sizes on PDMS substrate. MSCs were seeded on these protein islands, either 10,000 or 1,024 μm^2, as single cells per island, and allowed to spread and adhere. MSCs were able to adhere and spread efficiently on large islands, presenting a flattened appearance. Conversely, on small islands, MSCs were observed to be rounded and did not spread due to the limited spacing available for spreading. The degree of osteogenic and adipogenic differentiation was then investigated, and MSCs on large islands differentiated only into osteoblasts while MSCs on small islands differentiated only into adipocytes. These results suggest preliminarily that independent of factors like cell seeding density and cell-cell contact, cell shape alone is a regulator of MSC differentiation.

Kilian *et al.* [213] performed a similar study where microislands of fibronectin were patterned in various shapes with a constant area, only changing the aspect ratio and curvature of the shape. The area of the microislands was optimised to allow only one individual cell to adhere and spread, giving the possibility for the cell to assume the shape of the underlying island. First, MSCs were cultured on rectangular microislands with a constant area and length-to-width ratios of 1:1, 3:2, and 4:1, and evaluated for osteogenic and adipogenic differentiation. It was found that osteogenesis increased with length-to-width aspect ratio, while the opposite trend was observed for adipogenesis. Osteogenesis was more prominent on rectangular microislands at 4:1 aspect ratio while adipogenesis was more apparent for 1:1. Further, MSCs were cultured on constant area microislands with pentagonal symmetry but varying curvature such as a flower-shaped island with convex curves, a perfect pentagonal island, and a star-shaped island with concave curves and sharp points at the vertices. With the increase in curve concavity, osteogenesis was more prevalent while adipogenesis showed a decreasing trend. They concluded that shape cues can be rationally used to control differentiation-specific signaling in MSCs. Taking into account the aforementioned studies, a general link can be drawn between cell morphology and differentiation. It is suggested that stem cell shapes that promote cytoskeletal contractility (flattened shape, high aspect ratio, concavity) lead to increased osteogenesis, while stem cell shapes that limit contractility (rounded shape, low aspect ratio, low concavity) lead to increased adipogenesis. These observations are consistent with the typical appearance of osteoblasts and adipocytes *in vivo*. However, the exact dependency of differentiation on cell shape involves the

interplay between complex signaling mechanisms and cannot be easily summarised without taking a look at other factors involved in cell fate determination.

Balloni *et al.* [214] also assessed the impact of surface topography on the differentiation of MSCs cultured on machined and dual acid-etched titanium surfaces. MSCs were allowed to adhere and proliferate on both types of surface. It was observed that on dual acid-etched surfaces in comparison with machined titanium, cells showed increased mRNA expressions of bone morphogenetic protein 2 (BMP-2), Runx2, and osterix, along with specific markers of osteoblastic phenotype, such as bone sialoprotein and osteocalcin. These proteins are all critical players which are interconnected in osteoblastic differentiation, as BMP-2 upregulates the expression of Runx2 and osterix. Runx2 induces MSC differentiation into preosteoblastic cells while osterix ensures that these cells fully develop into mature osteoblasts in the commitment process. Evidently, the increased expression of all of these proteins is a sign that bone formation is favored on dual acid-etched titanium, confirming that surface roughness indeed is a potent modulator of cell fate.

A lot of works have been done to prove that nanoscale variations in dimensions or even changes in order or disorder of the nanofeatures can have a clear impact on cell behaviour. Simple topographic features such as cliffs and grooves have been patterned on the microscale and shown to affect the alignment and elongation of cells (cell contact guidance). Wilkinson *et al.* [215] reported that upon interaction with these type of surface features, cells elongate and align along the grooves. This change in arrangement causes a rearrengement of the cell cytoskeleton, whereby the actin microfilaments reconfigure to the shape and dimensions of the surface topography. Yim *et al.* [216] reported similar effects on MSCs, where nanogratings 350 nm in depth were produced on tissue culture plastic and PDMS substrates using the nanoimprinting method. Elongated MSCs were observed to organise in parallel to the nanogratings with an aligned actin cytoskeleton. Since this elongation was seen on two materials with different substrate properties, it may indicate that surface topography is a more dominant regulator of cell fate. The same research group looked at MSC differentiation on similar types of gratings but with altered lateral dimensions ranging from the microscale (1 μm) to the nanoscale (300 nm). A biochemical cue, retinoic acid, was present in culture to upregulate neuronal marker expression, with the aim of examine whether surface gratings facilitate or enhance MSC differentiation into a neuronal

phenotype. By evaluating microtubule associated protein 2 (MAP2) it was found that gratings with nanosized dimensions were indeed more effective in inducing neuronal differentiation than gratings with microsized dimensions [217].

Wang *et al.* [100] fabricated a three-dimensional wavy submicrometer laser-induced periodic surface structures (LIPSS) on polystyrene film by polarised laser irradiation. They found that rat C6 glioma cells exhibited directional migration and oriented division on laser-irradiated polystyrene, which was parallel to the direction of LIPSS. At the same time, LIPSS acted as an anisotropic and persistent mechanical stimulus outside the cell to induce dash-like FAs assembly at the two ends of the cell. Chen *et al.* [218] studied the initial cell spreading and adhesion on longitudinally-and transversally-oriented micro-grooves produced by laser irradiation of Ti-6Al-4V surfaces. They found that longitudinal contact guidance of human osteosarcoma (HOS) cells promoted cell adhesion due to the increase in interactions between the focal adhesions and the patterned extracellular matrix (ECM) proteins on the laser micro-grooved surfaces. Also the extent of longitudinal cell contact guidance increased with decreasing longitudinal groove spacing. Cell spreading and adhesion were enhanced by longitudinally- and transversally-oriented micro-grooves.

Interestingly, Crouch *et al.* [219] have used nanoimprinting to create a range of micro- and nanoscale gratings, or their combination, in bulk polystyrene plates to investigate anisotropic cell behaviour of human dermal fibroblasts with respect to the aspect ratio (depth-width) of gratings. They found that both cell alignment and elongation increase with increasing aspect ratio, and even a shallow grating (aspect ratio of ~0.05) is sufficient to induce 80 % cell alignment. Finally, by re-plotting data recently published by other groups versus aspect ratio they found a similar dependence, despite differences in cell types and surface structures. This consistency indicates that aspect ratio is a general factor to characterise cell behaviour in terms of aligment and elongation.

The order and symmetry of nanofeatures also appear to have a important impact on stem cell fate. Dalby co-workers [220] reported that the presence of nanoscale disorder stimulate MSC differentiation into bone in the absence of osteogenic factors or soluble factors. Using e-beam lithography, substrates with several types of topographic profiles were prepared. Nanopits of 120 nm in diameter and 100 nm in depth, with different

arrangements, including a hexagonal array, a square array, square arrays with slight displacements of varying degrees, and a random placement. Both osteoprogenitors and MSCs were cultured on these surfaces for 21 days and evaluated for the activities of two bone-specific ECM proteins, osteopontin and osteocalcin. Briefly, osteoblastic expression was observed on substrates where the nanofeatures were displaced at a slight offset from the original square array, with distinct positive immunofluorescent staining for both osteoblastic markers. In addition, bone-like nodules were observed at 28 days after cell seeding on the displaced square arrays, indicating the presence of matrix mineralisation.

Huang *et al.* [221] also addressed the issue of nanopattern order on cell adhesion. Nanobeads of RGD peptides were deposited on substrate surfaces via micelle nanolithography, resulting in ordered or random bead distributions with various spacings between the beads. MC3T3-E1 cells were cultured on the substrates and evaluated for integrin-related cell adhesion. The results demonstrated that whether on ordered or disordered beads, cell spreading was better at low bead spacings compared to higher spacings. However, the difference was more evident on ordered beads, which may indicate that although highly spaced disordered beads may inhibit cell spreading, cells can still spread better than on ordered beads with similar spacings. Huang attributed this observation to the mechanism of cell adhesion, noting that efficient adhesion can only occur when integrin spacing is less than 70 nm. To explain adhesion and spreading on disordered beads even at high spacings, it was proposed that integrin clustering must occur at the onset of adhesion. Taking into account global average inter-ligand spacing, it is reasonable to conclude that the polydispersity of the disordered nanopatterns leads to more clustering than an ordered one.

Even though nanotopographical effects on MSC differentiation clearly exist, an absolute cause-effect relationship cannot yet be established, as there have been some discrepancies. In a report by Park *et al.* [222], TiO_2 nanotubes with diameters ranging from 15 to 100 nm were fabricated by anodisation on titanium surfaces, and MSC adhesion and osteoblastic differentiation were studied as a function of tube dimension. Using the same materials and similar methods of fabrication, Oh *et al.* [223] performed a similar study, but the two experiments presented an interesting inconsistency. While both noted that MSC adhesion is inversely proportional to nanotube diameter (enhanced at smaller diameters and hindered at larger diameters), the observations of cell

differentiation yielded opposite results. Park and co-workers showed decreased osteoblastic expression on larger diameters compared with the smaller ones, attributing this effect to the lack of focal contact formation and thus inhibition of differentiation signaling. However, Oh *et al* demonstrated that osteoblastic was higher on larger diameters compared with the smaller ones, proposing that the cells that do adhere on the large diameters induce cell elongation that leads to cytoskeletal stress and selective differentiation. Evidently, it is difficult to draw a comprehensive conclusion that explains these phenomena, and ongoing studies are required to further probe into the detailed mechanisms of cell differentiation and its relationship with nanotopography. However, Zhao *et al*. [224] have been proposed some explanations for the apparent discrepancies in the works of Oh and Park. First, although both studies used MSCs, they were of different origins (human for Oh and rat for Park). The difference in cell type may be one of the reasons that account for the cytocompatibility of TiO_2 nanotubes. Also, different phases of TiO_2 influence cell function in different ways. The conditions of substrate fabrication in these studies may not have been completely identical, adding to the possibility that the substrates play a part in the controversial results. In addition, Park *et al* used an osteogenic cell culture medium in their study while Oh *et al* used culture media free of osteogenic growth factors. It would be reasonable to conclude that the composition of the cell culture media would have a substantial effect in cell growth and differentiation.

11.2. Impact of Chemical Composition on Tissue Cell Behaviour

In addition to topographical cues, surface chemical composition can also have a profound effect on cell behaviour. The simplest chemical modification that can be applied to a surface is the presence of functional groups. Lee *et al.* [225] performed a study whereby low density polyethylene (PE) surfaces were modified with different chargeable functional groups with similar wettabilities. These functional groups include –COOH, $–CH_2OH$, $–CONH_2$, and $–CH_2NH_2$. Subsequently, cell adhesion and growth were evaluated on these surfaces. The study showed that amine group-grafted PE ($–CH_2NH_2$) promoted cell adhesion most efficiently while the polyacrylic acid-grafted PE (–COOH) resulted in poor adhesion. Since the amine group is positively charged, and a large number of proteins and serums in culture are negatively charged, the electrostatic interaction between the surface and the biomolecules is favourable and directly enhances cell adhesion. Conversely, the polyacrylic acid functional group is negatively

charged, and limited cell adhesion is expected. This study showed that simple functionalisation and consequently alteration of surface charge is enough to have an impact on cell behaviour.

Proteins that play roles in promoting cell adhesion such as fibronectin, vitronectin, and laminin [226], can be coated on biomaterial surfaces to improve cell response. One common characteristic of these proteins is the presence of RGD peptide sequence [227]. When RGD is immobilised on a biomaterial surface and exposed to cells, integrins on the cell surface recognise the peptide sequence and anchor to it, resulting in adhesion. Because of this property, the peptide is often present on biomaterial surfaces as a chemical cue to enhance cell-material contact through the formation of specific focal contacts [228]. In a study of RGD-modified titanium, it was demonstrated that osteoblasts showed earlier osteocalcin (osteoblast marker) expression on RGD surfaces, which demonstrate earlier differentiation of osteoblasts on these surfaces [229]. Another study revealed similar results whereby RGD-coated PMMA surfaces accelerated cancellous bone growth in animal models compared with the uncoated implants [230]. Additionally, RGD peptides can take on many conformations that change their affinity to integrins. In addition to RGD, other cell recognition motifs exist and some have been immobilised for cell attachment. One example is KRSR (lysine-arginine-serine-arginine), a sequence found in a number of bone-relative adhesive proteins, including fibronectin and osteopontin. Its use was shown in a study where conventional titanium and nanophase titanium (material with grain sizes less than 100 nm) surfaces were functionalised with KRSR peptides [231]. Osteoblast adhesion was then evaluated on control and modified surfaces. On both conventional and nanophase titanium, KRSR-modified surfaces showed increased osteoblast adhesion compared with their respective non-functionalised surfaces. Kim *et al.* [232] further observed that peptide-based promotion of cell adhesion is specific to cell types. RGD was able to enhance the adhesion and spreading of normal human dermal fibroblasts, while KRSR was more effective on normal human osteoblasts. FHRRIKA (Phenylalanine-Histidine-Arginine-Arginine-Isoleucine-Lysine-Alanine) is another adhesion sequence derived from bone sialoprotein. In a study by Schuler *et al.* [233], it was demonstrated that FHRRIKA-coated titanium surfaces increased rat calvarial osteoblast adhesion when compared with bioinactive surfaces. However, cell numbers did not reach the level found on RGD-

coated surfaces, indicating that different adhesion mechanisms may affect efficiency on different cell recognition motifs.

In terms of bone development, bone morphogenetic proteins (BMPs) are a class of growth factors in the transforming growth factor beta family (TGF-β) that play strong roles in inducing the formation of bone and cartilage [234]. The primary role of BMPs is to stimulate bone formation by interacting with specific receptors on the cell surface. There are two types of receptors to which BMPs can bind, known as type I and type II receptors. BMPs bind with weak affinity to type I or type II receptors alone, but with high affinity to type I/type II heteromeric receptor complexes [235]. Activated receptors influence the dynamics of the cell cytoskeleton by activating several signaling pathways that direct cell migration and regulate the expression of differentiation-inducing genes, such as Runx2 by activating the Smad 1/5/8 pathway [236]. BMPs have been used in combination with synthetic degradable polymers to successfully repair bone defects in the humeri of adult rabbits, inducing the formation of new bone at the site of defect and demonstrating its ability to enhance the regeneration of bone [237].

11.3. Impact of Surface Topography on Bacterial Cell Behaviour

Bacteria adhesion to abiotic surfaces does not implicate specific ligand-receptor-like binding, such as the existing between integrins and ECM proteins, but is strongly affected by physico-chemical properties of both the surface and the bacteria cell wall, including its structural features such as flagellae, fimbriae, and lypopolysaccharides. Recently, several studies regarding the impact of the surface topography of biomaterials on the bacteria behaviour have been developed due to the increasing antibiotic resistance of *Staphylococci* (vancomycin and meticillin-resistant strains), combined with the greater opportunity for infection afforded by escalating numbers of orthopaedic surgical procedures.

Strategies based on the modification of surface topography lies in the fact that bacteria and tissue cells respond differently to topographical features of a surface. The small size of bacteria compared with tissue cells might be thought to be a favourable factor for bacteria to sense submicrometre and nanometre topographical features. However, bacteria have a characteristic shape and are much less deformable (higher rigidity) than tissue cells and upon attachment to a surface they will tend to maintain their shape. This will hinder interaction between a bacterium and topographical surface

features with typical dimensions less than the size of the bacterium, thus limiting the possibility for bacteria to sense them. Therefore, bacteria should be unable to react to submicrometre and nanometre topographical features. In this section some relevant works on the impact of surface topography on the bacteria behaviour, mainly on *Staphyloccoci*, will be revisited.

Ploux *et al.* [238] fabricated grooves with 1.6 and 25 μm in periodicity and 50 nm in depth on a polymer-coated silicon wafers obtained by combination of pulsed plasma polymerisation and UV-lithography. By precise controll of the topography and chemical composition of the surfaces they could enhance the proliferation of human osteoprogenitor (HOP) cells while decreasing the adhesion of *Escherichia coli* PHL628. In another study, Wu *et al.* [239] investigated the behaviour of *S. epidermidis* and human foetal osteoblastic cells (hFOB) on Ti-6Al-4V disks with different surface conditions such as mirror-polished, satin, grit-blasted, and commercially pure Ti plasma-sprayed coating, presenting different length scales roughness in both the vertical and lateral directions. They found a relation between the lateral roughness scale and the dimensions of bacteria and osteoblasts. At lateral length scales slightly larger than the size of individual bacteria substantially enhanced bacterial colonisation. In contrast, desirable osteoblast adhesion, spreading and differentiation were all promoted by the microscopically smooth and macroscopically rough surfaces, in which the surface topography changes at length scales on the order of tens of microns corresponding roughly to the size of an individual cell.

Braem *et al.* [240] have investigated the adhesion and biofilm formation of *S. aureus* and *S. epidermidis* on newly developed porous Ti coatings with 50 % porosity and pore sizes up to 50 μm, which was compared to various dense and porous Ti or Ti-6Al-4V reference surfaces. They found that surface roughness and hydrophobicity are the main determinants for bacterial adherence. The novel coatings showed a significant reduction of up to five times less bacterial surface colonisation when compared to a commercial vacuum plasma sprayed coating. However, further expansion of the porosity with over 15 % and/or the pore size up to 150 μm is correlated to a significant increase in the roughness parameters resulting in an ascent of bacterial attachment. Finally, chemical modified Ti surfaces with improved hydrophilicity and preserved average roughness was found to strongly decrease bacteria quantities.

Ivanova *et al.* [241] have analysed the adhesion and biofilm formation of *S. aureus* (CIP 68.5) and *Pseudomonas aeruginosa* (ATCC 9025) on titanium thin films, with different roughness (R_q = 1.6, 1.2, and 0.7 nm), deposited on glass substrata. They found that the extent of attachment of two strains of bacteria indicated that they had the ability to differentiate between surfaces with very small differences in surface roughness, of the order of about 0.3-0.5 nm in the R_a and R_q parameters. The attachment and biofilm formation was observed in the smoother thin films (R_q = 0.7 nm). In another study, Ivanova *et al.* [242] have investigated the bactericidal efficiency of black silicon produced by reactive-ion beam etching (RIE) with SF_6 and O_2. The high aspect ratio nanoprotrusions present on the surface of black silicon induced disruption in the cellular integrity of *Pseudomonas aeruginosa* and *S. aureus*. The surfaces are highly bactericidal against the tested Gram-negative and Gram positive bacteria, exhibiting an estimated average killing rates of up to ~ 450,000 cells min^{-1} cm^{-2}.

Xu and Siedlecki [243] investigated the *S. epidermidis* and *S. aureus* adhesion and biofilm formation on Poly(urethane urea, PUU) films textured with ordered arrays of submicron pillars differently sized using a soft lithography two-stage replication molding technique. They found that the textured surfaces reduced the bacteria-accessible contact area by more than 70 %. Adhesion of *Staphylococcal* strains to the textured PUU surfaces was significantly reduced compared to smooth controls, and subsequent biofilm formation was also inhibited on the textured materials.

Puckett *et al.* [244] examined the adhesion of *S. aureus* and *S. epidermidis*, and *Pseudomonas aeruginosa* on conventional Ti (nano-smooth), nanorough Ti produced by e-beam evaporation, and nanotubular and nanotextured Ti produced by two different anodisation processes. They found that nanorough Ti surfaces decreased the adhesion of all of the bacteria, while nanotubular and nanorough Ti increased bacteria attachment. In terms of surface chemistry, the conventional and nanorough Ti surfaces were found to have crystalline TiO_2 while the nanotubular and nanotextured Ti surfaces were found to be amorphous and incorporated with fluorine. They attributed the increasing of bacteria adhesion on these surfaces due to the presence of both amorphous TiO_2 and fluorine. Ercan *et al.* [245] also investigated the *S. aureus* growth on nanotubular titanium fabricated by anodisation combined with electrical stimulation. They found that biofilm formation was significantly reduced on the anodised titanium surface combined with electrical stimulation (15-30 V), compared with the non-anodised and

non-electrically stimulated titanium. However, contraly to Puckett and co-workers, the decrease in biofilm formation was explained by the presence of fluorine on the surfaces of anodised nanotubular titanium.

Truong *et al.* [246] showed the impact of extreme grain refinement in the bulk of pure titanium, produced by severe plastic deformation using equal channel angular pressing (ECAP), on the behavior of *S. aureus* (CIP 65.8) and *Pseudomonas aeruginosa* (ATCC 9025). They found that both bacteria showed preference for surfaces of ECAP-processed titanium. *Staphylococcal* cells were found to have a greater propensity for attachment to surfaces of ECAP-modified titanium, while *Pseudomonas* cells showed to be less sensitive to the ECAP processing. It is noteworthy that optical profilometry performed on large scanning areas showed no significant difference between the roughness parameters R_a and R_q for the surfaces of different conditions, the overall level of roughness being lower for the ECAP processed surfaces. Otherwise, topographic profile analysis at the nanoscale by AFM did reveal a difference in these parameters. The surface chemistry was similar for both material conditions.

Fedeeva *et al.* [247] investigated the behaviour of both *S. aureus* and *Pseudomonas aeruginosa* on micro- and nanoscale quasi-periodic self-organised structures (mimicking the lotus leaf) on titanium surfaces fabricated by femtosecond laser ablation. They found a highly selective retention pattern for the two pathogenic bacteria. While *Staphylococcal* cells were able to successfully colonise and produce biofilm on the superhydrophobic laser textured titanium surfaces, no pseudomonas cells were able to attach to the surface. It is important to note that this is one of the types of surface texture produced in the present research work.

Rizzello *et al.* [248] showed how highly controlled nanostructured gold films with different levels of roughness impact the *Escherichia coli* morphology, genomic, and proteomic response. It was observed that type-1 fimbriae, which is an adhesive organelle involved in adhesion of bacteria to specific cells of host tissues, disappear in escherichia coli adherent onto nanostructured substrates, as opposed to bacteria onto reference glass or flat gold surfaces. A genetic variation of the fimbrial operon regulation was consistently identified by real time qPCR in bacteria interacting with the nanorough substrates. In addition, the entire proteomic profile of bacteria was explored and significant changes in the regulation of proteins involved in stress processes and

defense mechanisms (biosynthesis, peptide transport, metabolic pathway, and DNA repair system) were observed on the bacteria adherent onto the nanorough substrates.

Finally, it is clear that nanotopography often decrease bacteria colonisation on the material surfaces, despite some controversial findings. Surface micro- and nanotextures, roughness, chemical composition, wettability, material grain refinement, among other properties are decisive factors influencing the antibacterial activity of materials. In addition, bacteria adhesion on material surfaces was showed to be dependent on the type of bacteria. Interestingly, some studies have shown the opposing behaviour of tissue cells and bacteria on material surfaces. It is particularly interesting since materials surfaces can be specifically designed to promote tissue cell function while reducing bacterial colonisation.

Chapter II. Experimental

The experimental part of this thesis is divided into three major sections.

In Section 1, the laser surface texturing methods, the techniques used for the characterisation of the textured surfaces and the biological studies performed on these surfaces are presented.

In Section 2, the methods of biofunctionalisation of the surfaces and the characterisations of the biofunctionalised surfaces are described.

In Section 3, statistical analyses methods employed to verify the significance level of the numerical data are described.

1. Laser Textured Surfaces

The Ti and Ti-6Al-4V samples were laser surface textured in the Laser Materials Processing Laboratory of Instituto Superior Técnico. The surface characterisation and the surface wettability measurements were also performed at the Instituto Superior Técnico. The *in vitro* studies were carried out at CNRS UMR5248, *Chimie et Biologie des Membranes et Nanoobjets* (*CBMN*) Laboratory, Bordeaux University. Studies involving human Mesenchymal Stem Cells and bacteria were performed at the facilities of the *Institut Européen de Chimie et Biologie* (*IECB*) and at the *Ecole Nationale d'Ingénieurs des Travaux Agricoles de Bordeaux* (*ENITAB*), respectively, Bordeaux University.

1.1. Preparation of the Titanium Alloys

Plates of Grade 2 Ti (cp-commercially pure) and Grade 5 Ti-6Al-4V alloy with dimensions of 150 x 150 mm^2, and 1.0 and 1.2 mm thick, respectively, were purchased from Titanium Industries UK Ltd. The nominal chemical composition of both titanium alloys according to the American Society for Testing and Materials (ASTM) Standards (F67 and B265) is given in **Table II-1**. The method of preparation of the samples prior to the laser surface treatment is shown in **Figure II-1**.

Table II-1. Nominal chemical composition of cp Ti (Grade 2) and Ti-6Al-4V alloy (Grade 5).

CP TI (GRADE 2)		TI-6AL-4V ALLOY (GRADE 5)	
ASTM F67		ASTM B265	
Elements	wt %	Elements	wt %
C	0.10	C	0.08
Fe	0.30	Fe	0.25
H	0.015	H	0.015
N	0.03	N	0.05
O	0.25	O	0.20
Ti	Balance	Al	5.50-6.75
-	-	V	3.50-4.50
-	-	Ti	Balance

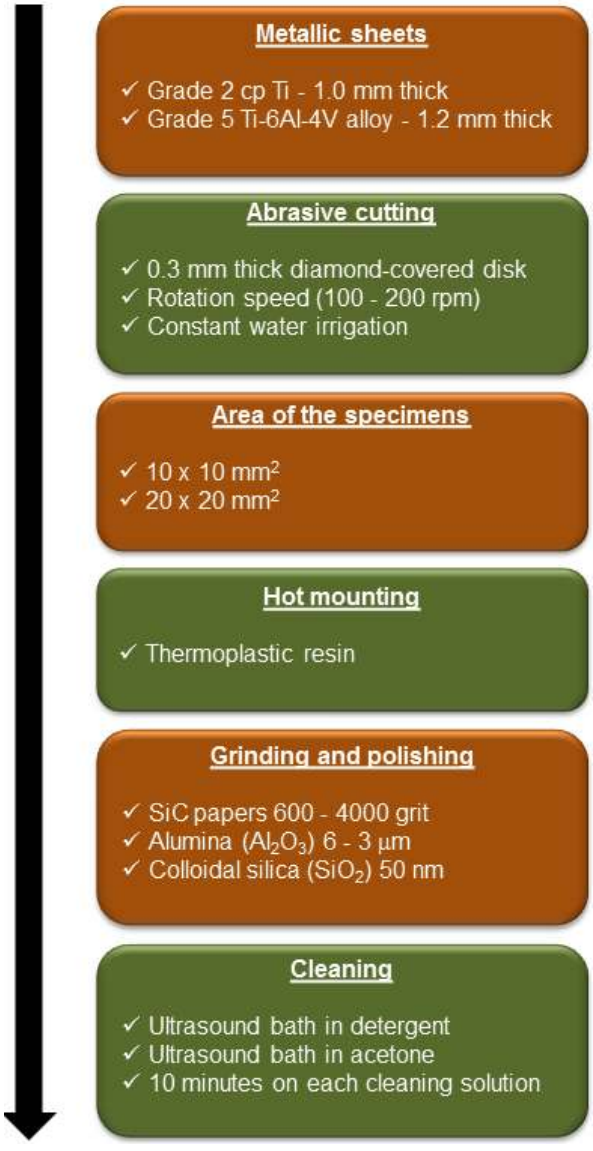

Figure II-1. Flow-chart describing the procedures to obtain mirror-polished titanium surfaces.

The plates were cut into square specimens with areas of 10 x 10 and 20 x 20 mm^2, depending on the type of analysis to be performed, using a 0.3 mm thick diamond disk at low rotation speed (100-200 rpm) under water irrigation in order to avoid mechanical and thermal damage. The specimens were mounted in thermoplastic resin using a hot mounting press, and ground using a low rotation speed (150 rpm) grinding wheel fitted with a 600-4000 grit sequence of SiC papers. After grinding, the specimens were mirror-polished using a cloth low rotation speed (200 rpm) wheel and 6.0 and 3.0 μm abrasive alumina (Al_2O_3) particles and, finally, 50 nm colloidal silica (SiO_2), suspended in distilled water as abrasives. Polishing was performed to ensure homogeneity of the surface optical properties and a reproducible behaviour during the laser surface texturing. Finally, the specimens were removed from the mounting resin, ultrasonically cleaned in a detergent solution and finally in acetone for 10 minutes for degreasing and removal of polishing residues.

1.2. Laser Surface Texturing

Surface texturing was performed by a laser direct writing technique, with a femtosecond laser [15]. Depending on the laser processing parameters and conditions a wide range of surface textures can be created in a reproducible fashion by ablation of the material. A Yb:KYW chirped-pulse regenerative amplification laser system (s-Pulse HP model, Amplitude Systèmes, France) with a central wavelength (λ_{laser}) of 1030 nm and a laser pulse duration (τ_{pulse}) of 500 fs (Full Width at Half Maximum-FWHM) was used for the laser treatments. This laser system presents high pulse energy, high repetition rate, and high beam quality. Its specifications according to the manufacturer (http://www.amplitude-systemes.com/amplifiers-s-pulse.html) are given in **Table II-2**.

Table II-2. Specifications of the s-Pulse HP model femtosecond laser system used for the surface texturing of the titanium specimens.

S-PULSE HP MODEL	
Pulse duration	500 fs
Maximum pulse energy	≈1 mJ
Repetition rate	0-300 kHz
Central wavelength	1030 nm (NIR)
Laser beam quality	TEM_{00}

The average fluence (F_{av}), i.e., the average energy density, was calculated using the following equation:

$$\mathbf{F_{av} = \frac{E_P}{\pi \omega_0^2}} \qquad \textbf{Eq. II-1}$$

where, E_p is the average laser pulse energy and ω_0 the laser beam radius at e^{-2} of the maximum intensity of the Gaussian beam profile.

The value of E_p was calculated as follows. The average power (P) was measured using a powermeter (Ophir Photonics model 10ASHV1.1 RoHS, Israel). Since after measuring P, the laser beam passes a sequence of mirrors and the focusing lens, an energy loss of about 20 % occurs before the laser beam interacts with the sample surface. Thus, a corrected average power ($P_{corrected}$) was obtained by $P - 20\%$ P. Part of the incident radiation is reflected on the titanium surface, and consequently the energy absorbed by the material is slightly smaller than the value estimated. E_p is independent of the pulse frequency for repetition rates ≤ 1000 Hz. Since all the experiments were performed at this repetition rate range, the average pulse energy was simply obtained by the following formula:

$$\mathbf{E_P = \frac{P_{corrected}}{1000}} \qquad \textbf{Eq. II-2}$$

The ω_0 value at the surface of the titanium specimens was estimated by using the method described in reference [17] or the D^2-method described in previous publications [66, 76, 249, 250]. The basis of the latter is as follows. Assuming that the laser beam has a Gaussian energy distribution, the fluence in a plane perpendicular to the laser beam is given by:

$$\mathbf{F(r) = F_0 e^{\frac{-2r^2}{\omega_0^2}}} \qquad \textbf{Eq. II-3}$$

where, r is the distance to the spot centre. The maximum fluence (F_0) and E_p can be related by:

$$\mathbf{F_0 = \frac{2E_P}{\pi \omega_0^2}} \qquad \textbf{Eq. II-4}$$

It was demonstrated that the diameter (D) of an ablation crater produced with a Gaussian beam with radius ω_0 is related to F_0 by:

$$D^2 = 2\omega_0^2 \ln\left(\frac{F_0}{F_{th}}\right) \qquad \text{Eq. II-5}$$

where, F_{th} is the ablation threshold fluence. Since F_0 increases linearly with E_p (see **Eq. II-4**), the ω_0 can be estimated from a plot of the square of the average crater diameter (D^2) versus the logarithm of the pulse energy ($\ln E_p$). Finally, ω_0 is calculated from the slope obtained from a linear fitting to the experimental data as follows:

$$\omega_0 = \sqrt{\frac{\text{slope value}}{2}} \qquad \text{Eq. II-6}$$

In order to calculate ω_0 using the D^2-method, several craters were produced on a Ti-6Al-4V alloy sample with average pulse energies and number of laser pulses (N) ranging from 80 to 640 μJ and 20 to 1000, respectively. The craters produced were observed with a JEOL JSM-7001F field emission gun scanning electron microscope, and their diameters measured using Image J freeware (NIH, http://rsb.info.nih.gov/ij/) after calibration. Taking into account that some craters were asymmetric, four diameters were measured in different directions for each crater, and an average was calculated. This method takes into account the incubation effect frequently observed in laser-induced damage phenomena, caused by the damage accumulation in materials submitted to multiple laser pulses. This effect means that, the higher the pulse energy and the number of laser pulses the larger the diameter of the craters. A representative scheme of the experiment performed for the determination of ω_0 is given in **Figure II-2**. A ω_0 of 169 ± 5 μm was calculated (see Section 2.1. of Chapter III for more details).

The direct writing femtosecond laser surface texturing setup is shown in **Figure II-3**. The laser processing parameters and conditions used for the production of the textured surfaces are summarised in **Table II-3**. The laser beam was focused by a 100 mm focal length lens and incident perpendicularly to the Ti specimen surfaces. The linear polarisations s (TE; transverse-electric) and p (TM; transverse-magnetic) and the circular polarisation of the laser beam were controlled by a half-wave plate ($\frac{\lambda}{2}$) and a quarter-wave plate ($\frac{\lambda}{4}$), respectively, put in the optical pathway of the laser beam. The pulse repetition rate was varied in the range 1-1000 Hz. The average pulse energy was varied in the range 64-720 μJ using an association of a half-wave plate and a beam

splitter or a beam attenuator, and measured by a powermeter. The average fluence at the surface of the specimens was in the range of 0.07-0.80 J/cm^2.

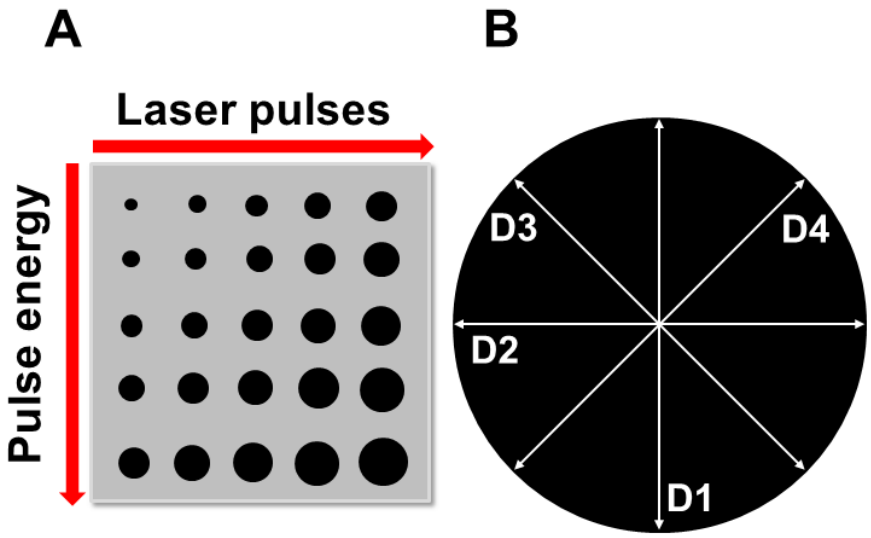

Figure II-2. Representative scheme of the experiment performed on a Ti-6Al-4V alloy surface for the determination of ω_0. (A) Several single craters were produced with increasing average pulse energy and number of laser pulses. (B) Four diameters were measured in different directions for each crater produced and an average diameter determined.

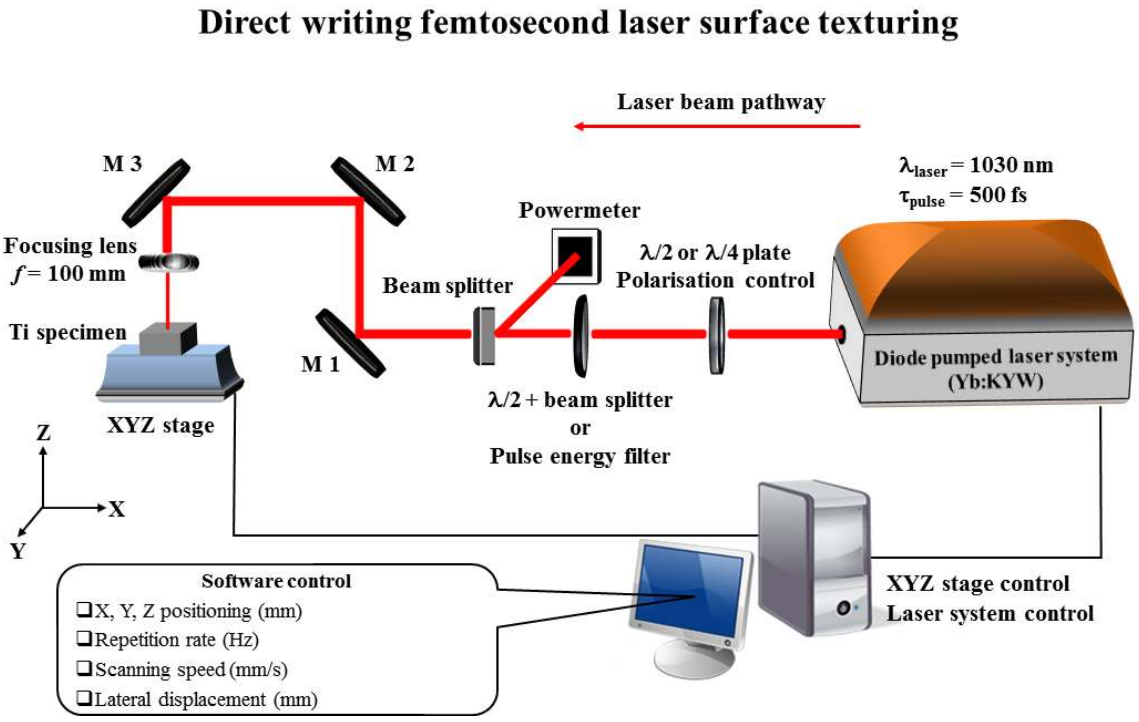

Figure II-3. Direct writing femtosecond laser surface texturing setup.

Table II-3. Laser processing parameters and conditions used for the production of the laser textured surfaces.

LASER PROCESSING PARAMETERS AND CONDITIONS	
Average laser beam power ($\mathbf{P_{corrected}}$)	64-720 mW
Average pulse energy ($\mathbf{E_p}$)	64-720 μJ
Average Fluence ($\mathbf{F_{av}}$)	0.07-0.80 J/cm^2
Repetition rate (**f**)	1-1000 Hz
Scanning speed (**ν**)	1-20 mm/s
Number of laser pulses (**N**)	2-1069
*Polarisation	linear s (TE) and p (TM), and circular
Lateral displacement ($\mathbf{d_{lat}}$)	0.09-0.2 mm
Processing atmosphere	Ambient atmosphere (air)
*The linear polarisations s (TE) and p (TM), and the circular polarisation are controlled by a half-wave plate ($\frac{\lambda}{2}$) and a quarter-wave plate ($\frac{\lambda}{4}$), respectively.	

Laser surface texturing was performed using two irradiation strategies, **Figure II-4**. The stationary condition was used for the creation of single craters and to study the evolution of specific surface features as a function of the average fluence and number of laser pulses. In this regime the laser beam is stationary in relation to the specimens during the laser treatment. In this situation, a particular surface point is submitted to a sequence of pulses with constant fluence, despite the Gaussian energy distribution in the cross section of the laser beam. The number of pulses is the product of the repetition rate (f) by the exposure time (t). This treatment method was employed to identify the surface textures resulting from a particular combination of fluence and number of laser pulses. A non-stationary condition (direct writing method) was used for the production of large textured areas for characterisation. In this regime the specimens were constantly moved under the stationary laser beam with different scanning speeds (ν) by a computer-controlled XYZ stage (PI miCos, Eschbach-Germany) with a positioning accuracy higher than 0.5 μm and a repeatability of 0.1 μm. In this situation, the fluence at each surface point increases first as the laser beam axis approaches this point, reaches a maximum value when the point is in the axis of the laser beam, and decreases as the beam moves away. To achieve complete surface coverage linear scanning in the x

direction were allowed with a lateral displacement (d_{lat}) of the laser beam in a direction perpendicular to the laser beam scanning direction in order to partially overlap adjacent laser tracks. The number of laser pulses per point of the surface is calculated as follows:

$$N = \frac{\pi D f}{(4 \nu \alpha)}; \ \alpha = \frac{d_{lat}}{D} \qquad \text{Eq. II-7}$$

where, α is the lateral overlap rate.

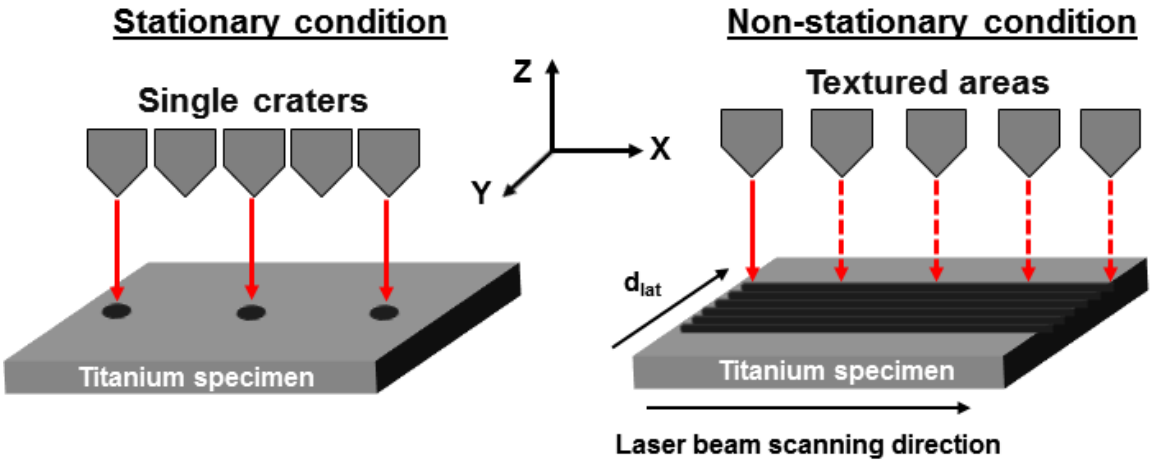

Figure II-4. Laser surface texturing strategies.

By controlling laser processing parameters such as the average fluence, laser beam polarisation, pulse repetition rate, scanning speed, and lateral displacement of the laser beam, three different types of surface textures could be reproducibly produced on titanium alloys. These textures consist of laser-induced periodic surface structures (LIPSS; II), arrays of nanopillars (NP; III), and array of microcolumns covered with LIPSS (MC-LIPSS; IV), forming a bimodal roughness distribution (see Section 2.2. of Chapter III). The colour of the textured samples depends on the surface texture, which affects the visible light scattering by the surface. This colour modification is reproducible (**Figure II-5**) and was used for a first control of the texture formed.

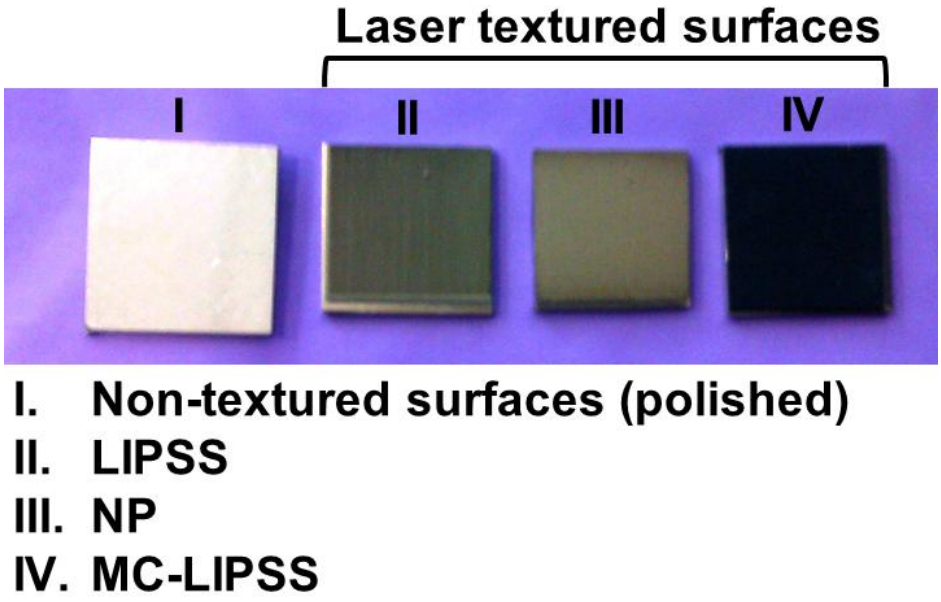

Figure II-5. Non-textured (polished) and laser textured surfaces of both titanium alloys. The reproducible colour modification of the surfaces is used as a complementary control of the production of each type of texture.

1.3. Surface Characterisation

The laser textured surfaces were characterised in terms of topography, chemical composition, and crystallographic structure. The surface topography was characterised by binocular optical microscopy, scanning electron microscopy (SEM) and three-dimensional (3D) surface reconstruction, and atomic force microscopy (AFM), the surface chemical composition by X-ray photoelectron spectroscopy (XPS) and micro-Raman spectroscopy (μ-Raman), and the crystallographic structure by X-ray diffraction (XRD). Prior to the analyses, the titanium specimens were ultrasonically cleaned in ethanol and acetone for 10 minutes in order to remove the ablation debris.

The surface topography was observed by a LEICA DM 5500B binocular optical microscope with a 10 times magnification objective lens (NA 0.25) under normal incidence, and in secondary electrons imaging mode using a JEOL JSM-7001F field emission gun scanning electron microscope (FEG-SEM) or a Hitachi S2400 (SEM), operating at 20 keV and with working distances (WD) varying between 10-20 mm. Electron micrographs were acquired at low and high magnification in order to visualise the morphology of the surfaces at different scales. At least 10 images for each type of

texture were taken in different regions of the sample. Two Specimens were analysed in order to confirm the reproducibility of the laser treatment.

The surface topography was quantified according to ISO 4287 standard using Alicona-MeX© software 2.0 (http://www.alicona.com/home/products/mex.html) [51]. This software allows creating three dimensional plots of the surface from stereoscopic pairs of SEM images obtained at 0 and 10º tilting angle. The images of the stereoscopic pair were acquired with similar contrast, brightness, magnification, and working distance in order to ensure consistent results. At least two stereoscopic pairs were acquired for each type of texture. The calculation requires knowing the values of the pixel size (μm), tilting angle (º), and working distance (mm) for each stereoscopic pair. The 3D plot and the 2D roughness parameters (namely R_a, R_z, R_{Sk} and R_{Ku}) were calculated for each surface texture. The dimensions of the surface features are the average of at least 50 measurements at different locations of the laser textured surfaces. The roughness parameters are the average of ten measurements for each stereoscopic pair, measured both in the laser scanning direction and perpendicularly to it. The topography of laser treated surfaces consisting of LIPSS and nanopillars (NP) was also assessed by AFM using a Veeco DI CP-II atomic force microscope. Images of 10 x 10 and 20 x 20 μm^2 areas were acquired in contact mode using standard silicon tips (Veeco MPP311), at room humidity and temperature. At least two images for each texture were taken. The amplitude roughness parameters are the average of 15 measurements. The AFM characterisation could not be performed on textures consisting of microcolumns covered with LIPSS (MC-LIPSS) because the height of the columns exceeds the measurement range of the equipment.

Surface chemical analysis was performed by XPS and μ-Raman. The XPS spectrometer used was a XSAM800 (KRATOS) operated in the fixed analyser transmission (FAT) mode, with a pass energy of 20 eV, non-monochromatized $Al_{K\alpha}$ radiation ($h\nu$ = 1486.6 eV), 120 W power (10 mA × 12 kV), and take-off angle (TOA) relative to the surface holder of 45°. Samples were analysed in ultra-high vacuum ($\approx 10^{-7}$ Pa) at room temperature. Spectra were collected and stored in 300 channels with a step of 0.1 eV, and 60 s of acquisition by sweep, using a Sun SPARC Station 4 with Vision software (KRATOS). Curve fitting for component peaks was carried out using Gaussian and Lorentzian products through the freeware XPS Peak 4.1 after subtracting a Shirley

background. For quantitative analysis, the following sensitivity factors were used: Ti 2p: 1.75, Al 2p: 0.19; O 1s: 0.66, C 1s: 0.25. One specimen per type of surface was analysed. The X-ray photoelectron spectroscopy database of the National Institute of Standards and Technology (NIST) was used for the assignment of the peak components [251]. μ-Raman was carried out using a Horiba LabRAM HR800 Evolution (Jobin-Yvon) spectrometer. A laser (He-Ne) with an excitation line with a wavelength of 633 nm and a power of 5 mW (ND filter 25 %) was used. A 100 x objective lens (NA 0.9) focused the laser beam to a 0.86 μm spot on the specimen's surface. The spectra were obtained in the range 100-1200 cm^{-1} with an acquisition time of 10 s and 10 accumulations. Prior to the measurements, the system was calibrated to better than 1 cm^{-1} using a silicon sample. A spectrograph with a 600 lines/mm grating was used to provide a spectral resolution of 2 cm^{-1}, and the confocal hole size was set to 200 μm. One specimen per type of surface was analysed.

Characterisation of the crystallographic structure was carried out by X-ray diffraction (XRD) using a Philips 3719 diffractometer with Bragg-Brentano geometry, and an increment and a step time in the range 0.2-0.5º and 2-5 s, respectively. A $Cu_{k\alpha}$ radiation (hν=1540.56 eV) was used and the specimens were analysed in a 2 theta (2θ) range between 20 and 90º. Some glancing incidence analyses (GI-XRD) were performed in a Siemens D 5000 diffractometer with an incidence angle of 1º, increment of 0.04º and integration time 8 s. The determination of the peaks positions was performed using the tool "Spectroscopy-Find peaks" avaiable in OriginPro 8 software. The diffraction peaks obtained were compared with the Powder Diffraction Files (PDF) of the International Centre for Diffraction Data (ICDD) database.

1.4. Wettability Measurements

Surface wettability was evaluated by the sessile drop method. The measurements were performed at room temperature using distilled-deionised (DD) water prepared with a Millipore system and characterised by 18 MΩ, and Hank's balanced salt solution (HBSS, Sigma Aldrich) as testing media. This salt aqueous solution was chosen to simulate body fluids, since its composition is similar to the blood plasma [98]. In addition, in the organism balanced salt solutions provide cells with water and inorganic ions, while maintaining the physiological pH and osmotic pressure. The ionic composition and pH of HBSS and human blood plasma are given in **Table II-4**.

Table II-4. Ionic composition (mM) and pH of HBSS and human blood plasma.

	Na^+	K^+	Ca^{2+}	Mg^{2+}	HCO_3^-	Cl^-	HPO_4^{2-}	SO_4^{2-}	pH
HBSS[a]	141.5	5.8	1.3	0.8	4.2	144.9	0.8	0.8	7.3
Blood plasma [252]	142.0	5.0	2.5	1.5	27.0	103	1.0	0.5	7.4[b]

[a]The HBSS also contains 5.5 mM of D-glucose ($C_6H_{12}O_6$)
[b]Variations between 6.8 and 8.0 may occur [253]

Prior to wettability measurements, the specimens were ultrasonically cleaned for 10 minutes in each of the following media: detergent solution (Extran®), twice in DD water and ethanol, and finally in DD water. After cleaning, the excess water was removed by blowing nitrogen over the samples followed by drying in vacuum at room temperature overnight. A scheme of the experimental setup for the measurements of the contact angles is depicted in **Figure II-6**.

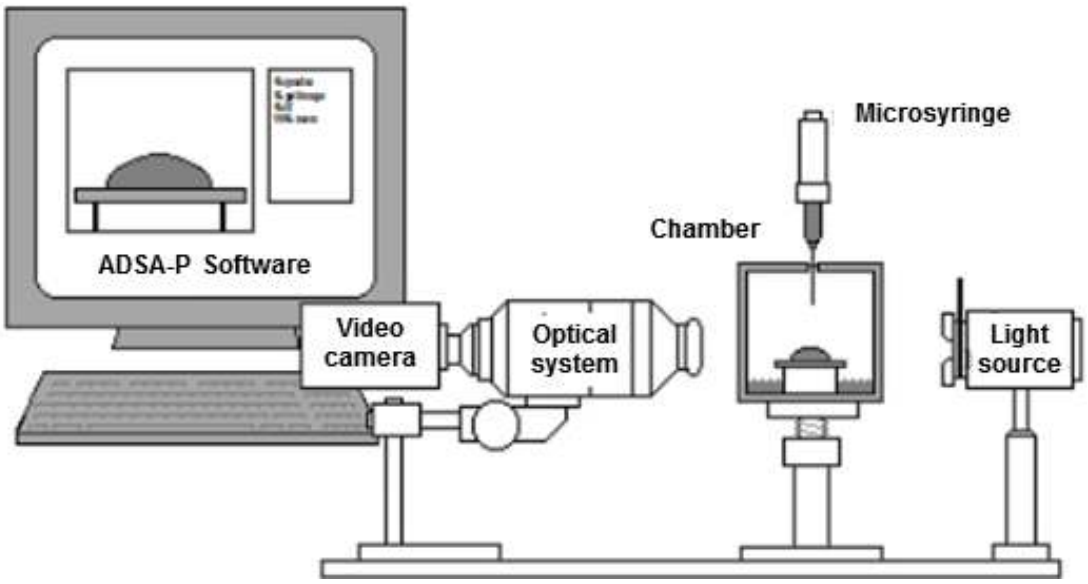

Figure II-6. Scheme of the experimental setup for the measurement of the contact angles (adapted from [253]).

Droplets of about 2-4 µL of the testing media were deposited with a micrometric syringe on the surface of specimens placed inside a closed chamber (Ramé-Hart, model 100-07-00) at room temperature, provided with high precision quartz windows in order to avoid optical distortion. Prior to the droplet deposition the chamber was saturated with water vapour in order to reduce evaporation. Several images of the droplets were

acquired with a video camera (jAI CV-A50) mounted on a microscope (Wild M3Z, magnification 40x) and connected to a Video Pix Framegrabber image processor (Sun Microsystems, Data Translation model DT3155) that performs a 640 x 480 pixels digitalisation in 256 (8 bits) grey levels. The measurements were performed at regular time lapses, starting at the droplet deposition instant (t = 0 s) until droplet spreading ceased or at least up to 600 s, **Figure II-7**.

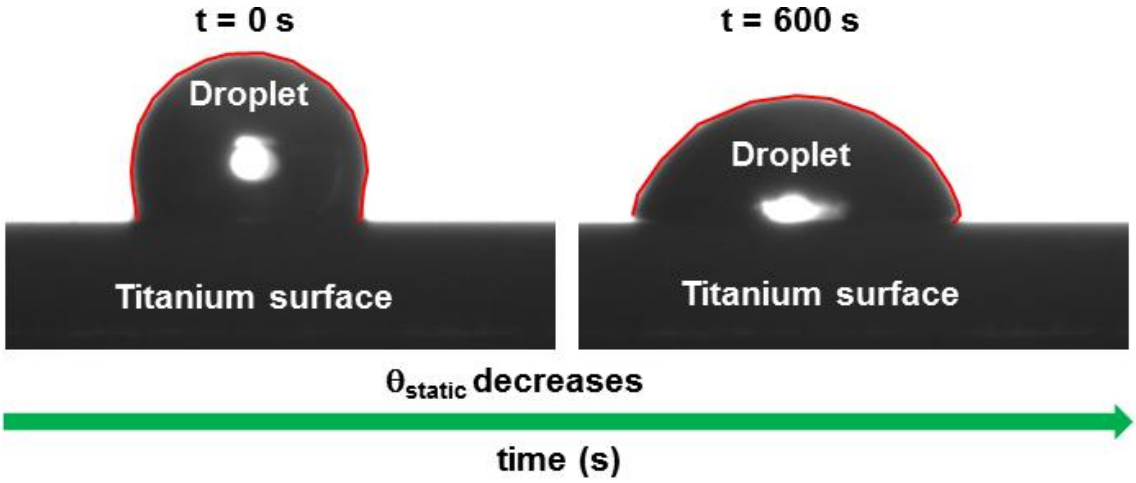

Figure II-7. Representative images of droplets of the two liquids on the same material, acquired with the video microscope.

The droplet profile was analysed using ADSA-P software (Applied Surface Thermodynamics Research Associates, Toronto, Canada) [151]. This software is based on the method known as axisymmetric drop shape analysis profile (ADSA-P), which was developed by Neumann *et al*. [254, 255]. It fits numerically the experimental droplet profile using a mathematical model based on Laplace equation, and allows estimating the static contact angles (θ_{static}). The values presented for θ_{static} are the average of at least ten measurements in different areas of each type of surface topography.

The kinetics of drop spreading was also evaluated because a time-dependent wetting behaviour was observed. A regression analysis was performed on the variation of the static contact angle over time by fitting the following function to the experimental data:

$$\theta_{static}(t) = k.t^n \qquad \text{Eq. II-8}$$

where, k and n are constants to the experimental data [256, 257]. Special attention was given to the value of the constant n, often designated as spreading coefficient, which provides information on the drop spreading velocity.

The surface free energy of the titanium surfaces was also estimated. For this, DD water and diiodomethane (Merck, 98.5 % purity) were used as testing liquids. Prior to the measurements, the diiodomethane was twice distilled under vacuum, and carefully stored in inert atmosphere protected from light. These precautions were adopted because diiodomethane easily oxidises in contact with air and is photodegradable. The surface free energy was determined by using the geometric mean approach [258, 259]. Basically, the work of adhesion (W_{SL}) of a liquid in a solid surface is given by:

$$\mathbf{W_{SL} = \gamma_{SV} + \gamma_{LV} - \gamma_{SL}} \qquad \textbf{Eq. II-9}$$

where, γ_{LV} is the surface tension of the testing liquid in equilibrium with its vapour, γ_{SV} is the surface free energy of the solid in equilibrium with the vapour of the liquid, and γ_{SL} is the interfacial tension between the solid and the liquid. The W_{SL} may be expressed as the geometric mean of the work of cohesion of the solid (W_{SS}) and the liquid (W_{LL}):

$$\mathbf{W_{SL} = \sqrt{W_{SS}\, W_{LL}}} \qquad \textbf{Eq. II-10}$$

Since, $W_{SS} = 2\gamma_{SV}$ and $W_{LL} = 2\gamma_{LV}$, the **Eq. II-10** can be rewritten as:

$$\mathbf{W_{SL} = 2\sqrt{\gamma_{SV}\gamma_{LV}}} \qquad \textbf{Eq. II-11}$$

Owens and Wendt considered that both the surface tension of the liquid and the surface free energy of the solid can be described as the sum of two independent contributions, resulting from different types of molecular interactions: dispersive and polar ($\gamma = \gamma^{d} + \gamma^{p}$) [260]. According to this, the **Eq. II-11** can be rewritten as:

$$\mathbf{W_{SL} = 2\sqrt{\gamma_{SV}^{d}\gamma_{LV}^{d}} + 2\sqrt{\gamma_{SV}^{p}\gamma_{LV}^{p}}} \qquad \textbf{Eq. II-12}$$

where the indexes d and p represent the dispersive and polar components of the γ_{LV} and γ_{SV}, respectively. Therefore, by replacing the **Eq. II-12** in the **Eq. II-9**, the interfacial tension between the solid and the liquid is obtained:

$$\mathbf{\gamma_{SL} = \gamma_{SV} + \gamma_{LV} - 2\sqrt{\gamma_{SV}^{d}\gamma_{LV}^{d}} - 2\sqrt{\gamma_{SV}^{p}\gamma_{LV}^{p}}} \qquad \textbf{Eq. II-13}$$

Finally, by combining the **Eq. II-13** with the Young's equation ($\gamma_{LV}\cos\theta = \gamma_{SV} - \gamma_{SL}$), the following equation is obtained:

$$\gamma_{LV}(1+\cos\theta) = 2\sqrt{\gamma_{SV}^{d}\gamma_{LV}^{d}} + 2\sqrt{\gamma_{SV}^{p}\gamma_{LV}^{p}} \quad \text{Eq. II-14}$$

By using the **Eq. II-14**, the dispersive and polar components of the surface free energy of the solid as well as its total surface free energy ($\gamma_{SV} = \gamma_{SV}^{d} + \gamma_{SV}^{p}$) can be calculated, based on the measured static contact angles of two different liquids whose dispersive and polar components of the surface tension are known.

1.5. Human Mesenchymal Stem Cells Studies

The cell culture experiments were performed in a laboratory designed for biological studies (L2 class; cell culture room) at the facilities of the *Institut Européen de Chimie et Biologie* (*IECB*), University of Bordeaux. Cells manipulations were carried out in a biosafe cabinet (cell culture hood) providing an enclosed and ventilated laboratory workspace for safe work with biological materials.

1.5.1. Cell Culture

Prior to cell manipulation, the biosafe cabinet was properly disinfected (Aniospray 29, Laboratoires Anios) and sterilised with 70 % ethanol in order to avoid contamination of the specimens during the cell experiments. Prior to cell seeding, the 10 x 10 mm^2 titanium specimens were ultrasonically cleaned in absolute ethanol (Sigma-Aldrich, 99.8 % purity) for 15 minutes. Then, the samples were put on 12-well plates (cell culture dishes), sterilised in 70 % ethanol for 10 minutes and washed twice with phosphate buffered saline (PBS, pH 7.4, 1x, GIBCO by Life technology).

Human Mesenchymal Stem Cells (hMSCs) and MSCGM (Mesenchymal Stem Cell Growth Medium) were purchased from Lonza Poietics™. α-MEM was purchased from GIBCO. Cells were precultured in MSCGM containing growth supplements such as L-glutamine, gentamicin, amphotericin-B, and 10 % (v/v) foetal bovine serum (FBS), and incubated at 37 ºC, in a humidified atmosphere containing 5 % (v/v) CO_2. Confluence of the cells was verified by optical microscopy, and the culture medium was removed from the plastic culture T-tubes. Cells were re-suspended using trypsin-EDTA (1x, Sigma-Aldrich) for five minutes. The complete detachment of the cells was verified by optical microscopy. The excess trypsin was quenched using an aliquot of the full culture medium. The solution containing cells was then collected and centrifuged in an Eppendorf Centrifuge 5430 R at 300 g for 5 minutes. The supernatant was aspirated

from the centrifuge tube and α-MEM added to the cell pellet, followed by stirring for five minutes. For all experiments, cells at passage 4-6 were seeded at a density of about 10^4 cells/cm^2 on each well plate, and incubated at 37 ºC, in a humidified atmosphere containing 5 % (v/v) CO_2 for 24 h, 2 weeks, and 4 weeks. The culture media were replaced every three days. These time points were chosen to allow sufficient time for hMSCs to undergo commitment and differentiation before being fixed for immunofluorescent staining. Cell adhesion was evaluated after 24 h, cell proliferation and commitment were evaluated after 2 weeks, and cell differentiation was assessed after 4 weeks. The experiments were performed in duplicate or triplicate (2 or 3 specimens per group).

For cell differentiation studies, the α-MEM was replaced by a differentiation basal medium-osteogenic (Lonza Poietics^{TM}) at 24 h after cell seeding. This medium includes soluble factors such as β-glycerolphosphate, dexamethasone, and ascorbic acid, which are known to promote Mesenchymal Stem Cells osteogenesis. When cultured in the presence of these supplements cells are known to acquire an osteoblastic morphology with upregulation of alkaline phosphatase activity and deposition of calcium-rich mineralised extracellular matrix [172, 261]. The specimens cultured in the osteogenic medium were considered as a positive control for cell differentiation.

1.5.2. Cell Immunostaining and Staining

After the specified times, the specimens were taken from the incubator. The culture medium was carefully aspirated from the well plates and cells were fixed with 4 % (w/v) solution of paraformaldehyde (PFA) in PBS for 30 minutes at 4 ºC. Then, samples were washed twice in PBS, and cells permeabilised with 0.5 % triton-X-100 in milli-Q water (pH 7.2) for 30 minutes at 4 ºC and blocked with 1 % bovine serum albumin (BSA) in PBS for 30 minutes at 37 ºC. A list of primary antibodies and stainings used for fluorescence imaging of the cells cytoskeleton, nuclei, focal adhesions (FAs), osteoblast markers, and matrix mineralisation is given in **Table II-5**.

Staining of F-actin fibre filaments and cell nuclei, and immunostaining of FAs, osterix (OSX), and osteopontin (OPN) were performed as follows. Cells were incubated with the primary antibodies for 1 h at 37º C. After washing, they were stained with either Alexa Fluor® 568 or Alexa Fluor® 647 secondary antibody for 30 minutes at

room temperature, and then stained for F-actin fibre filaments using Alexa Fluor® 488 *phalloidin* for 1 h at 37 ºC. All primary and secondary antibodies (1:200) and Alexa Fluor® 488 *phalloidin* (1:40) were diluted in 1 % BSA in PBS. The specimens were washed twice with 0.05 % Tween 20 in PBS between each staining step. Finally, they were mounted on microscope slides and the cells nuclei stained with a Prolong Gold antifade reagent with DAPI by adding one droplet to each specimen surface. Then, the specimens were covered with plastic covering slips and protected from ambient light for post epifluorescence microscopy analyses.

Table II-5. List of primary antibodies and stainings used for fluorescence imaging of cells cytoskeleton, cells nuclei, FAs, osteoblast markers, and matrix mineralisation.

PRIMARY ANTIBODIES & STAININGS	PURCHASED FROM	MAJOR ANALYSIS	TIME POINT	WHAT IT DETECTS
Alexa Fluor® 488 Phalloidin	Invitrogen	▪ Cell Spreading ▪ Cell elongation ▪ Cytoskeleton organisation	All	F-actin fibre filaments (cytoskeleton)
Vinculin	Sigma-Aldrich	▪ Cell Adhesion	24 h	Focal adhesion (FAs)
DAPI	Invitrogen	▪ Cell adhesion ▪ Cell nucleus spreading ▪ Cell nucleus deformation ▪ Cell proliferation	All	Cell nucleus
Osterix (OSX)	Santa Cruz Biotechnology	▪ Cell commitment	2 weeks	Osteoblastic commitment
Osteopontin (OPN)	Santa Cruz Biotechnology			
Xylenol Orange (XO)	Sigma-Aldrich	▪ Matrix mineralisation	4 weeks	Calcium portion of mineralised matrix produced by osteoblasts
OsteoImage™ (OI)	Lonza Poietics™			Hydroxyapatite (HA) crystals in the mineralised matrix produced by osteoblasts

Matrix mineralisation was evaluated by staining with Xylenol orange (XO) and by the OsteoImage™ (OI) assay. Xylenol orange is a calcium-chelating fluorophore that detects the calcium in the mineralised matrix produced by osteoblasts. Xylenol orange powder was dissolved in milli-Q water to obtain 20 µM of solution. This solution was added to the culture medium in each well one day before the end of the cell culture and incubated overnight. The OsteoImage™ assay is based on the specific binding of the fluorescent OsteoImage™ staining reagent to the hydroxyapatite (HA) in the mineralised matrix deposited by osteoblasts. Prior to the experiments, the OsteoImage™ wash buffer (10 x) was diluted in milli-Q water (1:10), and the OsteoImage™ staining reagent was diluted in the OsteoImage™ staining reagent dilution buffer (1:100). Specimens were rinsed twice with 1.5 ml of diluted wash buffer

for five minutes. Then, 0.75 ml of the diluted staining reagent was added to each well and incubated for 30 minutes at room temperature, protected from ambient light. After incubation, the specimens were washed three times with 1.5 ml of diluted wash buffer for five minutes.

1.5.3. Epifluorescence Microscopy

Specimens were fluorescently labelled following cell culture and imaged using a LEICA DM5500B epifluorescence microscope with a motorized, programmable stage using a CoolSnap HQ camera, controlled by Metamorph 7.6 software. The following filter cubes from Leica Microsystems were used: A4 for the visualization of DAPI, L5 for Alexa Fluor® 488, TX2 for Alexa Fluor® 568, and CY5 for Alexa Fluor® 647. The excitation and emission wavelengths of the fluorochromes are given in **Table II-6**. Images were taken at different magnifications using 2.5 times (NA 0.07) and 10 times (NA 0.25) dry objectives, and a 40 times (NA 1.03) oil immersion objective. For each magnification, at least 10 images per type of surface were taken in different regions.

Table II-6. List of the excitation and emission wavelengths of the fluorochromes used for labeling different cellular structures and osteoblast markers.

FLUOROCHROME	EXCITATION [nm]	EMISSION [nm]	STRUCTURE COLOUR
DAPI	345	455	Blue
Alexa Fluor® 488	499	519	Green
Alexa Fluor® 568	579	603	Red
Alexa Fluor® 647	652	668	Far red

Quantitative analyses of the cell density, cell area, cell elongation, nucleus area and shape, FAs area, cell proliferation, expression levels of specific osteoblast markers (OSX and OPN) as well as the observation of calcium- and hydroxyapatite-rich zones were performed using Image J freeware (NIH, http://rsb.info.nih.gov/ij/). Prior to the analyses, the system was spatially calibrated according to the effective pixel size of the images. Images of stained F-actin fibre filaments were used to measure the cell area and elongation. The measurements of the number of adhered cells, nucleus area and shape were performed on images based on nucleus staining. Images of stained vinculin were used to measure the area of the FAs. At least 50 cells per each type of surface were

analysed for the measurements of cell area, cell elongation, nucleus area and shape, and area of the FAs.

Finally, the images were converted to 8-bits depth, followed by an adjustment of contrast and brightness. Then, a threshold was applied in order to clearly separate the regions of interest (ROI) from the background. The function "Analyse Particles" was used for quantification of the parameters, **Figure II-8**. After the measurements, cell elongation [219] was calculated by the following equation:

$$\textbf{Cell elongation factor} = \frac{l_l}{l_s - 1} \qquad \textbf{Eq. II-15}$$

where, l_l and l_s are the lengths of the long and short axis of the cells, respectively. Cell proliferation was estimated using the following equation:

$$\textbf{Cell proliferation } (\%) = \frac{N_{cells}^{2weeks} - N_{cells}^{24h}}{N_{cells}^{2weeks}} \textbf{x } 100 \qquad \textbf{Eq. II-16}$$

where, $N_{cells}^{24\,h}$ and N_{cells}^{2weeks} are the average number of nuclei, counted in the total area of low magnification images, at 24 h and 2 weeks post cell seeding, respectively.

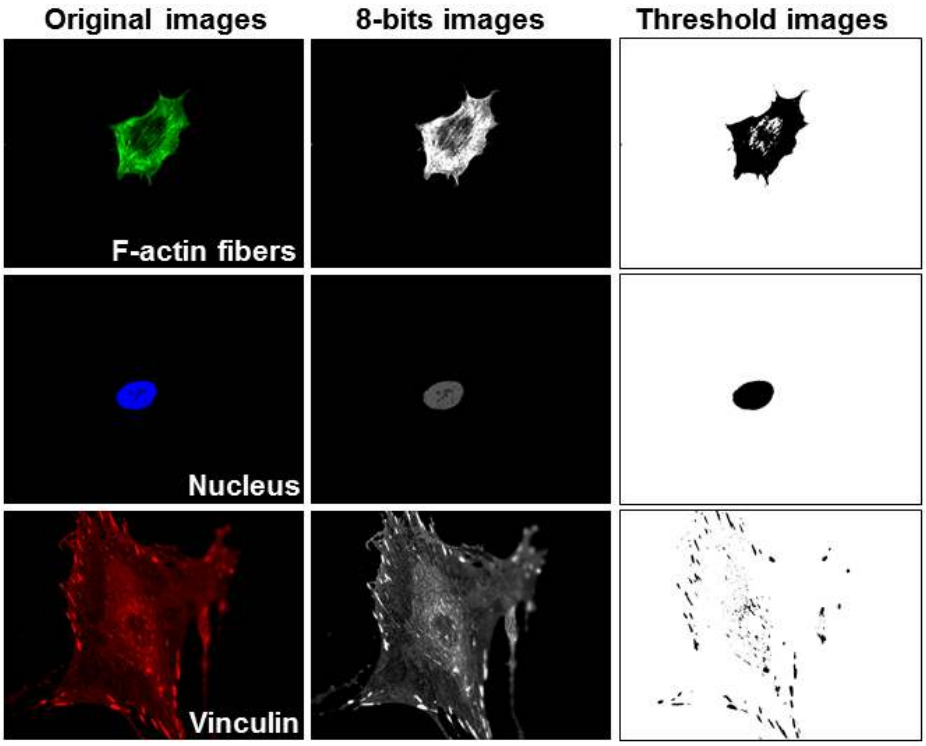

Figure II-8. Demonstration of how quantifications were performed using Image J freeware. The original images of F-actin fibers, nucleus, and vinculin are first converted into 8-bits images followed by optimisation of contrast and brightness. Then, threshold is applied and the parameters are measured with the "Analyse Particles" tool.

For quantification of OSX, OPN, calcium- and hydroxyapatite-rich zones, the images were acquired with the same exposure in order to avoid differences in the fluorescence intensity (FI). The images were also converted to 8-bits depth, and the FI estimated in terms of "Integrated density" (ID), which is the product between the area of the region of interest (A_{ROI}) and the mean grey value (GV). A scheme of the quantification method is given in **Figure II-9**.

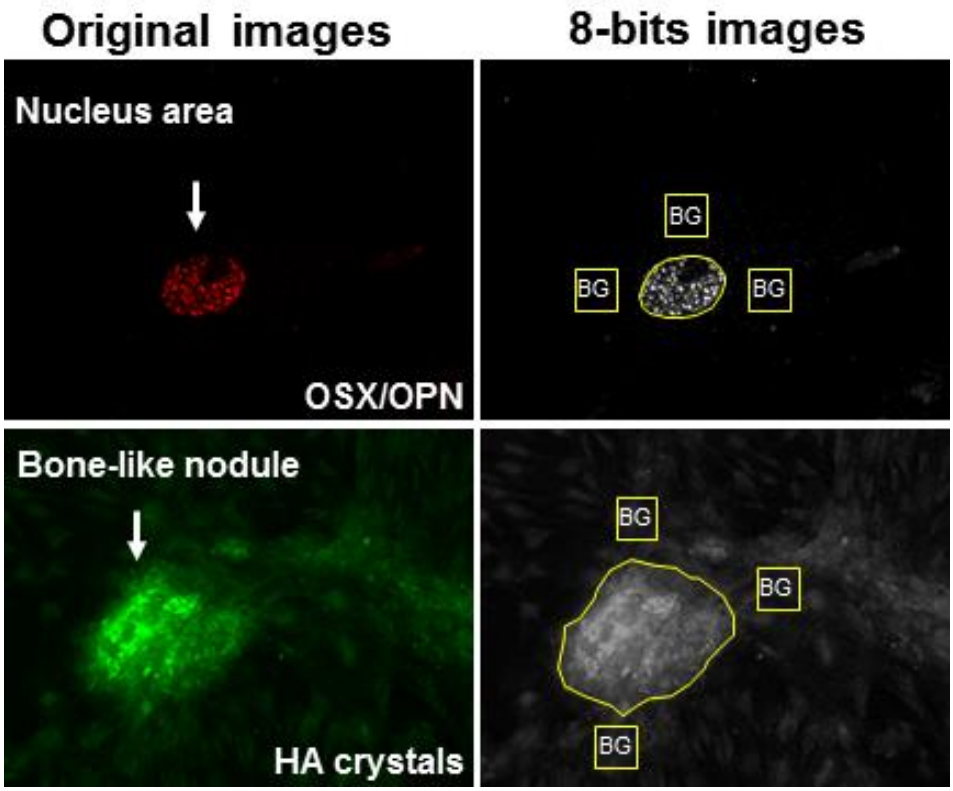

Figure II-9. Demonstration of how quantifications were performed using Image J freeware. The original images of OSX, OPN, calcium-rich and hydroxyapatite-rich zones are first converted into 8-bits images. The regions of interest are selected by using the polygon tool and the area of the region of interest, mean grey value, and the integrated density are measured. Image background is subtracted by performing at least three measurements of the mean grey value around the regions of interest.

First, the cell nucleus (expression of OSX and OPN), the calcium- and hydroxyapatite-rich zones were selected by using the polygon selection tool. Then, parameters such as A_{ROI}, GV, and the ID were measured. Image background (BG) was subtracted from the measurements by performing at least three measurements of the GV around the cell nucleus and the calcium- and hydroxyapatite-rich zones. The average

value of the GV (GV_{BG}) was considered as the background. Then, the "Corrected integrated density" was considered as the FI according to the following equation:

$$\mathbf{FI = ID - (A_{ROI} \times GV_{BG})} \qquad \textbf{Eq. II-17}$$

1.5.4. Scanning Electron Microscopy

Specimens were analysed by scanning electron microscopy in order to simultaneously visualise the cells and the underlying surfaces for cell adhesion studies (24 h) as well as the formation of bone-like nodules during the cell differentiation phase (4 weeks). For these observations, cells were fixed with 4 % (w/v) solution of paraformaldehyde (PFA) in PBS for 30 minutes at 4 ºC, followed by dehydration with a series of ethanol with increasing concentrations (30, 50, 60, 70, 80, 90, 95, and 100 %). The last dehydration step was carried out with hexamethyl-disilazane (HMDS) overnight, followed by air-drying. To avoid charging effects, the specimens were sputter coated with gold-palladium or carbon thin films (Quorum Technologies, Q150T ES). SEM observations were carried out in the secondary electron imaging mode using a JEOL JSM-7001F field-emission gun or a Hitachi S2400 scanning electron microscopes. The electron beam acceleration voltages were in the range 15-20 keV. At least 10 images were taken per each type of surface in different regions. Two specimens were analysed per group.

Cell alignment on surfaces with LIPSS was measured at 24 h after cell seeding, in SEM images using the "Angle" tool of Image J freeware (NIH, http://rsb.info.nih.gov/ij/). The cell alignment angle ($\theta_{alignment}$) was estimated by measuring the angle between the orientation of the LIPSS and the long axis of the cells [218, 262]. At least 20 cells were analysed for each specimen.

1.6. Bacteria Studies

In this section the materials and procedures used for the assessment of bacteria behaviour on the titanium surfaces are described. The *in vitro* studies were performed in the laboratories of the CNRS UMR5248, *Chimie et Biologie des Membranes et Nanoobjets* (*CBMN*), at the *Ecole Nationale d'Ingénieurs des Travaux Agricoles de Bordeaux* (*ENITAB*), University of Bordeaux.

1.6.1. Bacteria Culture

Prior to bacteria seeding, the 10 x 10 mm^2 titanium specimens were ultrasonically cleaned in absolute ethanol (Sigma-Aldrich, 99.8 % purity) for 15 minutes. Then, samples were put on 12-well plates (cell culture dishes), sterilised in 70 % ethanol for 10 minutes, and washed five times with phosphate buffered saline (PBS, pH 7.4, 1x, GIBCO by life technology).

Staphylococcus aureus (American Type Culture Colection; ATCC 25923) was used as the target bacteria in the present study. This strain was chosen because it is reported as the main agent causing bone and implant-associated infections [202]. Prior to bacteria preculture, *S. aureus* was frozen at -80 °C in Tryptic Soy Broth (TSB) medium containing 20 % glycerol. Preculture was performed by adding 100 µl of the solution to 10 ml of TSB medium. The solution was then centrifuged and incubated at 37 °C for 24 h. The optical density (OD) was measured at a wavelength of 600 nm using a spectrophotometer (Genesis 20, Thermo Scientific). *S. aureus* was incubated on the titanium surfaces with a concentration of about 7.3 x 10^8 CFU/ml for 48 h at 37 °C, under static conditions. The bacteria cultured on the tissue culture polystyrene (TCPS; Falcon®) was considered as a positive control. The experiments were performed in triplicate (3 specimens per group).

1.6.2. Immunostaining

At 48 h after bacteria seeding, the TSB medium was aspirated from the well plates and the specimens were washed five times with sterile PBS solution to remove non-adherent and loosely adherent bacteria. The adherent bacteria were fixed with 4 % paraformaldehyde (PFA) in PBS solution for 30 minutes at 4 °C, and fluorescently labeled with 0.3 % carboxyfluorescein succinimidyl ester (CFSE) in PBS solution for 30 minutes at 37 °C. CFSE is a suitable fluorescent staining dye for bacterial cells, without causing undesirable effects on cell adhesion or viability [263, 264].

1.6.3. Epifluorescence Microscopy

At least 20 images were taken for each type of surface using a LEICA DM5500B epifluorescence microscope with a motorised, programmable stage using a CoolSnap HQ camera, controlled by Metamorph 7.6 software. A L5 filter cube from Leica

Microsystems was used for visualisation of the green fluorescent signal provided by the microorganisms. All the images were acquired with the same exposure in order to avoid differences in the fluorescent intensity. The fluorescent intensity (FI) of the 8-bits depth images was estimated in terms of "Integrated density" using Image J freeware (NIH, http://rsb.info.nih.gov/ij/). The latter is calculated by the product between the area of the region of interest (35,807 μm^2) and the mean grey value.

1.6.4. Crystal Violet Binding Assay

Quantification of biofilm formation was performed with crystal violet binding assay as previously described by Stepanovic *et al* [265]. At 48 h after bacteria seeding, the TSB medium was aspirated from the well plates, and the specimens washed five times with 1.0 ml of PBS in order to remove non-adherent bacteria. Then, the remaining adhered bacteria were stained with 1.0 ml of 50 % filtered crystal violet diluted in PBS for two minutes at room temperature. The excess stain was washed off several times with PBS until the observation of a non-coloured solution. Then, the dye bound to adherent cells was resolubilised with 700 µl of absolute ethanol for 20 minutes at room temperature. Then, 100 µl of coloured solution from each specimen was transferred to 96-well plates and the absorbance (OD) was measured at a wavelength of 550 nm using a spectrophotometer (Multiskan FC, Thermo Scientific). The OD_{550} of the TSB medium was considered as the blank reading (background) for all the measurements.

1.6.5. Scanning Electron Microscopy

The titanium specimens were observed by scanning electron microscopy in order to simultaneously visualise the adherent bacteria and the underlying surfaces, as well as biofilm formation. Prior to SEM observation, the specimens were dehydrated in a series of ethanol with increasing concentrations (70, 80, 90, and 100 %) for 30 minutes in each solution, followed by air drying. Then, they were sputter coated as aforementioned in section 1.5.4.

2. Surface Biofunctionalisation

In this section the materials and procedures used for the biofunctionalisation of the titanium surfaces are described. The biofunctionalisation of the titanium surfaces was performed in the laboratories of the CNRS, *Chimie et Biologie des Membranes et des*

Nanoobjets (*CBMN*) UMR5248, at the *Institut Européen de Chimie et Biologie* (*IECB*), University of Bordeaux. The XPS analyses were performed at *Plataforme Aquitaine de Caractérisation des Matériaux* (*PLACAMAT*), University of Bordeaux.

2.1. Molecular Structures

The 3-aminopropyltriethoxysilane (APTES) was purchased from ABC-Roth Sochiel, France. Anhydrous hexane, dry *N*,*N*-dimethylformamide (DMF), and 3-succinimidyl-3-maleimidopropionate (SMP; 99 %) were purchased from Sigma Aldrich, France. Custom-made KRGDSPC peptide sequence and KRGDSPC peptide sequence conjugated with fluorescein isothiocyanate (FITC) were synthesised by Genecust, Luxembourg. The molecular structure and the chemical formula of APTES, hexane, DMF, and SMP are given in **Figure II-10**. The molecular structure of the KRGDSPC peptide sequence conjugated with fluorescein isothiocyanate (FITC) fluorochrome is depicted in **Figure II-11**.

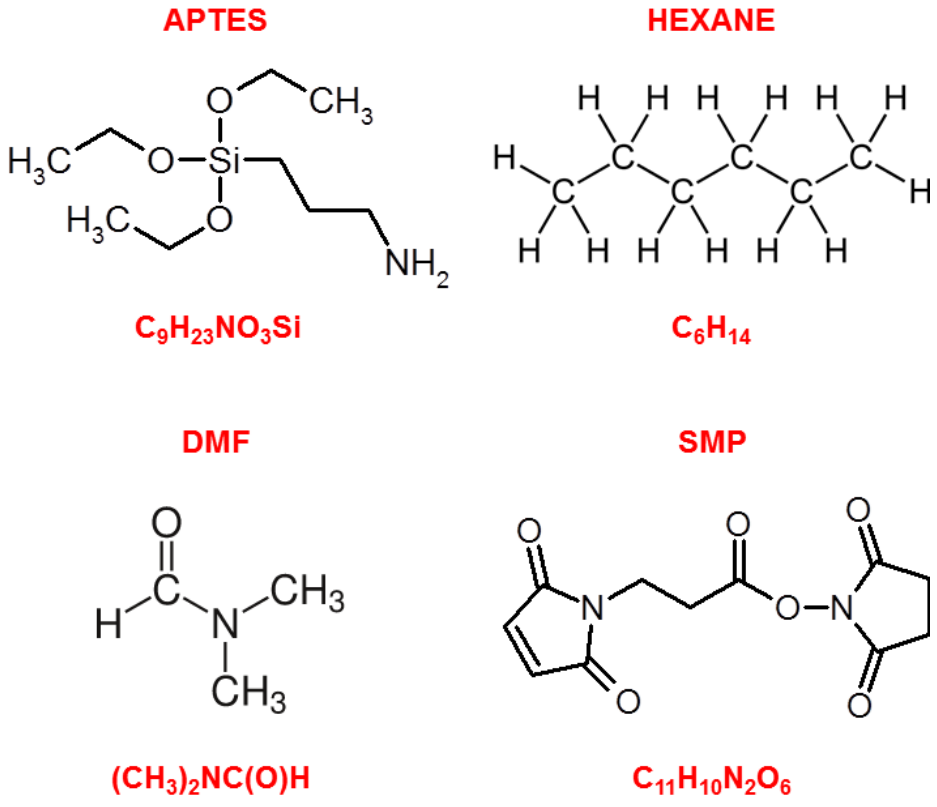

Figure II-10. Molecular structure and chemical formula of APTES, hexane, DMF, and SMP compounds used in the biofunctionalisation of the titanium surfaces.

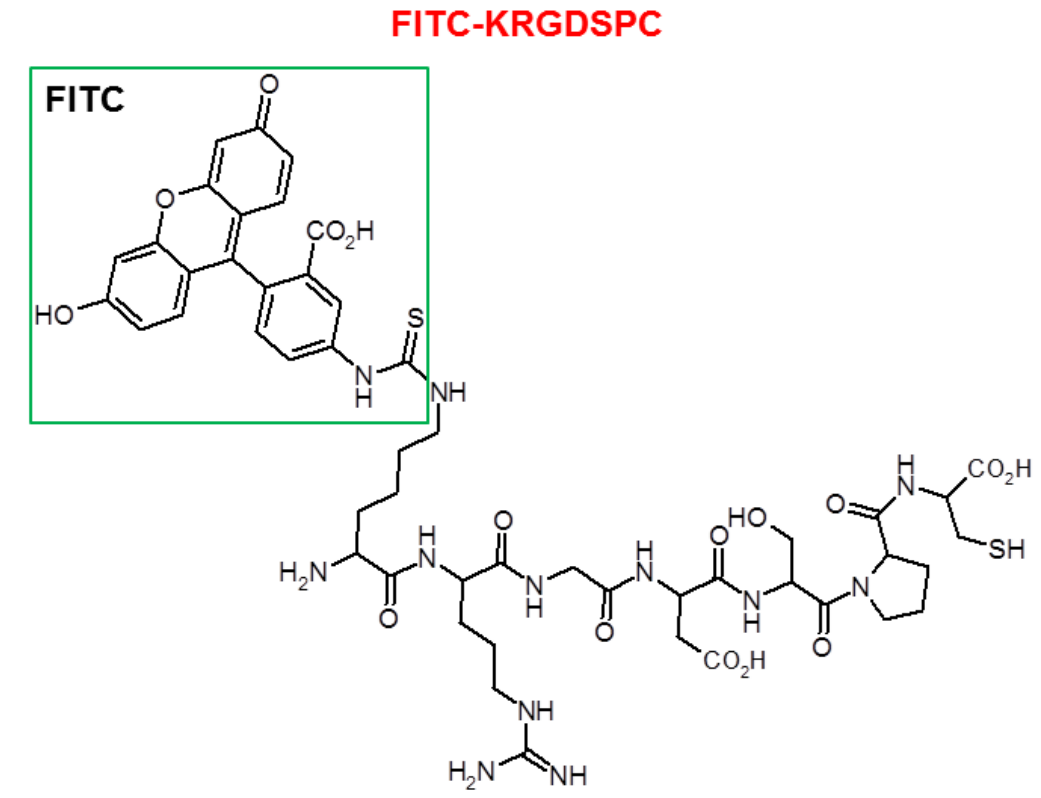

K	R	G	D	S	P	C
Lysin	Arginine	Glycine	Aspartic acid	Serin	Prolin	Cystein
$C_6H_{14}N_2O_2$	$C_6H_{14}N_4O_2$	$C_2H_5NO_2$	$C_4H_7NO_4$	$C_3H_7NO_3$	$C_5H_9NO_2$	$C_3H_7NO_2S$

Figure II-11. Molecular structure of the KRGDSPC peptide sequence conjugated with fluorescein isothiocyanate (FITC) fluorochrome.

2.2. Peptide Grafting

Prior to the biofunctionalisation, the 10 x 10 mm^2 titanium specimens were ultrasonically cleaned in liquid hand soap (Virunyl®, Laboratoire Garcin-Bactinyl) for 15 minutes and rinsed twice with milli-Q water. Then, they were ultrasonically cleaned in milli-Q water for 15 minutes. Finally, they were consecutively cleaned in baths of absolute ethanol (99.8 % purity) and acetone for 10 minutes at 80 and 50 °C, respectively. The biofunctionalisation of the titanium surfaces was performed in a purified Ar atmosphere chamber (Glove-box, Jacomex, France) in order to avoid surface contamination and ensure reproducibility and stability of the functionalisation molecules, **Figure II-12**.

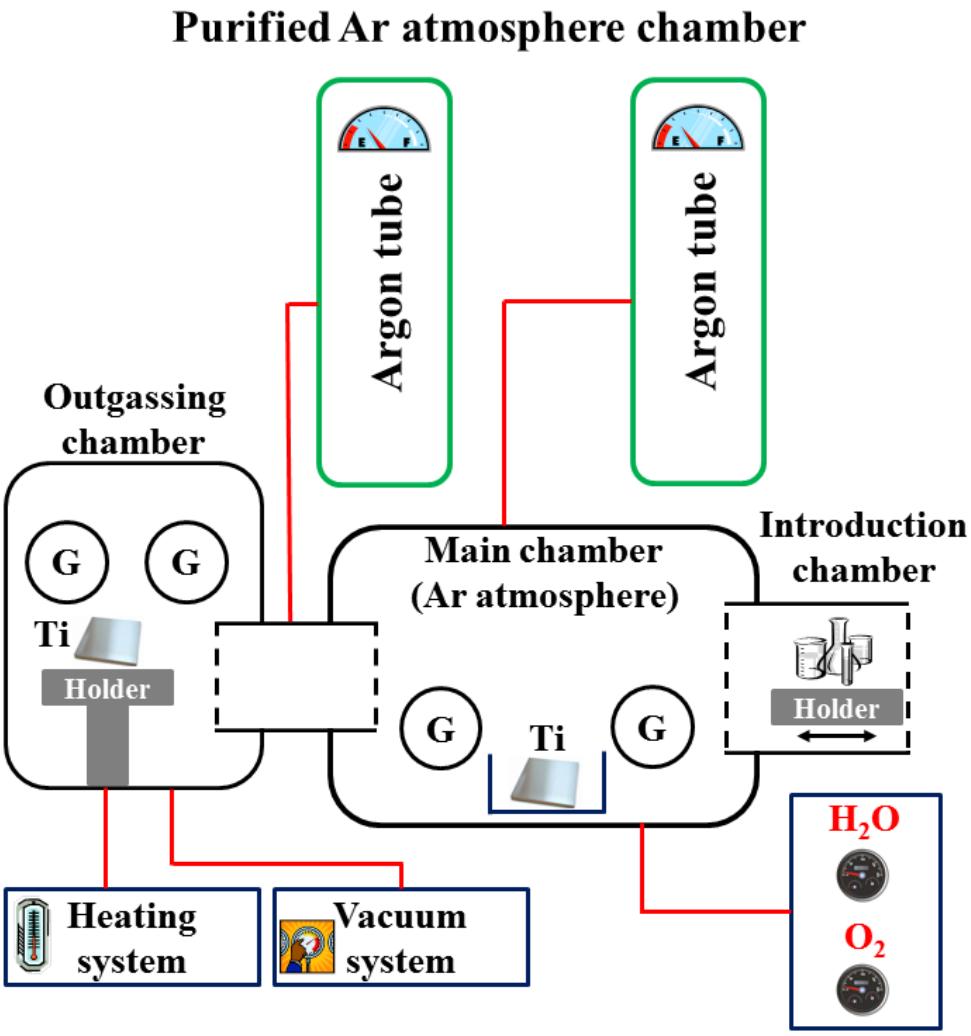

Figure II-12. Scheme of the purified Ar atmosphere chamber used for the biofunctionalisation of the titanium surfaces. Introduction chamber, main chamber, outgassing chamber, humidity (H_2O) gauge, oxygen (O_2) content gauge, heating system, vacuum system, and Argon tubes. G represents the gloves of the main and outgassing chambers.

The KRGDSPC peptide sequence was covalently grafted on the titanium surfaces according to a method previously described [21]. The strategy for peptide immobilisation involved three major steps as follows: (i) grafting of an aminofunctional organosilane (APTES) onto the OH groups of the titanium surfaces; (ii) substitution of the terminal amine (NH_2) for an hetero-bifunctional cross-linker (SMP); (iii) reacting the ‘‘outer’’ maleimide group with the thiol group present in the terminal cysteine (C) of the KRGDSPC peptide sequence. A scheme of the peptide immobilisation is shown in **Figure II-13**.

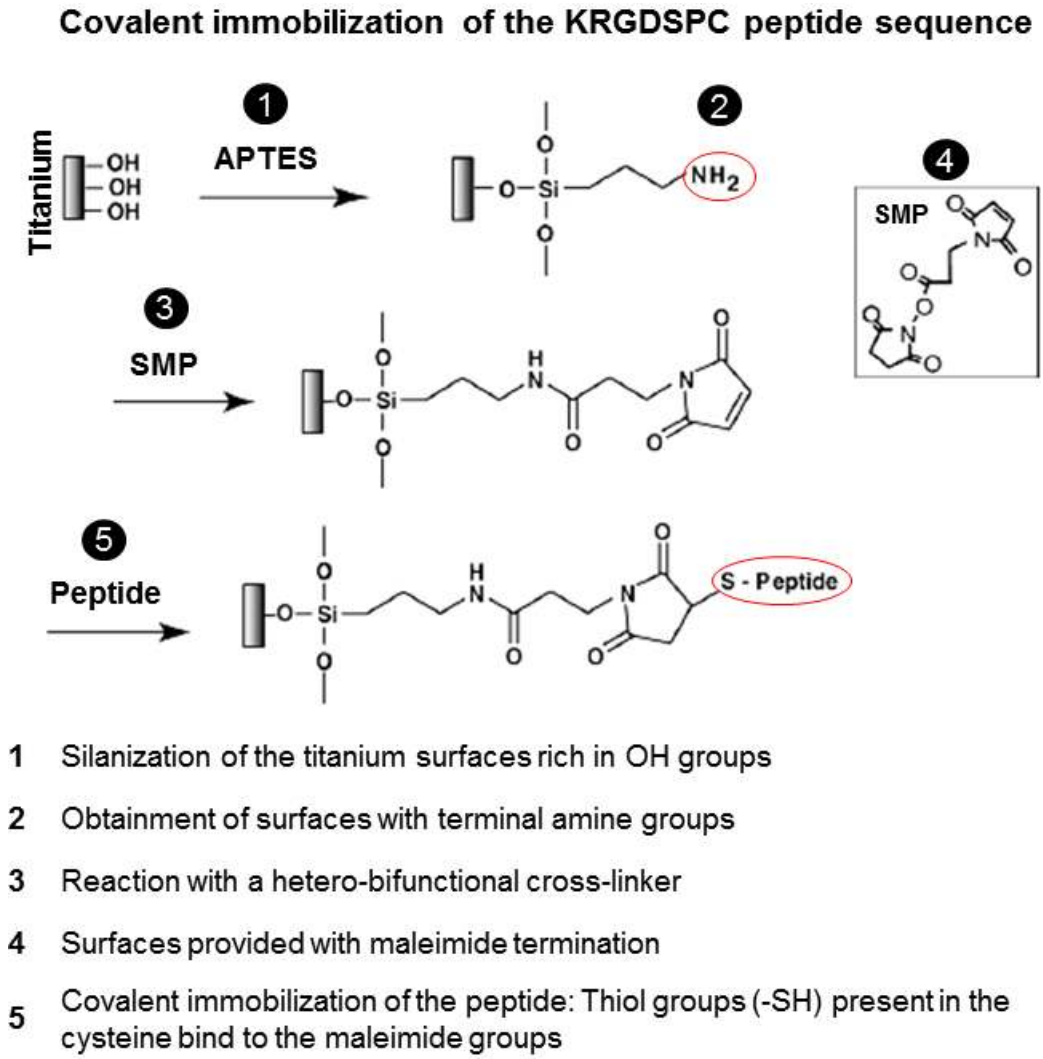

Figure II-13. Covalent immobilisation of the KRGDSPC peptide sequence on the titanium surfaces.

Experimentally, the biofunctionalisation of the titanium surfaces involved the following steps:

(a) After cleaning, the specimens were outgassed at 150 ºC under vacuum (10^{-5} Torr) during 20 h to remove physisorbed water and pollution;

(b) Silanization of the titanium surfaces was performed by immersing the specimens in a 4.7 µl APTES / 2.0 ml anhydrous hexane solution in an Ar atmosphere and under constant stirring during 2 h;

(c) The specimens were twice rinsed in anhydrous hexane during 30 minutes in an Ar atmosphere, followed by one rinsing overnight under constant stirring;

(d) The specimens were outgassed at 100 ºC under vacuum (10^{-5} Torr) during 4 h;

(e) The silanized surfaces were coupled with a hetero-bifunctional cross-linker by immersing the specimens in 1.1 mg SMP / 2.0 ml anhydrous DMF solution, in an Ar atmosphere and under constant stirring for 2 h;

(f) The specimens were three times rinsed in anhydrous DMF during 1 h in an Ar atmosphere, followed by one rinsing overnight under constant stirring, and sonication during 30 minutes;

(g) The specimens were outgassed at 70 ºC under vacuum (10^{-5}Torr) during 4 h;

(h) Finally, a 1 mM solution of the KRGDSPC peptide sequence in distilled water was immobilised on the titanium surfaces at ambient atmosphere and room temperature during 4 h;

(i) The specimens were rinsed and washed three times in distilled water under constant stirring during 1 h, and finally washed in milli-Q water during five days in order to remove adsorbed peptide not covalently grafted onto the titanium surfaces. The water was replaced daily.

2.3. X-ray Photoelectron Spectroscopy

X-ray Photoelectron Spectroscopy (XPS) was performed on the titanium surfaces to study the chemical composition alterations which might have occurred at each step of the peptide grafting procedure, namely:

(a) Outgassing;

(b) Outgassing + APTES;

(c) Outgassing + APTES + SMP;

(d) Outgassing + APTES + SMP + KRGDSPC.

Areas of 250 μm were analysed in a VG Scientific ESCALAB photoelectron spectrometer with non monochromatized $Al_{K\alpha}$ ($h\nu$ = 1486.6 eV) radiation and a power of 100 W. A flood gun was used for charge compensation. Spectra acquisition was performed at a constant pass energy of 10 eV. The peaks were fitted with VG Scientific software. The spectra were referenced to the position of carbon pollution peak at 284.8 eV. The binding energy values are given at ± 0.1 eV. Wide energy range spectra as well as expanded views of Ti 2p, Al 2p, Al 2s, O 1s, C 1s, N 1s, and Si 2p were acquired. Relative concentrations of chemical elements were calculated using Wagner's

method [266] and a standard set of VG ESCALAB sensitivity factors. At least four to five different points were analysed for each type of surface texture.

2.4. Fluorescence Microscopy

Fluorescent peptide grafting was also performed in order to verify the distribution and fluorescence intensity of the grafted peptide sequence on each type of surface. The peptide sequence was conjugated with fluorescein isothiocyanate fluorochrome (FITC-KRGDSPC), **Figure II-11**. The peptide immobilisation was performed as aforementioned in Section 2.2., but during the FITC-KRGDSPC grafting step the specimens were protected from ambient light. At least 10 images per type of surface were taken in different regions with a LEICA DM5500B epifluorescence microscope at different magnifications, using 2.5 times (NA 0.07) and 10 times (NA 0.25) dry objectives. A filter cube L5 (Leica Microsystems) was used for the visualisation of FITC fluorescence signal. Quantification of the fluorescence intensity (FI) was expressed in terms of "Integrated Density" (ID) using Image J freeware (NIH, http://rsb.info.nih.gov/ij/), by assuming the whole image area as the region of interest.

3. Statistical Analysis

Numerical data are presented as average value ± standard deviation. Statistical analysis was performed by one-way analysis of variance (ANOVA) and Tukey's test for multiple comparisons, using OriginPro 8 software (OriginLab Corporation, USA), for the calculation of the significance level of the data. Differences were considered statistically significant if the *p*-value was lower than 0.05 (confidence of 95 %).

Chapter III. Results

In this section, the major results obtained in the present thesis are presented with the following organisation:

- Laser surface texturing of titanium specimens in stationary conditions in order to study the influence of the processing conditions and parameters such as radiation fluence, number of pulses, and laser beam polarisation on the surface morphology;
- Large area laser surface texturing of titanium specimens in non-stationary conditions in order to study the influence of the surface texture on the biological response;
- Characterisation of the laser textured surfaces in terms of topography, chemical composition and crystallographic structure;
- Assessment of the wettability of water and HBSS, human Mesenchymal Stem Cells and *Staphylococcus aureus* behaviour;
- Characterisation of the biofunctionalised surfaces in terms of chemical composition alterations, peptide distribution and fluorescence intensity.

1. Experiments in Stationary Conditions

In these experiments craters were produced on cp Ti surfaces varying the radiation fluence, number of laser pulses, and laser beam polarisation. These experiments aimed at studying the relation between the surface morphology and the laser processing conditions and parameters. These different relations provide laser parameters selection criteria for the production of specific surface structures.

1.1. Influence of the Radiation Fluence

Craters were produced by laser treatment with average pulse energies in the range 44-518 μJ and 200 laser pulses at a repetition rate of 10 Hz [17]. SEM micrographs of the laser-induced craters are presented in **Figure III-1**. Different types of surface textures were observed depending on the pulse energy. At a pulse energy of 44 μJ, the whole crater consists of ripples, known as laser-induced periodic surface structures-LIPSS (**Figure III-1 a** and **a1**). When the pulse energy was increased to 86 μJ, columns

at the micrometre scale were observed in the centre of the crater**,** while LIPSS were still verified at its periphery **(Figure III-1 b** and **b1**). Increasing the pulse energy to 176 μJ, lead to an increase of the area occupied by columns and an increase to the columns size (**Figure III-1 c**). At a pulse energy of 262 μJ, melting/liquid spallation (flat region) of the material was clearly observed at the centre of the crater (**Figure III-1 d**). Further increases of the pulse energy in the range 340-518 μJ increased the area affected by liquid spallation significantly (**Figure III-1 e** and **f**). Taking into account these findings, it is evident that the formation of the specific laser-induced surface textures can be obtained by controlling the radiation fluence.

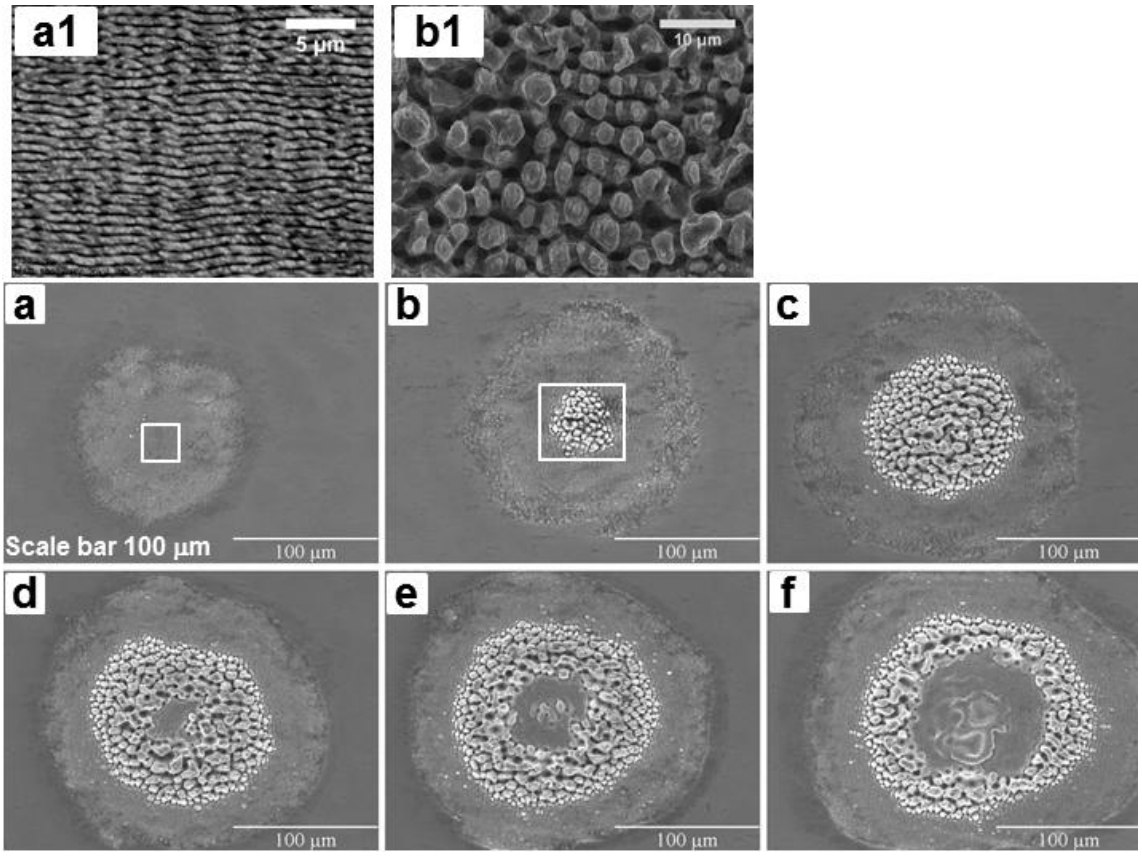

Figure III-1. SEM micrographs of different laser-induced craters produced on a cp Ti surface with average pulse energies of (a) 44, (b) 86, (c) 176, (d) 262, (e) 340, and (f) 518 μJ, and 200 laser pulses at a repetition rate of 10 Hz. (a1) and (b1) High magnification SEM micrographs of the centre of the craters in (a) and (b), respectively. The scale bar is 100 μm (a-f), 5 μm (a1), and 10 μm (b1).

In order to estimate the corresponding fluence thresholds, the laser beam radius ω_0 was estimated as follows [17]. For a Gaussian laser beam (a valid approximation in the present case) the spatial fluence profile $F(r)$ at the surface of the specimen is given by:

$$F(r) = \frac{2E_p}{\pi\omega_0^2} e^{-2\frac{r^2}{\omega_0^2}} \qquad \text{Eq. III-1}$$

where r is the distance from the laser beam axis. From **Figure III-1**, one may conclude that microcolumns form for pulse energies E_p higher than 44 μJ. On the other hand, the radius of the area occupied by microcolumns increases with increasing pulse energy. Therefore, if r_1 and r_2 are the radii of the areas occupied by microcolumns for pulse energies E_p1 and E_p2, the relationship $F_{th} = F(r_1) = F(r_2)$ holds. Hence, the fluence threshold for microcolumns formation can be calculated from:

$$\frac{2E_p1}{\pi\omega_0^2} e^{-2\frac{r_1^2}{\omega_0^2}} = \frac{2E_p2}{\pi\omega_0^2} e^{-2\frac{r_2^2}{\omega_0^2}} \qquad \text{Eq. III-2}$$

Since the distance between the focusing lens and the specimen surface was kept constant for all the experiments, and the pulse energy was controlled by means of a beam attenuator, ω_0 is independent of the pulse energy. As a result, ω_0 can be found using the following equation:

$$\omega_0 = \sqrt{\frac{2(r_1^2 - r_2^2)}{\ln\frac{E_p1}{E_p2}}} \qquad \text{Eq. III-3}$$

Taking into account the r values measured in the SEM micrographs of **Figure III-1**, a value of ω_0 of 105 ± 25 μm was found, leading to estimations of fluence thresholds for LIPSS and microcolumns formation of 0.2 ± 0.1 and 0.6 ± 0.2 J/cm², respectively. The maximum fluence for which microcolumns still form was 1.7 ± 0.2 J/cm². The addition of alloying elements such as Al and V in the Ti-6Al-4V alloy does not change significantly the fluence thresholds for the formation of LIPSS and columns as compared to those determined for cp grade 2 Ti.

1.2. Influence of the Number of Pulses and Laser Beam Polarisation

Once the fluence thresholds for the formation of LIPSS and columns were established, the influence of the number of pulses (N) and laser beam polarisation on the surface texture was investigated. Craters were produced with a number of laser pulses in the range 2-100 at a repetition rate varying between 1 and 10 Hz, using linearly and circularly polarised laser beams. Radiation fluences near the threshold for LIPSS (~ 0.2

J/cm^2) and microcolumns (~ 0.6 J/cm^2) formation were selected in order to avoid intense surface melting/liquid spallation, as observed for radiation fluences higher than approximately 1.0 J/cm^2 (**Figure III-1 e**). **Figure III-2** presents the evolution of LIPSS with the number of pulses when the surface is treated with a linearly p-polarised laser beam.

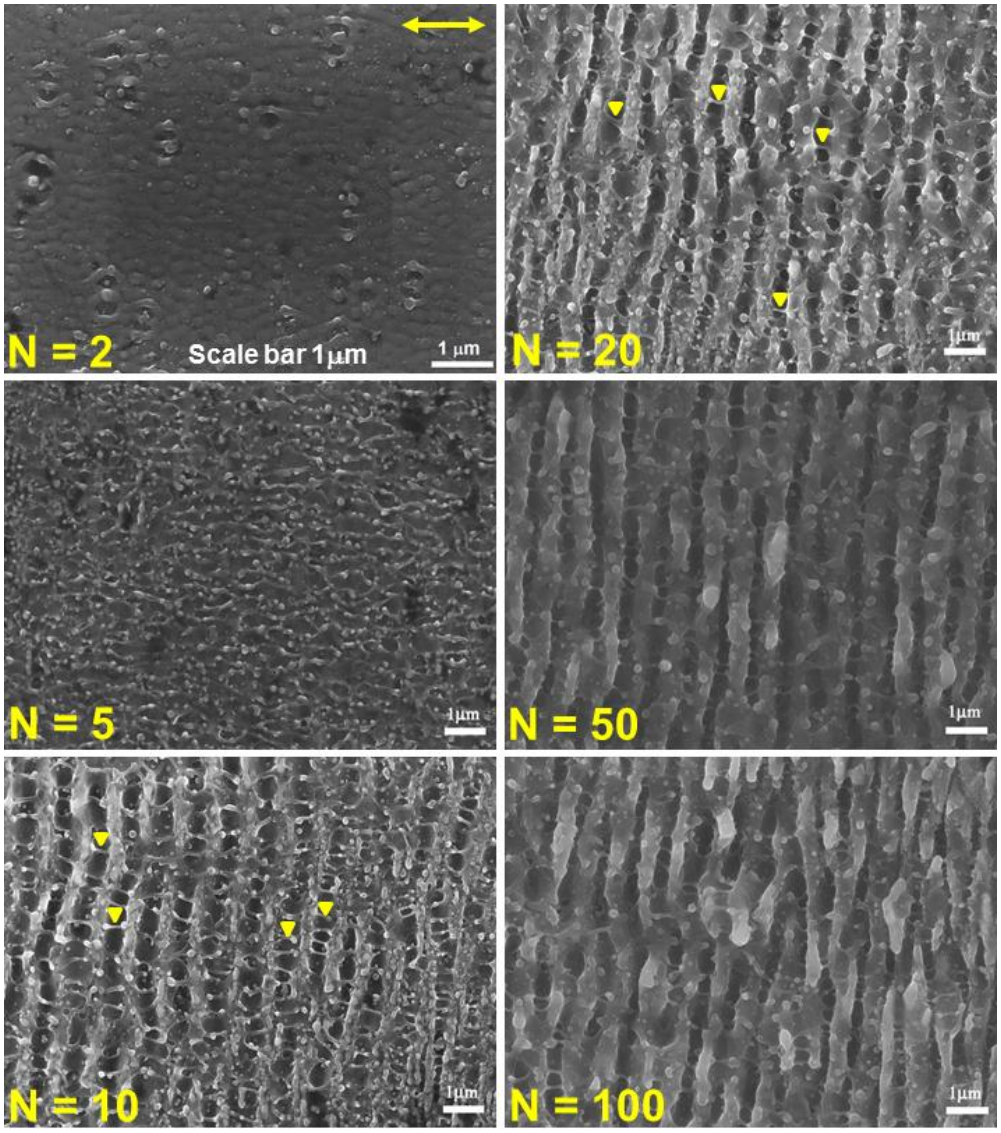

Figure III-2. SEM micrographs of the centre of the craters produced on a cp Ti surface, showing the LIPSS evolution with the number of pulses (N) and repetition rate in the ranges 2-100 and 1-10 Hz, respectively. The radiation fluence was ~ 0.2 J/cm^2. The yellow arrow indicates the polarisation direction of the linearly p-polarised laser beam. The yellow arrow-heads indicate the resolidified material between the LIPSS. The scale bar is 1 μm.

After 2 laser pulses, a faint wavy pattern consisting of parallel ridges oriented parallel to the polarisation vector as well as some resolidified dropltes were observed. With 5 laser

pulses, the amount of resolidified material forming ridges parallel to the polarisation vector increased. After 10 laser pulses, a ripple pattern (LIPSS) perpendicular to the polarisation vector was observed, while some droplets of resolidified material bridge the crests of the LIPSS (indicated by the yellow arrow-heads). Finally, with further increase of the number of laser pulses in the range 20-100, the LIPSS became better defined and grow deeper, while the amount of resolidified material bridging the crests of the LIPSS decreases. **Figure III-3** presents the evolution of the LIPSS with the number of pulses with the polarisation direction of the laser beam oriented at about 45° towards the p-polarisation.

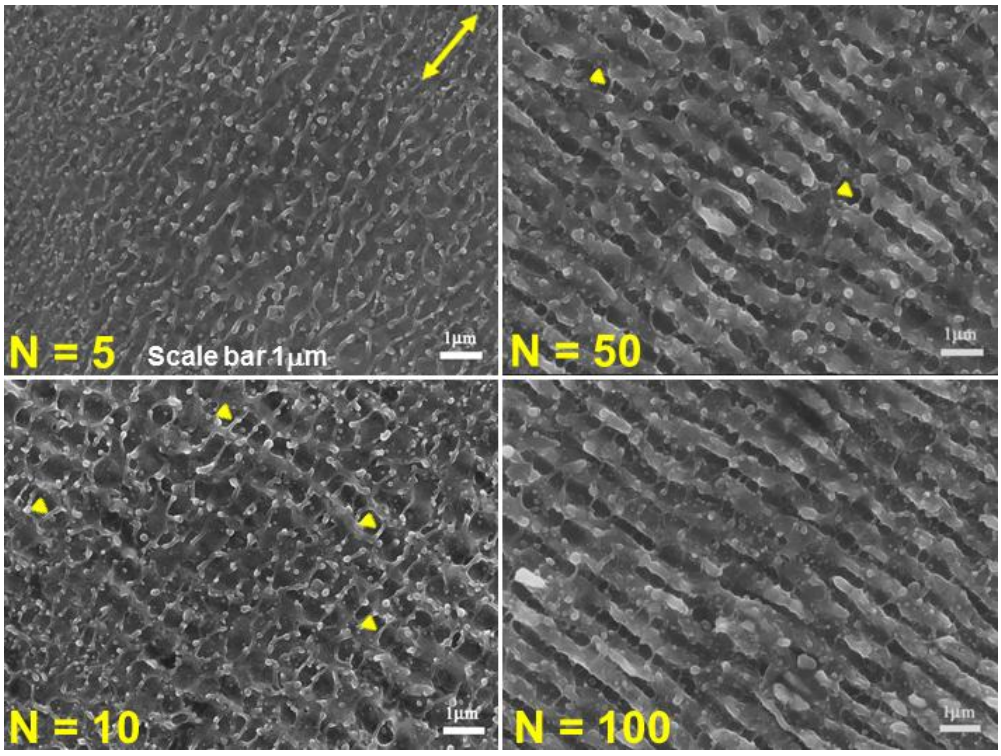

Figure III-3. SEM micrographs of the centre of the craters produced on a cp Ti surface, showing the LIPSS evolution with the number of pulses (N) and repetition rate in the ranges 5-100 and 1-10 Hz, respectively. The radiation fluence was ~ 0.2 J/cm^2. The yellow arrow indicates the polarisation direction of the laser beam (45° towards the p-polarisation). The yellow arrow-heads indicate the resolidified material between the LIPSS. The scale bar is 1 μm.

The evolution of the surface morphology was quite similar to that verified in **Figure III-2**, but the resolidified material (5-10 laser pulses) and the LIPSS (10-100 laser pulses) were observed paralelly and perpendicularly oriented, respectively, to the polarisation direction of the laser beam (45° towards the p-polarisation). It is

noteworthy that when the LIPSS were produced with a linearly s-polarised laser beam (90° towards the p-polarisation), they were observed perpendicularly oriented to those in **Figure III-2**. **Figure III-4** presents the evolution of the LIPSS with the number of pulses under irradiation with a circularly polarised laser beam.

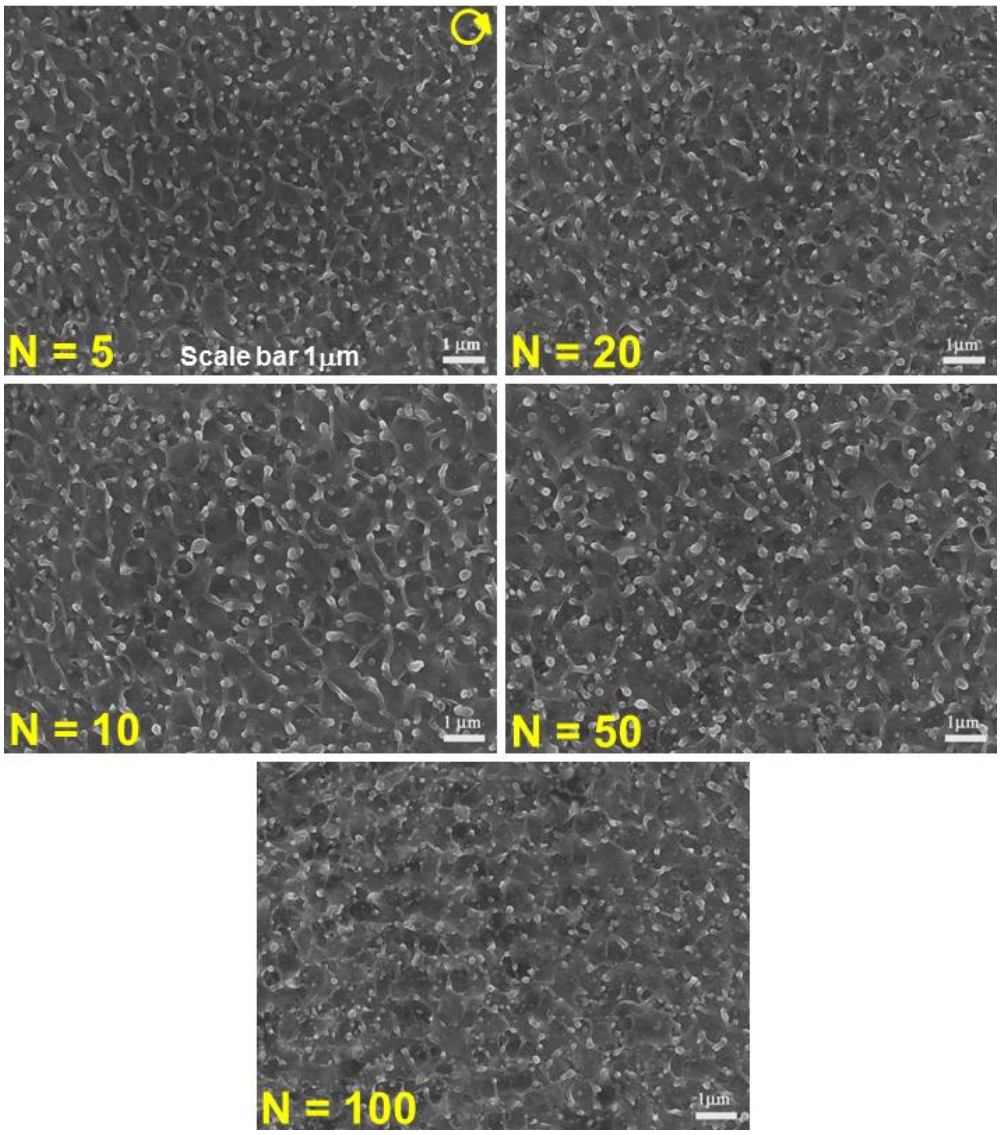

Figure III-4. SEM micrographs of the centre of the craters produced on a cp Ti surface, showing LIPSS evolution with the number of pulses (N) and repetition rate in the ranges 5-100 and 1-10 Hz, respectively. The radiation fluence was ~0.2 J/cm^2. LIPSS were produced with a circularly polarised laser beam. The scale bar is 1 μm.

LIPSS were not observed to form, independently of the number of pulses (5-100). Resolidified material randomly oriented as well as some resolidified droplets were observed.

Figure III-5 presents the evolution of the microcolumns under irradiation with a linearly p-polarised laser beam.

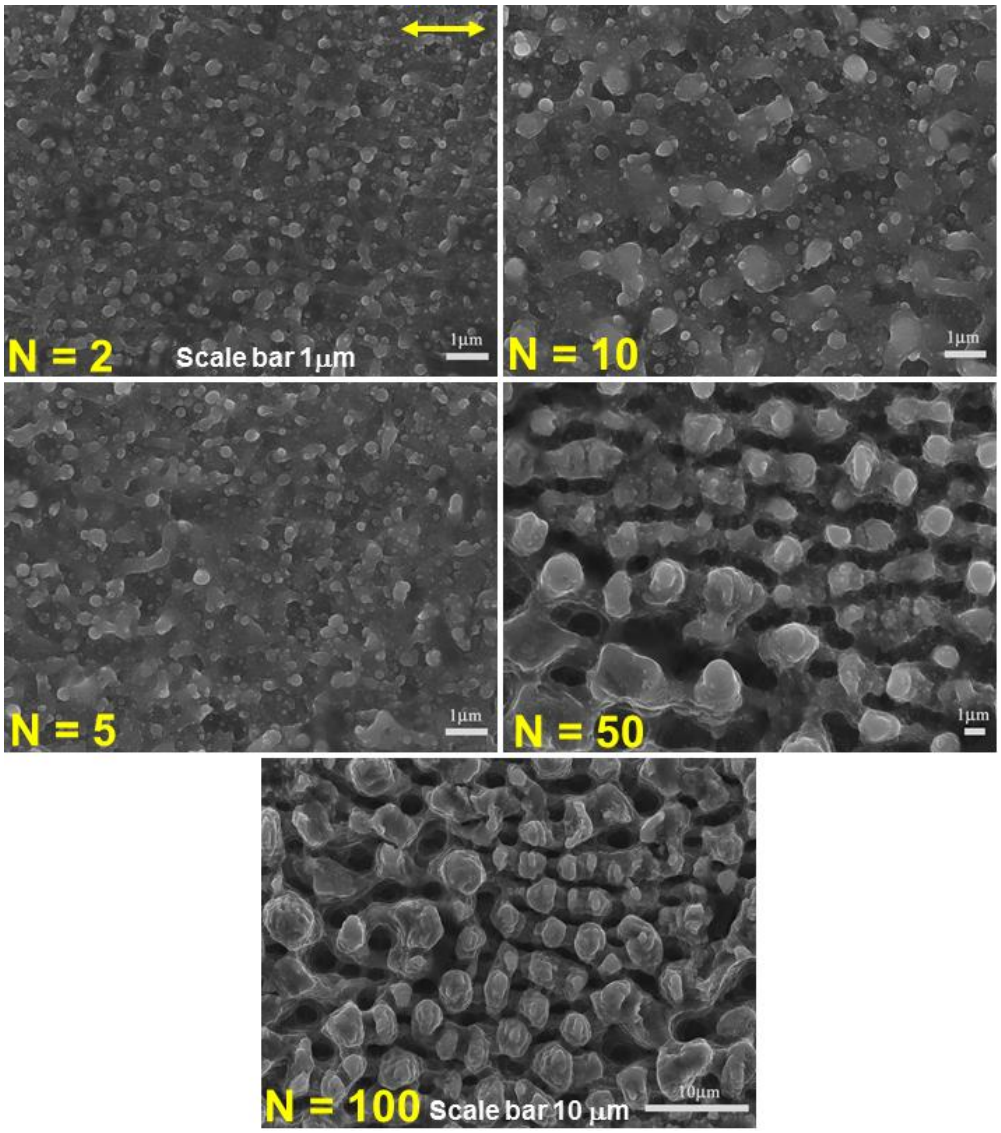

Figure III-5. SEM micrographs of the centre of the craters produced on a cp Ti surface, showing the microcolumns evolution with the number of pulses (N) and repetition rate in the ranges 2-100 and 1-10 Hz, respectively. The radiation fluence was ~ 0.6 J/cm^2. The yellow arrow indicates the polarisation direction of the linearly p-polarised laser beam. The scale bar is 1 μm (N = 2-50) and 10 μm (N = 100).

After 2 laser pulses, the surface was covered by random nanostructures and with some resolidified droplets. After 5-10 laser pulses, the nanostructures became larger and denser. With 10-50 laser pulses, micron-scale self-organised structures (microripples) were formed. These microripples were observed parallelly oriented to the polarisation direction of the laser beam. Finally, after 50-100 laser pulses, domes were formed along

the peaks of the microripples, and further irradiation (100-1000 laser pulses) of the surfaces produced microcolumns with well-defined boundaries and increased size. When a linearly s-polarised laser beam was used the microripples were observed parallely oriented to the s-polarisation of the laser beam. **Figure III-6** presents the evolution of the microcolumns under irradiation with a circularly polarised laser beam. The modification of the surface morphology was similar to that observed in **Figure III-5**, but for the same number of laser pulses (2-10), the random nanostructures covering the surface were larger and denser than those observed under irradiation with a lineraly polarised laser beam. In addition, microripples formation was not clearly observed.

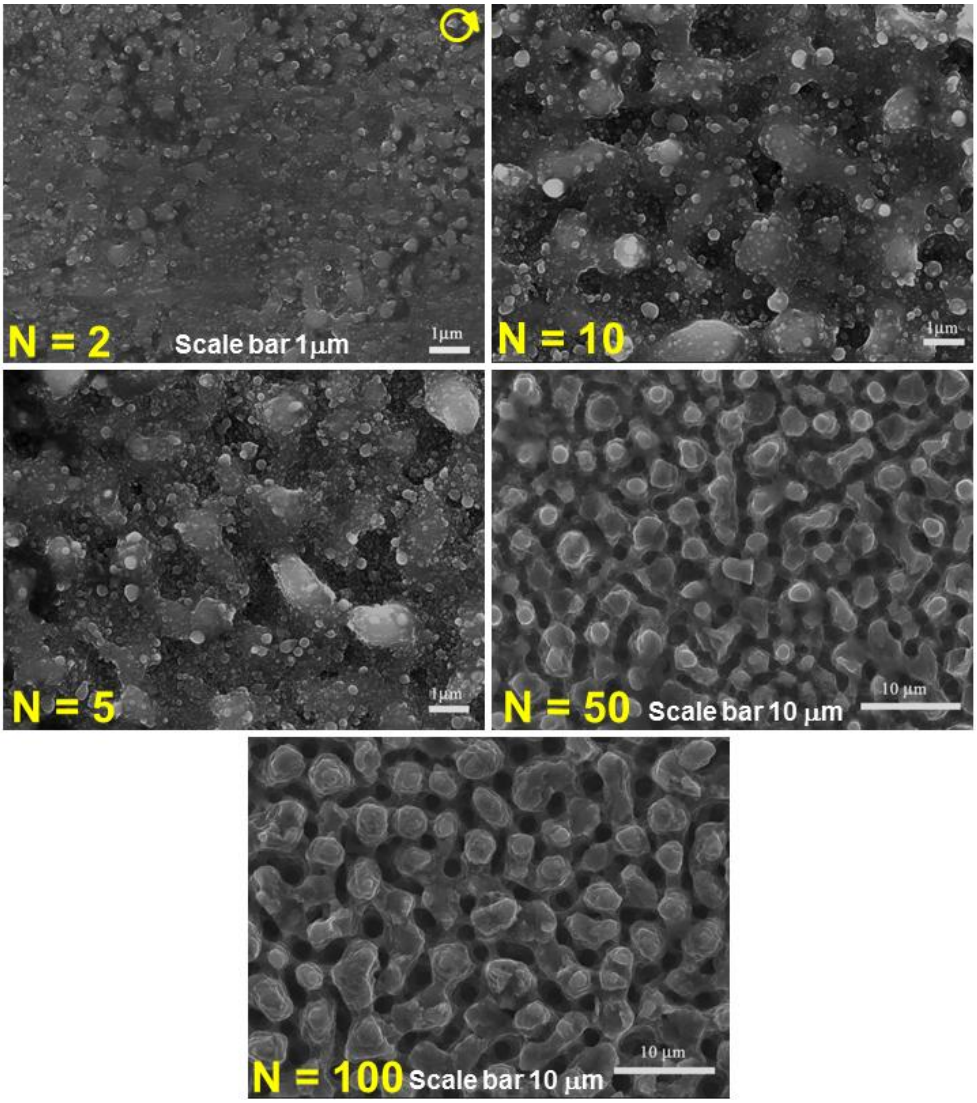

Figure III-6. SEM micrographs of the centre of the craters produced on a cp Ti surface, showing the microcolumns evolution with the number of pulses (N) and repetition rate in the ranges 5-100 and 1-10 Hz, respectively. The radiation fluence was 0.6 J/cm^2. Microcolumns were produced with a circularly polarised laser beam. The scale bar is 1 μm (N = 2-10) and 10 μm (N = 50-100).

1.3. Summary

The major results presented in Sections 1.1. and 1.2. of Chapter III are summarised as follows:

(a) LIPSS form with fluences near the damage-threshold of titanium (~ 0.1 J/cm^2);
(b) At least 50-100 laser pulses are required to obtain well-defined LIPSS;
(c) LIPSS only form when the laser beam is linearly polarised;
(d) LIPSS are polarisation-sensitive features, i.e., their orientation can be reproducibly changed by controlling the polarisation direction of the laser beam;
(e) LIPSS are perpendicular to the polarisation direction of the laser beam;
(f) Microcolumns form with fluences in the range 0.4-1.0 J/cm^2;
(g) Between 50 and 100 laser pulses are required to obtain well-defined microcolumns, but these features persist for higher numbers of pulses at least up to 1000;
(h) Since the laser beam spatial profile is approximately Gaussian, microcolumns and LIPSS form in the centre and in the periphery of the craters, respectively, when the radiation fluence is in the range of microcolumns formation.

2. Experiments in Non-stationary Conditions

In these experiments large areas consisting of three different types of surface structures were produced on grade 2 cp Ti and grade 5 Ti-6Al-4V alloy to study the influence of the surface textures on wettability, human Mesenchymal Stem Cells, and *Staphylococcus aureus* behaviour.

2.1. Determination of the Laser Beam Radius

In order to reduce the laser treatment time, the surface of the specimens was located a few centimeters below the focal point of the focusing lens, where the laser beam radius ω_0 is larger than the corresponding radius in the focal plane. The value of ω_0 at the specimens' surface was estimated using the D^2-method, previously described in Section 1.2. of Chapter II. **Figure III-7** shows the laser-induced craters produced on a Ti-6Al-4V alloy surface in stationary conditions, with average pulse energies and number of pulses in the ranges 240-640 μJ and 20-1000, respectively. The larger the pulse energy and number of pulses the larger the craters diameter. This increase results

from an incubation effect, caused by damage accumulation on surfaces submitted to multiple laser pulses.

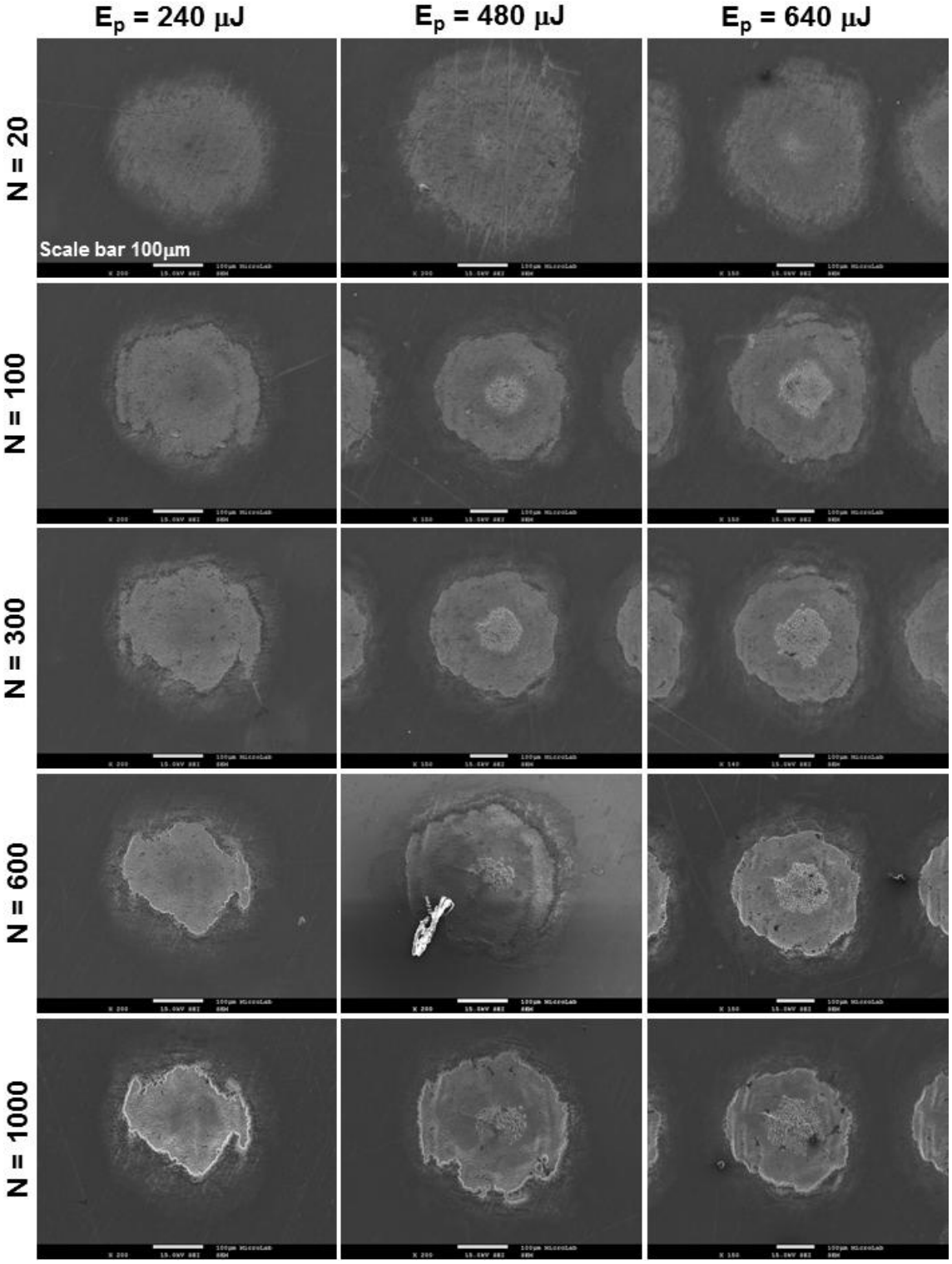

Figure III-7. Laser-induced craters produced on a Ti-6Al-4V alloy surface in stationary conditions. The average pulse energy (E_p) and the number of pulses (N) were in the ranges 240-640 µJ and 20-1000, respectively. The scale bar is 100 µm.

Figure III-8 presents plots of the square of the average crater diameter (D^2) versus the logarithm of the average pulse energy ($\ln E_p$) for number of pulses in the range 20-1000. The experimental data is well fitted by linear functions, with correlation coefficients R^2 of ~ 0.99. By using the **Eq. II-6** (see Section 1.2. of Chapter II) a ω_0 of about 169 ± 5 μm was estimated.

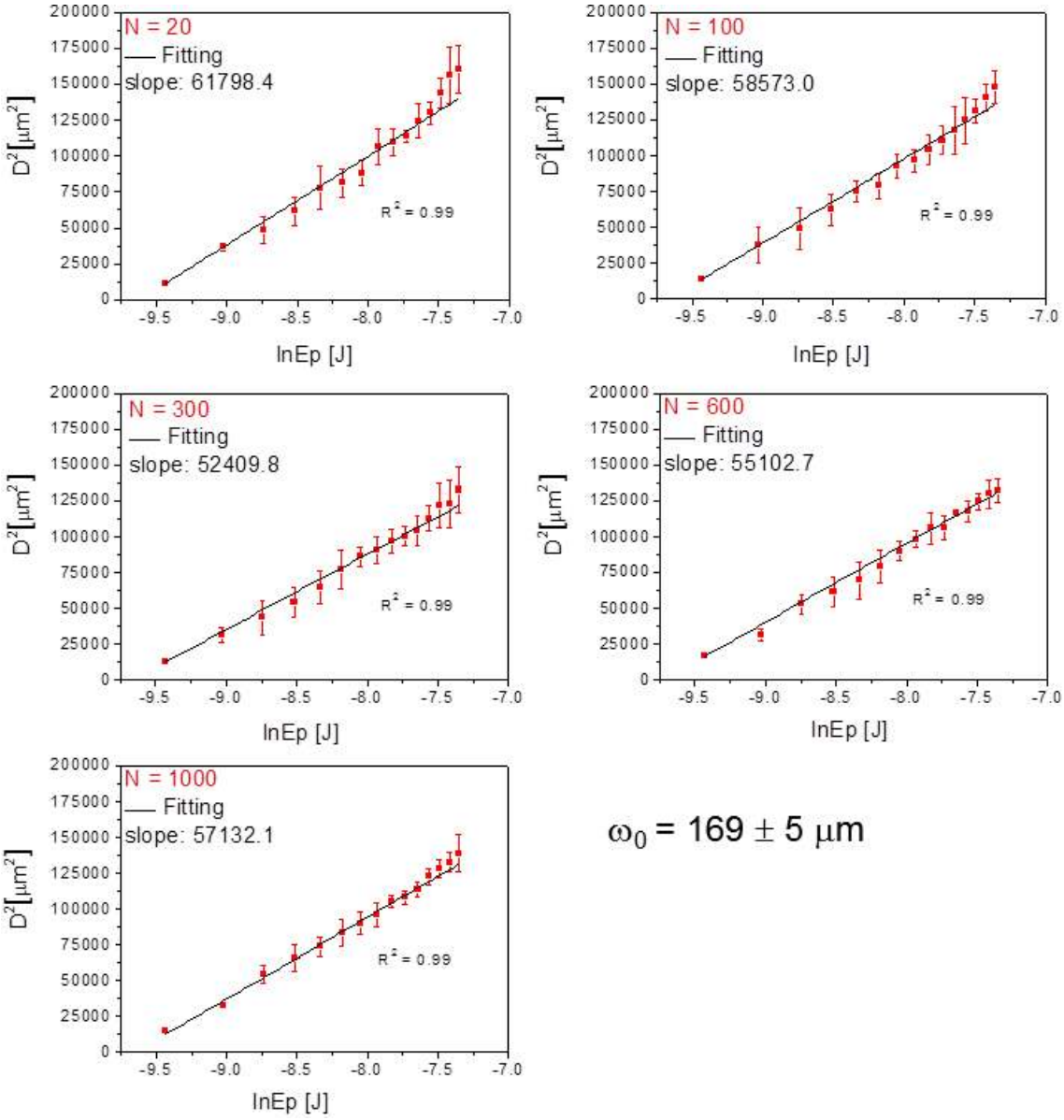

Figure III-8. Plots of the square of the average crater diameter (D^2) versus the logarithm of the average pulse energy ($\ln E_p$) for number of pulses (N) in the range 20-1000.

2.2. Surface Morphology and Topography

Figure III-9 presents optical micrographs of the laser textured surfaces. The surfaces were textured by partially overlapping laser tracks obtained by linear displacement in the X direction of the positioning stage.

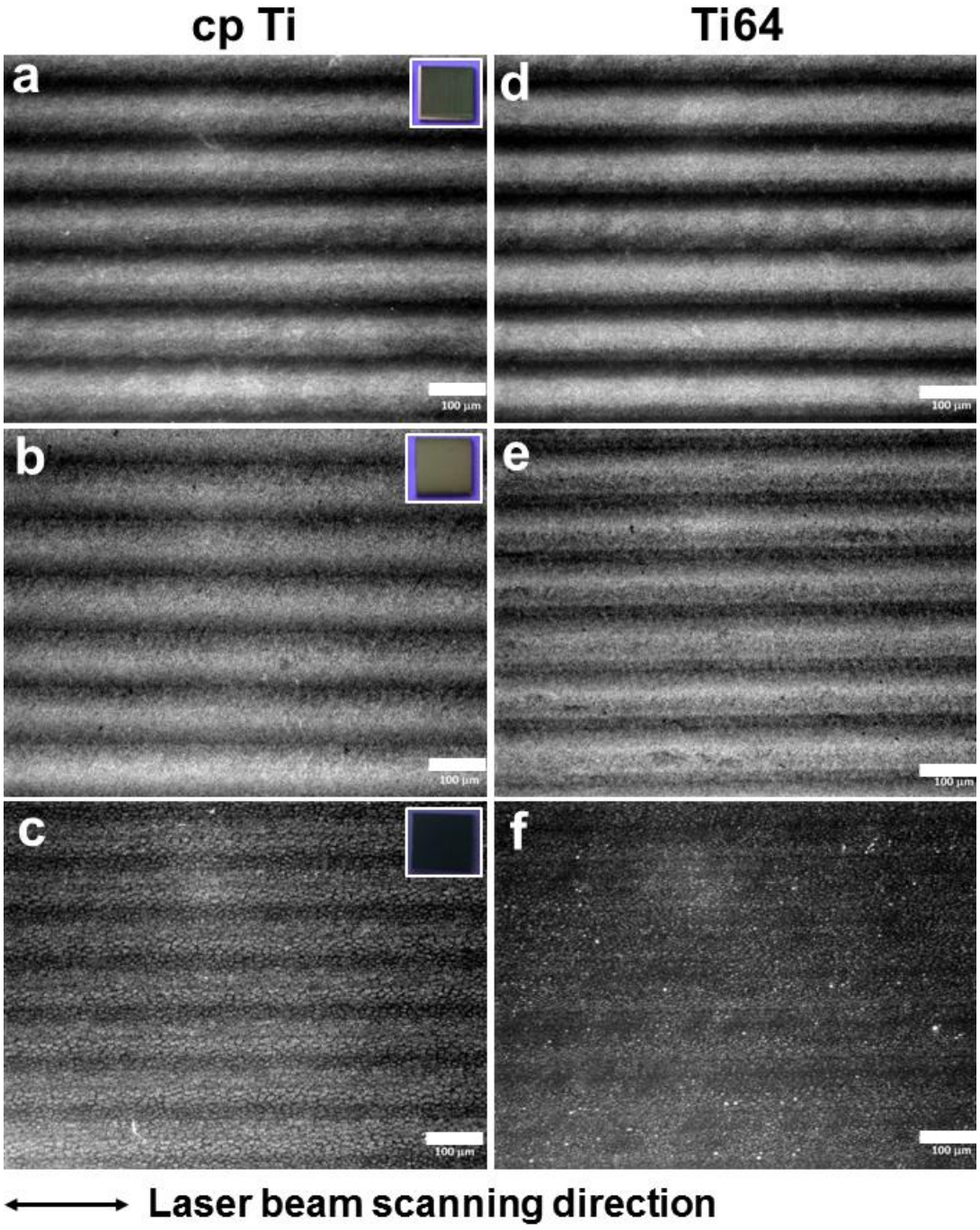

Figure III-9. Optical micrographs of the laser textured surfaces of cp Ti and Ti-6Al-4V alloy specimens. The inset pictures in (a-c) show the characteristic colours of the different laser textured surfaces. The radiation fluence and the repetition rate were in the ranges 0.2-0.8 J/cm^2 and 50-1000 Hz, respectively. The scale bar is 100 µm. The laser-induced surfaces structures produced in (a-f) are depicted in Figure III-10.

The centre-to-centre distance of the laser tracks is either about 100 μm (**Figure III-9 a-b** and **d-e**) or 90 μm (**Figure III-9 c** and **f**), which corresponds to the lateral displacement of the laser beam. These lateral displacements were chosen to ensure the homogeneity of the distribution of the laser-induced surface structures along the textured areas. The inset pictures in **Figure III-9 a-c** show the characteristic colour of each type of laser textured surface. As aforementioned in Section 1.2. of Chapter II, the colour depends strictly on the surface texture produced, which affects the light scattering by the surface. Laser textured surfaces consisting of LIPSS (**Figure III-9 a** and **d**), nanopillars (**Figure III-9 b** and **e**), and microcolumns (**Figure III-9 c** and **f**) were grey, light grey, and black, respectively. The characteristic colour of the modified surfaces is reproducible and was used for a first control of the surface texture formed.

Figure III-10 depicts high magnification SEM micrographs of the laser textured surfaces of Ti-6Al-4V alloy. **Figure III-11** presents the three-dimensional (3D) reconstruction (Digital Elevation Mode-DEM) and the corresponding 2D roughness profiles of the surfaces of both Ti alloys. Three different types of surface textures can be reproducibly produced, depending on the radiation fluence and number of pulses. The first type of texture (**Figure III-10 a-b**) consists of LIPSS perpendicular to the polarisation direction of the laser beam. They are observed on surfaces treated with 0.20 J/cm^2 and 192 laser pulses. The periodicity of the LIPSS was independent of the material (708 ± 59 and 715 ± 86 nm for cp Ti and Ti-6Al-4V alloy surfaces, respectively), and the maximum height was 251 ± 77 and 296 ± 58 nm, respectively, as shown in **Figure III-11**. The second type of texture (**Figure III-10 c-d**) consists of an array of nanopillars with rounded tops (hereafter designated by NP). These features are observed on surfaces submitted to a two-step treatment with processing parameters in the LIPSS formation range. In the first step, the surfaces were treated with 0.3 J/cm^2 and 192 laser pulses per point of the specimens' surface, while the second step was performed with lower fluence and number of pulses (0.10 J/cm^2 and 47, respectively). Taking into account the polarisation dependence of LIPSS, in the second step the polarisation direction was rotated by 90° in relation to the polarisation direction used in the first step treatment. The bottom diameter of the nanopillars was 747 ± 132 and 696 ± 88 nm for the cp Ti and Ti-6Al-4V alloy surfaces, respectively, and their maximum height 174 ± 41 and 228 ± 63 nm (**Figure III-11**). It is important to note that

significant redeposition of droplets occurred on both types of laser textured surfaces, with a larger amount of particles for the Ti-6Al-4V alloy.

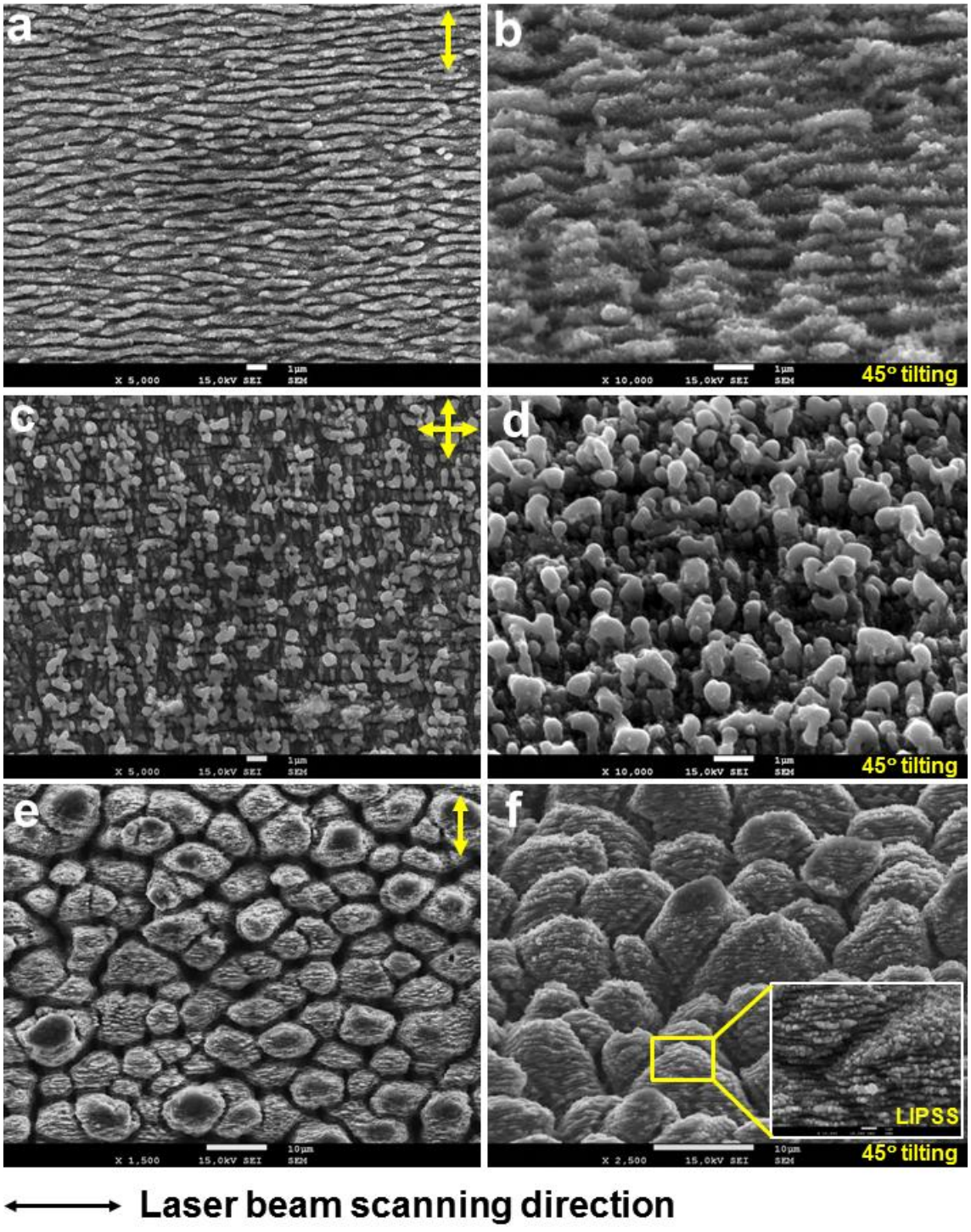

Figure III-10. High magnification SEM micrographs of the laser textured surfaces of Ti-6Al-4V alloy. Surface textures consist of LIPSS (a-b), NP (c-d), and MC-LIPSS (e-f). The inset micrograph in (f) shows LIPSS covering the top of microcolumns. The SEM micrographs in (b, d, and f) were acquired at 45° tilting. The yellow arrows indicate the polarisation direction of the linearly polarised laser beam. The radiation fluence and the repetition rate were in the ranges 0.2-0.8 J/cm^2 and 50-1000 Hz, respectively. The scale bar is 1 μm (a-d) and 10 μm (e-f).

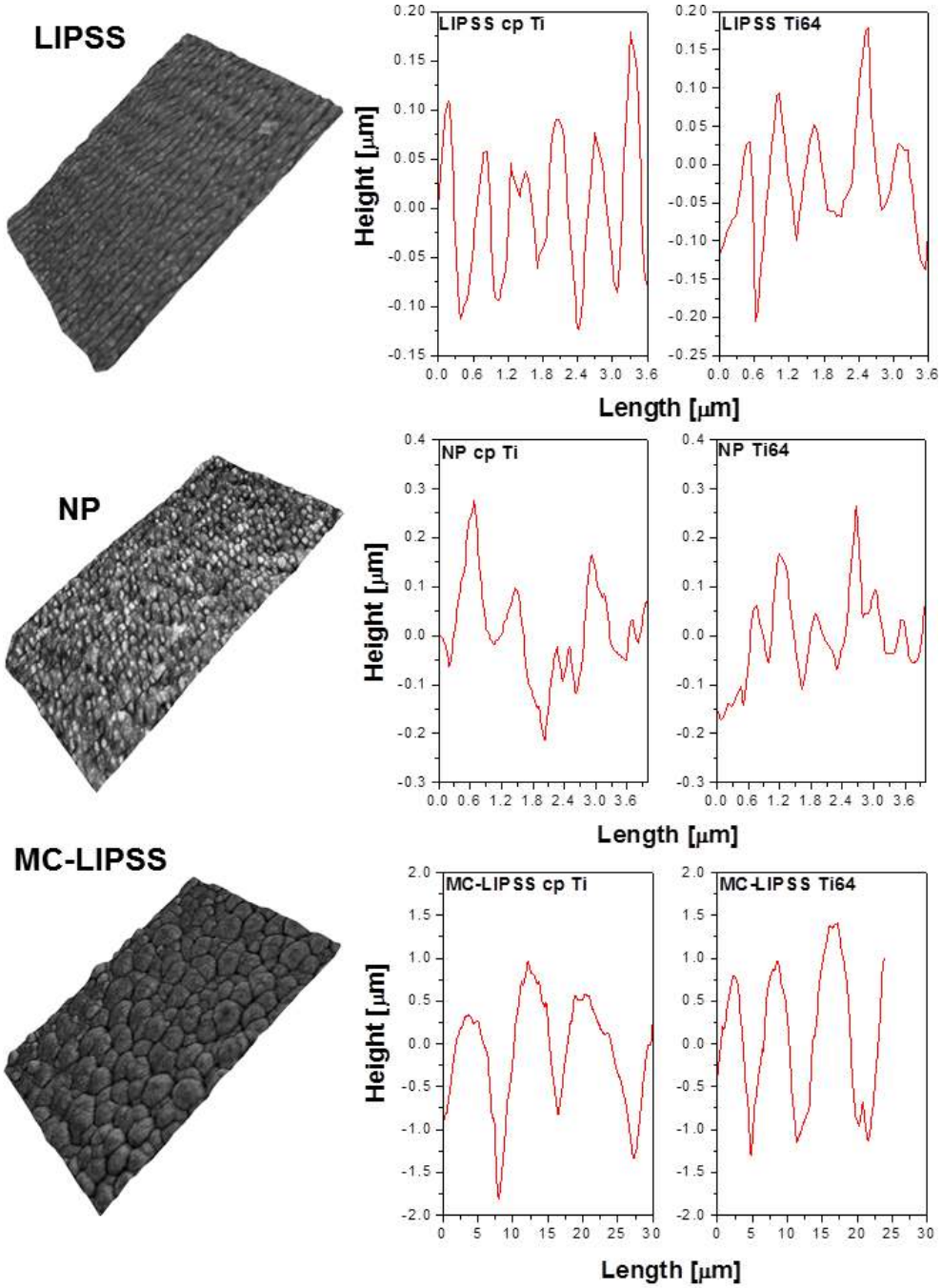

Figure III-11. Representative three-dimensional (3D) reconstruction (Digital Elevation Mode-DEM) and the corresponding 2D roughness profiles of the laser textured surfaces of both Ti alloys obtained from Alicona-MeX© software 2.0. The roughness profiles were taken in a direction perpendicular to the laser beam scanning direction indicated in Figure III-10.

The third type of texture (**Figure III-10 e-f**) consists of an array of microcolumns with a roughly elliptical cross-section, frequently covered with LIPSS (hereafter designated by MC-LIPSS). These microcolumns are observed on surfaces treated with 0.80 J/cm^2 and

1069 laser pulses. The length of the major and minor axis of the columns was 11 ± 2 and 8 ± 2 μm, and 10 ± 2 and 6 ± 1 μm for cp Ti and Ti-6Al-4V alloy, respectively. Their maximum height was 3 ± 1 and 4 ± 1 μm (**Figure III-11**). These columns are covered with LIPSS (inset micrograph in **Figure III-10 f**) with a similar periodicity and the same orientation as those depicted in **Figure III-10 a-b**, forming a bimodal surface roughness distribution.

The 2D roughness parameters (R_a, R_z, R_{Sk} and R_{Ku}) of these surfaces are given in **Table III-1**. These parameters were calculated from surface profiles taken in a direction perpendicular to the laser beam scanning direction, as indicated in **Figure III-10**. The parameters R_a and R_z indicate the arithmetic mean height and the maximum height (distance between the highest peaks and the lowest valleys), respectively, while the parameters R_{Sk} (Skewness) and R_{Ku} (Kurtosis) provide information about the distribution of heights of the surfaces, characterising their peakedness or sharpness. For a Gaussian surface R_{Sk} and R_{Ku} are equal to 0 and 3, respectively. These parameters are usually employed to distinguish surfaces with similar values of R_a [51, 267].

Table III-1. 2D Roughness parameters of the laser textured surfaces obtained from the three-dimensional (3D) surface reconstruction (Digital Elevation Mode-DEM) using Alicona-MeX© software 2.0. The roughness parameters were calculated from surface profiles taken in a direction perpendicular to the laser beam scanning direction indicated in Figure III-10.

CP TI SURFACES				
Textures	**R_a [μm]**	**R_z [μm]**	***R_{Sk}**	***R_{Ku}**
LIPSS	0.3 ± 0.1	1.5 ± 0.2	1.4 ± 0.1	2.3 ± 0.4
NP	0.3 ± 0.2	1.6 ± 0.8	1.5 ± 0.1	2.6 ± 0.4
MC-LIPSS	1.2 ± 0.1	5.3 ± 1.0	1.4 ± 0.1	2.1 ± 0.5
TI64 SURFACES				
Textures	**R_a [μm]**	**R_z [μm]**	***R_{Sk}**	***R_{Ku}**
LIPSS	0.3 ± 0.02	1.4 ± 0.1	1.4 ± 0.1	2.1 ± 0.3
NP	0.3 ± 0.1	1.3 ± 0.6	1.4 ± 0.1	2.1 ± 0.3
MC-LIPSS	1.1 ± 0.2	5.4 ± 0.7	1.5 ± 0.1	2.4 ± 0.4
*For a Gaussian surface, R_{Sk} = 0 and R_{Ku} = 3. For R_{Sk} > 0 and R_{Ku} > 3 the surface is said to consist of more and/or higher peaks than valleys.				

Both the R_a and R_z parameters are larger for surfaces textured with MC-LIPSS (1.1-1.2 and 5.3-5.4 μm, respectively) as compared to surfaces textured with LIPSS (0.3 and

1.4-1.5 μm, respectively) and NP (0.3 and 1.3-1.6 μm, respectively), but the differences were not statistically significative when comparing the same surface textures of the different Ti alloys. The R_{Sk} parameter is a measure of the asymmetry of a distribution probability, and when describing surface topography, a positive skewness ($R_{Sk} > 0$) represents elevations emerging from a relatively flat surface, whereas a negative skewness ($R_{Sk} < 0$) corresponds to wide plateaus eroded by deep valleys [268, 269]. The R_{Sk} values were in the range 1.4-1.5, indicating that the surfaces consist of more peaks than valleys. Surfaces with kurtosis above 3 ($R_{Ku} > 3$) present sharp peaks, whereas those with kurtosis below 3 ($R_{Ku} < 3$) have more rounded peaks with wider shoulders. The R_{Ku} values were in the range 2.1-2.6, indicating that the surfaces are composed with more rounded peaks than sharp ones. The differences in R_{Sk} and R_{Ku} were found to be independent of the surface textures and Ti alloy.

2.3. Surface Chemical Composition

The chemical composition of the surfaces of both Ti alloys was investigated by XPS before and after the laser treatment. **Figure III-12** presents XPS survey spectra of a polished surface and of the laser textured surfaces. All spectra present peaks corresponding to titanium, oxygen, and carbon. For the Ti-6Al-4V alloy, an Al peak is also observed, while the vanadium peaks are partially overlapped by the oxygen satellite peaks and cannot be distinguished in the spectra. In addition, peaks corresponding to Ti, O and C Auger electrons are also visible.

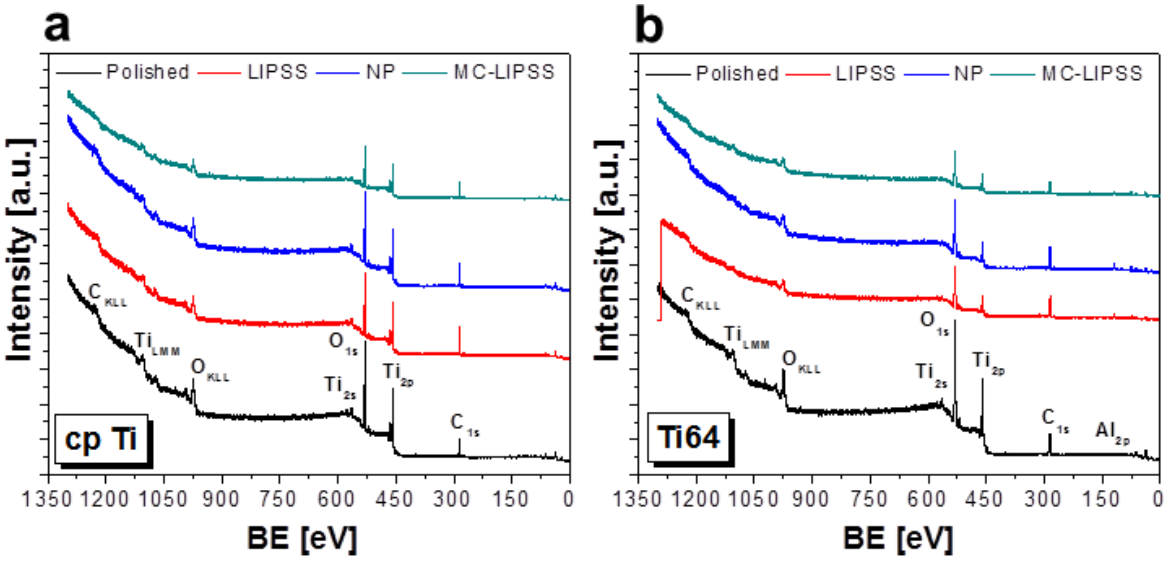

Figure III-12. XPS survey spectra for cp Ti (a) and Ti-6Al-4V alloy (b) surfaces.

In order to analyse in more detail the qualitative variations of the chemical composition, expanded views of the Ti 2p, O 1s, and Al 2p regions of the spectra are shown in **Figure III-13** and **Figure III-14**.

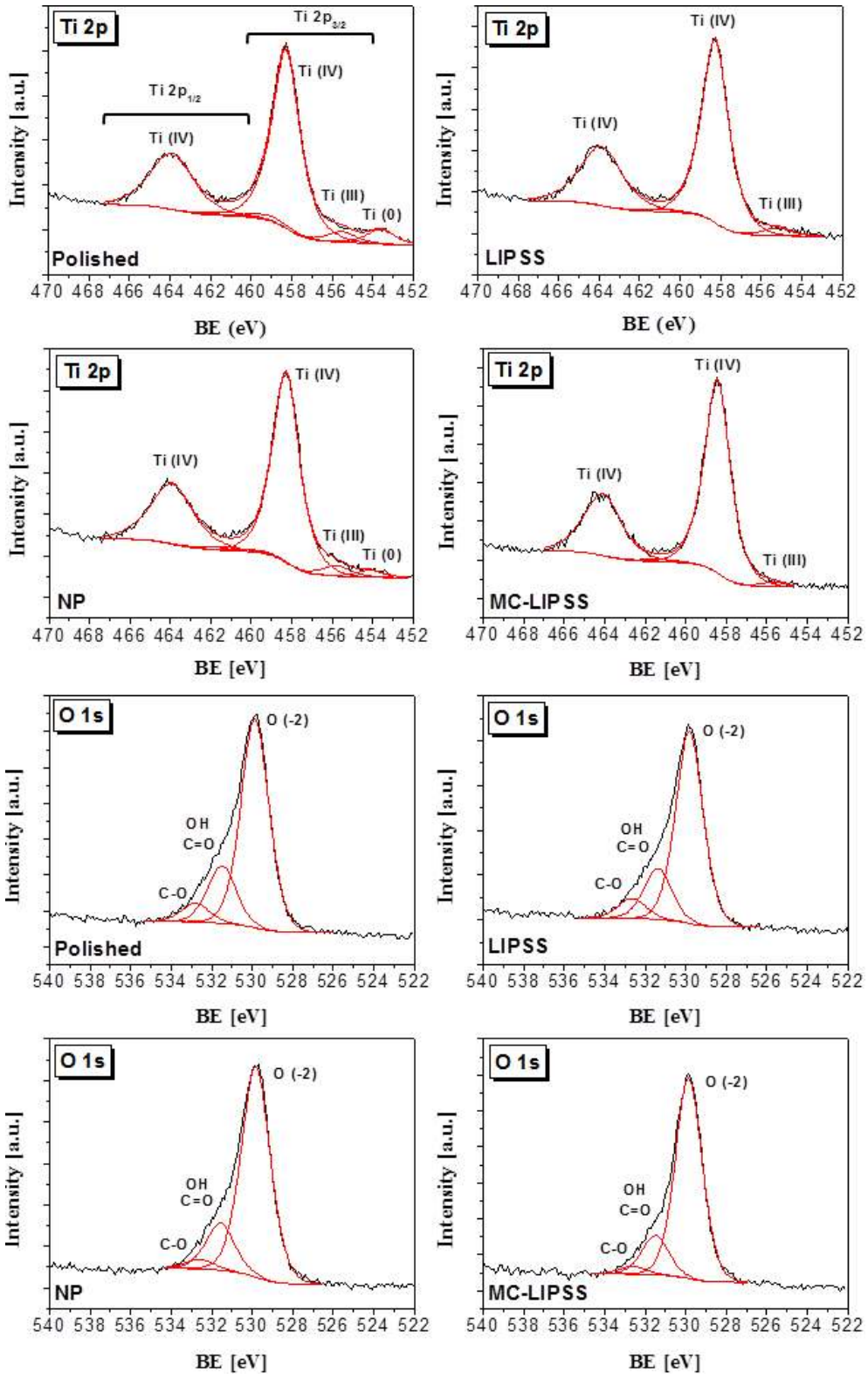

Figure III-13. Expanded views of the XPS spectra of the Ti 2p and O 1s regions for cp Ti surfaces.

Three Ti 2p doublets with a spin-orbit split of 5.7 ± 0.1 eV were fitted. The main component (Ti $2p_{3/2}$) of the major doublet is centred at 458.3 ± 0.1 and 458.5 ± 0.1 eV for the cp Ti and Ti-6Al-4V alloys, respectively, and assigned to Ti (IV) in Titania (TiO_2). A less intense doublet Ti $2p_{3/2}$ centred at 455.6 ± 0.2 and 455.8 ± 0.1 eV for the cp Ti and Ti-6Al-4V alloys, respectively, can be assigned to Ti (III) in Ti_2O_3. In addition, a component centred at 453.8 ± 0.2 eV can be assigned to metallic titanium Ti (0). This peak is observed in the spectra of the polished surface and NP textured surfaces of both alloys. Regarding the O 1s region, three components were found for all spectra at 529.9 ± 0.2, 531.5 ± 0.1, and 532.7 ± 0.3 eV, which can be assigned to oxide (O^{-2}), a mixture of hydroxyl (OH) and carbonyl groups (C = O), and oxygen singly bound to carbon (C – O), respectively. The C 1s region of the spectra (not shown) also confirmed the existence of C – O and C = O groups. In principle, these groups result from the solvents used for surface cleaning or from surface contamination by carbon-containing species. The evolution of the peaks components is similar for the Ti-6Al-4V and cp Ti alloys.

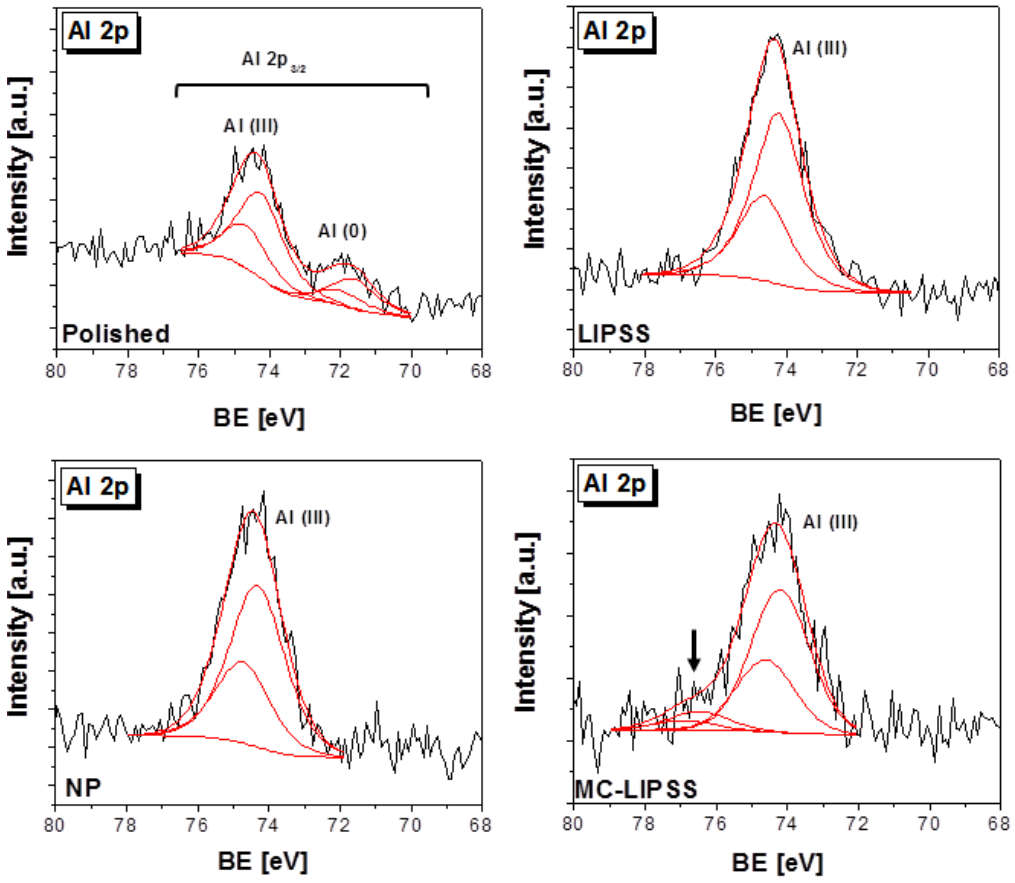

Figure III-14. Expanded views of the XPS spectra of the Al 2p region for Ti-6Al-4V alloy surfaces.

For the Ti-6Al-4V alloy, a doublet Al $2p_{3/2}$ with a split orbit-spin of 0.41 eV was observed. Its main component was centred at 74.3 ± 0.1 eV, and assigned to Al (III) in alumina (Al_2O_3). A doublet with the Al $2p_{3/2}$ component centred at 71.6 ± 0.1 eV was observed for the polished surface, and assigned to metallic aluminium (Al (0)). Finally, a low intensity doublet with the Al $2p_{3/2}$ component centred at 76.5 ± 0.1 eV (black arrow) was observed for MC-LIPSS textured surfaces, which can be assigned to aluminium bound to hydroxyl (OH) groups.

The atomic ratios obtained by XPS are summarised in **Table III-2**. In general, the laser treatment further oxidises the surfaces. The ratio Ti(0)/Ti(total) shows that the metallic titanium Ti (0) signal dissappears after the laser treatment, except for NP textured surfaces, where traces of Ti (0) can be still observed. The ratio Ti(IV)/Ti(total) indicates that the proportion of TiO_2 increases significantly after the laser treatment, while the Ti(III)/Ti(total) ratio shows a decrease in the proportion of Ti_2O_3, mainly for the MC-LIPSS textured surface. For the Ti-6Al-4V alloy an increase of the ratio Al/Ti is observed after the laser treatment, indicating the preferential oxidation of Al during the laser treatment, as compared to Ti.

Table III-2. XPS atomic ratios.

Ti alloy	Ratios	Surfaces			
		Polished	LIPSS	NP	MC-LIPSS
cp Ti	Ti(0)/Ti(total) x 100 [%]	7.2	-	3.3	-
	Ti(III)/Ti(total) x 100 [%]	5.2	4.2	5.1	2.2
	Ti(IV)/Ti(total) x 100 [%]	87.6	95.8	91.6	97.8
Ti64 alloy	Ti(0)/Ti(total) x 100 [%]	8.1	-	4.8	-
	Ti(III)/Ti(total) x 100 [%]	5.9	4.6	2.9	2.9
	Ti(IV)/Ti(total) x 100 [%]	86.0	95.4	92.3	97.1
	Al/Ti	0.8	1.2	1.1	0.9

Figure III-15 presents the μ-Raman spectra for cp Ti surfaces. Raman bands of TiO_2 around 144 (B_{1g}), 147 (E_g), 198 (B_{1g}; A_{1g}), 398 (B_{1g}), 515 (E_g), and 640 cm^{-1} (E_g) have been reported as a fingerprint of anatase (A), while those around 248 (second order phonon or scattering), 448 (E_g), 612 (A_{1g}), and 827 (B_{2g}) cm^{-1} correspond to rutile (R) [270, 271]. The spectra showed Raman bands corresponding to both TiO_2 polymorphs. For anatase, the bands around 144-147 and 198 cm^{-1} were observed for all the surfaces.

For rutile, only the band around 827 cm^{-1} was not observed for the laser textured surfaces. In addition, the bands around 248 and 344 cm^{-1} (wide shoulder) could be also assigned to Ti_2O_3 active modes. Broadening of Raman bands was verified for all the surfaces, but it is less intense and defined for polished surfaces as compared to that for the laser textured surfaces. The bands were more intense and defined for MC-LIPSS textured surfaces. Finally, it is noteworthy that the spectra were acquired on different locations of the laser textured surfaces. The detection of Raman bands corresponding to anatase and rutile were dependent on the analysed region, indicating that the laser-induced oxide layer may be discontinuous and/or varies significantly in thickness.

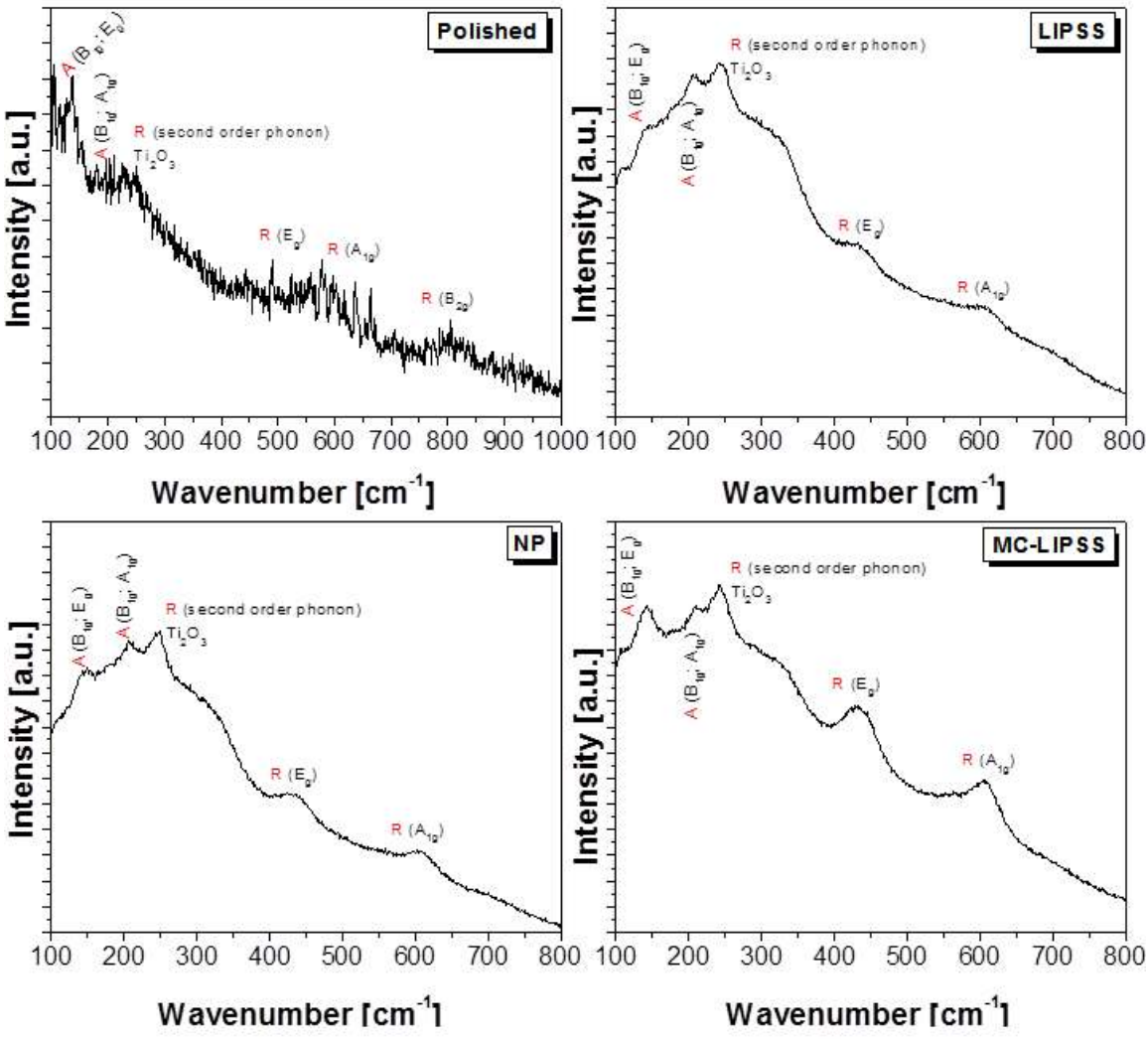

Figure III-15. μ-Raman spectra for cp Ti surfaces. A and R denote the TiO_2 polymorphs anatase and rutile, respectively. The assigned active modes are presented in parentheses.

Figure III-16 presents the μ-Raman spectra for Ti-6Al-4V alloy surfaces. The TiO_2 Raman bands were observed as for cp Ti surfaces. Nevertheless, the anatase band around 198 cm^{-1} was absent, and the rutile band around 827 cm^{-1} appeared as a weak shoulder for MC-LIPSS textured surfaces, as compared to that of polished surface. The rutile bands around 448 and 612 cm^{-1} appeared much less intense for LIPSS textured surfaces. For NP textured surfaces, the anatase and rutile bands were not clearly verified. The broadening of the Raman bands was similar to that verified for cp Ti surfaces. No Raman bands corresponding to Alumina (Al_2O_3) were observed.

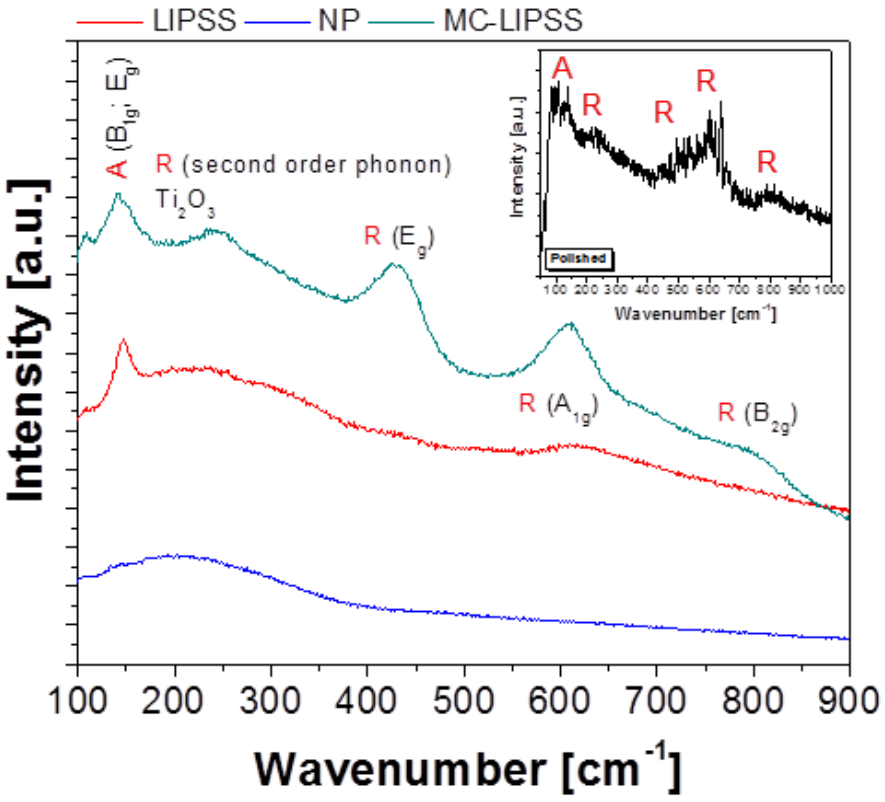

Figure III-16. μ-Raman spectra for Ti-6Al-4V alloy surfaces. A and R denote the TiO_2 polymorphs anatase and rutile, respectively. The assigned active modes are presented in parentheses. The inset graphic shows the spectrum of the polished surface.

2.4. Crystallographic Structure

The crystallographic structure of the surfaces was investigated by means of both Bragg-Brentano and glancing incidence X-ray diffraction (XRD). The X-ray diffractograms for cp Ti surfaces obtained by Bragg-Brentano geometry and glancing incidence are given in **Figure III-17** and **Figure III-18**, respectively. The diffraction

peaks obtained were compared with the Powder Diffraction Files (PDF) of the International Centre for Diffraction Data (ICDD) database.

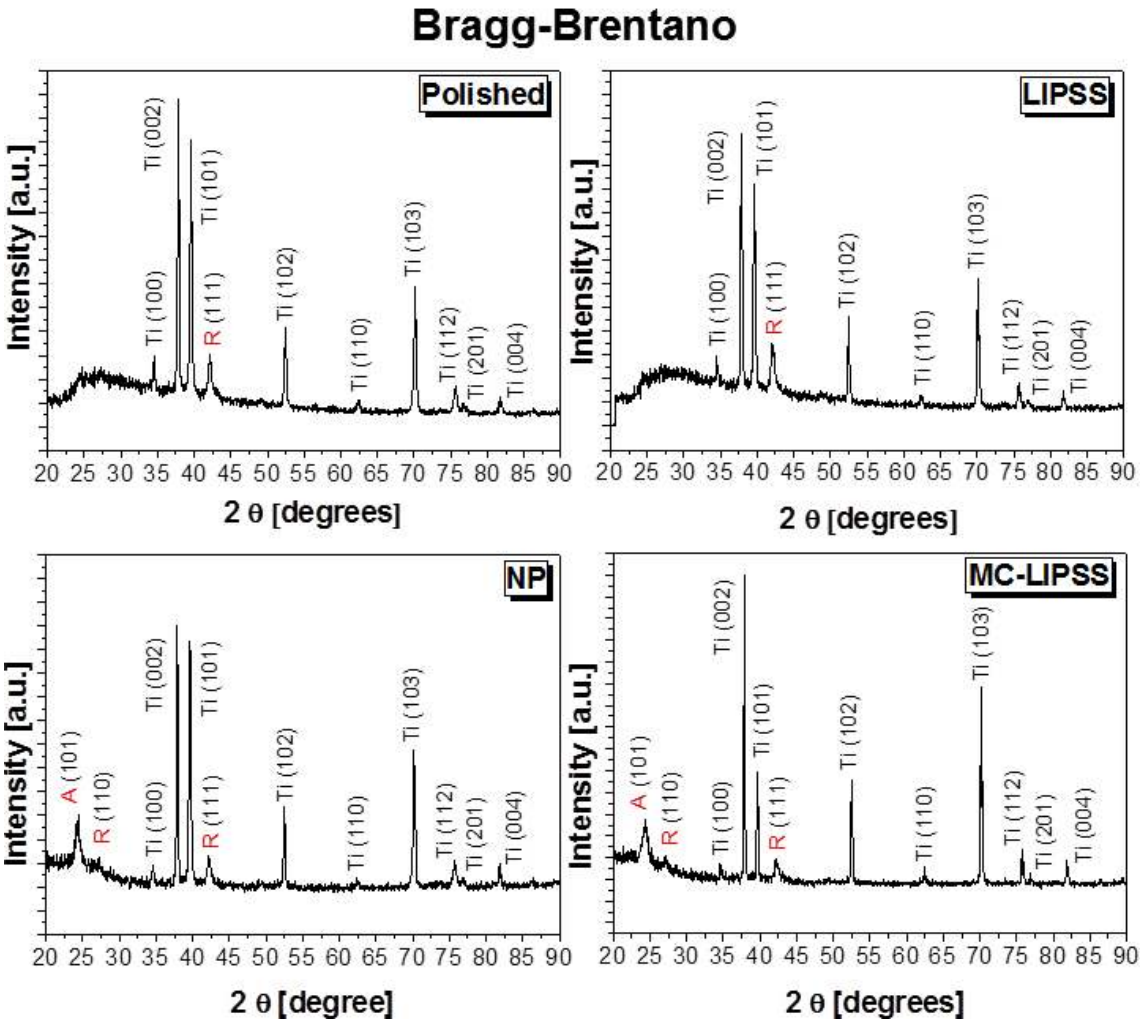

Figure III-17. X-ray diffractograms for cp Ti surfaces obtained by Bragg-Brentano geometry. A and R denote the TiO_2 polymorphs anatase and rutile, respectively.

Diffraction peaks referent to the (100), (002), (101), (102), (110), (103), (112), (201), and (004) crystallographic planes of the hcp structure of the α-phase of Ti were observed on all surfaces. A diffraction peak referent to the (111) crystallographic plane of rutile was observed for all the surfaces, except for polished surfaces when glancing incidence is carried out. Diffraction peaks referent to the (101) and (110) crystallographic planes of anatase and rutile, respectively, were observed for NP and MC-LIPSS textured surfaces when Bragg-Brentano geometry is used.

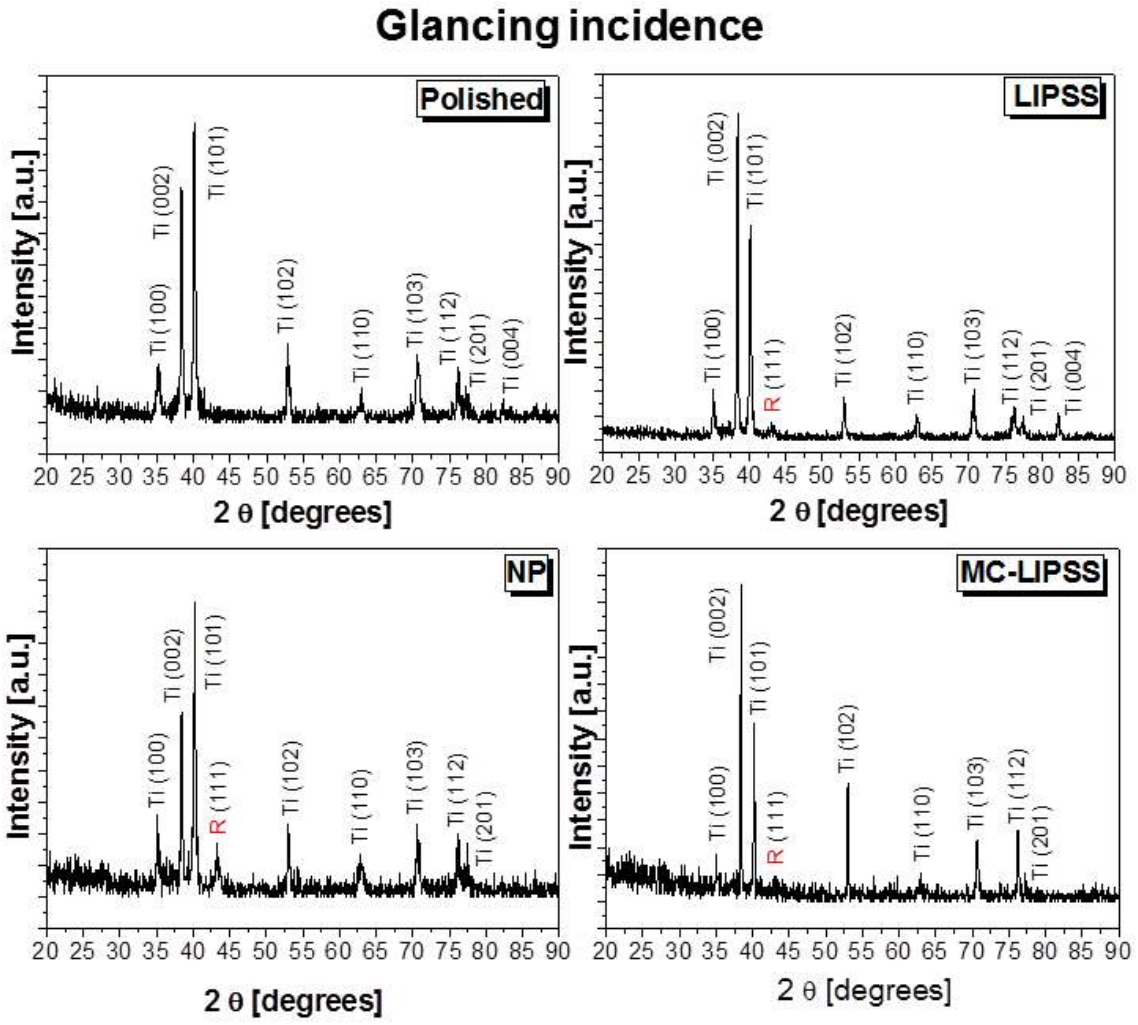

Figure III-18. X-ray diffractograms for cp Ti surfaces obtained by glancing incidence. A and R denotes the TiO_2 polymorphs anatase and rutile, respectively.

2.5. Wettability

Surface wettability was evaluated by the sessile drop method. The time evolution of the contact angle for water and HBSS droplets on polished and laser textured surfaces of Ti-6Al-4V alloy is presented in **Figure III-19** [98]. The polished surfaces presented a time-independent hydrophilic behaviour and a high affinity for HBSS, with negligible variation between the initial and final contact angle (1.3 and 7.2° for water and HBSS after 600 s of contact, respectively). These surfaces were wetted by both liquids and the equilibrium contact angles were similar for the two liquids (68.0 and 63.4◦ for DD water and HBSS after 600 s of contact, respectively). On the contrary, the contact angle on laser textured surfaces presented a time-dependent behaviour, with significant variation

during the 600 s contact time (13.3-27.5° and 24.7-34.8° for water and HBSS after 600 s of contact, respectively). At t = 0 s all surfaces except those with MC-LIPSS texture (**Figure III-19 a**) are wetted by water (contact angle < 90°). HBSS wetted all laser textured surfaces, including those with MC-LIPSS texture (**Figure III-19 b**). The best wetting for both liquids was achieved for LIPSS textured surfaces, with equilibrium contact angles of 43.4° and 21.9° for water and HBSS, respectively. Surfaces with NP and MC-LIPSS textures presented a wetting behaviour similar to the polished surface, with equilibrium contact angles of 56.2 and 76.2° for water and 61.8 and 47.6° for HBSS, respectively.

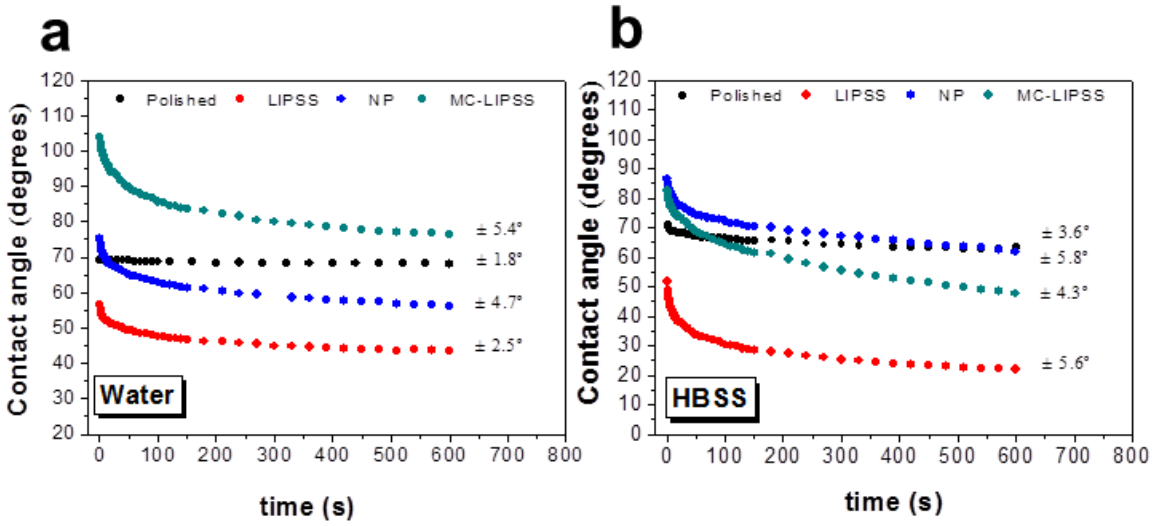

Figure III-19. Time evolution of the contact angle for DD water (a) and HBSS (b) droplets on polished and laser textured surfaces of Ti-6Al-4V alloy. The presented values were measured based on the droplet profiles taken in a direction perpendicular to the laser beam scanning direction (Figure III-10).

The drop spreading kinetics for both liquids on the laser textured surfaces was evaluated for the Ti-6Al-4V alloy, because the wetting behaviour was clearly time-dependent, as previously mentioned. For this purpose, a regression analysis was performed by fitting the function $\theta_{static}(t) = kt^n$, where k and n are constants, to the experimental data (see Section 1.4. in Chapter II). Special attention was given to the value of the spreading coefficient (n), which provides information on the surface drop spreading velocity (**Table III-3**).

Table III-3. Spreading coefficient (n) calculated by fitting of the experimental data with a power function θ_{static} (t) = kt^n. The presented values were measured from droplet profiles taken in a direction perpendicular to the laser beam scanning direction (Figure III-10).

TEXTURES (TI64 ALLOY)	DD WATER		HBSS	
	n	R^2	n	R^2
LIPSS	-0.04	0.99	-0.1	0.98
NP	-0.05	0.97	-0.05	0.97
MC-LIPSS	-0.05	0.97	-0.09	0.92

The function fitted well the experimental data, with correlation coefficients (R^2) in the range 0.92-0.99. HBSS droplets spread faster than water on all laser textured surfaces, except NP textured surfaces, where no significant difference was observed. The spreading velocity of water is similar on all laser textured surfaces ($|n| \sim 0.05$), while the spreading velocity of HBSS is significantly higher on surfaces textured with LIPSS ($|n| = 0.1$) and MC-LIPSS ($|n| = 0.09$) surfaces.

The anisotropy of the LIPSS textured surfaces induced an anisotropic wetting behaviour with both testing liquids, the droplets spreading mainly in the LIPSS direction (**Figure III-20**). The equilibrium contact angles were 43.4 and 21.9° for water and HBSS (**Figure III-20 a**), respectively, when the droplets were imaged perpendicularly to the LIPSS (**Figure III-20 b**), and 58.2 and 83.2° (**Figure III-20 a**) when they were observed parallell to them (**Figure III-20 c**). This effect of surface anisotropy was more prominent for HBSS than for water dropltes ($\Delta\theta$ = 61.3° and 14.8° for HBSS and water, respectively).

The time evolution of the contact angle for water on polished and laser textured surfaces of cp Ti was also evaluated (**Figure III-21**) in order to verify potential differences in the wetting behaviour in comparison with that observed for the Ti-6Al-4V alloy surfaces. The behaviour was hydrophilic for all the surfaces, with two main differences: (a) first, the contact angles were lower (< 50°), showing that the wettability of water is significantly increased on all the surfaces, mainly for the laser textured surfaces; (b) second, all the surfaces present a time-independent wetting behaviour, with negligible variation of contact angle (1.3 to 5.9° after 600 s of contact).

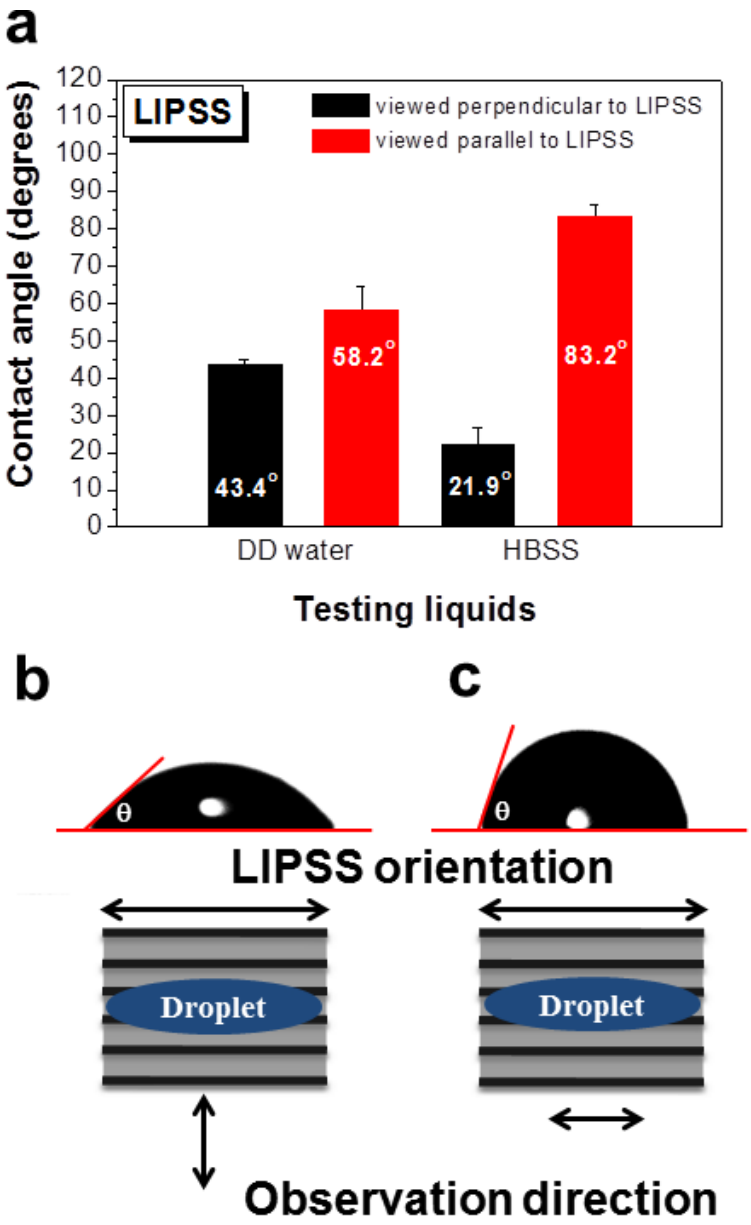

Figure III-20. Anisotropic wetting of DD water and HBSS droplets on LIPSS textured surfaces. Contact angle values measured for both testing liquids viewed perpendicularly and parallelly to LIPSS orientation (a). Representative droplet profiles for both liquids when viewed perpendicularly (b) and parallelly (c) to LIPSS orientation.

The polished surfaces presented an equilibrium contact angle of 48.2°, while the LIPSS, NP, and MC-LIPS textured surfaces showed equilibrium contact angles of 12.6, 32.1, and 21.8°, respectively. Once more, the LIPSS textured surfaces presented the best wetting, while water wets better MC-LIPSS textured surfaces than those with a NP texture. Wetting was anisotropic for water on LIPSS textured surfaces, but much less than for the Ti-6Al-4V alloy. The wettability of HBSS on cp Ti surfaces was not

evaluated, but taking into account the higher hydrophilicity of cp Ti and the faster spreading of HBSS droplets on the Ti-6Al-4V alloy surfaces, one can be stated that the cp Ti surfaces could potentially present a high affinity to HBSS or even better than that observed for the Ti-6Al-4V alloy surfaces.

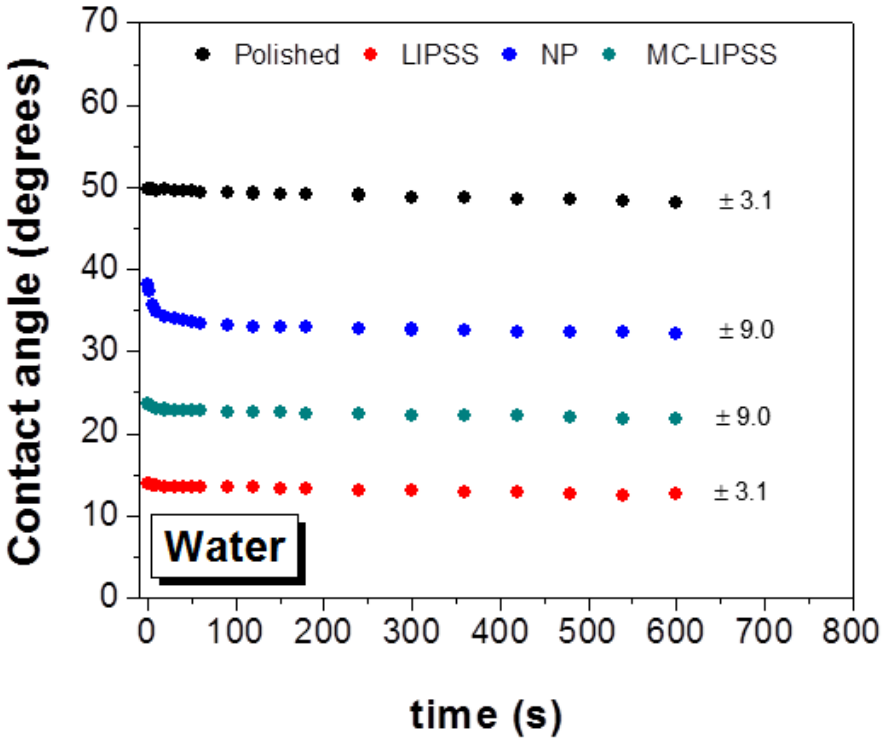

Figure III-21. Time evolution of the contact angle for DD water droplets on polished and laser textured surfaces of cp Ti. The presented values were measured based on the droplet profiles taken in a direction perpendicular to the laser beam scanning direction (Figure III-10).

The surface free energy (γ_{SV}) of the surfaces, calculated by using the geometric mean approach combined with the method of Owens and Wendt (see **Eq. II-14** in Section 1.4. of Chapter II), are given in **Table III-4**. The equilibrium contact angles of water and diiodomethane measured experimentally and the surface tension of both liquids (γ_{LV}) are summarised in **Table III-5**. The γ_{SV} was higher on cp Ti surfaces (54.7-74.5 mN/m) than that of Ti-6Al-4V alloy surfaces (42.3-50.0 mN/m). The γ_{SV} of the laser textured surfaces was significantly higher as compared to that of the polished surfaces. These findings fairly agree with the enhanced hydrophilicity of the laser textured surfaces of cp Ti in comparison with that of Ti-6Al-4V alloy. The highest values of γ_{SV} were found for LIPSS and MC-LIPSS textured surfaces, while those

found for NP textured surfaces were similar to the polished surfaces. Both the γ_{SV}^{p} and γ_{SV}^{d} also increased for the laser textured surfaces, except the γ_{SV}^{p} and γ_{SV}^{d} of the MC-LIPSS (Ti-6Al-4V alloy) and the NP surfaces, respectively.

Table III-4. Surface free energy (γ_{SV}) of the surfaces of both Ti alloys calculated by using the geometric mean approach combined with the method of Owens and Wendt. The polar (γ_{SV}^{p}) and dispersive (γ_{SV}^{d}) components are also given.

CP Ti	γ_{SV} [mN/m]	γ_{SV}^{p} [mN/m]	γ_{SV}^{d} [mN/m]
Polished	54.7 ± 2.1	22.6 ± 2.4	32.1 ± 0.6
LIPSS*	74.5 ± 1.0	33.2 ± 1.2	41.3 ± 0.4
NP	62.3 ± 5.2	36.6 ± 6.1	25.6 ± 1.2
MC-LIPSS	73.1 ± 3.1	30.3 ± 3.5	42.8 ± 0.5
Ti64 ALLOY	**γ_{SV} [mN/m]**	**γ_{SV}^{p} [mN/m]**	**γ_{SV}^{d} [mN/m]**
Polished	42.3 ± 0.7	11.9 ± 0.6	30.3 ± 0.8
LIPSS*	50.0 ± 2.5	15.4 ± 2.5	34.6 ± 1.6
NP	43.7 ± 1.2	16.3 ± 1.3	27.5 ± 0.8
MC-LIPSS	49.4 ± 1.0	1.5 ± 1.5	47.9 ± 0.9
*The surface free energy is the average of the values measured in both directions (perpendicular and parallel to the laser beam scanning direction).			

Table III-5. Equilibrium contact angles of water and diiodomethane measured experimentally, and the surface tension (γ_{LV}) of both liquids and their polar (γ_{LV}^{p}) and dispersive (γ_{LV}^{d}) components [253].

EQUILIBRIUM CONTACT ANGLES [°]					
cp Ti	**Water**	**Diiodomethane**	**Ti64 alloy**	**Water**	**Diiodomethane**
Polished	48.2 ± 3.1	43.7 ± 0.7	Polished	67.1 ± 0.6	49.8 ± 1.3
LIPSS*	15.5 ± 3.1	15.8 ± 1.6	LIPSS*	57.9 ± 3.2	40.1 ± 2.8
NP	32.1 ± 9.0	54.3 ± 1.6	NP	61.9 ± 1.5	54.2 ± 1.2
MC-LIPSS	21.8 ± 9.0	8.4 ± 0.9	MC-LIPSS	82.6 ± 6.8	6.6 ± 1.9
SURFACE TENSION [mN/m]					
Water			**Diiodomethane**		
γ_{LV}	**γ_{LV}^{p}**	**γ_{LV}^{d}**	**γ_{LV}**	**γ_{LV}^{p}**	**γ_{LV}^{d}**
72.0	50.7	21.3	49.4	0.4	49.0
*The equilibrium contact angles for water and diiodomethane are the average of the values measured in both directions (perpendicular and parallel to the laser beam scanning direction).					

Chapter III. Results

2.6. Summary

The major results presented in Sections 2.1.-2.5. of Chapter III are summarised as follows:

(a) By controlling the laser processing parameters such as the radiation fluence and number of laser pulses, specific surface textures at both the nano- and the microscale can be reproducibly produced on Grade 2 Ti (cp-commercially pure) and Grade 5 Ti-6Al-4V alloy;

(b) These textures can be classified in the follow types: (a) laser-induced periodic surface structures-LIPSS; (b) arrays of nanopillars (NP); (c) arrays of microcolumns covered with LIPSS (MC-LIPSS), forming a bimodal roughness distribution;

(c) The laser textured surfaces present roughness parameters in the ranges 0.3-1.2 μm (R_a) and 1.6-5.4 (R_z) μm.

(d) The laser treatment, carried out in air, oxidises the surface of the materials. XPS analyses show that the most abundant oxide present in the surfaces is titania (TiO_2), but a significant amount of alumina (Al_2O_3) is also present on laser textured surfaces of Ti-6Al-4V. μ-Raman spectroscopy and XRD indicate that anatase and rutile are the TiO_2 polymorphs present;

(e) The laser textured surfaces of both Ti alloys present enhanced wettability on water and Hank's balanced salt solution as compared to polished surfaces, mainly for cp Ti surfaces;

(f) The laser treatment increases significantly the surface free energy of the surfaces, mainly for cp Ti surfaces;

(g) The LIPSS textured surfaces induce anisotropic wetting.

2.7. Human Mesenchymal Stem Cells Behaviour

In this section, the spreading, shape, adhesion, collective cytoskeleton organisation, proliferation, commitment, and differentiation of hMSCs on the different surfaces of both Ti alloys are analysed. Cell spreading, shape, and adhesion were investigated at 24 h after cell seeding, while collective cytoskeleton organisation, proliferation and commitment, and differentiation were assessed, 2 and 4 weeks after cell seeding, respectively.

2.7.1. Cell Spreading and Shape (after 24 h of cell culture)

Cell spreading (growth) and shape were studied by staining of F-actin fibres and cell nucleus using Alexa Fluor® 488 *phalloidin* and 4',6-diamidino-2-phenylindole (DAPI), respectively. Phalloidin is a toxin that specifically binds to the F-actin subunits, maintaining them together and preventing their depolymerisation, while DAPI binds to the DNA (genetic code) present in the nucleus of eukaryotic cells. Representative low magnification fluorescence images of MSCs on the surfaces of both Ti alloys at 24 h after cell seeding are shown in **Figure III-22**. These images allow detecting cell growth and spreading. MSCs growth and spreading were more significant on Ti-6Al-4V alloy surfaces (**Figure III-22 e-h**) than on those of cp Ti (**Figure III-22 a-d**). MSCs spreading is also higher on polished surfaces than on laser textured surfaces. Cell spreading was quantitatively assessed by calculating the average cell area (**Figure III-23**). The average cell area was larger on polished surfaces (~ 12500 and 31000 μm^2 for cp Ti and Ti-6Al-4V alloy, respectively) than on laser textured surfaces (~ 4000 and 9000 μm^2 for cp Ti and Ti-6Al-4V alloy, respectively), indicating a 3.5- and 2-fold increase in cell spreading, respectively. The average cell area on NP textured surfaces (~ 4500 and 13000 μm^2 for cp Ti and Ti-6Al-4V alloy, respectively) was slightly larger than on surfaces textured with LIPSS and MC-LIPSS, but the difference is not statistically significative.

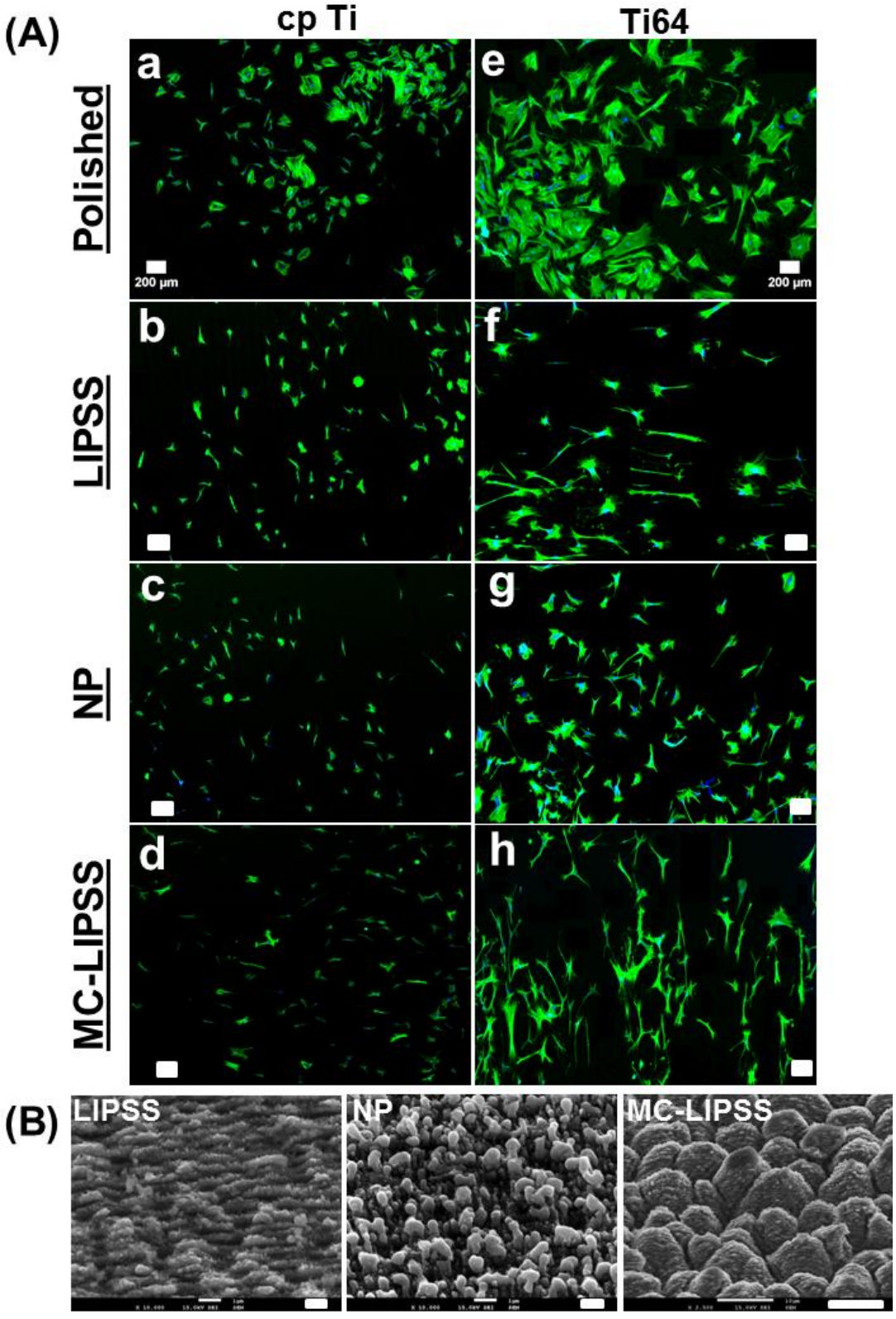

Figure III-22. (A) Representative low magnification fluorescence images of MSCs on the surfaces of both Ti alloys at 24 h after cell seeding. Polished (a and e), LIPSS (b and f), NP (c and g), and MC-LIPSS (d and h) surfaces. F-actin fibres (Alexa Fluor® 488 *phalloidin*) and cell nucleus (DAPI) were stained green and blue, respectively. The scale bar is 200 µm. (B) SEM micrographs of the corresponding surface textures are also showed (see Figure III-10). The scale bar is 1 µm (LIPSS and NP) and 10 µm (MC-LIPSS).

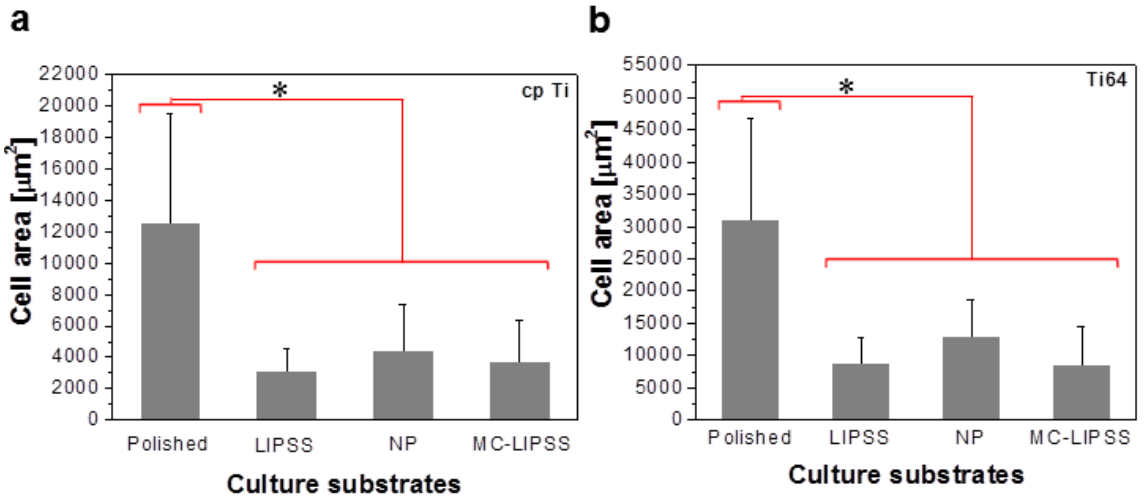

Figure III-23. Quantification of MSCs spreading by analysing the average cell area on the cp Ti (a) and Ti-6Al-4V alloy (b) surfaces at 24 h after cell seeding. Statistical analysis was performed using ANOVA and Tukey's test. ∗ indicates statistically significant differences between the average values ($p < 0.05$). At least 50 cells were analysed for each type of surface.

The shape changes of MSCs as well as the presence of cell membrane extensions (filopodia) were also investigated. Representative high magnification fluorescence images of stained F-actin fibres and nuclei of MSCs cultured on cp Ti surfaces are presented in **Figure III-24**. These images are representation of the MSCs shapes observed on the different types of surface for both Ti alloys. Cell shape and filopodia formation were strongly affected by the distinct surface topographies. MSCS cultured on polished surfaces (**Figure III-24 a-c**) spread uniformly in all directions, and the amount of filopodia in the cytoskeleton edges is negligible. On the contrary, the spreading of MSCs on LIPSS and MC-LIPSS textured surfaces is anisotropic (yellow arrows indicate the cell stretching direction) (**Figure III-24 d-f** and **j-l**), and the amount of filopodia in the leading edge of the stretched cells increases. Finally, cells cultured on NP textured surfaces do not stretch significantly and present long filopodia structures (yellow arrow-heads) distributed around their outer edge (**Figure III-24 g-i**). MSCs shape and the amount and location of filopodia were quite similar for cells cultured on Ti-6Al-4V alloy surfaces (not shown). Cell stretching was quantitatively evaluated by calculating the cell elongation factor (**Figure III-25**). A 7-8 fold increase was found for cells cultured on the LIPSS (~ 14) and MC-LIPSS (~ 11) textured surfaces in comparison with those cultured on the polished (~ 1.7) and NP textured surfaces (~ 1.7).

The average stretching was slightly larger on LIPSS textured surfaces in comparison with MC-LIPSS surfaces for Ti-6Al-4V (**Figure III-25 b**).

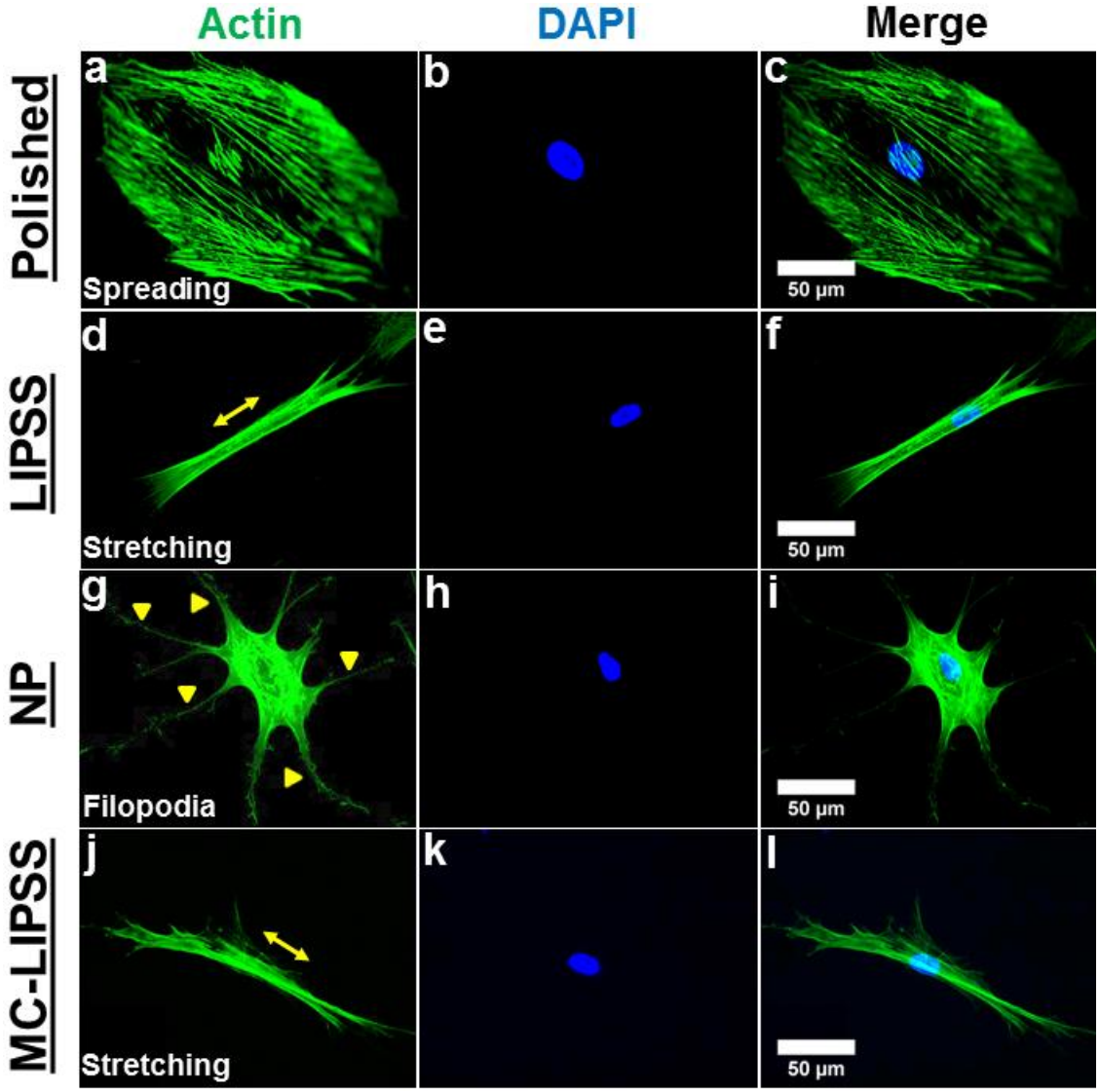

Figure III-24. Representative high magnification fluorescence images of MSCs shape on cp Ti surfaces at 24 h cell seeding. Polished (a-c), LIPSS (d-f), NP (g-i), and MC-LIPSS (j-l) surfaces. F-actin fibres and cell nucleus were stained green and blue, respectively. The yellow arrows and arrow-heads (d and j, and g) indicate the cell stretching direction and filopodia structures, respectively. Similar MSCs shapes were observed for Ti-6Al-4V alloy surfaces. The scale bar is 50 µm. The corresponding surface textures are presented in Figure III-10.

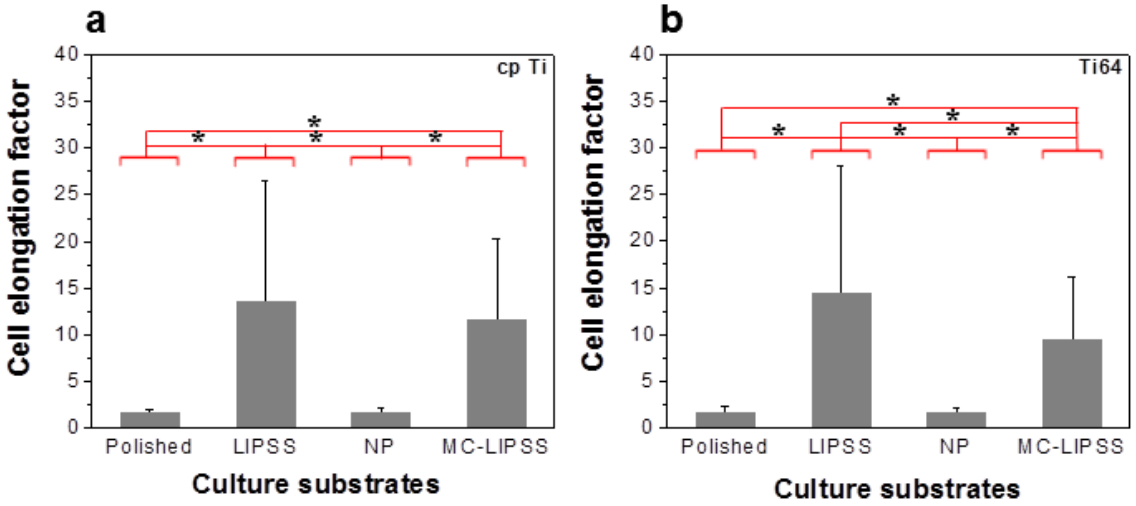

Figure III-25. Quantification of the average MSCs stretching by analysing the cell elongation factor on the cp Ti (a) and Ti-6Al-4V alloy (b) surfaces at 24 h after cell seeding. Statistical analysis was performed using ANOVA and Tukey's test. ∗ indicates statistically significant differences between the average values ($p < 0.05$). At least 20 cells were analysed for each type of surface.

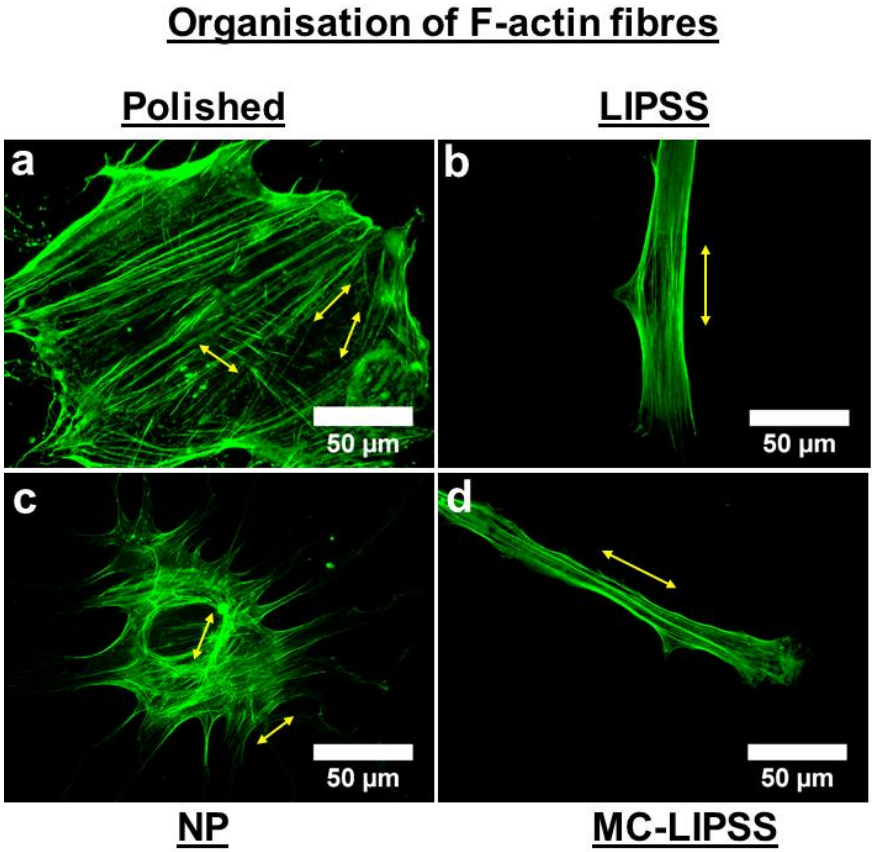

Figure III-26. Representative high magnification fluorescence images showing the F-actin fibres filaments organisation on the Ti-6Al-4V alloy surfaces at 24 h after cell seeding. Polished (a), LIPSS (b), NP (c), and MC-LIPSS (d) surfaces. F-actin fibres filaments were stained green. Similar organisation of the F-actin fibres filaments was observed for the cp Ti surfaces. The scale bar is 50 µm. The corresponding surface textures are presented in Figure III-10.

The organisation of the F-actin fibres filaments depends on the surface topography as well (**Figure III-26)**. The F-actin fibres filaments of MSCs cultured on polished surfaces of Ti-6Al-4V alloy were randomly oriented (yellow arrows) (**Figure III-26 a**). Conversely, those of cells cultured on LIPSS (**Figure III-26 b**) and MC-LIPSS (**Figure III-26 d**) textured surfaces were preferentially oriented parallel to the cytoskeleton stretching direction. Finally, the F-actin fibres filaments of cells cultured on NP laser textured surfaces (**Figure III-26 c**) were randomly oriented. The organisation of the F-actin fibres filaments was quite similar for MSCs cultured on cp Ti surfaces (not shown).

2.7.2. Cell Adhesion (after 24 h of cell culture)

MSCs adhesion was quantitatively investigated by calculating the average cell density (see Section 1.5.3. of Chapter II) and by immunostaining of vinculin, which is one of the several intracellular proteins involved in cell adhesion. It binds to integrins (intercellular adhesion proteins), inducing the formation of focal adhesions (FAs) (see Section 8.3. of Chapter I). The average cell density was in the range 1300-1500 cells/cm^2 for most surfaces of both Ti alloys (**Figure III-27 a-b)**, except for the LIPSS and NP textured surfaces of cp Ti (**Figure III-27 a**), which present values of 1900 and 1100 cells/cm^2, respectively, but the difference is not statistically significative.

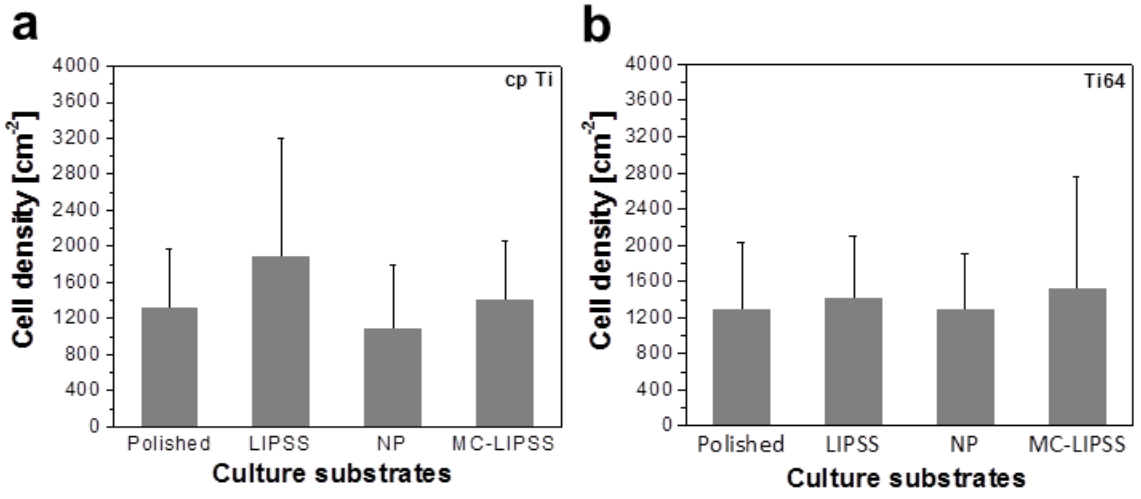

Figure III-27. Quantification of MSCs adhesion by analysing the average cell density on cp Ti (a) and Ti-6Al-4V alloy (b) surfaces at 24 h after cell seeding. Statistical analysis was performed using ANOVA and Tukey's test. There is no statistically significant differences among the average values. At least 10 low magnification images were used for estimation of the cell density.

High magnification fluorescence images of stained vinculin in MSCs cultured for 24 h on cp Ti surfaces are shown in **Figure III-28**. To demonstrate the specific interaction between vinculin (primary antibody) and the Alexa Fluor ® 568 (secondary antibody), a negative control was prepared by staining the cells only with Alexa Fluor ® 568. The focal adhesions (FAs) were not observed and only a background was verified around the cell nucleus. On the contrary, when vinculin is conjugated with Alexa Fluor ® 568, FAs (white squares) were clearly observed on cells cultured on all the surfaces. Both the amount and distribution of FAs were significantly affected by the surface topography. It seems that there is more FAs for cells cultured on polished surfaces (**Figure III-28 b**) as compared to laser textured surfaces (**Figure III-28 c, e,** and **g**). For polished surfaces, FAs were distributed around the edges of the cytoskeleton as well as near the cell nucleus. In contrast, for cells cultured on LIPSS (**Figure III-28 c**) and MC-LIPSS (**Figure III-28 g**) textured surfaces, FAs concentrated at the leading edge of the stretched cytoskeleton, close to the filopodia structures. The cells cultured on NP textured surfaces (**Figure III-28 e**) presented a slightly higher number of FAs localised in the filopodia and at the edges of the cytoskeleton. High magnification fluorescent images of the FAs (zoomed FAs) on Ti-6Al-4V alloy surfaces are depicted in **Figure III-28 b, d, f,** and **h**. FAs presented an elongated shape (yellow arrow-heads) for all surface topographies and no focal complexes (dot-like structures) were observed, indicating maturation of FAs. The average FAs area is given in **Figure III-29**. Their area is significantly larger for cells cultured on polished surfaces as compared to laser textured surfaces. Average FAs areas of about 2.8 and 3.7 μm^2 were found for the polished surfaces of cp Ti (**Figure III-29 a**) and Ti-6Al-4V alloy (**Figure III-29 b**), respectively. For the laser textured surfaces of cp Ti and Ti-6Al-4V alloy they varied in the ranges 0.8-0.9 μm^2 and 1.1-1.6 μm^2, respectively. Among the Ti-6Al-4V textured surfaces, the FAs area for cells cultured on MC-LIPSS surfaces was slightly larger than those of cells cultured on LIPSS and NP surfaces, but the difference is not statistically significative.

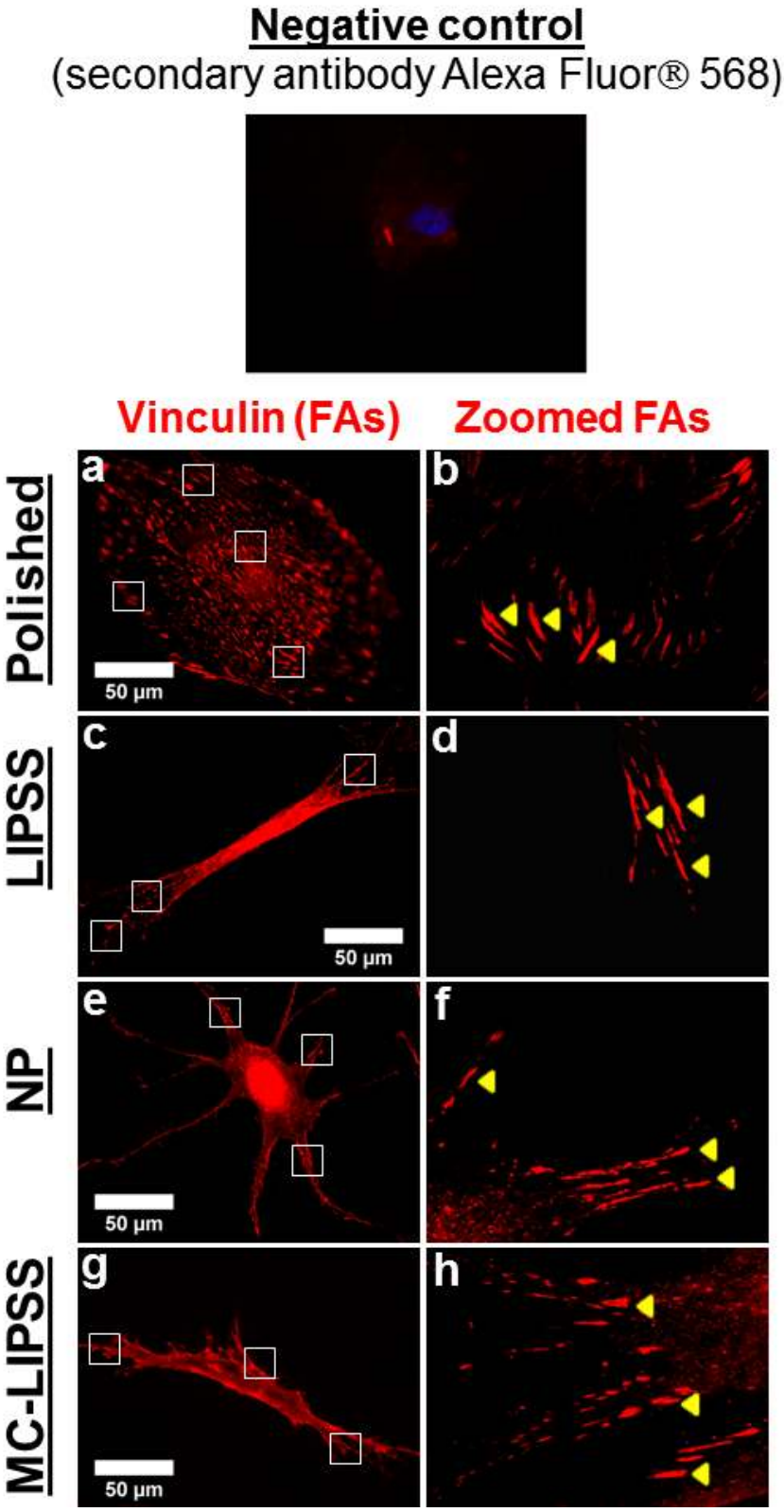

Figure III-28. Representative high magnification fluorescence images of vinculin showing the FAs (white squares) for both Ti alloys surfaces at 24 h after cell seeding. Polished (a-b), LIPSS (c-d), NP (e-f), and MC-LIPSS (g-h) surfaces. Vinculin and nucleus were stained red and blue, respectively. The yellow arrow-heads indicate the shape of the FAs. A representative image of the negative control (secondary antibody Alexa Fluor® 568) is shown on the top. The corresponding surface textures are presented in Figure III-10.

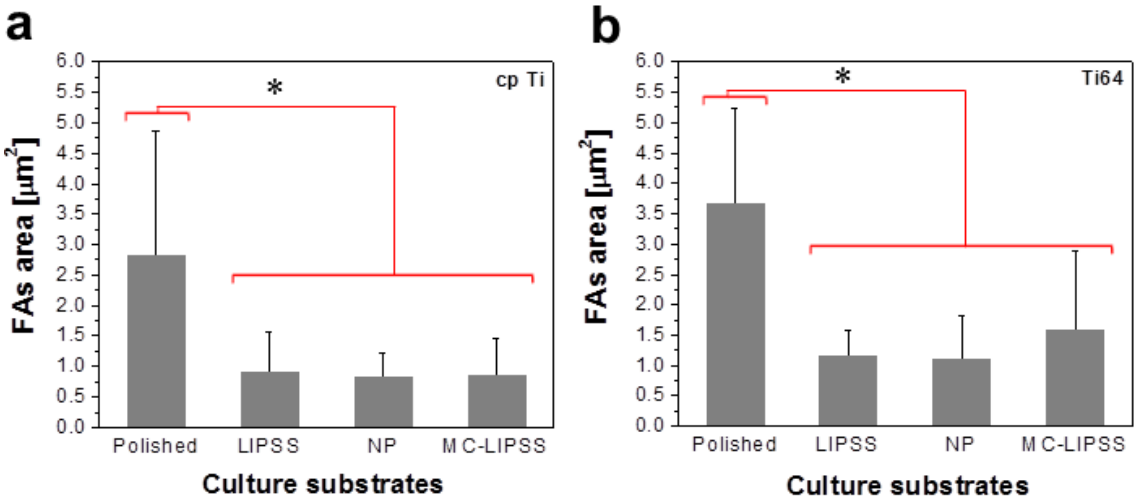

Figure III-29. Quantification of focal adhesions (FAs) area on cp Ti (a) and Ti-6Al-4V alloy (b) surfaces at 24 h after cell seeding. Statistical analysis was performed using ANOVA and Tukey's test. ∗ indicates statistically significant differences between the average values ($p < 0.05$). At least 50 cells were taken for estimation of the FAs area.

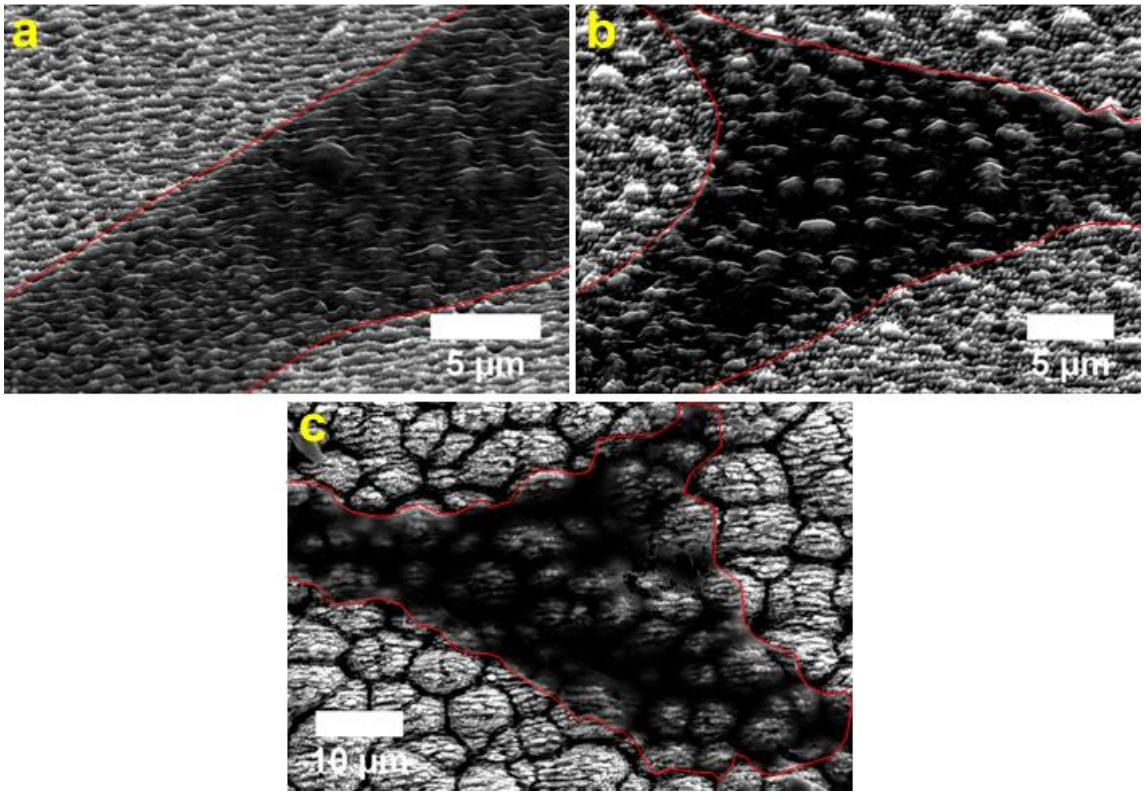

Figure III-30. Representative SEM micrographs of the MSCs on the laser textured surfaces of cp Ti at 24 h after cell seeding. LIPSS (a), NP (b), and MC-LIPSS (c) surfaces. The red lines were drawed to highlight the cell edges. The scale bar is 5 µm (a-b) and 10 µm (c). Similar cytoskeleton deformation was observed for cells cultured on Ti-6Al-4V alloy surfaces.

The cells were also observed by SEM (**Figure III-30**). These observations confirmed that the cell cytoskeleton deformed according to the underneath surface textures. They indicate that cells do not only lay on the laser textured surfaces, but interact with them.

2.7.3. Nucleus Spreading and Deformation (after 24 h of cell culture)

The effect of the distinct surface topographies on the cell nucleus spreading and deformation was also investigated (**Figure III-31**). Similarly to cell spreading, nucleus spreading was assessed by calculating the average nucleus area (**Figure III-31 a** and **b**). The average nucleus area of cells cultured on polished surfaces (~ 350 and 600 μm^2 for cp Ti and Ti-6Al-4V alloy, respectively) was approximately 1.4-1.7 times larger than for cells cultured on laser textured surfaces (~ 250 and 350 μm^2 for cp Ti and Ti-6Al-4V alloy, respectively). Contrarily to the average cell area, statiscally significant differences were found for laser textured surfaces of cp Ti. The largest average nucleus area (~ 280 μm^2) was observed for cells cultured on LIPSS surfaces, while the lowest (~ 211 μm^2) was found for the MC-LIPSS surfaces. The analysis of the nucleus circularity provides information about its deformation (**Figure III-31 c** and **d**). A circularity of 1.0 indicates a perfect circular nucleus. Nevertheless, it is known that the cell nucleus is slightly deformed naturally (not a perfect circle). Thus, the circularity of the cell nucleus of cells cultured on polished surfaces is considered as a control. It allows us to analyse the influence of the laser textured surfaces on the cell nucleus deformation. The average nucleus circularity was in the range 0.8-0.9 for all surface topographies of both Ti alloys, confirming that the cell nucleus slightly deforms, but the difference is not statistically significative. That is, the laser-induced structures do not deform the cell nucleus significantly in contrast to what is observed for the cytoskeleton.

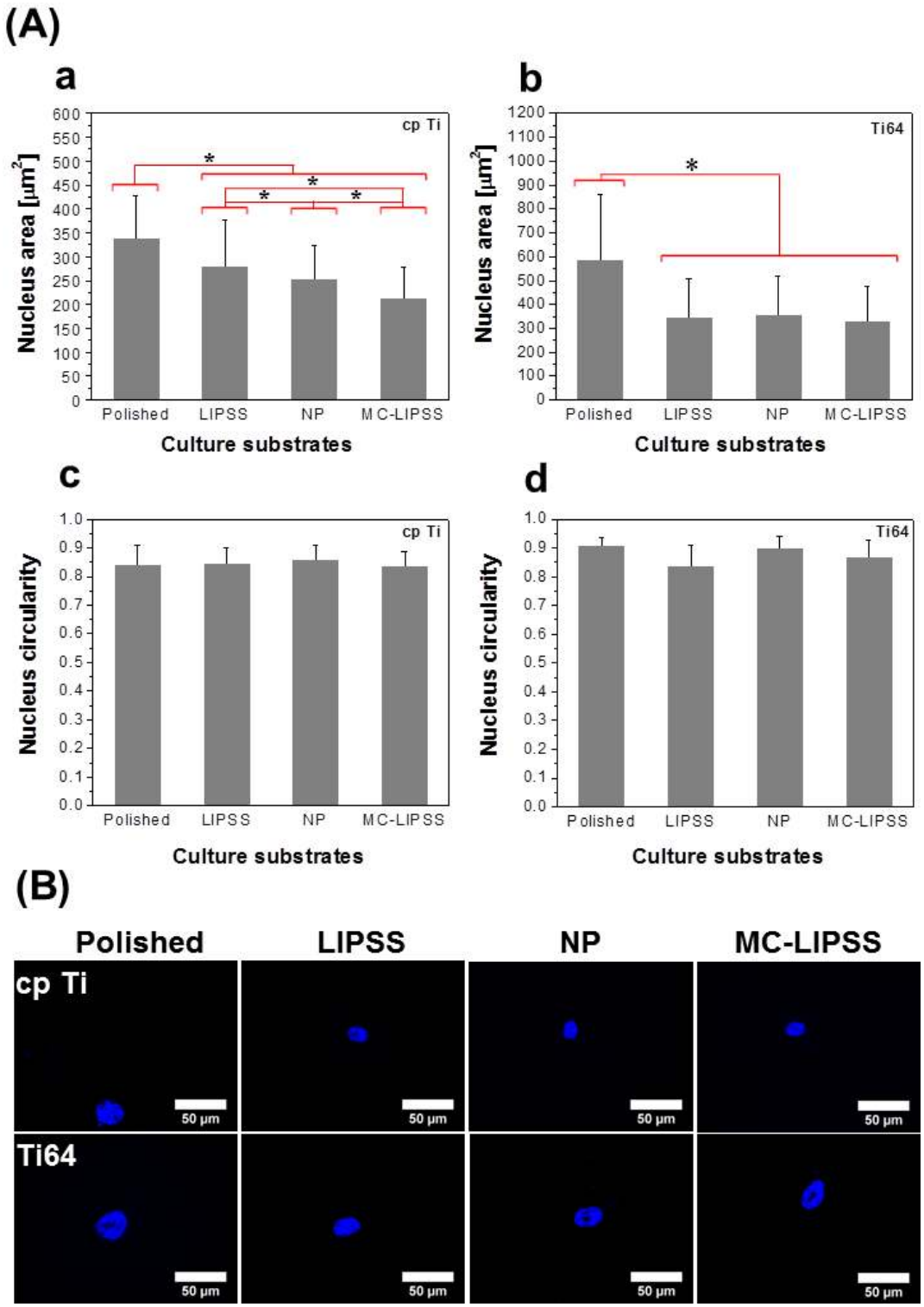

Figure III-31. (A) Quantification of cell nucleus spreading and deformation by analysing the average cell nucleus area and circularity on cp Ti (a and c) and Ti-6Al-4V alloy (b and d) surfaces, respectively, at 24 h after cell seeding. Statistical analysis was performed using ANOVA and Tukey's test. ∗ indicates statistically significant differences between the average values ($p < 0.05$) in (a) and (b). There is no statistically significant differences among the average values in (c) and (d). At least 100 cells were analysed for each type of surface. (B) Representative high magnification fluorescence images of cell nucleus are also presented. The scale bar is 50 µm. The corresponding surface textures are presented in Figure III-10.

2.7.4. Cell Contact Guidance (after 24 h of cell culture)

In the present work, cell contact guidance was observed on MSCs cultured on LIPSS textured surfaces, as shown in **Figure III-32.** MSCs partially aligned in the LIPSS direction, as can be seen in the SEM micrographs. The cell contact guidance was quantified by the cell alignment angle, which is the angle between the long axis of the cell and the LIPSS direction (orientation). Histrograms of the relative frequency of cell alignment angle (**Figure III-32 a** and **b**) show a large scatter of orientation from nearly 0° (complete alignment) to approximately 80° (no alignment), but more than 30-35 % of the cells align within 0-30° with the LIPSS direction.

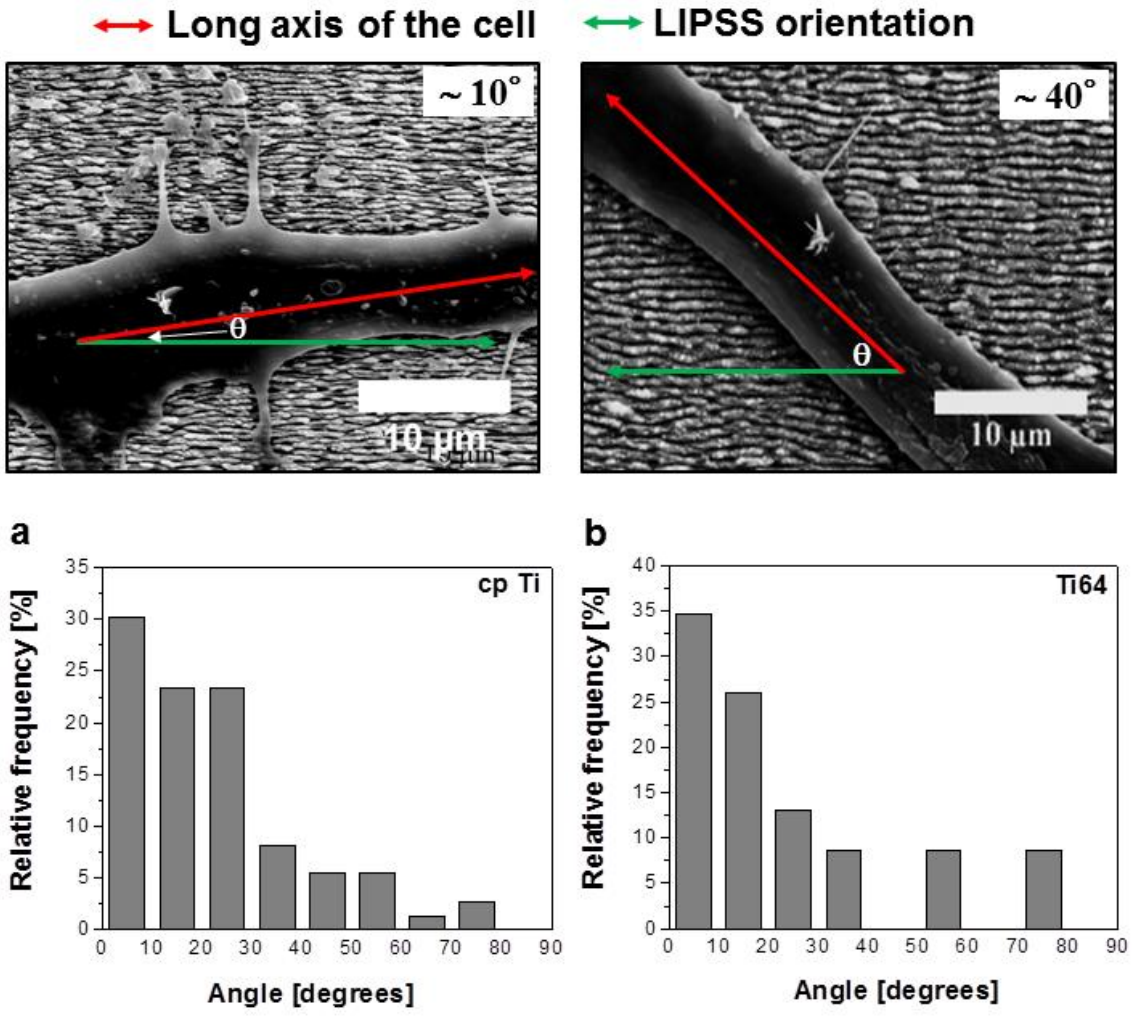

Figure III-32. Representative SEM micrographs of MSCs partially aligned (cell contact guidance) on LIPSS textured surfaces at 24 h after cell seeding. Histograms presenting the relative frequency of the cell alignment angle on the cp Ti (a) and Ti-6Al-4V alloy (b) surfaces. At least 20 cells were analysed for each type of Ti alloy. The scale bar is 10 µm.

2.7.5. Summary of the Results After 24 h of Cell Culture

The major results presented in Sections 2.7.1.-2.7.4. of Chapter III are summarised as follows:

(a) The growth of human Mesenchymal Stem Cells (hMSCs) is significantly larger on Ti-6Al-4V than on cp Ti surfaces;
(b) The spreading of hMSCs is strongly decreased by the surface textures on both Ti alloys, as compared to polished surfaces;
(c) The surface topography affects significantly the hMSCs shape. Cell stretching and stress fibres are induced by LIPSS and MC-LIPSS textures, while significant filopodia formation seems to be induced by the NP textures;
(d) The number of adhered cells is independent of the texture and similar for both Ti alloys, but the focal adhesions (FAs) area is strongly reduced on laser textured surfaces as compared to polished surfaces;
(e) The spreading of cell nucleus is significantly decreased on laser textured surfaces of both Ti alloys as compared to polished surfaces;
(f) Cell nucleus slightly deforms, but it is independent of the surface topography and of the Ti alloy;
(g) LIPSS textures promote cell contact guidance;

2.7.6. Collective Cytoskeleton Organisation (after 2 weeks of cell culture)

The collective organisation of the cell cytoskeleton was investigated after 2 weeks of culture (**Figure III-33**). A similar organisation was observed as compared to that observed after 24 h of culture. Nevertheless, slight differences were observed depending on the surface topography. Cells cultured on polished surfaces spread well and a slight increase of the cytoskeleton stretching was observed, with no preferential stretching direction (**Figure III-33 a** and **e**). Cells cultured on LIPSS (**Figure III-33 b** and **f**) and MC-LIPSS (**Figure III-33 d** and **h**) textured surfaces presented strong cytoskeleton stretching and collective cell alignment (white arrows). It was more evident for cells cultured on LIPSS than for those cultured on MC-LIPSS, in which variations in the cell stretching direction could be observed.

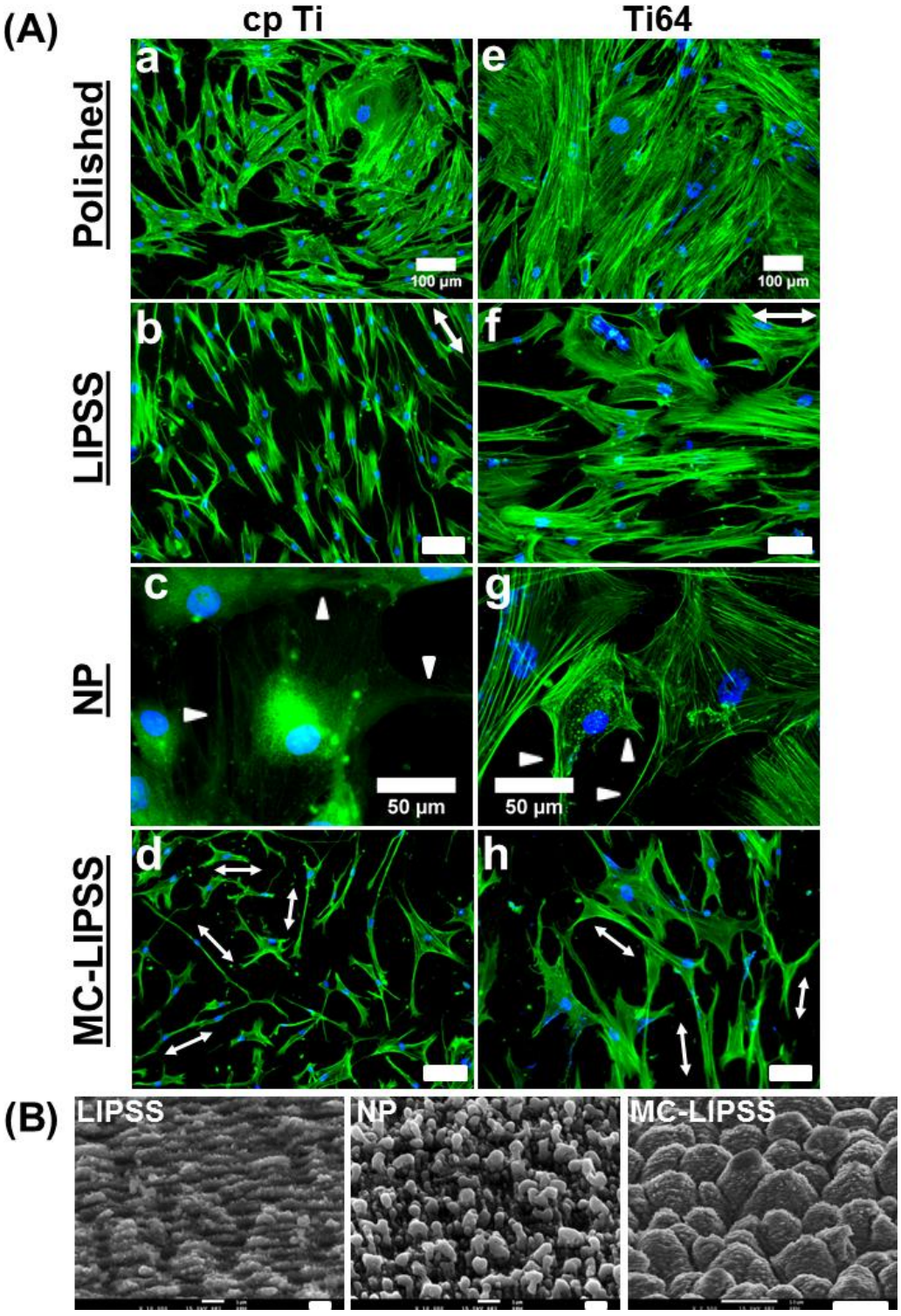

Figure III-33. (A) Representative fluorescence images of the collective cytoskeleton organisation on cp Ti and Ti-6Al-4V alloy surfaces at 2 weeks after cell seeding. Polished (a and e), LIPSS (b and f), NP (c and g), and MC-LIPSS (d and h) surfaces. F-actin fibres and cell nucleus were stained green and blue, respectively. The white arrows (b, f, d, and h) indicate the preferential stretching direction of cells. The white arrow-heads (c and g) indicate less filopodia structures in comparison with those observed at 24 h after cell seeding. The scale bar is 100 µm (a, b, d, e, f, and h) and 50 µm (c and g). (B) SEM micrographs of the corresponding surface textures are also presented. The scale bar is 1 µm (LIPSS and NP) and 10 µm (MC-LIPSS).

Cells cultured on NP textured surfaces (**Figure III-33 c** and **g**) seems to have less filopodia (white arrow-heads) and increased spreading. The similar characteristics of the cytoskeletons after 2 weeks of cell culture indicate that the different surface topographies were able to maintain the specific induced cell shapes, in the long-term, while proliferation takes place.

2.7.7. Cell Proliferation and Commitment (after 2 weeks of cell culture)

Cell proliferation was studied 2 weeks after cell seeding (**Figure III-34**). Low magnification fluorescence images of the stained cell nucleus at 24 h and 2 weeks after cell seeding are shown in **Figure III-34 a-p**. Cells cultured on cp Ti surfaces (**Figure III-34 a-h**) proliferate more than those cultured on Ti-6Al-4V alloy surfaces (**Figure III-34 i-p**). Cell proliferation was in the range 60-80 % on cp Ti surfaces (**Figure III-34 q**), independently of the type of surface. Conversely, for Ti-6Al-4V alloy cell proliferation was less noticeable on laser textured surfaces (~ 24-42 %) in comparison with the polished surfaces (~ 60 %) (**Figure III-34 r**). No statistically significant differences were found among the different textures for Ti-6Al-4V alloy. It is important to emphasise that the large standard deviation in the values was due to cell clustering in some regions of the surfaces, leading to large errors in cell number counts.

In order to assess MSCs commitment into an osteoblastic lineage, i.e., their tendency to form bone cells, cells were immunostained with two specific osteoblast markers, namely, osterix (OSX) and osteopontin (OPN) at 2 weeks after cell seeding. OSX is a transcription factor essential for osteoblast differentiation and bone formation, while OPN is a bone sialoprotein I involved in bone remodelling (see Section 7. of Chapter I). The representative fluorescence images after specific osteoblast marking and the quantification of their expression levels by fluorescence intensity are shown in **Figure III-35**. Both markers were clearly expressed (fluorescent red dots) independently of the topography and Ti alloy. The markers were observed in the cell nucleus, as shown in the images. Both markers were significantly upregulated on Ti-6Al-4V alloy surfaces (**Figure III-35 b** and **d**) in comparison with cp Ti surfaces (**Figure III-35 a** and **c**). No statistically significant differences were found in the expression levels of both markers for Ti-6Al-4V surfaces, while these differences were significant for cp Ti surfaces. The expression of OSX was downregulated on cells cultured on MC-LIPSS textured surfaces in comparison with the polished surface, while

the OPN expression was downregulated in comparison with both the polished and the NP textured surfaces.

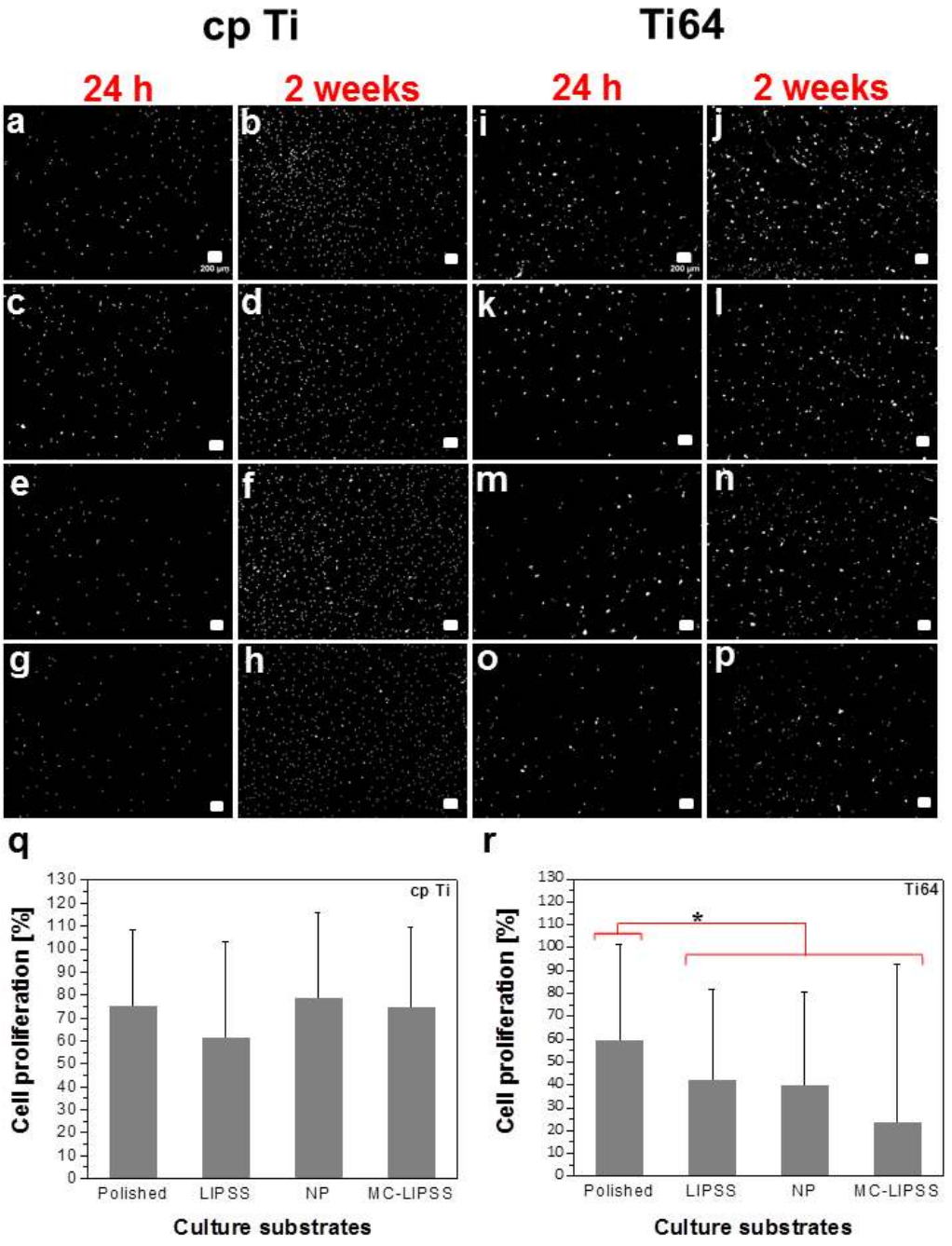

Figure III-34. Representative low magnification fluorescence images of cell nucleus on cp Ti (a-h) and Ti-6Al-4V alloy (i-p) surfaces at 24 h and 2 weeks after cell seeding. Polished (a, b, i, and j), LIPSS (c, d, k, and l), NP (e, f, m, and n), and MC-LIPSS (g, h, o, and p) surfaces. The scale bar is 200 μm. Quantification of cell proliferation at 2 weeks after cell seeding on cp Ti (q) and Ti-6Al-4V alloy (r) surfaces. Statistical analysis was performed using ANOVA and Tukey's test. ∗ indicates statistically significant differences between the average values ($p < 0.05$) in (r). There is no statistically significant differences among the average values in (q). At least 10 images were taken for counting the number of cell nucleus in the total area of the images. The corresponding surface textures are presented in Figure III-10.

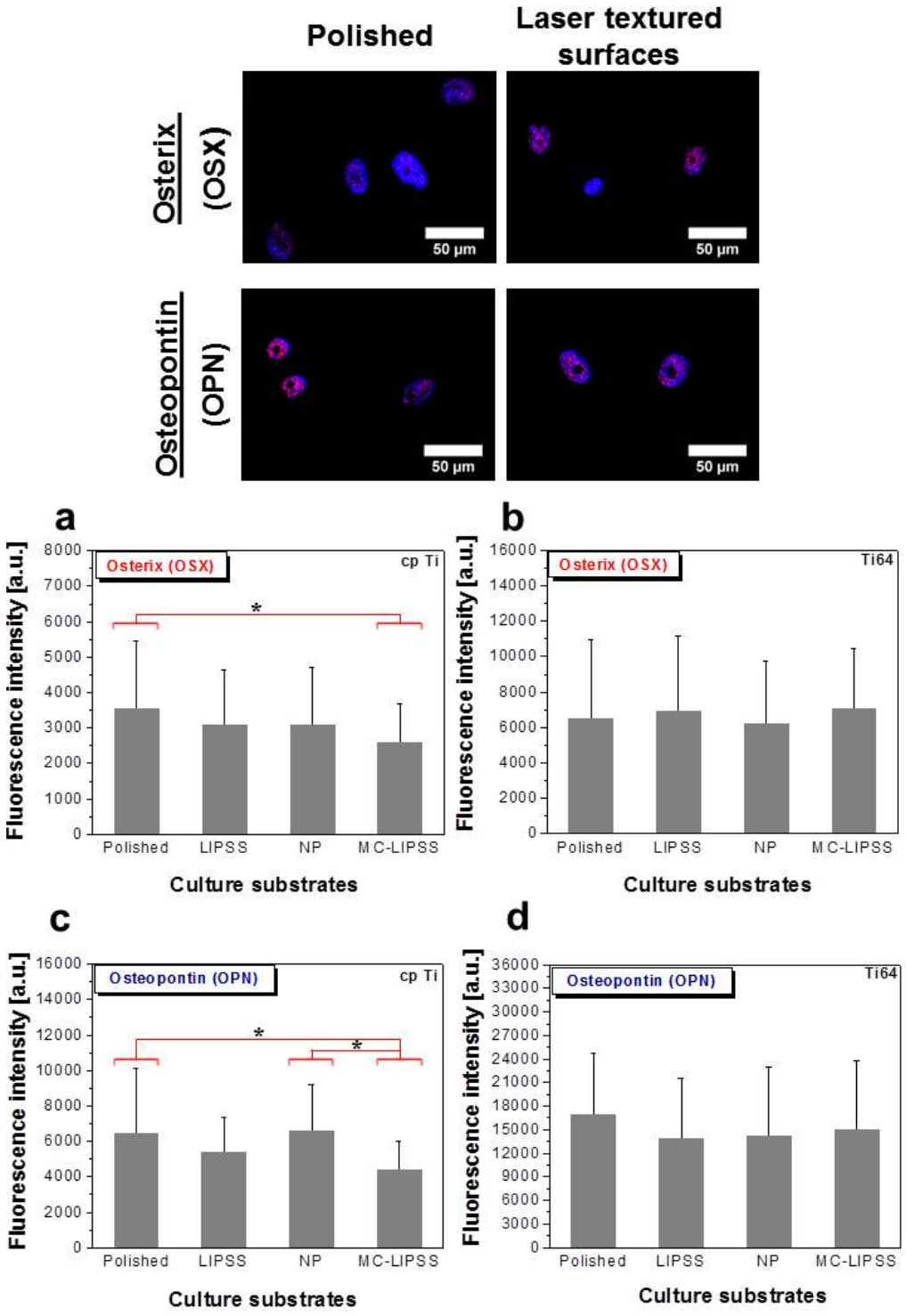

Figure III-35. Representative high magnification fluorescence images of cell nucleus, Osterix (OSX) and Osteopontin (OPN) osteoblast markers on polished and laser textured surfaces of Ti-6Al-4V alloy at 2 weeks after cell seeding. Cell nucleus, OSX and OPN were stained blue and red, respectively. The scale bar is 50 µm. Quantification of the expression levels (fluorescence intensity) of OSX and OPN on cp Ti (a and c) and Ti-6Al-4Valloy (b and d) surfaces, respectively. Statistical analysis was performed using ANOVA and Tukey's test. ∗ indicates statistically significant differences between the average values ($p < 0.05$) in (a) and (c). There is no statistically significant differences among the average values in (b) and (d). At least 50 cells were analysed for each type of surface. The corresponding surface textures are presented in Figure III-10.

2.7.8. Summary of the Results After 2 Weeks of Cell Culture

The major results presented in Sections 2.7.6. and 2.7.7. of Chapter III are summarised as follows:

(a) A collective cytoskeleton organisation is observed at 2 weeks after cell seeding, during the proliferation process;
(b) Cell proliferation is enhanced on cp Ti surfaces as compared to Ti-6Al-4V. On the other hand, cell proliferation is less noticeable on Ti-6Al-4V laser textured surfaces as compared to polished surfaces;
(c) MSCs undergo osteoblastic commitment, as indicated by the expression of markers such as osterix (OSX) and osteopontin (OPN). In general, the osteoblastic markers are upregulated for Ti-6Al-4V surfaces as compared to cp Ti, but their expression is independent of the type of surface texture.

2.7.9. Cell Differentiation (after 4 weeks of cell culture)

Cell differentiation on titanium surfaces was investigated at 4 weeks after cell seeding as follows:

i. Firstly, possible changes in the cytoskeleton organisation and nucleus deformation were investigated by staining of F-actin fibres filaments and cell nucleus;
ii. Secondly, the matrix mineralisation was assessed by staining of Xylenol Orange (XO) and OsteoImage^{TM} (OI). XO is a calcium-chelating fluorophore that detects calcium-rich zones, while the staining reagent of OI specifically binds to hydroxyapatite (HA) in the mineralised matrix produced by osteoblasts (see section 1.5.2. of Chapter II).

Cells were cultured in non-osteogenic (Alpha-MEM) and osteogenic (Lonza Poietics^{TM}) media, the latter containing soluble factors such as β-glycerolphosphate, dexamethasone, and ascorbic acid, which promote osteogenesis (see Section 1.5.1 of Chapter II). Prior to the experiments, the cells were cultured on tissue culture polystyrene (TCPS) in order to check if the osteogenic medium was able to promote Mesenchymal Stem Cells osteogenesis. **Figure III-36** presents representative fluorescent images of stained F-actin fibres, cell nucleus, and Xylenol Orange (XO). Cells cultured in the non-osteogenic medium presented no traces of calcium deposition,

indicating that no matrix mineralisation occurred. Conversely, cells cultured in the osteogenic medium presented large calcium-rich areas, which indicate matrix mineralisation. Bone-like nodules, marked by white arrows, formed, confirming an advanced stage of mineralisation. These experiments clearly showed that the osteogenic medium promoted Mesenchymal Stem Cells osteogenesis satisfactorily.

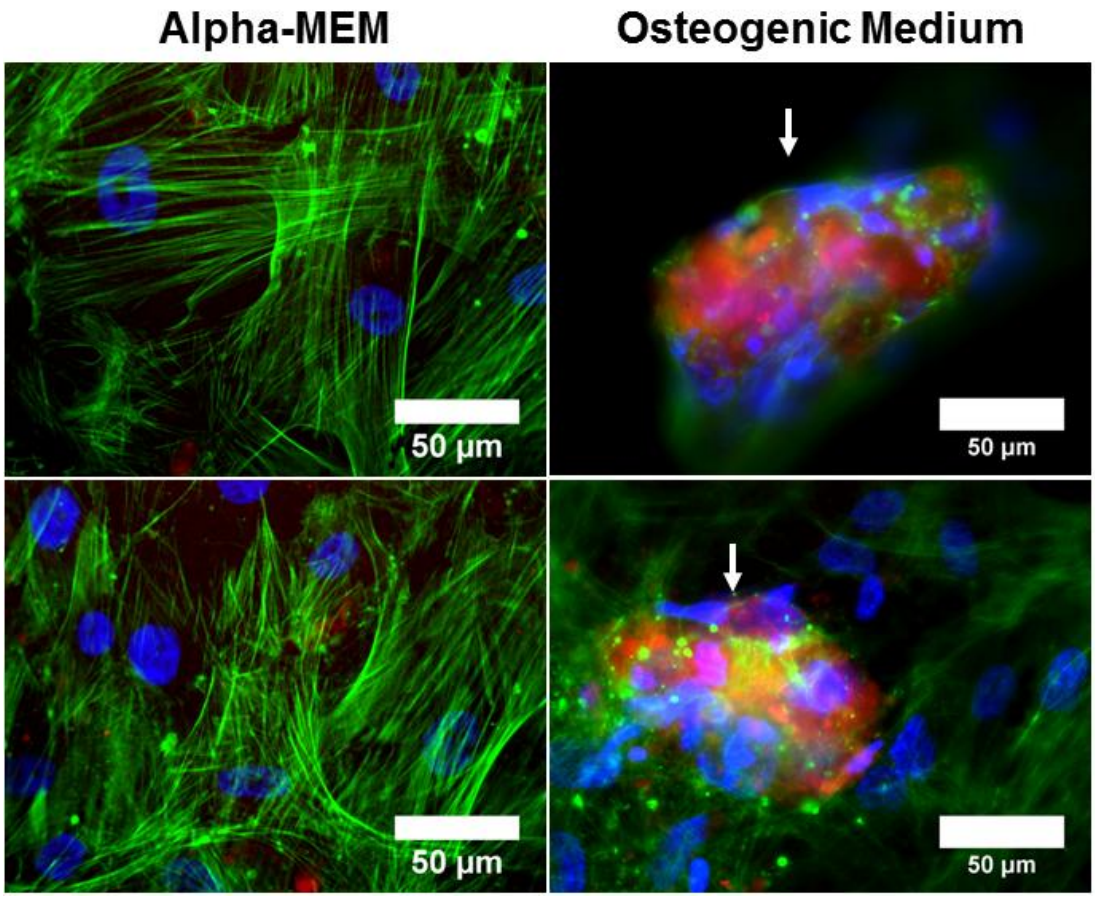

Figure III-36. Representative high magnification fluorescence images of F-actin fibres (green), cell nucleus (blue), and Xylenol orange (XO; red) on cells cultured on tissue culture polystyrene (TCPS) at 4 weeks after cell seeding. Cells were cultured in non-osteogenic (Alpha-MEM) and osteogenic (Lonza Poietics™) media. TCPS was used as a control to confirm if the osteogenic medium was able to promote Mesenchymal Stem Cells osteogenesis. The scale bar is 50 µm.

Differences in the cytoskeleton organisation and nucleus deformation were observed depending on the surface topographies and culture media. Representative fluorescent images of stained F-actin fibres and cell nucleus of cells cultured for 4 weeks on cp Ti and Ti-6Al-4V surfaces are shown in **Figure III-37** and **Figure III-38**, respectively.

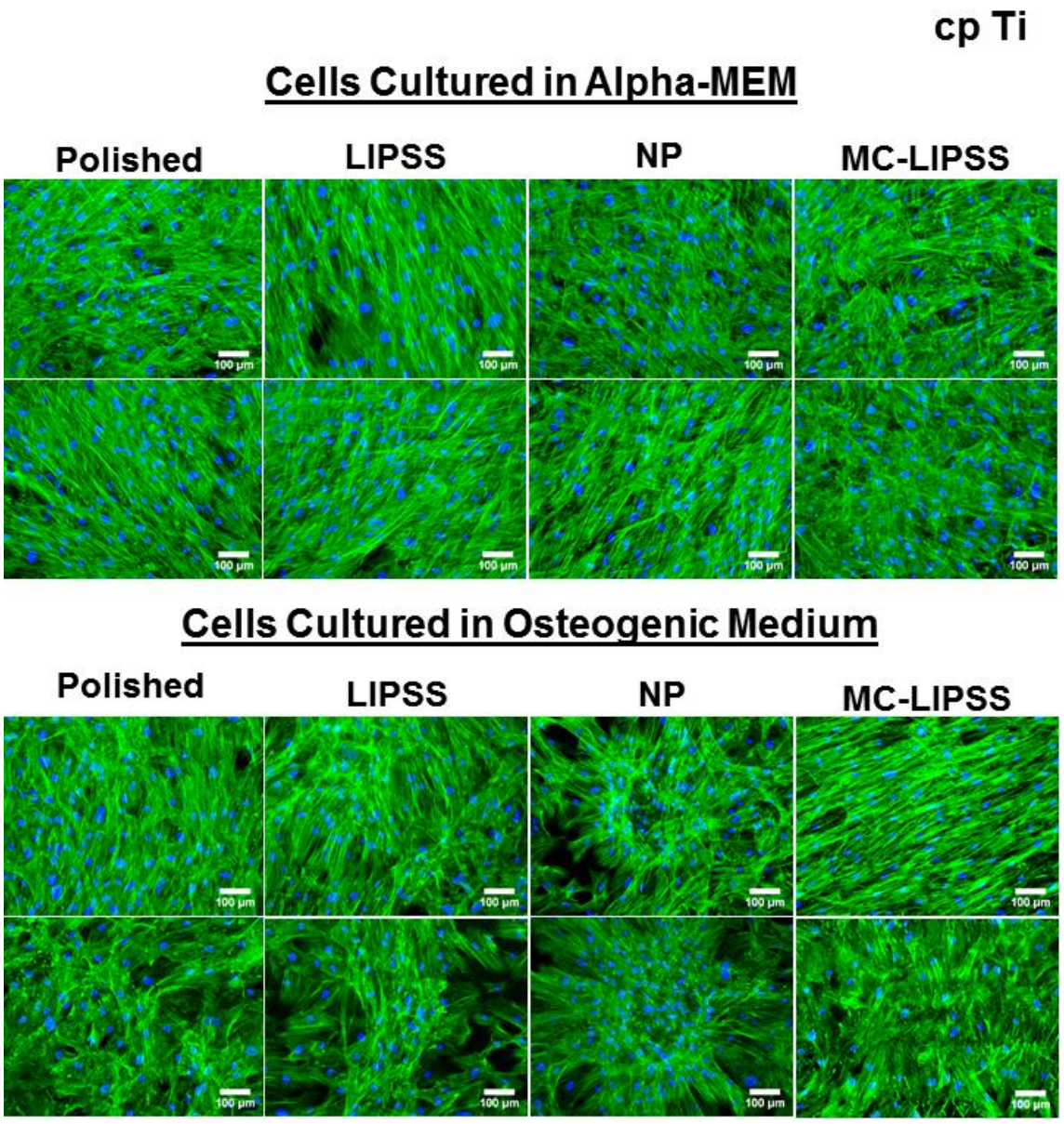

Figure III-37. Two representative fluorescence images of cells cultured on cp Ti surfaces at 4 weeks after cell seeding. Cells were cultured in non-osteogenic (Alpha-MEM) and osteogenic (Lonza Poietics^{TM}) media. F-actin fibres and cell nucleus were stained green and blue, respectively. The scale bar is 100 µm. The corresponding surface textures are presented in Figure III-10.

Cells cultured in Alpha-MEM show a well-organised cellular layer of stretched cells (confluence) covering almost the whole area, for both Ti alloys, but no bone-like nodules seem to be observed. On the contrary, cells cultured in osteogenic medium displayed a different organisation on LIPSS and NP textured surfaces of both Ti alloys. Cell clustering and stacking as well as concentric organisation of strongly deformed cell nucleus were evident on these laser textured surfaces. These observations most probably

characterise the formation of bone-like nodules. It seems that these nodules were more developed on LIPSS and NP textured surfaces of Ti-6Al-4V as compared to cp Ti surfaces. Finally, the cellular layer formed in contact with polished and MC-LIPSS textured surfaces was less well-organised.

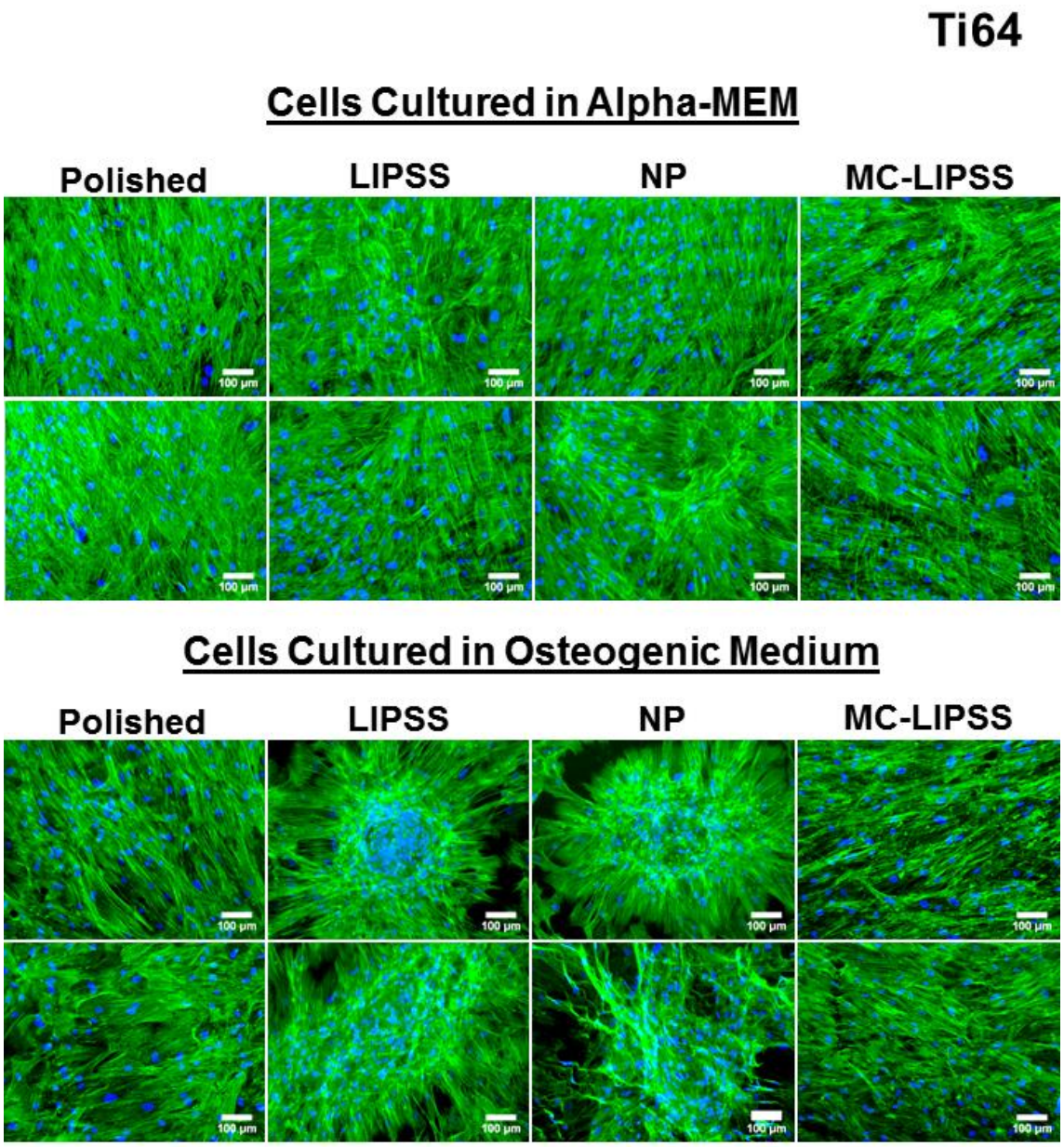

Figure III-38. Two representative fluorescence images of cells cultured on Ti-6Al-4V alloy surfaces at 4 weeks after cell seeding. Cells were cultured in non-osteogenic (Alpha-MEM) and osteogenic (Lonza Poietics^{TM}) media. F-actin fibres and cell nucleus were stained green and blue, respectively. The scale bar is 100 μm. The corresponding surface textures are presented in Figure III-10.

To study matrix mineralisation, cells were stained with Xylenol orange (XO) and OsteoImage™ (OI). Differences in the matrix mineralisation were found depending on the surface topographies and culture media. Representative fluorescent images of cell nucleus and XO and OI stained cells cultured with the osteogenic medium on cp Ti and Ti-6Al-4V surfaces are shown in **Figure III-39** and **Figure III-40**, respectively. The quantification of the expression levels (fluorescence intensity) of XO and OI is presented in **Figure III-41**.

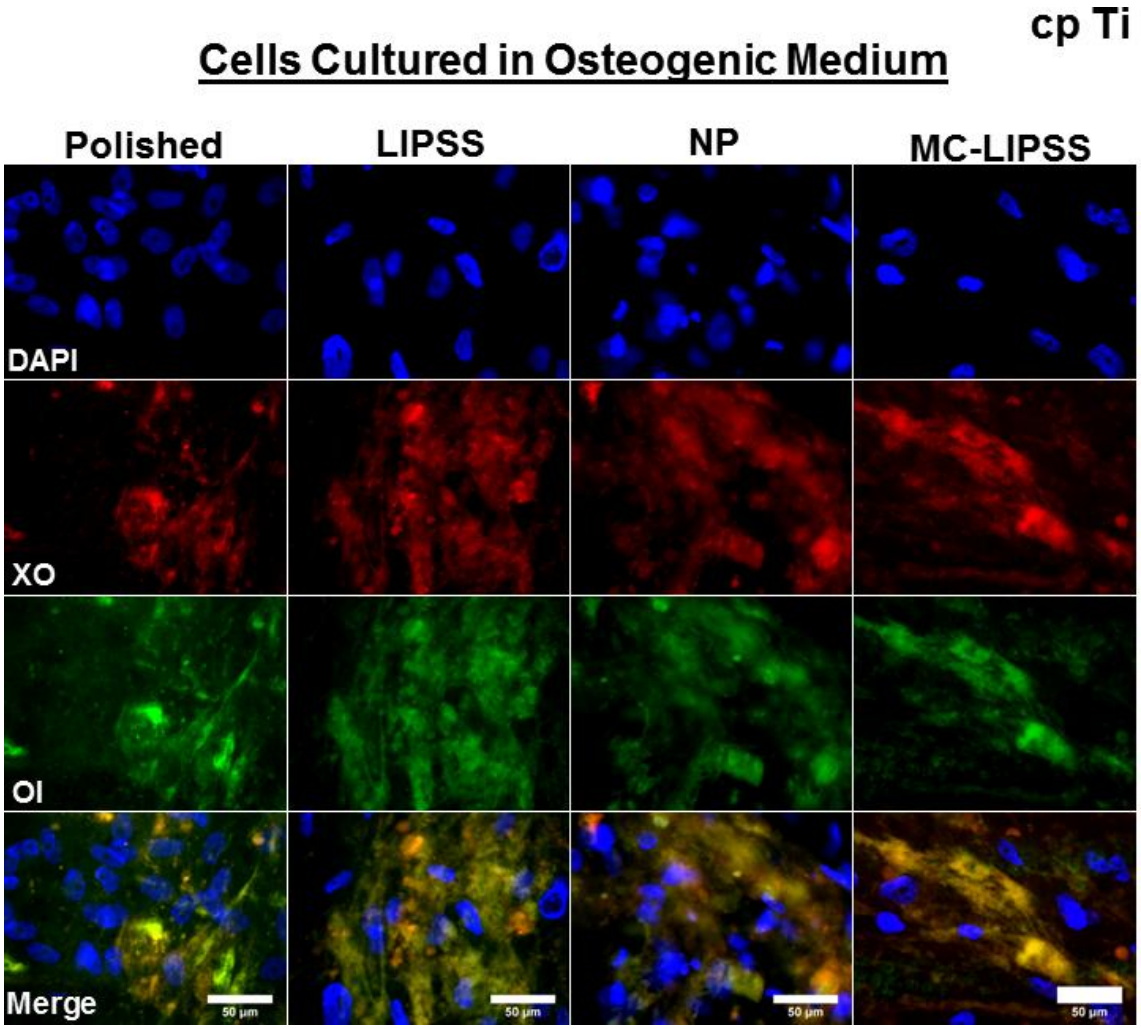

Figure III-39. Representative high magnification fluorescence images of cells cultured on cp Ti surfaces at 4 weeks after cell seeding. Cells were cultured in osteogenic medium (Lonza Poietics™). Cell nucleus, Xylenol orange (XO), and OsteoImage™ (OI) were stained blue, red, and green, respectively. The scale bar is 50 μm for all the images. The corresponding surface textures are presented in Figure III-10.

Since calcium is a component of HA, the fluorescence signals of XO and OI stained cells are observed at the same regions. The formation of bone-like nodules and

enhanced matrix mineralisation was confirmed on LIPSS and NP textured surfaces by the remarkable presence of large calcium- (red fluorescence) and HA-rich (green fluorescence) zones, more conspicuous for Ti-6Al-4V. It is also confirmed by the upregulation of XO and OI expression levels, showed by a higher fluorescence intensity (**Figure III-41**). Despite the abscence of nodules, calcium- and HA-rich zones were also observed in cells cultured on polished and MC-LIPSS textured surfaces of both Ti alloys, indicating that matrix mineralisation also occurs on these surfaces.

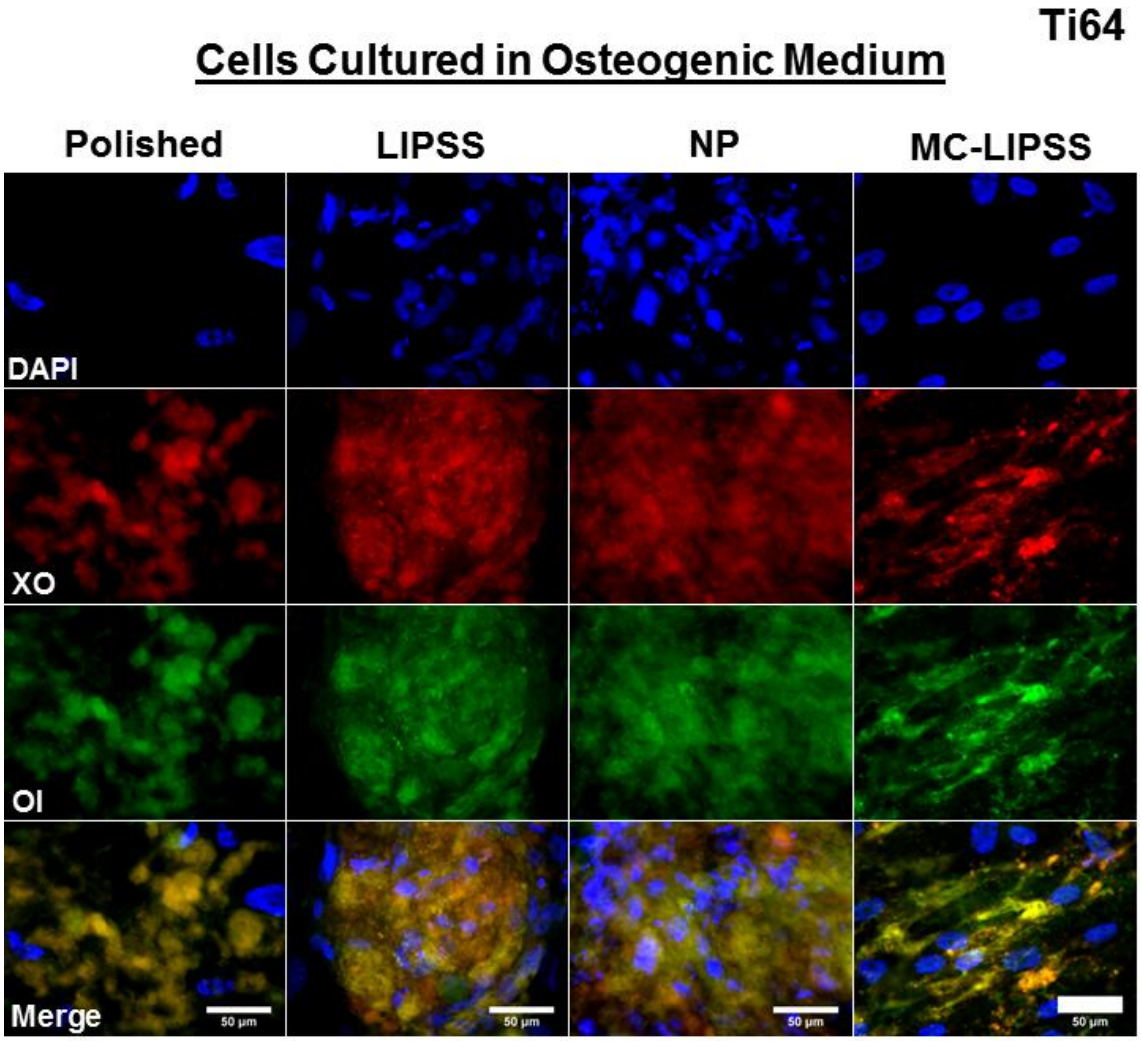

Figure III-40. Representative high magnification fluorescence images of cells cultured on Ti-6Al-4V alloy surfaces at 4 weeks after cell seeding. Cells were cultured in osteogenic medium (Lonza Poietics™). Cell nucleus, Xylenol orange (XO), and OsteoImage™ (OI) were stained blue, red, and green, respectively. The scale bar is 50 µm for all the images. The corresponding surface textures are presented in Figure III-10.

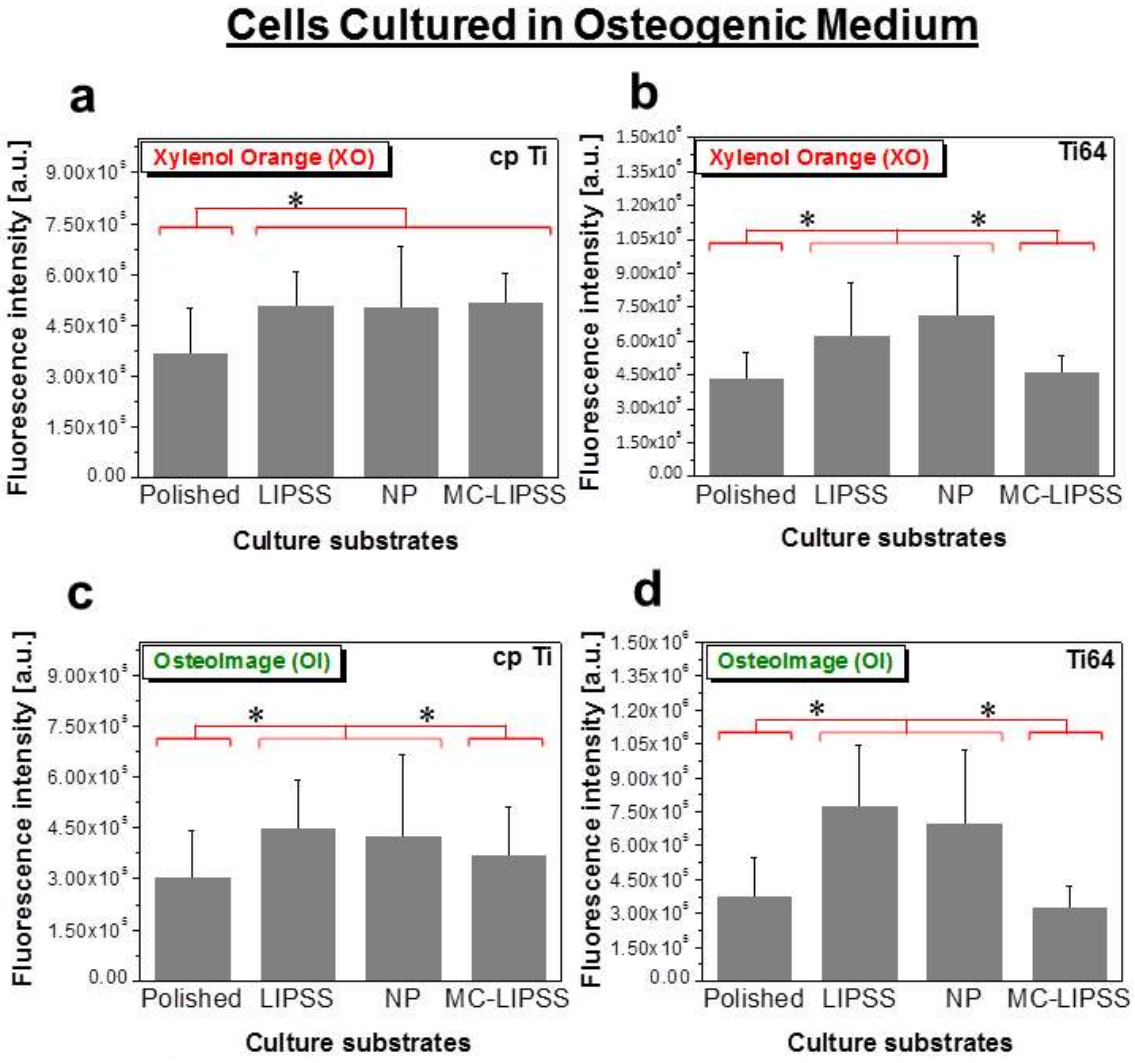

Figure III-41. Quantification of the expression levels (fluorescence intensity) of Xylenol orange (XO) and OsteoImage™ (OI) markers of matrix mineralisation on cells cultured on cp Ti (a and c) and Ti-6Al-4V alloy (b and d) surfaces. Cells were cultured in osteogenic medium (Lonza Poietics™). Statistical analysis was performed using ANOVA and Tukey's test. ∗ indicates statistically significant differences between the average values ($p < 0.05$). At least 25 images were analysed for each type of surface.

Representative fluorescent images of cell nucleus, and XO and OI stained cells cultured with the non-osteogenic medium on cp Ti and Ti-6Al-4V surfaces are shown in **Figure III-42** and **Figure III-43**, respectively.

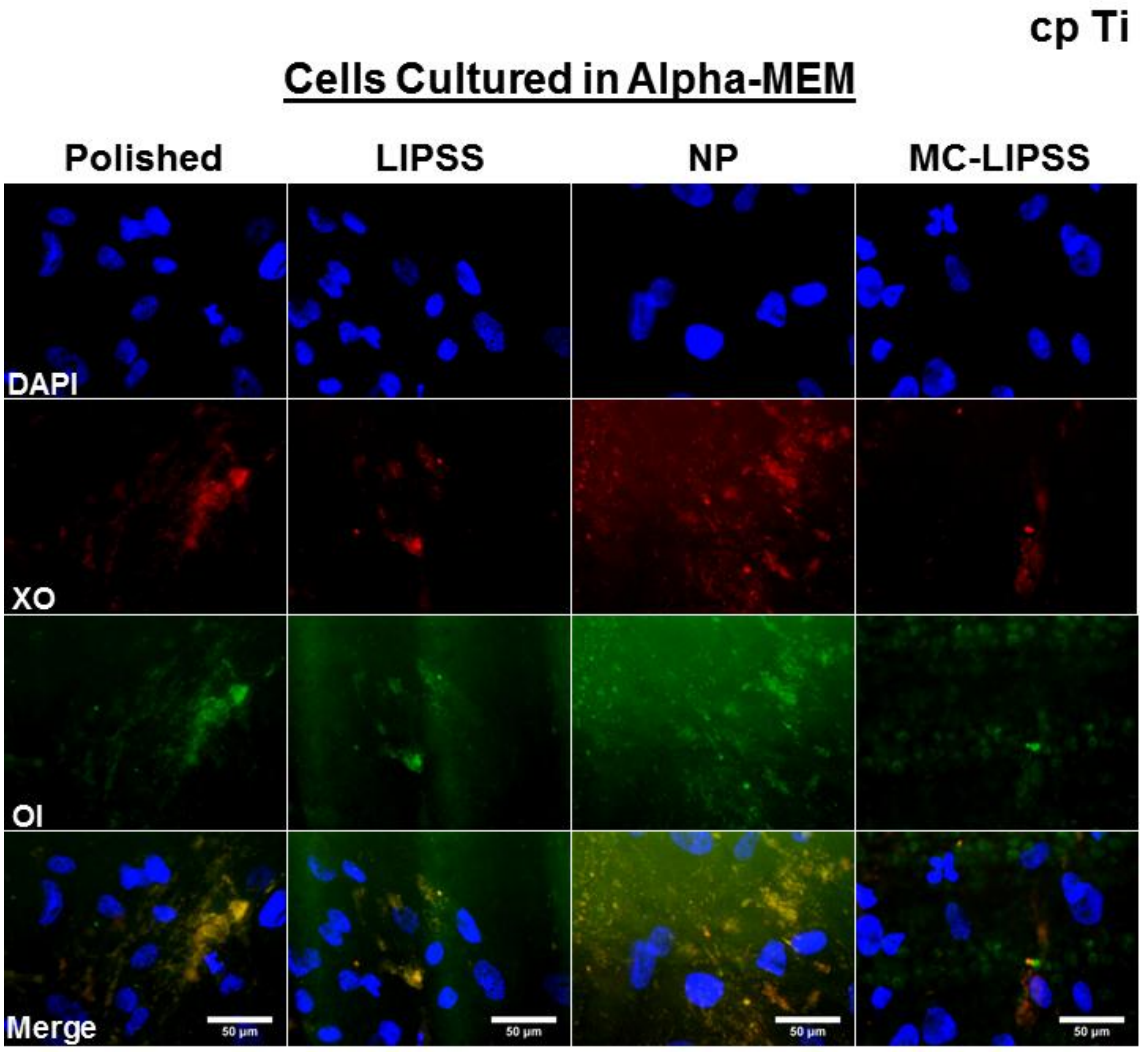

Figure III-42. Representative high magnification fluorescence images of cells cultured on cp Ti surfaces at 4 weeks after the initial cell seeding. Cells were cultured in non-osteogenic medium (Alpha-MEM). Cell nucleus, Xylenol orange (XO), and OsteoImage™ (OI) were stained blue, red, and green, respectively. The scale bar is 50 μm for all the images. The corresponding surface textures are presented in Figure III-10.

In general, no calcium- and HA-rich zones are observed independently of the surface topography and the Ti alloy, indicating that matrix mineralisation does not take place on these surfaces when cells are cultured in a non-osteogenic medium. In particular, the markers are barely observed on polished (cp Ti) and NP textured surfaces (Ti-6Al-4V alloy). It was impossible to quantify both markers due to the low fluorescence intensity and high background.

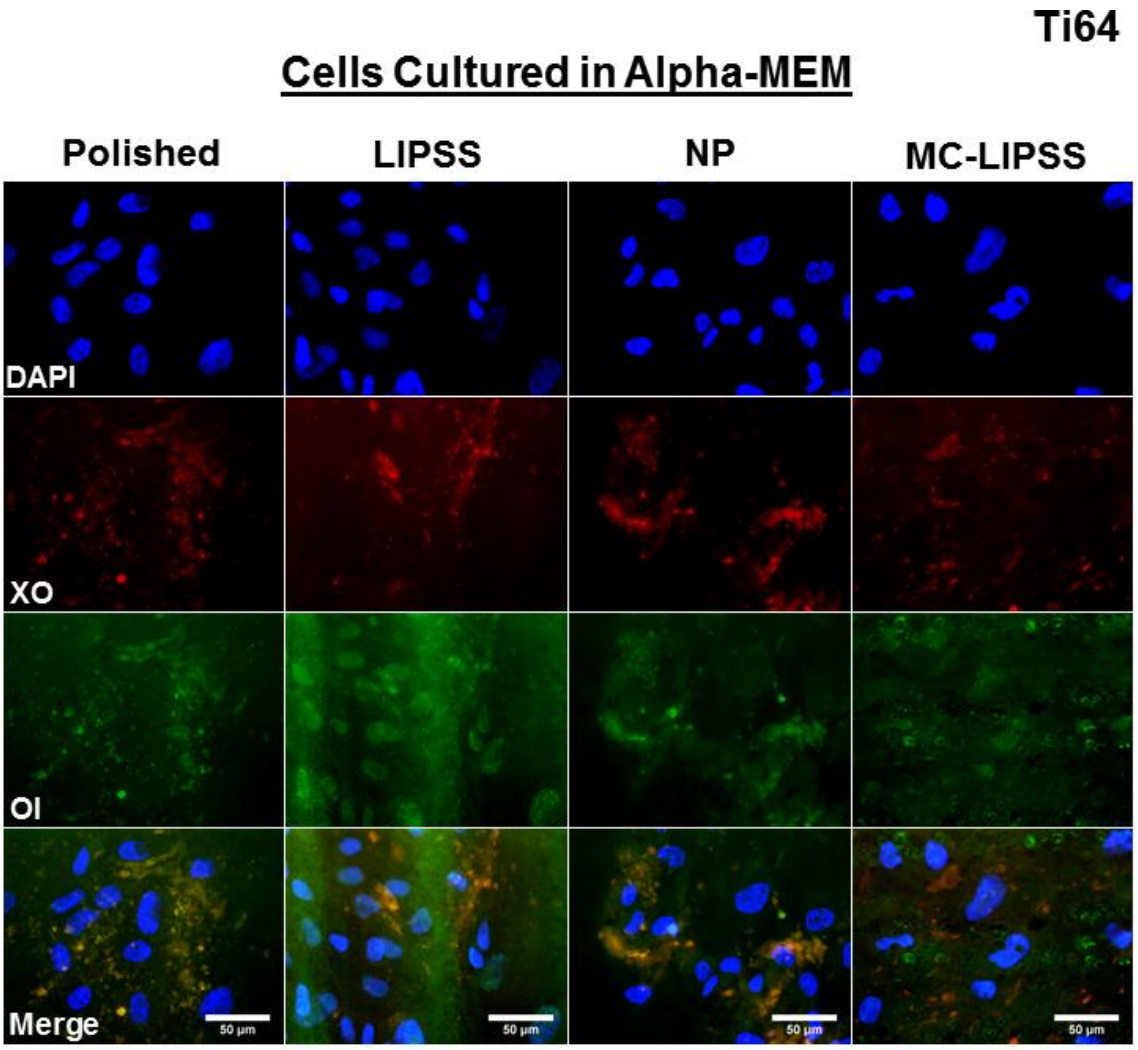

Figure III-43. Representative high magnification fluorescence images of cells cultured on Ti-6Al-4V alloy surfaces at 4 weeks after the initial cell seeding. Cells were cultured in non-osteogenic medium (Alpha-MEM). Cell nucleus, Xylenol orange (XO), and OsteoImage™ (OI) were stained blue, red, and green, respectively. The scale bar is 50 µm for all the images. The corresponding surface textures are presented in Figure III-10.

2.7.10. Summary of the Results After 4 weeks of Cell Culture

The major results presented in Section 2.7.9. of Chapter III are summarised as follows:

(a) Matrix mineralisation and bone-like nodules are not observed when cells are cultured in a non-osteogenic medium;

(b) Matrix mineralisation is observed on all surfaces and Ti alloys when cells are cultured in an osteogenic medium;

(c) Matrix mineralisation is strongly enhanced on LIPSS and NP textured surfaces, mainly for Ti-6Al-4V, and these textures promote the formation of bone-like nodules;

(d) Cell clustering and stacking as well as concentric organisation of strongly deformed cell nucleus are evident when bone-like nodules form;

2.8. Bacteria Behaviour

In this section, preliminary results on the adhesion of *Staphylococcus aureus* and biofilm formation on laser textured surfaces of both Ti alloys are reported. This bacteria strain was chosen because it is responsible for most of bone and implant-associated infections.

2.8.1. *Staphylococcus Aureus* Adhesion (after 48 h of cell culture)

Representative fluorescence images of *Staphylococcus aureus* adhered on all cp Ti surfaces at 48 h after bacteria seeding are shown in **Figure III-44**. Tissue culture polystyrene (TCPS) were used as a positive control for bacteria growth (see Section 1.6.1 of Chapter II). Bacteria adhesion was observed on all the surfaces, but important differences in the colonisation of the tested surfaces are observed. As expected, bacteria cultured on TCPS grew significantly and formed very large colonies (**Figure III-44 a-b**). In comparison with these, the amount of bacteria attached to the polished surfaces of titanium is lower (**Figure III-44 c**), only small circular colonies are observed (**Figure III-44 d**). In contrast, the amount of bacteria attached to LIPSS and NP textured surfaces is much lower, putting into evidence a significant reduction of bacterial biofilm formation (**Figure III-44 e** and **g**). Despite this significant reduction of bacteria adhesion, a few small colonies are observed (**Figure III-44 f** and **h**). Finally, bacteria presented an increased adhesion on MC-LIPSS textured surfaces (**Figure III-44 i)**, where large bacterial colonies are observed mainly in the depressions between the microcolumns (**Figure III-44 j**, white arrows). The results for Ti-6Al-4V alloy are similar (not shown).

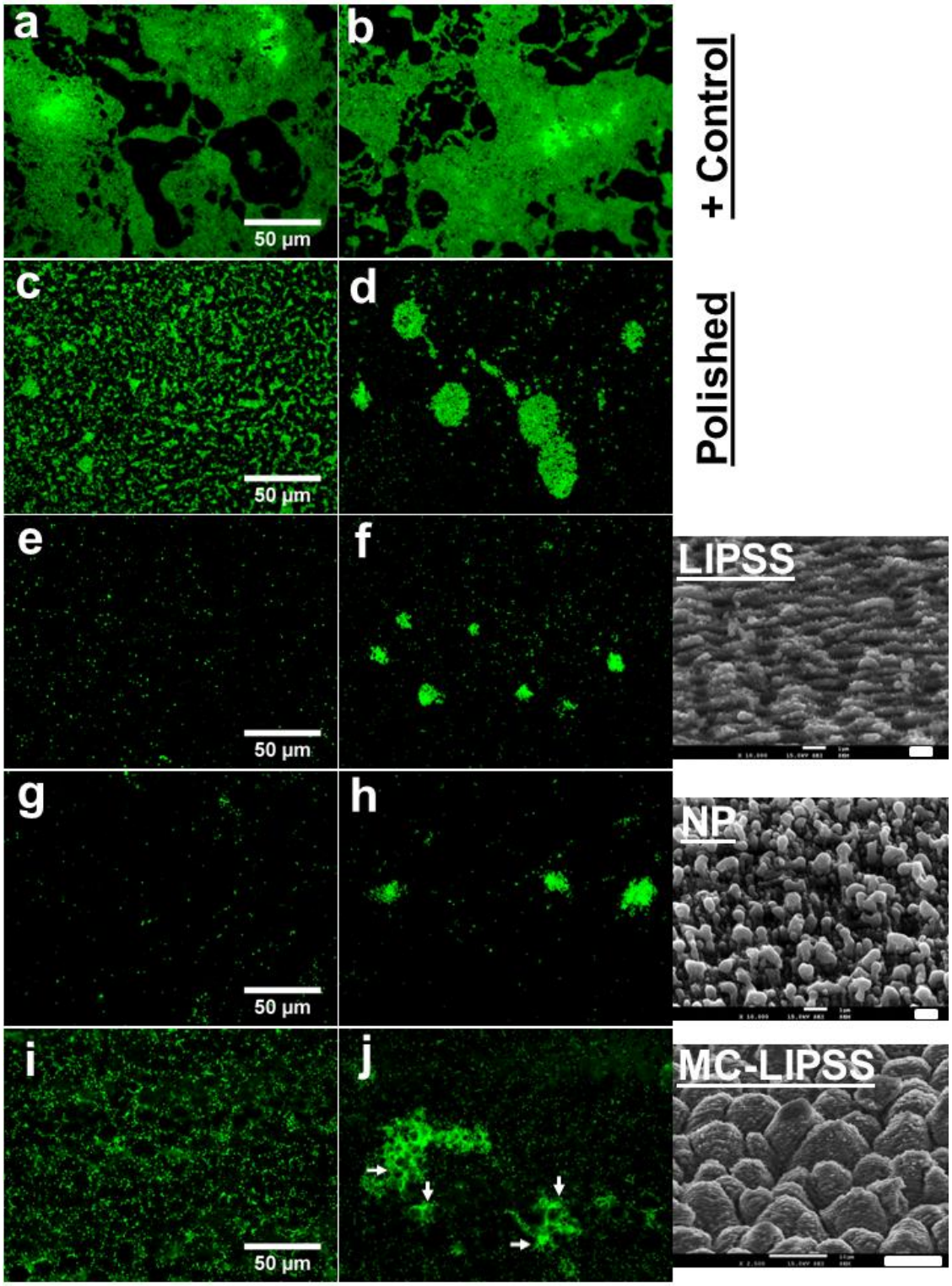

Figure III-44. Representative fluorescence images of *Staphylococcus aureus* (ATCC 25923) on cp Ti surfaces at 48 h after bacteria seeding. TCPS (a-b), polished (c-d), LIPSS (e-f), NP (g-h), and MC-LIPSS (i-j) surfaces. TCPS was used as a positive control for bacteria growth. Bacteria were immunostained with carboxyfluorescein succinimidyl ester (CFSE), which provides a green fluorescence signal. The scale bar is 50 µm for all the images. SEM micrographs of the corresponding surface textures are also presented. The scale bar is 1 µm (LIPSS and NP) and 10 µm (MC-LIPSS). Similar bacteria adhesion was observed for Ti-6Al-4V alloy surfaces.

The measured fluorescence intensity of the bacteria adhered to the surfaces of both Ti alloys is plotted in **Figure III-45**. The fluorescence intensity of bacteria cultured on TCPS was the highest among all surfaces. Statistically significant differences were also observed among the surfaces of both Ti alloys. The fluorescence intensity of bacteria adhered on LIPSS and NP textured surfaces was significantly lower as compared to those adhered to the polished and MC-LIPSS textured surfaces. The fluorescence intensity for MC-LIPSS textured surfaces is slightly higher than for the polished surfaces.

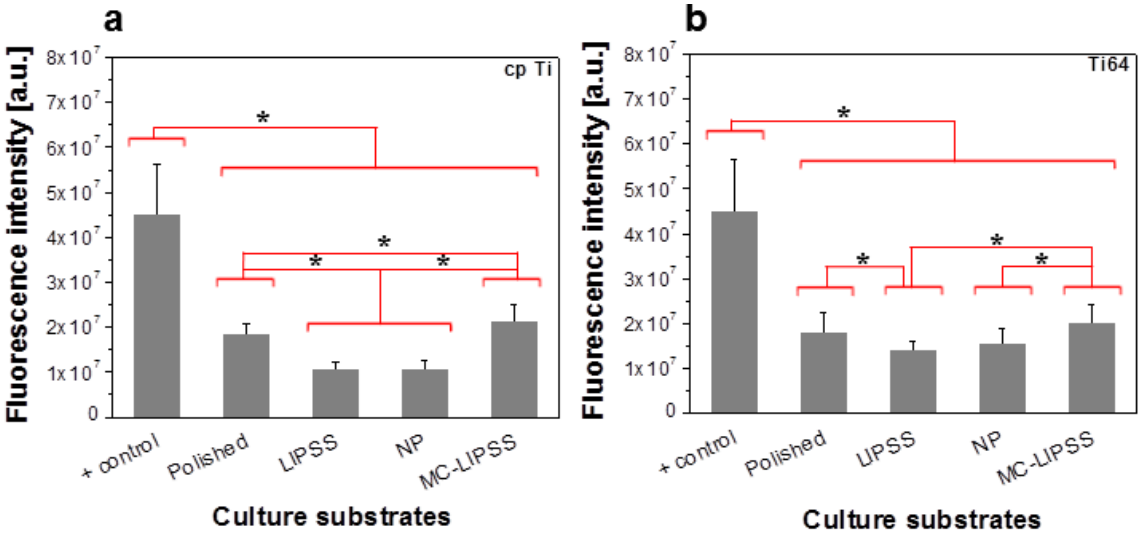

Figure III-45. Quantification of the fluorescence intensity of *Staphylococcus aureus* (ATCC 25923) on cp Ti (a) and Ti-6Al-4V alloy (b) surfaces at 48 h after bacteria seeding. TCPS was used as a positive control for bacteria growth. Statistical analysis was performed using ANOVA and Tukey's test. ∗ indicates statistically significant differences between the average values ($p < 0.05$). At least 15 images were analysed for each type of surface.

2.8.2. Biofilm Formation (after 48 h of cell culture)

Biofilm formation was assessed quantitatively and qualitatively by Crystal Violet binding assay and SEM observations (**Figure III-46** and **Figure III-47**), respectively (see Sections 1.6.4. and 1.6.5. of Chapter II). Representative photographs of the solubilised Crystal Violet dye and its optical density (OD_{550nm}) at a wavelength of 550 nm are shown in **Figure III-46 a-c** and **d-e**, respectively. The $OD_{550\,nm}$ value measured for the Tryptic Soy Broth (TSB) culture medium was considered as a background reading and subtracted from the values measured for all the surfaces. The highest amount of biofilm was clearly observed on the TCPS, as shown by the strongest violet colour of the solution (**Figure III-46 a**) and the highest OD_{550nm} value (~ 0.1). In

contrast, the biofilm formation was significantly reduced on the surfaces of both Ti alloys, as shown by the almost colourless solubilised Crystal Violet dye (**Figure III-46 b**) and the negligible OD_{550nm} value, except for the MC-LIPSS textured surfaces, mainly for Ti-6Al-4V, where the colour of the solubilised Crystal Violet dye and the OD_{550nm} value (~ 0.001-0.02) are slightly higher. In addition, **Figure III-46 c** depicts the solubilised Crystal Violet dye obtained from the bacteria adhered on TCPS used for the culture of the Ti specimens. The increased intensity of the violet colour (OD_{550nm} ~ 0.03-0.05) of the solution indicates that the bacteria biofilm is more noticeable on TCPS than on both Ti alloys.

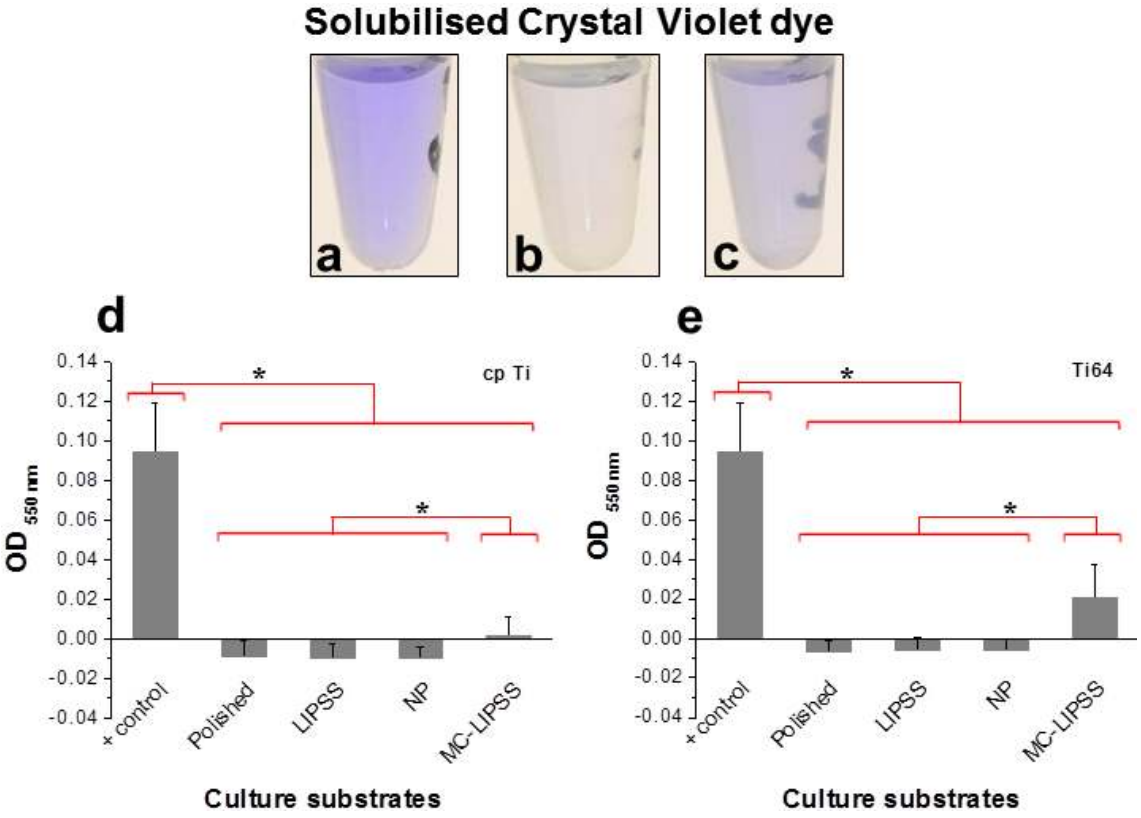

Figure III-46. Representative photographs of the solubilised Crystal Violet dye collected from the TCPS (a), cp Ti and Ti-6Al-4V alloy surfaces (b), and the bacteria adhered on the TCPS used for the culture of the Ti specimens (c). Optical density (OD_{550nm}) at a wavelength of 550 nm of the solubilised crystal violet dye collected from the cp Ti (d) and Ti-6Al-4V alloy (e) surfaces.

SEM observations were carried out in order to provide additional information about the biofilm formation on cp Ti surfaces. Representative high magnification SEM micrographs of *Staphylococcus aureus* biofilm on cp Ti surfaces at 48 h after bacteria seeding are presented in **Figure III-47**.

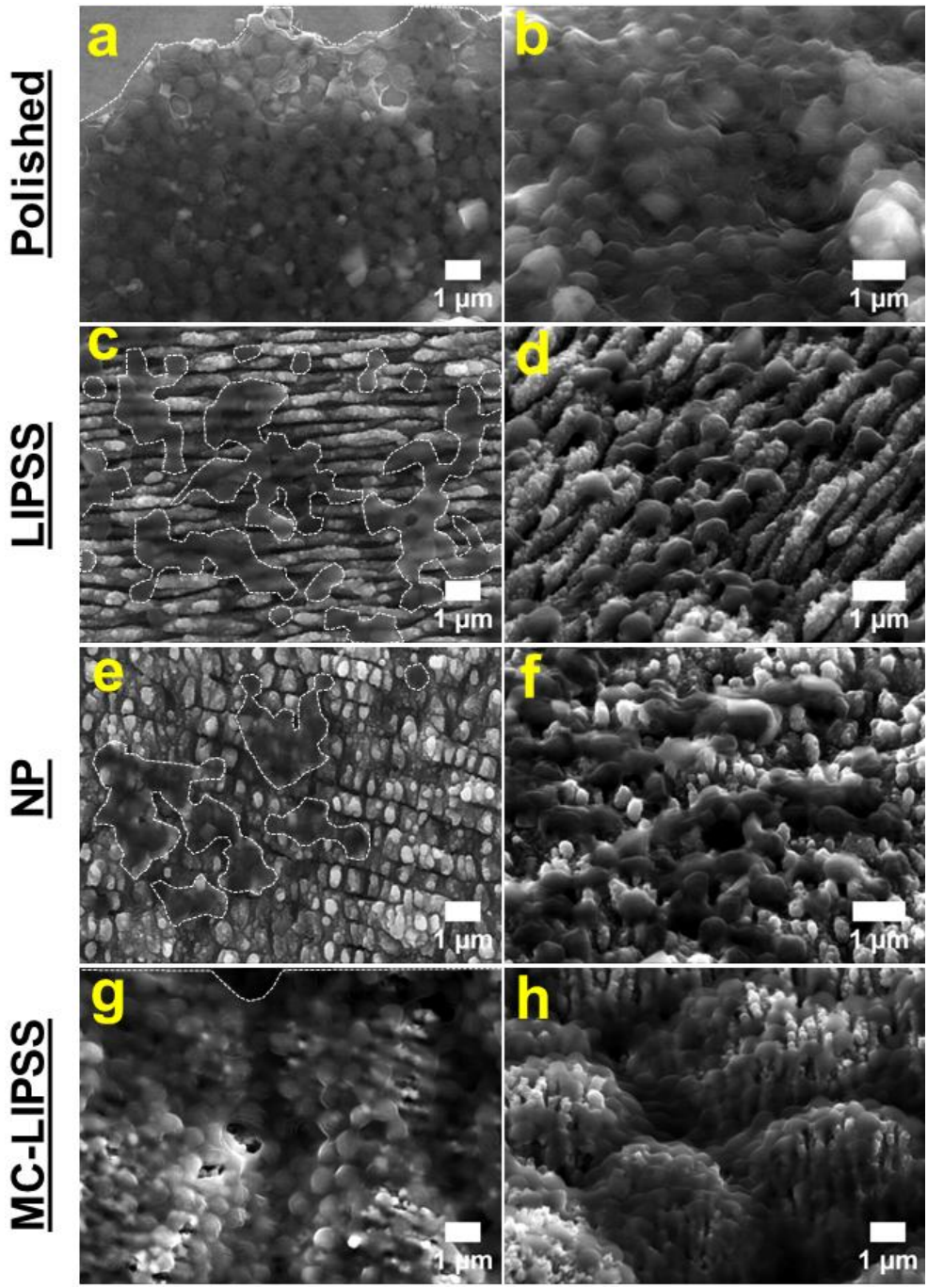

Figure III-47. Representative high magnification SEM micrographs of *Staphylococcus aureus* (ATCC 25923) biofilm on cp Ti surfaces at 48 h after bacteria seeding. Polished (a-b), LIPSS (c-d), NP (e-f), and MC-LIPSS (g-h). SEM micrographs (b, d, f, and h) were acquired at 45° tilting. The dashed white lines (a, c, e and g) were drawed to highlight the bacterial colonies. The scale bar is 1 µm for all images. Similar bacterial biofilm formation was observed for Ti-6Al-4V alloy surfaces.

The Extracellular Polymeric Substance (EPS), which forms the biofilm, is observed on all surfaces. Nevertheless, its development depends on the different surface

topographies. An sticky agglomeration of bacteria (individual cocci), embedded in an continuous EPS layer, is noticeable on polished surfaces (**Figure III-47 a** and **b**). In contrast, two main differences in biofilm formation are evident on LIPSS and NP textured surfaces (**Figure III-47 c** and **e**). First, bacteria agglomeration is strongly decreased, and second, the EPS layer is discontinuous and significantly reduced. In addition, bacteria penetration on these textures is clearly hampered (**Figure III-47 d** and **f**). For instance, in the case of LIPSS textures, the biofilm is formed either along or across the LIPSS crests, but not in their valleys. Finally, bacteria agglomeration is enhanced in the depressions between the microcolumns of MC-LIPSS textured surfaces (**Figure III-47 g** and **h**). The bacteria are continuously covered by the EPS layer in these regions. The biofilm formation was similar for Ti-6Al-4V alloy surfaces (not shown).

2.8.3. Summary of the Results After 48 h of Cell Culture

The major results presented in Sections 2.8.1. and 2.8.2. of Chapter III are summarised as follows:

(a) The adhesion of *Staphylococcus aureus* and biofilm formation are significantly reduced by LIPSS and NP textures as compared to polished and MC-LIPSS textured surfaces;
(b) The Extracellular Polymeric Substance (EPS) layer is discontinuous on LIPSS and NP textured surfaces. On the contrary, the bacteria are covered with a continuous EPS layer on polished and MC-LIPSS textured surfaces.
(c) Large bacterial colonies form in the depressions between the microcolumns of the MC-LIPSS textured surfaces.

3. Biofunctionalised surfaces

In this section, preliminary results on the biofunctionalisation of cp Ti surfaces are presented. As previously mentioned, the strategy for peptide grafting involved three major steps as follows: (i) grafting of an aminofunctional organosilane (APTES) onto the OH groups of the titanium surfaces; (ii) substitution of the terminal amine (NH_2) for an hetero-bifunctional cross-linker (SMP); (iii) reacting the ‘‘outer’’ maleimide group with the thiol group present in the terminal cysteine (C) of the KRGDSPC peptide sequence (**Figure II-13**). The covalent grafting of KRGDSPC peptide sequence was

evaluated by XPS analyses. The distribution and fluorescence intensity of the grafted peptides conjugated with fluorescein isothiocyanate fluorochrome (FITC-KRGDSPC) were evaluated by fluorescence microscopy.

3.1. Confirmation of RGD Peptide Grafting

The alterations of the chemical bondings and atomic composition after each reaction step were monitored by XPS analyses. The atomic composition in percentages (at %) of Ti, Si, O, C, and N on cp Ti surfaces after outgassing, silanization (APTES), reaction with the cross-linker (SMP), and peptide grafting (KRGDSPC) are given in **Table III-6**. After outgassing, trace amounts of impurities (Ca, Na, F, Cl, S, Zn, and Sn) are verified on all the surfaces. These elements may be attributed to bulk material impurities, atmospheric pollution and material manipulation.

Table III-6. XPS atomic composition (at %) of cp Ti surfaces (Polished, LIPSS, NP, and MC-LIPSS) after outgassing, silanization (APTES), reaction with the cross-linker (SMP), and peptide grafting (KRGDSPC).

OUTGASSING								SILANIZATION (APTES)							
Surfaces	**Ti**	**Si**	**O**	**C**	**N**	**Ca**	**Other**	**Surfaces**	**Ti**	**Si**	**O**	**C**	**N**	**Ca**	**Other**
Polished	17.0	-	53.2	27.4	1.1	0.8	Zn: 0.4	Polished	7.7	4.0	41.1	41.2	4.1	0.9	Cl: 1.2
LIPSS	14.5	0.5	48.5	34.2	1.8	0.4	F; Zn: limit	LIPSS	4.1	5.7	32.9	50.7	5.3	0.2	Cl: 1.0
NP	15.7	0.7	50.3	30.0	1.9	0.8	F: 0.8	NP	7.7	4.4	38.8	42.8	5.1	0.3	Cl: 1.0
MC-LIPSS	15.7	0.7	49.9	31.7	1.8	0.3	-	MC-LIPSS	7.2	4.6	38.1	44.0	4.9	0.3	Cl: 0.8
CROSS-LINKER (SMP)								**PEPTIDE GRAFTING (KRGDSPC)**							
Surfaces	**Ti**	**Si**	**O**	**C**	**N**	**Ca**	**Other**	**Surfaces**	**Ti**	**Si**	**O**	**C**	**N**	**Ca**	**Other**
Polished	3.6	5.2	32.8	51.5	4.7	0.6	F; S: limit Zn: 1.0 Cl: 0.7	Polished	5.3	4.6	36.7	46.4	6.6	-	Sn: 0.5
LIPSS	4.8	5.0	34.1	48.1	5.4	0.3	Na: 0.9 Zn: 0.3 F: 0.6 Cl: 0.5	LIPSS	5.2	3.6	36.2	44.6	6.7	0.3	Sn: 0.7 Na: 2.0 Cl: 0.8
NP	3.7	5.3	31.7	51.6	5.9	0.2	Na: 0.5 Zn: 0.5 Cl: 0.6	NP	3.4	4.8	33.0	52.2	5.7	-	Sn: 0.7 Cl: 0.2
MC-LIPSS	7.1	4.2	37.6	43.4	4.9	0.3	Na: 1.1 Zn: 0.3 F: 0.5 Cl: 0.5	MC-LIPSS	7.2	3.9	40.8	41.9	4.9	-	Sn: 1.2

It is noteworthy that the grafted surfaces are quite homogeneous. At least three to five different points of each surface were analysed and the quantifications of the atomic

composition were very similar. Successfully silanization of the surfaces was confirmed by the significant increasing of Si and N concentrations. After silanization, the Si concentration increased to 4.0-5.7 at %, despite its trace amounts (0.5-0.7 at %) on laser textured surfaces before silanization. Similarly, N concentration increased to 4.1-5.3 at %, despite its low concentration (1.1-1.9 at %) before silanization. The experimental measurements lead to a Si:N ratio values in the range 0.9-1.1, which is close to the expected ratio (1:1). The C concentration increased from 27.4-34.2 to 41.2-50.7 at %, due to CH_2-CH_2 and O-CH_2-CH_3 present in the aminosilane (APTES) (**Figure I-14**). Finally, the Ti concentration in the top layer diminished from 14.5-17.0 to 4.1-7.7 at %, as the surfaces are covered by the silane chains. After reaction with the cross-linker (SMP), the addition of maleimide groups from SMP is confirmed by the slight increase of N and C in the ranges 4.7-5.9 and 43.4-51.6 at %. The experimental measurements lead to a N:Si ratio values in the range 0.9-1.2, which is lower than the expected ratio (2:1). It indicates that SMP grafting takes place but without systematic hanging (**Figure I-14**). It may be due to the inacessability of certain amino groups or to the over-size of the cross-linker molecule. Grafting of the RGD peptide sequence is verified by the significant increasing of N concentration (4.9-6.7 at %). The C concentration increased negligibly after RGD peptide grafting.

The alterations of the chemical bondings were studied by analysing the Ti 2p, Si 2p, O 1s, N 1s, and C 1s peaks and their components. The average spectra are presented after each reaction step, since similar peak components were verified for all surfaces. **Figure III-48** depicts the expanded views of Ti 2p and Si 2p regions as well as the peak fitting for polished surfaces of cp Ti. After outgassing, the spectra of Ti 2p region showed peaks (Ti $2p_{3/2}$ and Ti $2p_{1/2}$) with major components centred at 454.0, 455.4, 456.8, and 458.8 and 464.6 eV, which may be assigned to metallic Ti, TiO, Ti_2O_3, and TiO_2, respectively. The component referent to metallic Ti was not verified for LIPSS and MC-LIPSS textured surfaces, but it was still observed on NP textured surfaces (see **Figure III-13**). No additional peak components were observed after APTES, SMP, and peptide grafting steps.

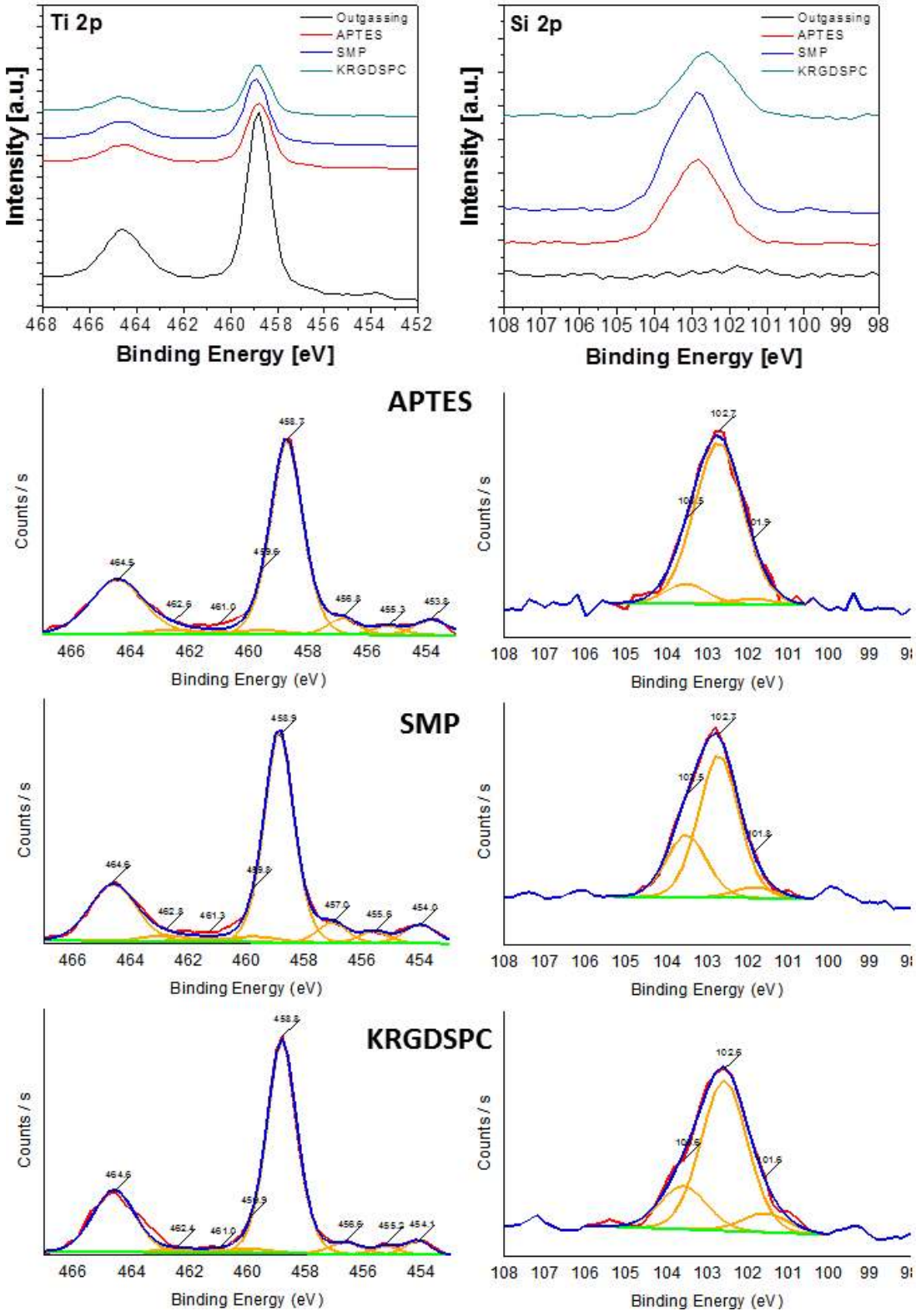

Figure III-48. Expanded views of Ti 2p and Si 2p regions. The average spectra are presented after each reaction step, since similar peak components were observed for all surfaces. Peak fitting for polished surfaces of cp Ti after silanization (APTES), reaction with the cross-linker (SMP), and peptide grafting (KRGDSPC).

The spectra of O 1s region (**Figure III-49**) showed a peak component at 530.4 eV, which indicates oxygen in oxidised state (O^{-2}) due to Ti-O bondings. Before silanization, the spectra of Si 2p region displayed no peak, but a peak (Si $2p_{3/2}$ and Si $2p_{1/2}$) consisting of three components was observed after silanization. The major component centred at 102.7 eV refers in many cases to suboxides of SiO_2 and, more precisely, to oxidation state 3+ of Si [272]. Therefore, this component was attributed to a typical $Si(O_3C)$ bonding. The other two components centred at 101.8 and 103.5 eV correspond to $Si(OC_3)$ pollution forms and SiO_2, respectively. No additional peak components were observed after SMP and peptide grafting steps. The spectra of O 1s presented a new major peak component at 532.8 eV, which may be attributed to Ti-O-Si bondings, confirming a covalent link between the APTES and titanium surfaces.

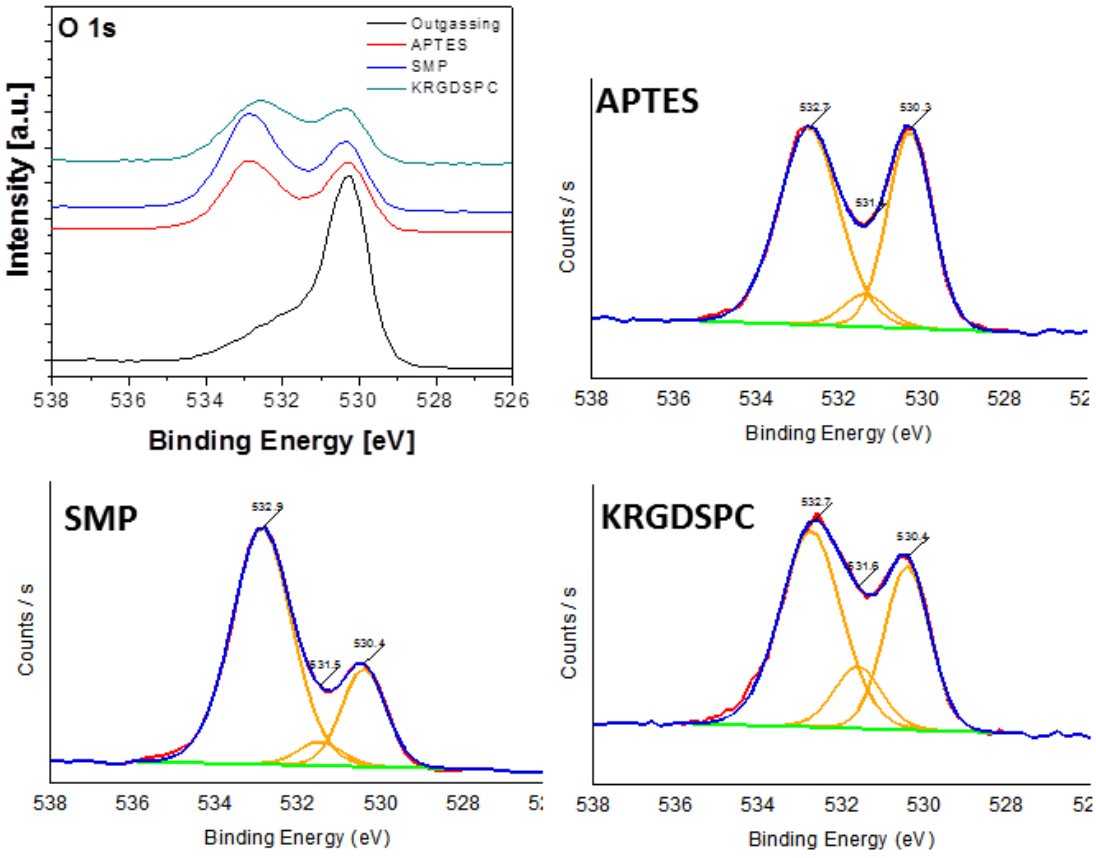

Figure III-49. Expanded views of O 1s region. The average spectra are presented after each reaction step, since similar peak components were observed for all surfaces. Peak fitting for polished surfaces of cp Ti after silanization (APTES), reaction with the cross-linker (SMP), and peptide grafting (KRGDSPC).

While no significant alterations of the chemical bondings were found for Ti 2p and Si 2p regions between the APTES and KRGDSPC steps, the spectra of N 1s and C 1s regions were clearly affected. **Figure III-50** presents the expanded views of N 1s region as well as the peak fitting for LIPSS textured surfaces of cp Ti.

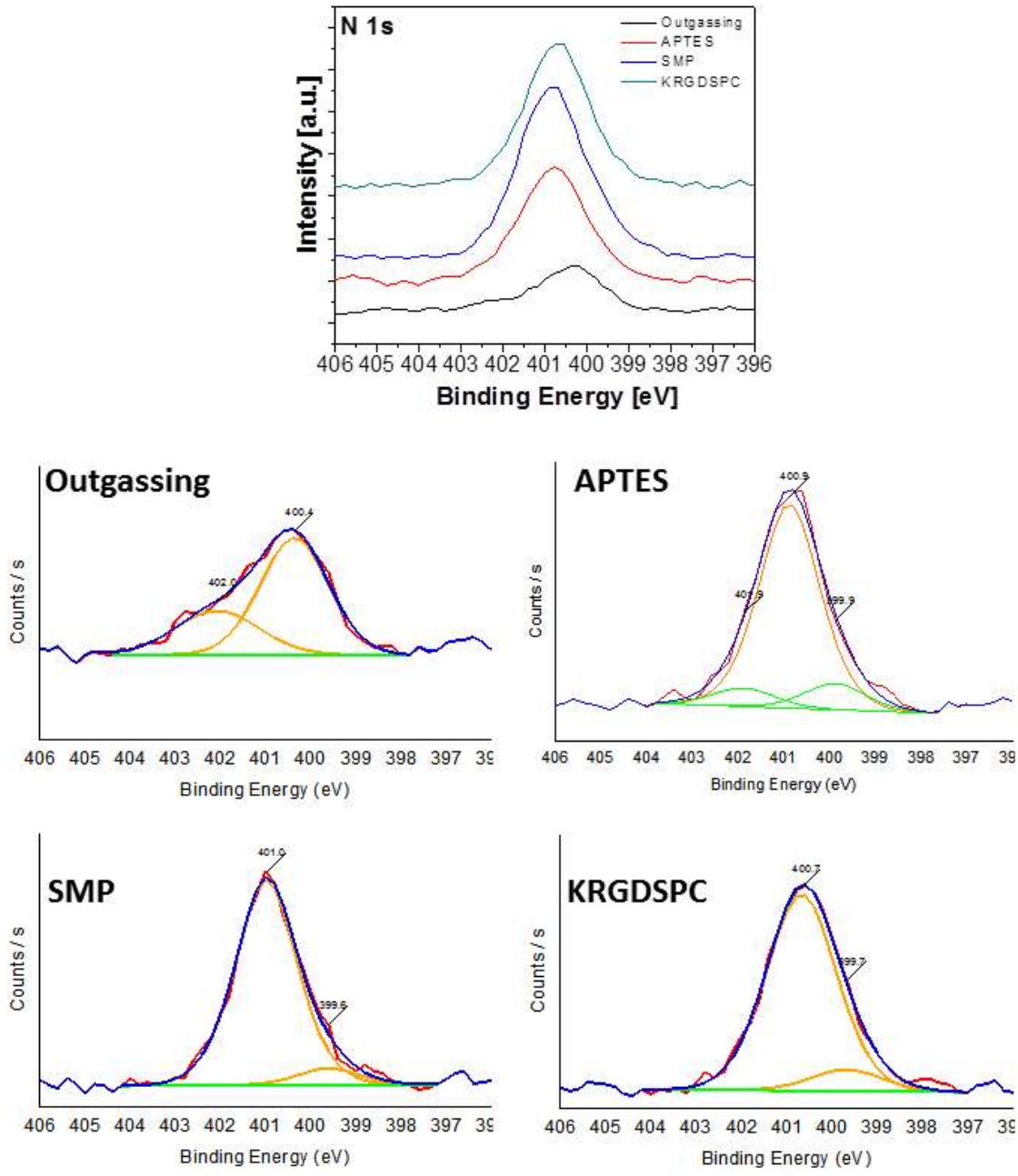

Figure III-50. Expanded views of N 1s. The average spectra are presented after each reaction step, since similar peak components were observed for all surfaces. Peak fitting for LIPSS textured surfaces of cp Ti after outgassing, silanization (APTES), reaction with the cross-linker (SMP), and peptide grafting (KRGDSPC).

After outgassing, a low-intensity and broad peak was verified, consisting of two components centred at about 400.4 and 402.0 eV. The major component (400.4 eV) may indicate nitrogen involved in oxidised environment (N-C=O) or aromatic groups. The high energy component (402.0 eV) could be attributed to surface nitrate (NO_3^-), which may form on metal oxides under environmental conditions [273], or to interactions between NH_2 and OH groups on the surface, or to ionic bonds. Nevertheless, further investigation must be performed in order to elucidate its origin. One possibility could be the existence of TiN, but it presents a lower binding energy (397-398 eV). After silanization, a new component appeared at about 399.8 eV, which can be assigned to -NH_2, while the component at 402.0 eV became much less intense. The increased contribution of the component at about 400.4 eV may be due to some interactions between the terminal amino group (NH_2) and oxygen groups near the surface [21]. After reaction with the cross-linker, the component at 402.0 eV simply vanished, and the other two remained. The component at 399.8 eV decreased, as expected, and the component at about 400.4 eV increased probably due to amide and imide groups. No additional peak components were observed after peptide grafting step.

Figure III-51 presents the expanded views of C 1s region as well as the peak fitting for LIPSS textured surfaces of cp Ti. After outgassing, the spectra of C 1s showed carbon components such as C – C, C – CO, C – O, C = O, and COOR, which are characteristics of pollution contributions. After silanization, the increase of the carbon contribution with smaller oxidised components such as C – CO (285.7 eV), C – O (286.7 eV), and C = O (287.7 eV) may be related to some remaining ethoxy groups of the silane molecules. Unfortunately, it was not possible to determine the exact number of Si-O-Ti bondings per silane molecule, since these latter concentrations cannot be isolated. Regarding the O 1s region (**Figure III-49**), the component at 532.8 eV may not be only attributed to Ti-O-Si bondings, but also to C – O. In addition, the other component at about 531.6 eV can be assigned to C = O. After reaction with the cross-linker, the low-intensity component at about 289.7 eV indicates carboxyl groups (COOH). After RGD peptide grafting, the smaller oxidised components slightly increased, while the ester (COOR) component at 288.7 eV increased significantly. There is an increase of NC=O and COOH groups as expected (**Figure I-14**). Finally, the components centred at about 285.0 eV (C-C; hybridised carbon sp^2 and sp^3) indicate that carbon contamination was present during all the reaction steps.

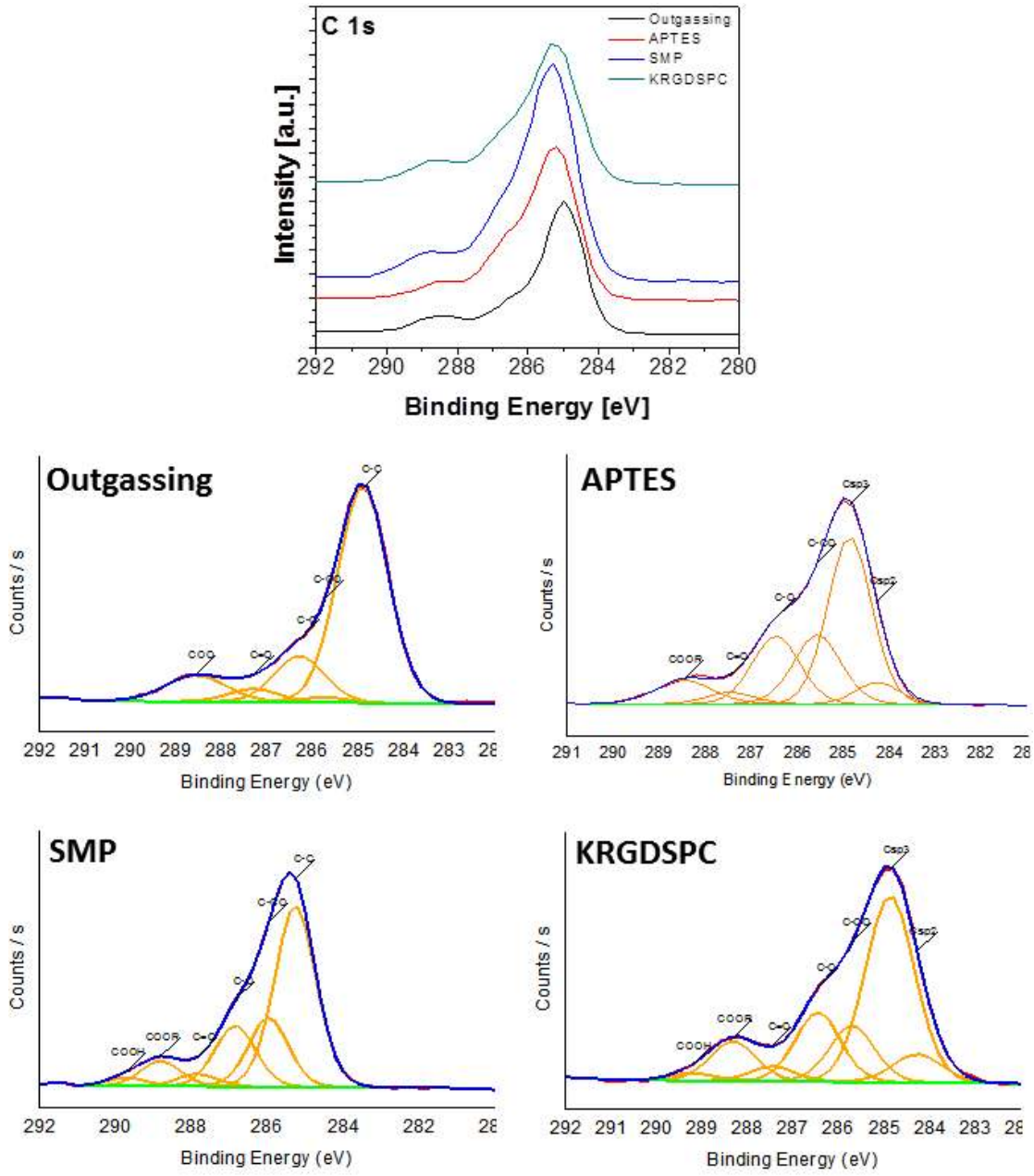

Figure III-51. Expanded views of C 1s. The average spectra are presented after each reaction step, since similar peak components were observed for all surfaces. Peak fitting for LIPSS textured surfaces of cp Ti after outgassing, silanization (APTES), reaction with the cross-linker (SMP), and peptide grafting (KRGDSPC).

3.2. Distribution and Fluorescence Intensity of RGD Peptides

Representative fluorescence images of the FITC-KRGDSPC peptide sequence (green fluorescence) covalently grafted on the laser textured surfaces of cp Ti and its fluorescence intensity are presented in **Figure III-52**.

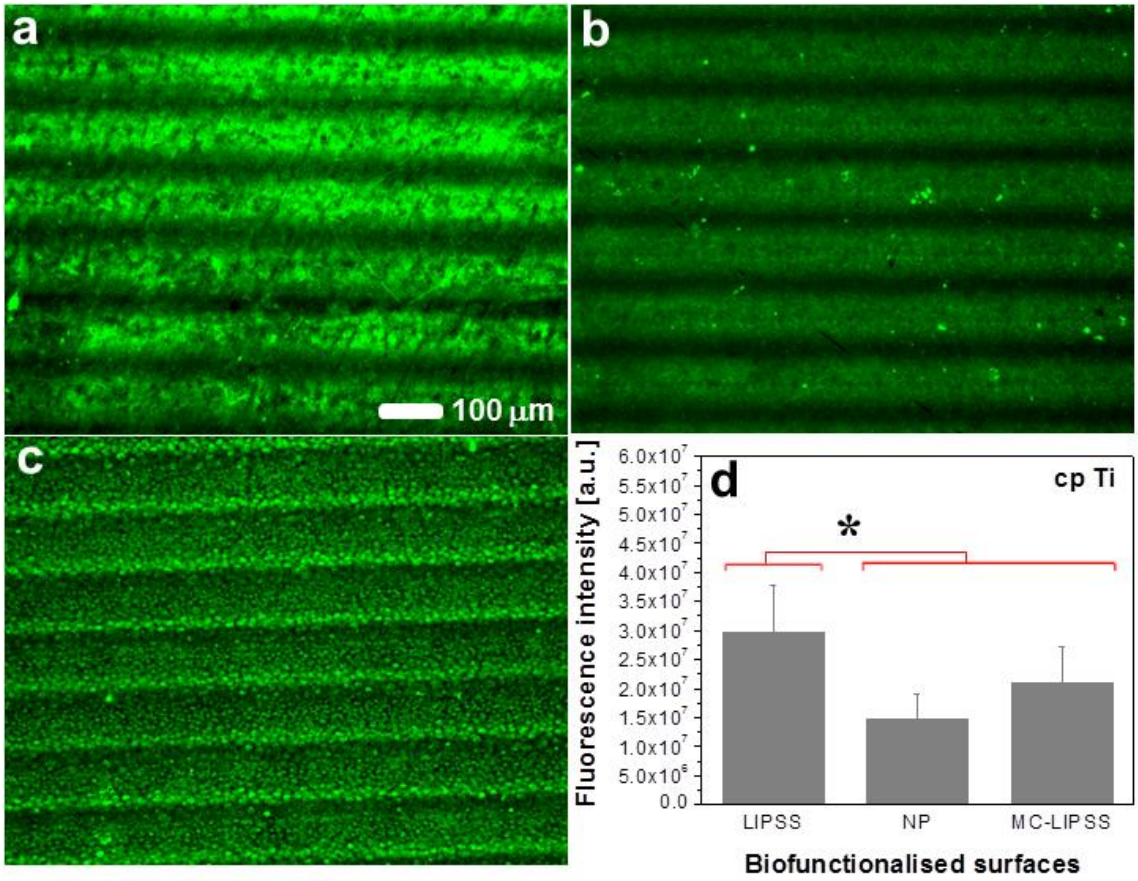

Figure III-52. Representative fluorescence images of the FITC-KRGDSPC peptide sequence (green fluorescence) covalently grafted on LIPSS (a), NP (b), and MC-LIPSS (c) textured surfaces of cp Ti. Fluorescence intensity of the grafted peptides (d). Statistical analysis was performed using ANOVA and Tukey's test. ∗ indicates statistically significant differences between the average values ($p < 0.05$). At least 10 images were analysed for each type of surface. The scale bar is 100 µm for all images. The corresponding surface textures are presented in Figure III-10.

Grafted peptides are clearly observed on all surfaces (**Figure III-52 a-c**) after our RGD grafting process (see Section 2.2. of Chapter II). In general, they seem to be homogeneously distributed around the centre of each laser track for all laser textured surfaces. For LIPSS textured surfaces (**Figure III-52 a**), the peptide aggregation increases significantly as compared to the other surfaces. For NP textured surfaces (**Figure III-52 b**), small aggregates with high fluorescence signal are observed, but it is not possible to confirm if they are grafted peptides. Finally, for MC-LIPSS textured surfaces (**Figure III-52 c**), a slightly larger amount of grafted peptides is observed on microcolumns located in the overlapped regions of the laser tracks. Unfortunately, it was not possible to study the peptide distribution in more detail (higher magnifications) due to the limited magnification of the available lenses. The fluorescence intensity of

the grafted peptides is presented in **Figure III-52 d**. The largest amount of grafted peptides was verified on LIPSS textured surfaces, while it was slightly larger on MC-LIPSS as compared to NP textured surfaces, but the difference is not statistically significative.

3.3. Summary

The major results presented in Sections 3.1. and 3.2. of Chapter III are summarised as follows:

(a) The XPS analyses (atomic compositions and peak fittings) show that KRGDSPC peptide grafting on cp Ti surfaces was successfully achieved;
(b) Both the XPS and fluorescence microscopy analyses indicate that the grafted surfaces are quite homogeneous;
(c) The fluorescence microscopy analysis shows that the grafted peptides seem to be homogeneously distributed around the centre of each laser track for all laser textured surfaces;
(d) The largest amount of grafted peptides was observed on LIPSS textured surfaces, while no statistically significative differences between MC-LIPSS and NP textured surfaces were found.

Chapter IV. Discussion

This Section is organised according to the main topics of the present work.

- Surface modification of titanium implants vs Biological response;
- Laser-induced surface textures;
- Surface topography, chemical composition, and crystallographic structure of titanium implants;
- Wettability of titanium implants;
- MSCs adhesion, spreading and shape;
- MSCs proliferation, commitment and differentiation;
- Implant-associated infections;
- Biofunctionalisation of titanium implants.

1. Surface Modification of Titanium Implants vs Biological Response

With the discovery of the osseointegration phenomena [274], the search for an "ideal" implant surface has been one of the key issues in the search for improved dental and orthopaedic implants. The ideal implant surface should promote rapid and controlled healing of the surgical wound and bone formation, while reducing bacteria colonisation and biofilm growth. Currently, the behaviour of cells (MSCs, osteoblasts, fibroblasts, bacteria, etc) in contact with implant surfaces and its dependence on surface properties (roughness, surface anisotropy, wettability, surface free energy, chemical composition, among others) is established, but it is still an open research field. Taking profit of this improved knowledge of cell-surface interactions, surface modification methods have been widely used for the tailoring of Ti-implants topography and chemical composition in order to promote the intended cell behaviour.

The major goal of the present work was to explore the potential of ultrafast lasers for the surface modification of Grade 2 Ti (cp-commercially pure) and Grade 5 Ti-6Al-4V alloys. These alloys are widely used in dental and orthopaedic implants, due to their low Young modulus, superior biocompatibility and high corrosion resistance as compared to stainless steel and cobalt-based alloys (see Section 3.2. of Chapter I).

2. Laser-Induced Surface Textures

The laser textured surfaces consist of surface structures such as laser-induced periodic surface structures (LIPSS) and microcolumns (see Sections 5.2.1. and 5.2.2. of Chapter I). When the laser treatment is performed with average fluences in the range 0.1-0.3 J/cm^2, a surface waviness, usually called LIPSS appears. It is oriented perpendicularly to the polarisation direction of the linearly polarised laser beam. LIPSS are observed in a wide range of laser textured materials and exist in two types differentiated by their periodicity as compared to the radiation wavelength. Low spatial frequency LIPSS (LSFLs) have a period of the same order of magnitude of the radiation wavelength (in general slightly inferior), while high spatial frequency LIPSS (HSFLs) have periods of a few hundred nanometres. The formation of LSFLs was explained by the interference between the incident laser beam and surface scattered electromagnetic waves [105], and a first-principles theory for their formation was proposed by Sipe *et al.* [108]. Currently, these surface electromagnetic waves are believed to be surface plasmons polaritons (SPPs) [111]. In contrast, the mechanisms of formation of HSFLs is still under debate. Several mechanisms were proposed to explain their formation such as self-organisation [275], second-harmonic generation [120], and Mie scattering [96]. The periodicity and orientation of LIPSS depend on the radiation wavelength, angle of incidence, and laser beam polarisation. The LIPSS textured surfaces produced in the present work consist of LSFLs with a periodicity slightly smaller than the radiation wavelength (~700-800 as compared to 1030 nm, respectively). Since LIPSS are polarisation-sensitive structures their orientation in relation to the laser beam scanning direction can be varied by rotating the polarisation vector by optical means. In the present case, a half-wave plate was introduced in the optical path to rotate the polarisation vector. Taking profit of the possibility of controlling the polarisation direction, a surface texture consisting of an array of nanopillars (NP) was produced by treating the same area twice with the beam polarisation, mutually oriented in perpendicular directions and parameters suitable to form LIPSS. To our knowledge this nanopillar-like structures is a novel type of laser-induced texture. The NP only formed when the second laser treatment was performed with a fluence and number of pulses slightly lower than those applied in the first treatment to avoid obliteration of the original texture. In these conditions the LIPSS formed in the first treatment were partially fragmented, giving rise to the nanopillars. When similar parameters were used

for the two treatments, the LIPSS formed in the second one obliterate completely those produced in the first treatment, and only the latter were observed.

For larger values of the average fluence (0.4-1.0 J/cm^2) ablation is more intense and a columnar texture forms (MC-LIPSS). These micron-sized features (columns, cones, pillars, etc.) have been observed since many years in laser textured surfaces. They are highly dependent on the properties of the material as well as on the laser processing parameters and conditions, including the radiation fluence, number of pulses, radiation wavelength, laser pulse duration, and atmospheric conditions. Their formation mechanisms were the object of intense controversy, being attributed to radiation shadowing by impurities [127], differential ablation [128], hydrodynamic effects [129], or to the influence of the material phase distribution on radiation absorption [130], the latter mechanism leading to columnar textures which are commensurate with the material microstructure. Very recently, Zuhlke *et al.* [131] demonstrated that the development of these surface structures on nickel (Ni) is characterised by a balance of growth mechanisms, such as scattering from surface structures and geometric effects causing preferential ablation in the valleys, flow of the molten material, and redeposition of ablated material. Fadeeva *et al.* [247] suggested that the main processes responsible for columns formation on titanium surfaces, include melting, resolidification, and surface roughening at the early stage, followed by ablation during the late-stage of formation. Depending on the fluence and number of pulses, these structures may growth below (below-surface-growth, BSG) or above (above-surface-growth, ASG) the original surface of the material. In the present work, the columnar structures formed below the original titanium surfaces and may be classified as BSG structures. Interestingly, when the laser treatment is performed in non-stationary conditions, these columnar structures are covered with LIPSS, leading to a surface texture with a bimodal roughness distribution. The formation of this texture was explained in a previous publication [16]. Since the spatial profile of the laser beam is Gaussian, each point of the material surface is subjected to varying fluences when the sample moves linearly under the stationary laser beam. When the fluence corresponding to the maximum radiation intensity in the transverse cross-section of the laser beam is considerably higher than the damage-threshold (~0.1 J/cm^2) columns will form. As the laser beam moves away the same area is irradiated with lower fluences, at the periphery of the spot, and LIPSS will form. As a result all points of the surface are consecutively

submitted to high fluences, leading to the formation of microcolumns, then to low fluences, leading to the formation of LIPSS, which overlap the microcolumns. Very recently, Ionin *et al.* [133] developed a new method for manipulating the nanotopography of these columnar microstructures. This method involves laser beam shaping, e.g., by breaking the symmetry of the Gaussian spatial profile of the laser beam using an oblique knife-edge screen before the laser beam impinges on the sample surface. The cut laser beam is then scanned over the material surface in two opposite directions. Depending on the scanning direction LIPSS will form or not. In the present work, LIPSS always form on the top of the columnar structures.

3. Surface Topography, Chemical Composition and Crystallographic Structure of Titanium Implants

We investigated the topography, chemical composition, and crystallographic structure of the laser textured surfaces (see Sections 2.2., 2.3., and 2.4 of Chapter III). The results achieved show that femtosecond lasers allow creating different types of textures with various degrees of anisotropy and different roughness distributions on Ti implants. In terms of anisotropy, LIPSS textured surfaces are clearly anisotropic due to the preferential orientation of the surface structures. On the contrary, NP textured surfaces are isotropic because the anisotropy resulting from the first treatment is obliterated when the LIPSS initially produced are fragmented by the second treatment. MC-LIPSS textured surfaces may be also considered isotropic because the cross-section of the microcolumns is roughly circular and they are randomly distributed over the treated area. In terms of surface roughness, the amplitude roughness parameters R_a and R_Z were measured because they are the most frequently used surface roughness parameters [51]. Since these parameters only give information on the asperities height, R_{Sk} and R_{Ku} were also assessed because they provide information on the sharpness or peakedness of the textured surfaces [269]. The present results show that the surface roughness (R_a and R_z) is affected by the radiation fluence and number of laser pulses. A more detailed study of the variation of the roughness parameters with the laser processing parameters is suggested for a future work. At this point, we showed that an increase of the radiation fluence and number of laser pulses by about 8 and 6 times, respectively, promotes a 4-fold increase in surface roughness, due to more intense ablation of the material. This increase in roughness is evident when comparing LIPSS

and NP textured surfaces with the MC-LIPSS surfaces. In terms of peak distribution and shape, the R_{Sk} and R_{Ku} parameters show that the laser textured surfaces present more peaks than valleys. The peaks are rounded as can be seen in the 2D surface profiles (see **Figure III-11**). These roughness parameters are independent of the laser processing parameters. Finally, it may be concluded that the ablation threshold and the ablation behaviour of the two Ti alloys are similar, and the surface texture does not depend on the alloy composition.

In terms of surface chemical composition, XPS analysis indicates the presence of an oxide layer, consisting mainly of TiO_2 for cp Ti and a mixture of TiO_2 and Al_2O_3 for Ti-6Al-4V alloy, independently of the surface texture. In addition, minor amounts of substoichiometric TiO and Ti_2O_3 oxides were also observed for both Ti alloys. The presence of oxide on titanium surfaces is expected, since this is a highly reactive metal and reacts with oxygen within microseconds after exposure to air [37]. The laser treatment in ambient atmosphere causes further oxidation of the metal. This laser-induced oxidation may be attributed to the high temperatures attained on metallic titanium surfaces during the laser treatment [276]. The presence of a titanium oxide layer leads to excellent biocompatibility and high corrosion resistance, due to its low electronic conductivity and a thermodynamically stable nature at physiological pH values [277, 278]. The oxide layer also easily incorporates mineral ions (calcium-phosphates), water, and other constituents when in contact with the biological environment favouring mineralisation [45-48]. Trace amounts of S, Cl, Si, Na, Zn, Ca, and N were also found. These inorganic elements are often observed in some titanium surfaces by using XPS and AES [279]. They may originate from segregation to the surface of small amounts of bulk impurities or from contamination. The high carbon content observed in the laser treated surfaces may be attributed to surface contamination by adsorbed carbon-containing molecules, which occurs frequently on air exposed surfaces. These carbon-containing molecules may also originate from the solvents used for cleaning the specimens.

Micro-Raman spectroscopy provides complementary information on the composition of the oxide layer. The results achieved show that the TiO_2 layer consists of both anatase and rutile polymorphs. A significant broadening and slight shift of the TiO_2 Raman bands was observed, indicating the presence of short-range order and/or oxygen vacancies in the TiO_2 crystals [280, 281]. The oxide layer varies in thickness

from point to point, as shown by both the absence of TiO_2 Raman bands in some areas of the analysed surface, and the observation of a metallic Ti peak by XPS in NP laser textured surfaces. A possible explanation must take into account the size and depth of the analysed region inherent to both techniques. Due to the large spot size (~ 250 μm) and reduced depth of analysis (~ 7-11 nm) of XPS, the Ti oxide signature peaks are always observed and information regarding the homogeneity and thickness of the oxide layer is lost. On the contrary, the small spot size (~ 1μm) and large analysis depth (~ 4 μm) of μ-Raman, allow observing very localised areas deeper into the oxide layer, revealing its discontinuities and differences in thickness. Finally, Al_2O_3 is reported to have active Raman bands [282, 283], but these were not detected on the Ti-6Al-4V surfaces showing that Al_2O_3 exists only in small proportion in the surface oxide film and concentrates near its outer surface (it was observed by XPS and not μ-Raman). The presence of TiO_2 in the surface oxide layer in the anatase and rutile forms were also coinfirmed by XRD. The other diffraction peaks detected correspond to the α-phase (hcp) of Ti.

4. Wettability of Titanium Implants

During the early stages of bone formation the adsorption of biological fluids, such as water, blood, saline and proteins solutions on the implant surface plays a crucial role in cell adhesion and differentiation [8]. In particular, the cells interact directly with the proteins adsorbed at the implant surfaces, and consequently the proteinaceous film plays an essential role on cell behaviour. Therefore, controlling the wettability of the implant surface is one of the key issues for ensuring biocompatibility. The results achieved show that the laser treatment increases significantly the wettability of the surfaces by biological fluids (see Section 2.5. of Chapter III). This enhanced wettability as compared to polished surfaces may be attributed to the larger surface free energy (γ_{SV}) of the laser textured material, mainly due to its polar component (γ_{SV}^{p}). Enhanced adsorption and spreading of cell adhesion proteins such as fibronectin and vitronectin on hydrophilic surfaces have been reported [135, 284]. Conversely, albumin, which inhibits cell adhesion, is known to have high affinity to hydrophobic surfaces [285]. Thus, the enhanced wettability of the laser textured surfaces may facilitate the adsorption of cell adhesion proteins while reducing the adsorption of albumin. Further

research is required in order to understand the effect of the improved wettability of the laser treated surfaces on the adsorption of proteins.

The wettability depends on the surface chemical composition and topography [134]. Oxidised titanium surfaces were reported to be hydrophilic [286], so laser-induced oxidation will certainly contribute to enhanced hydrophilicity. The polished (control) surfaces of both Ti alloys are also oxidised (native oxide layer), so the fact that the laser textured surfaces present contact angles smaller or similar to polished surfaces indicates that surface topography plays an important role in controlling wettability. The wetting behaviour of rough surfaces is commonly described by Wenzel and Cassie-Baxter models [136, 139]. In general, laser textured surfaces conform to Wenzel's model, leading to the conclusion that surface roughness enhances the wettability of the material. Thus, the liquid is assumed to be in contact with the whole area of the rough surface.

The wetting behaviour is affected by the anisotropy of the surface texture. For instance, LIPSS and NP textured surfaces have very similar R_a and R_z (~ 300 nm and 1.2 μm, respectively), but their wettability is quite different, especially for HBSS due to the anisotropy of LIPSS. The preferential orientation of LIPSS drives spreading of biological fluids along the nanogrooves, leading to lower contact angles in the LIPSS direction than in the perpendicular direction. In a previous publication [98], we studied the wetting behaviour of a fourth type of surface texture, consisting of microcolumns covered with LIPSS but in contrast to MC-LIPSS texture, it presents periodic ridges consisting of large elliptical columns aligned in the laser beam scanning direction. The ridges are separated by wide depressions consisting of columns similar to those found in MC-LIPSS texture. The periodicity of the ridges is equal to the lateral displacement of the laser beam to overlap contiguous laser tracks (d_{lat} = 200 μm). The roughness parameters of this surface are R_a = 4.7 ± 0.6 μm and R_z = 26.8 ± 2.3 μm. According to the Cassie-Baxter's model, very rough surfaces (for instance, R_a = 4.7 μm) should be treated as having two distinct components, the substrate and air because air tends to remain trapped in the surface irregularities, and this interface structure should lead to low wettability ($\theta_r^C > \theta_c$; see Section 6.2. of Chapter I). However, this texture leads to better wettability than polished surfaces, as shown by the very low contact angles observed for both liquids, and HBSS even spread spontaneously all over the treated

area, forming a continuous film (superwetting). This behaviour can be explained by the effect of capillarity, which drives the liquid into the deep valleys existing between the ridges, expulsing the trapped air as the liquid penetrates. These findings indicate that the surface anisotropy plays an important and crucial role in the wetting, and anisotropic textures lead to better wettability than isotropic ones. Anisotropic wetting was previously observed on several studies using periodic grooved surfaces [146, 287]. Chung *et al.* [287] observed anisotropic wetting on micro-wrinkled surfaces with well-defined aspect ratio (amplitude vs wavelength of wrinkles) groove patterns, which resemble the LIPSS. The authors observed smaller contact angles in the direction of the grooves than in the direction perpendicular to them. This behaviour can be explained by the fact that the periodic grooves create an energy barrier to the movement of a three-phase contact line moving perpendicularly to them and facilitate the movement in the grooves direction. As a result, droplets are elongated in the direction of the grooves, because no barriers to contact-line motion that would cause pinning exist in this direction.

We also investigated the droplets spreading kinetics. Previous studies showed that the dynamic contact angle and the droplet contact area radius usually vary with time according to a power law $y(x) = kx^n$ [256, 257]. The exponent n, known as the spreading coefficient, characterises the spreading velocity, with higher absolute values of n indicating faster spreading. In general, the droplets of both liquids spread faster on the anisotropic LIPSS texture than on isotropic NP and MC-LIPSS ones, especially for HBSS. This confirms the importance of surface anisotropy on wettability. The larger n values observed for HBSS as compared to water cannot be explained by a surface tension effect because the surface tensions of HBSS and water at ambient temperature are similar (72.2±0.3 and 72.0±0.9 mN/m, respectively) [288], and the HBSS solution is too diluted to affect significantly the properties of the liquid. The faster spreading observed of HBSS droplets suggests a high affinity of the ionic species and/or D-glucose in solution in this liquid to the laser textured surfaces. The values of n found in the literature are mostly in the range 0.1-0.2 [256, 257], but values as low as 0.06 and as high as 0.6 were measured, depending on the wetting regime. In the present work, the values of n vary in the range 0.04-0.1. These low spreading coefficients are certainly due to the specific geometry of the laser-induced textures, but chemical changes in the surface may also play a role and this point requires further investigation. It should be

emphasised that this power law cannot be applied to cp Ti surfaces because the variation in contact angle during 600 s is negligible. We hypothesise that this different wetting behaviour is due to differences in surface chemistry of both Ti alloys, but further studies are necessary to elucidate this.

It has been reported that the wettability of laser textured surfaces of semiconductor and metallic materials may change over time [137, 151]. Kietzig *et al.* [137] found that the wettability of Ti-6Al-4V alloy surfaces with textures similar to those produced in this work, evolved from a superhydrophilic to a superhydrophobic state over time during the first 60 days after the laser treatment. This evolution was slower for surfaces treated with fluences higher than 2.83 J/cm^2. To avoid this problem, the fluence used in the present work was limited to the range 0.2-0.8 J/cm^2, and the XPS and μ-Raman results and the wettability measurements performed at least two months after the laser treatment. They revealed that the surface properties were stable in the long term.

In summary, we show that surface texturing of Ti implants using direct writing with a femtosecond laser enhances the wettability of the surfaces by water and HBSS, and is a potential method for increasing the adsorption and spreading of cell adhesion proteins such as fibronectin and vitronectin.

5. MSCs Adhesion, Spreading and Shape

Adhesion is a key factor for cell viability and subsequent development of cellular functions. In contrast, lack of cell adhesion leads to programmed cell death (apoptosis) [289, 290]. *In vivo*, cells adhere to the ECM, other cells, and implant surfaces. Therefore, the cytocompatibility of an implant may be directly related to cell adhesion.

In this work, the MSCs adhesion was evaluated after 24 h of culture. Cells spread on all surfaces of both Ti alloys and the cytoskeleton and cell nucleus preserve their integrity. The interaction between the cells and the laser textured surfaces was supported by our SEM micrographs. They show that the cell cytoskeleton deforms according to the underlying texture, indicating a strongly contact with the surface features through topography imprinting onto the cells cytoskeletons. Previous studies have also demonstrated the effect of nanotopography imprinting onto cell behaviour [291, 292], and it was found that when cells adhere to nanostructured surfaces they develop an imprint of the topography not only on the cell surface but also visible from

the other side of the cell, when the cell is thin. Nevertheless, it is not known yet if this nanoimprinting mechanism affects the signal transduction system. Moreover, our results on the cell density indicate satisfactory cell adhesion. Cells were initially seeded at a density of ~ 10^4 cells/cm^2, and after 24 h of culture a cell density of ~ 10^3 cells/cm^2 was verified on the titanium surfaces. Taken together, all these observations show that the investigated titanium surfaces provide a friendly environment for MSCs recruitment.

Importantly, the laser treatment does not lead to a decrease of the cell density, which is similar to the one verified for polished surfaces. This suggests that the topographical and chemical differences between the surfaces do not affect the cell density significantly. On the contrary, the surface free energy (γ_{SV}) play an important role on the observed cell density. A previous study showed that γ_{SV} affects fibroblasts adhesion to surfaces [293], the highest cell density being observed for surfaces with the larger γ_{SV} (40-50 mN/m). In the present study, the γ_{SV} values for cp Ti (55-75 mN/m) and Ti-6Al-4V alloy (42-50 mN/m) surfaces are in this range, and this may contribute for the large cell density. Moreover, the fact that γ_{SV} is larger for cp Ti as compared to Ti-6Al-4V does not increase significantly the number of adhered cells. This point needs further investigation in order to better elucidate the impact of the surface free energy on the MSCs adhesion.

Cells may alter their adhesive behaviour in response to changes in the molecular composition and physical forces present in their environment [62, 216]. Once cells bind to some motif located on the extracellular matrix (ECM) molecules, a signalling feedback pathway initiates integrin clustering and focal adhesion formation, in association with cytoskeleton proteins such as vinculin, talin, paxillin, focal adhesion kinase (FAK) and tensin, linking dynamically the ECM to intracellular actin filaments (see **Figure I-27**). In the present work, the formation of adhesion sites was confirmed by the observation of vinculin which demonstrates integrin clustering (see **Figure III-28**). Despite the similarity of cell density for all textures and both Ti alloys, the quantitative analysis of the focal adhesions (FAs) area indicates that the cells adhesion strength depends on the surface topography. It is evident that the laser treatment decreases the adhesion strength of cells as compared to the polished surfaces. In fact, model surfaces with well defined topography provided detailed information on the cell response to these topographies [294]. Surface topography, in particular at the nanoscale, may increase or decrease cellular adhesion, depending on the dimensions and density of

the surface features [295]. The reinforcement or disruption of adhesion sites depend on the efficiency of integrin clustering. The surface structures investigated here resembles protusions (NP and MC-LIPSS) and grooves (LIPSS) [218, 296]. Increasing the height of random or semirandom protusions (> 70 nm) tends to decrease focal adhesion formation by disrupting integrin clustering. The protusion diameter and density also play an important role on cell adhesion, because they dictate whether cells adhere exclusively at their apexes or on the basal surface. Large interprotusion distances (> 70 nm) also decrease focal adhesion formation. Our results are in agreement with these observations. The dimensions of the surface features present on NP and MC-LIPSS surfaces are significant larger than the reported thresholds, and they are expected to hinder effective integrin clustering. The same rationale is likely to apply to the periodicity and height of LIPSS.

Grooved topographies such as LIPSS usually cause cell alignment and contact guidance [9, 100, 262, 297]. Our findings for LIPSS agree well with those results. When the front edge of the cell encounters a ridge or groove wall, the cell experiences unfavourable forces that inhibit actin polymerisation. In response to these forces the cell elongates along the grooves, where less resistance is offered. Surfaces providing cell contact guidance are useful for reduction of scar tissue formation, which occurs due to random cell growth and leads to poor tissue integration [298, 299]. In this sense, LIPSS could reduce scar tissue formation. Previous studies show that cell alignment depends on the groove periodicity and depth, but depth is more influential. [300]. Recently, the anisotropic behaviour of human dermal fibroblasts was studied in function of the aspect ratio of gratings in the range 0.01 to 1.0 [219]. The authors showed that the aspect ratio of the gratings is the more consistent parameter to interpret the topographic dependence of the cell morphology, and that cell alignment and elongation depend on this ratio. The LIPSS produced in the present work have an aspect ratio in the range 0.3-0.4, favouring cell alignment. It must also be emphasised that the definition of cell alignment is controversial in itself. The established threshold value of the orientation angle (~ 10-20°) varies for different studies [301-303], either due to differences in the type of cell used and different definitions of alignment. Our results on cell alignment show that most of the cells align at an angle ranging from nearly 0 to 30°. It fairly agrees with the reported range of alignment angles previous established.

The formation of filopodia extensions and low cell spreading characterise surfaces where adhesion is low [292]. These observations agree with the extensive production of filopodia when cells adhere to the laser textured surfaces, mainly to NP surfaces. Cellular spreading is also significantly reduced on these surfaces. Filopodia are the main nanosensory tools of cells and are responsible for probing the external environment to gather spatial, topographical and chemical information. Therefore, filopodia formation is directly linked to cell movement. These principles help us explaining the cell adhesion and spreading behaviour on laser textured surfaces as compared to polished surfaces. On the laser textured surfaces cells exist in a dynamic state and consequently form transient focal adhesions (FAs) until they find suitable sites for permanent adhesion and spreading.

The adhesion sites assume different sizes, structure, composition, and stability depending on their degree of maturation. Ward and Hamer [304] developed a model of adhesion strengthening, which predicts a large increase in the adhesion strength after increased integrin clustering and adhesion size, marked by an elongation of the adhesion plaque. This process is believed to occur due to an increase in intracellular and/or extracelullar tension at the adhesion site, since the focal adhesion size is proportional to the force applied by the cell to it. Based on this model, well developed adhesion sites are indicated by an elongated focal adhesion shape. Accordingly, the presence of elongated FAs on cultured cells indicates mature FAs and shows that despite the low-adhesion character of the laser textured surfaces, the FAs mature and cell survival is ensured.

Finally, in this study the FAs were studied after 24 h of cell culture, but it is strongly suggested the study of FAs after 6 h, 2 and 4 weeks of cell culture in order to perceive how cell adhesion strength evolves with time.

6. MSCs Proliferation, Commitment and Differentiation

The positive values of cell proliferation (2 weeks) indicate that cells were able to undergo proliferation and colonised the implant surfaces. Nevertheless, cell proliferation varies with the substrate. While cell proliferation on laser textured cp Ti surfaces is similar to polished surfaces, it is lower for the textured Ti-6Al-4V alloy surfaces. The possible explanation is the difference in oxide composition, namely the

concentration of Al_2O_3 at the surface of the TiO_2 film formed in this alloy, but further investigation must be performed to better understand this behaviour. The study of MSCs proliferation on TiO_2 / Al_2O_3 coatings, with varying concentrations, on polished substrates is suggested as one strategy to investigate this hypothesis.

Osteoblastic commitment (2 weeks) was observed for all surface topographies and both Ti alloys. This is confirmed by the expression of specific osteoblast markers such as osterix (OSX) and osteopontin (OPN) [157]. The laser treatment preserves the bone-forming capability of the implant surfaces. This observed osteoblastic differentiation may be compared with the studies reported in the literature. Firstly, it has been shown that cell proliferation and differentiation are inversely related (see **Figure I-32**). It suggests that a high proliferative state exists prior to differentiation and that proliferation is significantly reduced in mature differentiated cells [305]. In the present work, both the large expression levels of osteoblast markers and matrix mineralisation on Ti-6Al-4V alloy surfaces as compared to cp Ti surfaces, can be explained by the lower proliferation rate of the cells. Secondly, there is strong evidence that both the focal adhesions and the cytoskeleton shape are regulators of cellular survival, growth, and differentiation and may be indicators of the cell fate [294, 306-308]. Based on this hypothesis, osteoblastic lineage commitment is normally observed on cells that are allowed to spread, generating tension on the actin filaments, since high actomyosin contractility is one of the factors responsible for inducing osteogenic differentiation. The stresses on actin filaments are transmitted to the FAs, which tend to growth and elongate in the stress direction. Although we did not measure the cytoskeleton tension, it is clear that tensions exist (stress fibres and elongated FAs) in cells cultured on all the textures and both Ti alloys.

In general, we found that the laser treatment does not affect significantly the expression of the osteoblast markers (OSX and OPN) after 2 weeks of culture, as compared to polished surfaces. If we consider the lower cell adhesion and spreading on the laser textured surfaces in comparison with the polished surfaces after 24 h of culture, a significant decrease of the osteoblast markers expression would be expected for cells cultured on the textured surfaces. However, this is not observed. We believe that the similar expression levels of the osteoblast markers is due to an strong increase in cell adhesion and spreading between 24 h and 2 weeks on the laser textured surfaces.

For instance, this is evident on NP textured surfaces in which cell spreading increases and the number of filopodia decreases after 2 weeks as compared to 24 h of culture.

Our results also show the important role of soluble factors, namely β-glycerophosphate, dexamethasone, and ascorbic acid on the osteoblastic differentiation and matrix mineralisation. After 4 weeks of culture, there are no traces of matrix mineralisation for cells cultured in Alpha-MEM medium while the opposite occurs when the cells are cultured in an osteogenic medium. Most importantly, we found that LIPSS and NP textures enhance the effect of the osteogenic factors, as indicated by bone-like nodules formation.

7. Implant-Associated Infections

The formation of pathogenic bacterial biofilms on the surface of implants is one of the most common causes of their failure, often resulting in the necessity to surgically remove the implant [207, 309]. Biofilms trigger infections that prevent osseointegration and lead to inflammatory destruction of joints and bone [7]. Moreover, the rise of bacterial resistance to antibiotics and the difficult of treating these infections after biofilm growth, increase considerably the risk of infection. Therefore, the development of implant surfaces capable of preventing or reducing bacteria adhesion and biofilm formation is of upmost importance. Currently, silver- and silver nitrate-based coatings, composites of silver or titania nanoparticles in polymer matrices, drug-functionalised polymeric nanoparticles, protein-resistant coatings, and covalent immobilisation of antibacterial molecules have all been tested for this purpose [53]. However, the antibacterial effect of most of these surface treatments is not achieved without risk for the patient, due to the potential toxicity of the agents used. Silver is known to be cytotoxic and some antibacterial substances may lyse the membrane of host cells. Thus, the design and fabrication of antifouling surfaces by surface structuring is an attractive solution for the prevention of bacterial adhesion and subsequent biofilm formation.

The laser treatment has the advantage that topographical modifications do not produce any harmful effect on host tissues. In addition, the risk of surface degration in the physiological environment is negligible. Our results show that LIPSS and NP surfaces reduce significantly the adhesion of *S. aureus* and biofilm formation as compared to polished surfaces, within the first 48 h of bacteria culture. One may

conclude that nanotexturing seems to be an effective method for reducing the susceptibility of implant surfaces to bacterial colonisation and infection in the short-term after the implantation. Nevertheless, further studies are required to better understand this behaviour. On the contrary, we verified that bacteria adhesion and biofilm formation is encouraged on laser microtextured surfaces (MC-LIPSS surfaces), in agreement with a previous study [247].

Similarly to tissue cells, bacteria adhesion on implants surfaces depends on the surface physicochemical properties, such as wettability, roughness, contact area, surface topography and composition [52, 241, 310, 311]. Bacteria adhesion occurs preferentially on hydrophobic surfaces [53, 135]. So, the hydrophilicity of laser textured surfaces may contribute to decrease bacteria adhesion. According to our results, it seems that bacteria adhesion is not only affected by wettability, because the MC-LIPSS surfaces are hydrophilic and do not avoid bacteria adhesion. Since the chemical composition of the surfaces is quite similar for the same Ti alloy, these results suggest that surface topography plays the major role on bacteria adhesion.

Traditionally, implant surfaces are roughened to promote osseointegration, but roughened surfaces have generally been thought to encourage infectious bacteria accumulation. In fact, reduced adhesion of coccal microorganisms was observed for surfaces with R_a values less than 0.8 μm, while surfaces with roughness close to the bacteria size (~ 1-2 μm) tend to increase their retention [312]. These observations agree with our results. Bacteria adhesion is decreased on LIPSS and NP surfaces, with R_a ~ 0.3 μm, below the reported threshold of R_a ~ 0.8 μm while it increases significantly on MC-LIPSS surfaces, with R_a ~1.2 μm, similar to the *Staphylococci* size. The effective contact area available for adhesion of microorganisms is significantly reduced by nanotopographic features, so the shape, size, and orientation of surface structures may play an important role in controlling bacteria retention [9, 52]. In fact, bacteria and tisue cells respond differently to the surface topography [9, 238, 239]. At first sight, the small size of bacteria compared to tissue cells might facilitate bacteria adhesion to submicro surface structures but bacteria are much less deformable than tissue cells, and maintain their shape even when attached to a surface. This limits the interaction between bacteria and surfaces when these surfaces present structures with dimensions smaller than the bacteria size, limiting the possibility for bacteria to sense them and

adhere. The laser treatment increases the total surface area by a factor of 1.2-1.5 as compared to a polished surface but not all of this area is available for bacterial adhesion. Thus, it is likely that the resistance to bacterial colonisation of LIPSS and NP textured surfaces arises from a smaller surface area available for adhesion in comparison with a polished surface. The dimensions of the surface structures strongly affect bacteria adhesion. For instance, LIPSS and NP textured surfaces present nanometre scaled surface structures, much smaller (~ 3-7 times) than the bacterial cell size. The periodicity (0.7-0.8 μm) and height (0.2-0.3 μm) of LIPSS hinders the penetration of bacteria in the valleys of the texture, as shown by the SEM images (bacteria adhere only on the LIPSS crests). On the contrary, MC-LIPSS structures are larger (~ 1.5-4 times) than bacteria size, and bacteria colonise the depressions between microcolumns. This agrees with previous studies, which showed that *Staphylococcal* cells tend to colonise grooves or depressions with dimensions similar to the bacteria size [239].

We also investigated the biofilm formation on the different surfaces. Biofilm growth depends on bacteria adhesion to the surface and bacteria clustering [313]. Unlike tissue cells, bacteria must live in colonies in order to proliferate and form a biofilm. Our SEM and crystal violet binding assay indicate that the formation of biofilm is less conspicuous on LIPSS and NP textured surfaces than on the MC-LIPSS and polished surfaces. This is explained by the fact that bacteria adhesion is lower on these surfaces and this hampers biofilm growth. Avoidance of biofilm growth and further bacteria dispersion is ideal for preventing infection on neighbouring tissues. Conversely, biofilm growth is fast on MC-LIPSS textured surfaces and bacteria penetrate and form large colonies between the columns. This increases the chance for infectious desease. Previous studies showed that the phase constitution of the TiO_2 film also affects bacteria adhesion [314, 315]. Amorphous films promote bacteria attachment as compared to anatase, which presents antibacterial characteristics. Thus, the presence of an anatase film on the titanium surfaces may also explain the reduced bacteria adhesion. It should be emphasised that the results achieved with *S. aureus* cannot be extrapolated to other bacteria and strains, because bacterial colonisation of implant surfaces is also related to several microbial characteristics such as gram-positive/gram-negative, genus/species, bacterial shape, and strain type [53].

In summary, we showed that surface topography affect considerably the *S. aureus* adhesion and biofilm formation on titanium surfaces while wettability and surface chemical composition seem to play a minor role on the bacteria behaviour. Our results also suggest that the laser-induced nanotextures hold the potential to reduce bacteria adhesion and biofilm formation on titanium implants.

8. Biofunctionalisation of Titanium Implants

Two different approaches are commonly used in the surface modification of endosseous implants. The first one is based on surface topography modification. In the present work, a femtosecond laser-based method was applied for this purpose. In the second approach, molecules of specific organic compounds are adsorbed at the surface in order to enhance cell adhesion and differentiation towards a particular lineage. This is achieved by the formation of a thin layer of proteins, enzymes or peptides present in the extracellular matrix (see Section 4.3. of Chapter I).

Currently, the biomimetic modification of titanium implants is achieved by immobilisation of RGD peptide sequences, which improve cell adhesion and bone formation [20]. A method for biomimetic modification of Ti-6Al-4V alloy surfaces, which employs the covalent grafting of RGD peptide sequence was developed by the Bordeaux group [21]. This work showed that the peptide film was stable even in harsh conditions and the biochemical layer promoted the adhesion of osteoprogenitor cells. In the present thesis, we investigated the applicability of this method to laser textured surfaces of titanium. Our results suggest that covalent grafting of the KRGDSPC peptide sequence can be applied to all cp Ti surfaces. Silanization is the most important step for the reproducibility of biochemical functionalisation [316, 317]. It consists of an hydrolysis of alkoxy groups followed by condensation of surface titanium hydroxyls with silane molecule silanols. The silanization was confirmed by the incorporation of suitable amounts of Si and N on the surfaces and their respective chemical bondings. Moreover, we carried out an anhydrous silanization using an anhydrous organic solvent in water free atmosphere, which is claimed to yield better coverage and higher stability of bonded silane as compared to aqueous phase silanization [21]. Grafting of the cross-linker (SMP) and of the RGD peptide sequence is revealed by increased amounts of C-CO and C-O bonds as well as N concentration and its respective chemical bondings. In addition, the RGD peptide grafting on cp Ti surfaces was visually confirmed by

fluorescence microscopy. The peptide grafting was homogeneous, as indicated by the reproducibility of the XPS analysis (at least 3-5 points per surface) as well as by the fluorescence images.

The peptide surface concentration is known to have a significant effect on cell response [318]. Further studies must be performed in order to determine accurately the peptide concentration on each type of surface, for example by grafting RGD peptides containing radioactive atoms and measuring the radioactivity [21, 319].

Very recently, nanostructured surfaces with bioactive patterns motifs were produced by combining nanoimprint lithography and biomimetic modification [320]. Patterns of nanodots were fabricated on silicon surfaces and modified with a RGD peptide for study hMSCs adhesion and differentiation. The authors demonstrated that bioactive nanopatterned surfaces have a noticeable effect on the maturation of FAs and cell differentiation. Therefore, the combination of femtosecond laser surface texturing and biomimetic modification is a promising method for the fabrication of implant surfaces. We hypothesise that the grafted peptides will be able to increase MSCs adhesion and osteoblastic differentiation through biochemical signals, at short-term periods, while the mechanical interlocking between the bone tissue and the implant surface is improved, at long-term periods, due to the laser-induced textures.

Chapter V. Conclusions and Suggestions for Future Work

Conclusions

In the present thesis, surface texturing of Ti alloys using direct writing with a femtosecond laser system was explored as a potential method for enhancing the wettability and osseointegration, while reducing bacteria adhesion and biofilm formation on dental and orthopaedic implants by itself or after covalent grafting of a RGD peptide sequence.

By controlling the main laser processing parameters, such as radiation fluence and number of laser pulses, a range of surface textures can be produced on grade 2 cp Ti and grade 5 Ti-6Al-4V alloy. These textures can be classified in the follow types: (a) laser-induced periodic surface structures (LIPSS); (b) arrays of nanopillars; and (c) arrays of microcolumns covered with LIPSS, forming a bimodal roughness distribution. Since the laser treatment was carried out in air, the surface of the material was further oxidised. TiO_2 is the predominant oxide present in both alloys, as anatase and rutile, but a significant amount of alumina is also present on Ti-6Al-4V.

The laser treatment enhances the wettability of water and Hank's balanced salt solution on both Ti alloys as compared to polished surfaces. The surface anisotropy was crucial in controlling the wetting behaviour.

The surface topography affects significantly the spreading, shape and adhesion of hMSCs. The surface textures of both Ti alloys decrease cell spreading as compared to polished surfaces. The LIPSS and MC-LIPSS textured surfaces induce cell stretching/stress fibres while the NP texture induce filopodia formation. The LIPSS textured surfaces also promote cell contact guidance. The number of adhered cells is independent of the texture and similar for both Ti alloys, but the laser textured surfaces decrease significantly the focal adhesions area as compared to the polished ones. The spreading of cell nucleus is significantly decreased by the laser textures for both Ti alloys as compared to a polished surface. The cell nuclei deform slightly, independently of the surface texture and of the alloy. Cell proliferation is more important on cp Ti surfaces than on Ti-6Al-4V alloy and less noticeable on Ti-6Al-4V laser textured surfaces than on polished surfaces. hMSCs undergo osteoblastic commitment, as

indicated by the osterix (OSX) and osteopontin (OPN) markers. In general, these osteoblastic markers are upregulated for Ti-6Al-4V surfaces as compared to cp Ti, independently of the surface texture. Matrix mineralisation does not occur when cells are cultured in a non-osteogenic medium, but it is observed in osteogenic media. In osteogenic media, matrix mineralisation is strongly enhanced by LIPSS and NP textures, more so for Ti-6Al-4V, in which bone-like nodules are clearly formed. The adhesion of *Staphylococcus aureus* and biofilm formation are significantly reduced by LIPSS and NP textures as compared to polished and MC-LIPSS textured surfaces. Large bacteria colonies form in the depressions between the microcolumns of the MC-LIPSS textured surfaces.

KRGDSPC peptide grafting on laser textured surfaces of cp Ti was successfully achieved. The grafted surfaces are quite homogeneous. The largest amount of grafted peptides was observed on LIPSS textured surfaces, while no statistically significative differences between NP and MC-LIPSS textured surfaces were found.

Direct writing with a femtosecond laser is a potentially useful method for the surface nanotexturing of dental and orthopaedic titanium implants. The laser treatment enhances the surface wettability by biological fluids and matrix mineralisation (bone formation), while bacteria adhesion and biofilm formation are hampered. Finally, the combination of femtosecond laser treatment and biofunctionalisation of titanium surfaces has the potential to become a new method for producing implant surfaces that may improve cell adhesion and bone formation, mainly on LIPSS and NP textured surfaces.

Suggestions for Future Work

Femtosecond Laser Treatment. Future work can be performed in order to explore the possibility of creating new laser-induced surface textures with varying surface chemistries, using different laser systems and setups and processing atmospheres. The titanium alloys surfaces could be laser textured using radiation wavelengths in the ultraviolet and visible ranges, such as the second and third harmonics of the radiation of the laser used in the present work. The laser treatment could be carried out by using interferometry methods to create well-controlled

geometrical patterns. Finally, the laser treatment could be performed under inert or reactive atmospheres (vacuum, reactive and inert gases).

Mechanical Properties. In the present work we investigated the topography, chemical composition, and crystallographic structure of the laser textured surfaces. Nevertheless, the mechanical properties of the surfaces also influences the cell behaviour and play a key role on the implants lifespan. Therefore, we suggest the evaluation of the surface hardness and Young modulus (rigidity) of the laser textured surfaces. This can be accomplished by performing indentation hardness tests.

Corrosion Resistance. Implant surfaces with low corrosion resistance may release metal ions or metallic fragments into the body, when interacting with the body fluids, causing allergic or toxic reactions most of the times. Therefore, this is also a critical issue that may determine the implants lifespan. Thus, we propose the investigation of the corrosion resistance of the laser textured surfaces through electrochemical assays. These assays can be performed by different methods such as electrochemical impedance spectroscopy, potentiodynamic and cyclic polarisation, among others. In addition, different simulated body fluids can be used as electrolytes.

Wettability. In the present work the surface wettability by water and a saline solution was investigated in order to simulate biological fluids. Nevertheless, it is known that the behaviour of both tissue and bacterial cells strongly depends on the proteinaceous layer adsorbed on the implant surfaces. Therefore, we suggest the investigation of the wettability by protein solutions such as fibronectin and vitronectin. These analyses could better elucidate the behaviour of Mesenchymal Stem Cells and *Staphylococcus aureus* on the laser textured surfaces. In addition, we recommend a detailed characterisation of the type, amount, and conformation of proteins adsorbed on the laser textured surfaces after immersion in different culture media.

***In vitro* studies**. Here, the formation of focal adhesions (FAs) was investigated only for one time point (24 h after cell seeding). Nevertheless, it is important to characterise the formation of FAs at short- and long-term culture periods to study how cell adhesion evolves with time and to understand its influence on cell differentiation. We also suggest the investigation of cell differentiation at 6 and 8 weeks after cell seeding, to study how matrix mineralisation evolves with time. In the present work we focused on

the analysis of the osteoblastic differentiation of Mesenchymal Stem Cells, but this type of cells may differentiate into other lineages. We suggest the assessment of specific markers of other type of cells (adipocytes, chondrocytes, myocytes, and neurocytes) to demonstrate whether the laser textured surfaces are able to induce other lineage commitments. The cell culture could be also performed with other types of tissue and bacterial cells such as osteoblasts-like cells and *Streptococcus salivarius*, respectively. Most of the *in vitro* studies try to predict the cell-surface interactions by studying bacterial and tissue cell-surface interactions independently, but this is not what occurs *in vivo*. Therefore, we suggest the culture of tissue and bacterial cells simultaneously in order to understand the competition between them ("race for the surface"). Once the biofunctionalisation of the laser textured surfaces with a RGD peptide sequence is viable, we propose the investigation of the behaviour of Mesenchymal Stem Cells, osteoblast-like cells, and bacteria on these surfaces. It will allow us to explore the biomedical potential of this combined surface modification method.

***In vivo* studies**. *In vivo* studies are of upmost importance to assess the osseointegration of an implant surface. Therefore, we suggest the use of animal models (sheep, rabbit, mouse, etc) to investigate the influence of the laser treatment on the fibrous tissue and *de novo* bone formation, bone mineral density, adhesion strength between the implant surface and the bone tissue, and the bone-implant contact (BIC) ratio.

Surface Biofunctionalisation. The silanization is undoubtedly the most important step for the reproducibility of biochemical functionalisation. The hydroxyl (OH) groups present on the implant surfaces influences the efficiency of silanization significantly. Therefore, we suggest the determination of the amount of OH groups on the laser textured surfaces. This can be accomplished by performing XPS analysis. In addition, the density of grafted peptides plays an important role on cell adhesion and differentiation. Thus, future work should be performed to determine the density of grafted peptides on the laser textured surfaces. Here, the surfaces were biofunctionalised with a RGD peptide sequence, but other biomolecules have been reported to enhance osteoblastic differentiation and matrix mineralisation. Therefore, we propose the biofunctionalisation of the laser textured surfaces using other active principles such as

type I collagen, recombinant human fibronectin peptide (hFNIII9-10), BMP-2 or even a mixture of two different active principles, for instance, RGD peptide and BMP.

References

1. American Academy of Orthopaedic Surgeons (AAOS). AAOS Orthopaedic Surgeon Census. AAOS, 2012, [Access Date 2014-07-04].
2. Elder, M. Advanced Orthopedic Technologies, Implants and Regenerative Products. BCC Research, 2010, [Access Date 2014-01-24].
3. Markets and Markets. Dental Implants & Prosthetics Market (Implants, Crowns & Bridges, Dentures, Abutments) Current Trends, Opportunities & Global Forecasts To 2018. Markets and Markets, 2013.
4. Geetha, M., Singh, A.K., Asokamani, R. and Gogia, A.K. Ti based biomaterials, the ultimate choice for orthopaedic implants – A review. Progress in Materials Science, 2009, 54, 397-425.
5. Ehrenfest, D.M.D., Coelho, P.G., Kang, B.S., Sul, Y.T. and Albrektsson, T. Classification of osseointegrated implant surfaces: materials, chemistry and topography. Trends Biotechnology, 2010, 28 (4), 198-206.
6. Harris, L.G. and Richards, R.G. Staphylococci and implant surfaces: a review. Injury, 2006, 37, S3-14.
7. Wright, J.A. and Nair, S.P. Interaction of staphylococci with bone. International Journal of Medical Microbiology, 2010, 300 (2-3), 193-204.
8. Koegler, P., Clayton, A., Thissen, H., Santos, G.N. and Kingshott, P. The influence of nanostructured materials on biointerfacial interactions. Advanced Drug Delivery Review, 2012, 64 (15), 1820-1839.
9. Anselme, K., Davidson, P., Popa, A.M., Giazzon, M., Liley, M. and Ploux, L. The interaction of cells and bacteria with surfaces structured at the nanometre scale. Acta Biomaterialia, 2010, 6 (10), 3824-3846.
10. Barrere, F., Mahmood, T.A., de Groot, K. and van Blitterswijk, C.A. Advanced biomaterials for skeletal tissue regeneration: Instructive and smart functions. Materials Science & Engineering R-Reports, 2008, 59 (1-6), 38-71.
11. Bauer, S., Schmuki, P., von der Mark, K. and Park, J. Engineering biocompatible implant surfaces Part I: Materials and surfaces. Progress in Materials Science, 2013, 58 (3), 261-326.
12. Balazic, M., Kopac, J., Jackson, M.J. and Ahmed, W. Review: titanium and titanium alloy applications in medicine. International Journal of Nano and Biomaterials, 2007, 1 (1), 3-34.
13. Liu, X., Chu, P.K. and Ding, C. Surface modification of titanium, titanium alloys, and related materials for biomedical applications. Materials Science and Engineering R, 2004, 47, 49–121.

References

14. Norman, J.J. and Desai, T.A. Methods for fabrication of nanoscale topography for tissue engineering scaffolds. Annals of Biomedical Engineering, 2006, 34 (1), 89-101.
15. Vorobyev, A.Y. and Guo, C. Direct femtosecond laser surface nano/microstructuring and its applications. Laser & Photonics Reviews, 2013, 7 (3), 385-407.
16. Oliveira, V., Ausset, S. and Vilar, R. Surface micro/nanostructuring of titanium under stationary and non-stationary femtosecond laser irradiation. Applied Surface Science, 2009, 255 (17), 7556-7560.
17. Oliveira, V., Cunha, A. and Vilar, R. Multi-scaled femtosecond laser structuring of stationary titanium surfaces. Journal of Optoelectronics and Advanced Materials, 2010, 12 (3), 654-658.
18. Rahmany, M.B. and Van Dyke, M. Biomimetic approaches to modulate cellular adhesion in biomaterials: A review. Acta Biomaterialia, 2013, 9 (3), 5431-5437.
19. Nguyen, M.N., Lebarbe, T., Zouani, O.F., Pichavant, L., Durrieu, M.-C. and Heroguez, V. Impact of RGD nanopatterns grafted onto titanium on osteoblastic cell adhesion. Biomacromolecules, 2012, 13 (3), 896-904.
20. Chen, C., Zhang, S.-M. and Lee, I.-S. Immobilizing bioactive molecules onto titanium implants to improve osseointegration. Surface and Coatings Technology, 2013, 228 S312-S317.
21. Porte-Durrieu, M.-C., Guillemot, F., Pallu, S., Labrugere, C., Brouillaud, B., Bareille, R., Amedee, J., Barthe, N., Dard, M. and Baquey, C. Cyclo-(DfKRG) peptide grafting onto Ti-6Al-4V: physical characterization and interest towards human osteoprogenitor cells adhesion. Biomaterials, 2004, 25 (19), 4837-4846.
22. Bobbio, A. Maya, the first authentic alloplastic, endosseous dental implant. A refinement of a priority. Revista da Associação Paulista de Cirurgioes Dentistas, 1973, 27 (1), 27-36.
23. Worthington, P., Lang, B.R. and Lavelle, W.E. Osseointegration in dentistry: An introduction. 18th edition, 1994, Chicago, Quintessence Publishing.
24. Tapia, J.L., Suresh, L., Plata, M. and Aquirre, A. Ancient esthetic dentistry in Mesoamerica. Journal of Alpha Omega International Dental Fraternity, 2002, 95 (4), 21–24.
25. Spiekermann, H. Implantology. 1st edition, 2000, Stuttgart, Thieme.
26. Doherty, P.J., Williams, R.L., Williams, D.F. and Lee, A.J.C. Biomaterials–tissue interfaces. Proceedings of the Ninth European Conference on Biomaterials, 1992, Chester, UK, Elsevier.
27. Williams, D.F. The Williams dictionary of biomaterials, 1999, Liverpool, Liverpool University Press.
28. Williams, D.F. On the nature of biomaterials. Biomaterials, 2009, 30 (30), 5897-5909.

References

29. Holzapfel, B.M., Reichert, J.C., Schantz, J.T., Gbureck, U., Rackwitz, L., Noth, U., Jakob, F., Rudert, M., Groll, J. and Hutmacher, D.W. How smart do biomaterials need to be? A translational science and clinical point of view. Advanced Drug Delivery Reviews, 2013, 65 (4), 581-603.
30. Long, M. and Rack, H.J. Titanium alloys in total joint replacement-a materials science perspective. Biomaterials, 1998, 19 (18), 1621-1639.
31. Kieswetter, K., Schwartz, Z., Dean, D.D. and Boyan, B.D. The Role of Implant Surface Characteristics in the Healing of Bone. Critical Reviews in Oral Biology & Medicine, 1996, 7 (4), 329-345.
32. Jackson, M.J. and Ahmed, W. Surface Engineered Surgical Tools and Medical Devices, 2007, Springer.
33. Hutmacher, D.W., Hürzeler, M.B. and Schliephake, H. A Review of Material Properties of Biodegradable and Bioresorbable Polymers and Devices for GTR and GRB Applications. The International Journal of Oral & Maxillofacial Implants, 1996, 11, 667-678.
34. Niinomi, M. Mechanical properties of biomedical titanium alloys. Materials Science and Engineering A, 1998, 243 (1-2), 231-236.
35. Puleo, D.A. and Nanci, A. Understanding and controlling the bone-implant interface. Biomaterials, 1999, 20 (23-24), 2311-2321.
36. Tengvall, P. and Lundstrom, I. Physico-chemical Considerations of Titanium as a Biomaterial. Clinical Materials, 1992, 9, 115-134.
37. Oshida, Y. Bioscience and Bioengineering of Titanium Materials, 2007, Elsevier.
38. Kasemo, B.H. Biocompatibility of titanium implants: surface science aspects. Journal of Prosthetic Dentistry, 1983, 49 (6), 832–837.
39. Dipankar, B. and Williams, J.C. Perspectives on Titanium Science and Technology. Acta Materialia, 2013, 61 (3), 844-879.
40. Teixeira, M., Loable, C., Almeida, A., Florêncio, O., Fernandes, J.C.S. and Vilar, R. Combinatorial Laser-Assisted Development of Novel Ti-Ta Alloys for Biomedical Applications. Proceedings of the 32nd International Congress on Applications of Lasers and Electro-Optics, Laser Institute of America, 2013, 106, Miami, Florida, USA.
41. Almeida, A., Gupta, D., Loable, C. and Vilar, R. Laser-assisted synthesis of Ti-Mo alloys for biomedical applications. Materials Science and Engineering C, 2012, 32, 1190-1195.
42. Douglass, D.L. Oxidation of metals and alloys. Columbus, OH: American Society for Metals, 1971, 142-143.
43. Diebold, U. The surface science of titanium dioxide. Surface Science Reports, 2003, 48, 53-229.

References

44. Hanawa, T., Asami, K. and Asaoka, K. Repassivation of titanium and surface oxide film regenerated in stimulated bioliquid. Journal of Biomedical Materials Research A, 1998, (40), 530-538.
45. Hanawa, T. Titanium and its oxide film; a substrate for formation of apatite. The Bone-Biomaterial Interface, University of Toronto Press, 1991, 49-61.
46. Sundgren, J.-E., Bodö, P. and Lundström, I. Auger electron spectroscopic studies of the interface between human tissue and implants of titanium and stainless steel. Journal of Colloid and Interface Science, 1986, 110 (1), 9-20.
47. McQueen, D., Sundgren, J.E., Ivarsson, B., Lundstrom, I., af Ekenstam, C.B., Svensson, A., Brånemark, P.I. and Albrektsson, T. Auger electron spectroscopic studies of titanium implants. Clinical applications of biomaterials, 1982, 179-185, New York, John Wiley & Sons.
48. Liedberg, B., Ivarsson, B. and Lundstrom, I. Fourier transform infrared reflection absorption spectroscopy (FTIR-RAS) of fibrinogen adsorbed on metal and metal oxide surfaces. Journal of Biochemical and Biophysical Methods, 1984, 9, 233-243.
49. Anil, S., Anand, P.S., Alghamdi, H. and Jansen, J.A. Dental implant surface enhancement and osseointegration. Implant Dentistry-A Rapidly Evolving Practice, 2011, 83-108, Croatia, InTech.
50. Mendonça, G., Mendonça, D.B.S., Aragão, F.J.L. and Cooper, L.F. Advancing dental implant surface technology: From micron-to nanotopography. Biomaterials, 2008, 29, 3822-3835.
51. Löberg, J., Mattisson, I., Hansson, S. and Ahlberg, E. Characterisation of Titanium Dental Implants I: Critical Assessment of surface roughness parameters. The Open Biomaterials Journal, 2010, 2, 18-35.
52. Crawford, R.J., Webb, H.K., Truong, V.K., Hasan, J. and Ivanova, E.P. Surface topographical factors influencing bacterial attachment. Advances in Colloid and Interface Science, 2012, 179-182, 142-149.
53. Campoccia, D., Montanaro, L. and Arciola, C.R. A review of the biomaterials technologies for infection-resistant surfaces. Biomaterials, 2013, 34 (34), 8533-8554.
54. Le Guehennec, L., Soueidan, A., Layrolle, P. and Amouriq, Y. Surface treatments of titanium dental implants for rapid osseointegration. Dental Materials, 2007, 23 (7), 844-854.
55. Hanawa, T. Biofunctionalization of titanium for dental implant. Japanese Dental Science Review, 2010, 46 (2), 93-101.
56. Hansson, S. and Norton, M. The relation between surface roughness and interfacial shear strength for bone-anchored implants. A mathematical model. Journal of Biomechanics, 1999, 32 (8), 829-836.

References

57. Davies, J.E. Understanding peri-implant endosseous healing. Journal of Dental Education, 2003, 67 (8), 932-949.
58. Schwartz, Z., Lohmann, C.H., Oefinger, J., Bonewald, L.F., Dean, D.D. and Boyan, B.D. Implant surface characteristics modulate differentiation behavior of cells in the osteoblastic lineage. Advances in Dental Research, 1999, 13, 38-48.
59. Cheng, A.Z., Biological Multi-Functionalization and Surface Nanopatterning of Biomaterials. École Doctorale Des Sciences Chimiques, 2013, University of Bordeaux, Bordeaux-France.
60. Wood, M.A. Colloidal lithography and current fabrication techniques producing in-plane nanotopography for biological applications. Journal of the Royal Society Interface, 2007, 4 (12), 1-17.
61. Chou, S.Y., Krauss, P.R. and Renstrom, P.J. Imprint Lithography with 25-Nanometer Resolution. Science, 1996, 272 (5258), 85-87.
62. Anselme, K. Osteoblast adhesion on biomaterials. Biomaterials, 2000, 21 (7), 667-681.
63. Bezerra de Oliveira, U.O. Laser treatment of alloys: processing, microstructure and structural Properties. Netherlands Institute for Metals research, 2007, University of Groningen, Netherlands.
64. Almeida, A., Gupta, D. and Vilar, R. Laser-assisted development of titanium alloys: the search for new biomedical materials. International Conference on Lasers, Applications, and Technologies, SPIE, 2010, 7994, Kazan, Russia.
65. Neves, P., Arronte, M., Vilar, R. and Botelho do Rego, A.M. KrF excimer laser dry and steam cleaning of silicon surfaces with metallic particulate contaminants. Applied Physics A: Materials Science & Processing, 2002, 74 (2), 191-199.
66. Cangueiro, L.T., Vilar, R., Botelho do Rego, A.M. and Muralha, V.S.F. Femtosecond laser ablation of bovine cortical bone. Journal of Biomedical Optics, 2012, 17 (12), 125005.
67. Peng, Q., Juzeniene, A., Chen, J., Svaasand, L.O., Warloe, T., Giercksky, K.-E. and Moan, J. Lasers in medicine. Reports on Progress in Physics, 2008, 71 (5), 056701.
68. Mirhosseini, N., Crouse, P.L., Schmidth, M.J.J., Li, L. and Garrod, D. Laser surface micro-texturing of Ti-6Al-4V substrates for improved cell integration. Applied Surface Science, 2007, 253 (19), 7738-7743.
69. Hao, L. and Lawrence, J. Laser Surface Treatment of Bio-Implant Materials, 2005, John Wiley & Sons.
70. Brown, M.S. and Arnold, C.B. Fundamentals of Laser-Material Interaction and Application to Multiscale Surface Modification. Laser Precision Microfabrication, 2010, 135, 91-120, Germany, Springer.

References

71. Mendes, M.A.M.D., Excimer Laser Micromachining of Al2O3-TiC Ceramics. Study of the Process. Materials Engineering Department, 2002, Instituto Superior Técnico-University of Lisbon, Lisbon-Portugal.
72. Miller, J. and Haglund-Jr, R.F. Laser Ablation and Desorption. Experimental methods in physical sciences, 1998, 30, San Diego, Elsevier.
73. Gamaly, E.G. and Rode, A.V. Physics of ultra-short laser interaction with matter: From phonon excitation to ultimate transformations. Progress in Quantum Electronics, 2013, 37 (5), 215-323.
74. Gamaly, E.G., Rode , A.V., Luther-Davies, B. and Tikhonchuk, V.T. Ablation of solids by femtosecond lasers: ablation mechanisms and ablation thresholds for metals and dielectrics. Physics of Plasmas, 2002, 9 (3), 949-957.
75. Gamaly, E.G., Rode, A.V., Tikhonchuk, V.T. and Luther-Davies, B. Electrostatic mechanism of ablation by femtosecond lasers. Applied Surface Science, 2002, 197-198, 699-704.
76. Mannion, P.T., Magee, J., Coyne, E., O'Connor, G.M. and Glynn, T.J. The effect of damage accumulation behaviour on ablation thresholds and damage morphology in ultrafast laser micro-machining of common metals in air. Applied Surface Science, 2004, 233 (1-4), 275-287.
77. Simon, P. and Ihlemann, J. Ablation of submicron structures on metals and semiconductors by femtosecond UV-laser pulses. Applied Surface Science, 1997, 109-110, 25-29.
78. Plech, A., Leiderer, P. and Boneberg, J. Femtosecond laser near field ablation. Laser & Photonics Review, 2009, 3 (5), 435-451.
79. Wu, C., Crouch, C.H., Zhao, L., Carey, J.E., Younkin, R.J., Levinson, J.A., Mazur, E., Farrel, R.M., Gothoskar, P. and Karger, A. Near-unity below-band gap absorption by microstructured silicon. Applied Physics Letters, 2001, 78, 1850-1852.
80. Vorobyev, A. and Guo, C. Enhanced absorptance of gold following multipulse femtosecond laser ablation. Physical Review B, 2005, 72 (19), 195422.
81. Ivanov, D.S., Rethfeld, B., O'Connor, G.M., Glynn, T.J., Volkov, A.N. and Zhigilei, L.V. The mechanism of nanobump formation in femtosecond pulse laser nanostructuring of thin metal films. Applied Physics A, 2008, 92 (4), 791-796.
82. Eversole, D., Luk'yanchuk, B. and Ben-Yakar, A. Plasmonic laser nanoablation of silicon by the scattering of femtosecond pulses near gold nanospheres. Applied Physics A, 2007, 89 (2), 283-291.
83. Vorobyev, A.Y. and Guo, C. Femtosecond laser structuring of titanium implants. Applied Surface Science, 2007, 253 (17), 7272-7280.

References

84. Wang, C., Chang, Y.C., Yao, J., Luo, C., Yin, S., Ruffin, P., Brantley, C. and Edwards, E. Surface enhanced Raman spectroscopy by interfered femtosecond laser created nanostructures. Applied Physics Letters, 2012, 100, 023107.
85. Bonse, J., Wrobel, J.M., Krüger, J. and Kautek, W. Ultrashort-pulse laser ablation of indium phosphide in air. Applied Physics A-Materials Science & Processing, 2001, 72, 89-94.
86. Costache, F., Henyk, M. and Reif, J. Modification of dielectric surfaces with ultra-short laser pulses. Applied Surface Science, 2002, 186, 352-357.
87. Costache, F., Henyk, M. and Reif, J. Surface patterning on insulators upon femtosecond laser ablation. Applied Surface Science, 2003, 208-209, 486-491.
88. Hansen, J.L., van Hecke, M., Haaning, A., Ellegaard, C., Andersen, K.H., Bohr, T. and Sams, T. Instabilities in sand ripples. Nature, 2001, 410, 324-325.
89. Eichstädt, J. and Huis in ‘t Veld, A.J. Analysis of Irradiation Processes for Laser-Induced Periodic Surface Structures. Physics Procedia, 2013, 41, 650-660.
90. Eichstädt, J., Römer, G.R.B.E. and Huis in ‘t Veld, A.J. Determination of irradiation parameters for laser-induced periodic surface structures. Applied Surface Science, 2013, 264, 79-87.
91. Varlamova, O. Evolution of Femtosecond Laser Induced Surface Structures at Low Number of Pulses near the Ablation Threshold. Journal of Laser Micro/Nanoengineering, 2013, 8 (3), 300-303.
92. Dufft, D., Rosenfeld, A., Das, S.K., Grunwald, R. and Bonse, J. Femtosecond laser-induced periodic surface structures revisited: A comparative study on ZnO. Journal of Applied Physics, 2009, 105 (3), 034908.
93. Varlamova, O., Bounhalli, M. and Reif, J. Influence of irradiation dose on laser-induced surface nanostructures on silicon. Applied Surface Science, 2013, 278, 62-66.
94. Ganeev, R.A., Baba, M., Ozaki, T. and Kuroda, H. Long- and short-period nanostructure formation on semiconductor surfaces at different ambient conditions. Journal of the Optical Society of America B, Optical Physics, 2010, 27 (5), 1077-1082.
95. Camacho-López, S., Rodger, E., Escobar-Alarcón, L., Camacho-López, M.A. and Camacho-López, M.A. Polarization-dependent single-beam laser-induced grating-like effects on titanium films. Applied Surface Science, 2008, 255 (5), 3028-3032.
96. Obara, G., Shimizu, H., Enami, T., Mazur, E., Terakawa, M. and Obara, M. Growth of high spatial frequency periodic ripple structures on SiC crystal surfaces irradiated with successive femtosecond laser pulses. Optics Express, 2013, 21 (22), 26323-26334.
97. Tagawa, N., Takada, M., Mori, A., Sawada, H. and Kawahara, K. Development of contact sliders with nanotextures by femtosecond laser processing. Tribology Letters, 2006, 24 (2), 143-149.

References

98. Cunha, A., Serro, A.P., Oliveira, V., Almeida, A., Vilar, R. and Durrieu, M.-C. Wetting behaviour of femtosecond laser textured Ti-6Al-4V surfaces. Applied Surface Science, 2013, 265, 688-696.
99. Wu, B., Zhou, M., Li, J., Ye, X., Li, G. and Cai, L. Superhydrophobic surfaces fabricated by microstructuring of stainless steel using a femtosecond laser. Applied Surface Science, 2009, 256 (1), 61-66.
100. Wang, X., Ohlin, C.A., Lu, Q. and Hu, J. Cell directional migration and oriented division on three-dimensional laser-induced periodic surface structures on polystyrene. Biomaterials, 2008, 29 (13), 2049-2059.
101. Vorobyev, A.Y. and Guo, C. Colorizing metals with femtosecond laser pulses. Applied Physics Letters, 2008, 92 (4), 041914.
102. Vorobyev, A., Makin, V. and Guo, C. Brighter Light Sources from Black Metal: Significant Increase in Emission Efficiency of Incandescent Light Sources. Physical Review Letters, 2009, 102, 234301.
103. Hamdorf, A., Olson, M., Lin, C.-H., Jiang, L., Zhou, J., Xiao, H. and Tsai, H.-L. Femtosecond and nanosecond laser fabricated substrate for surface-enhanced Raman scattering. Optics Letters, 2011, 36 (17), 3353-3355.
104. Birnbaum, M. Semiconductor Surface Damage Produced by Ruby Lasers. Journal of Applied Physics, 1965, 36 (11), 3688.
105. Emmony, D.C., Howson, R.P. and Willis, L.J. Laser mirror damage in germanium at 10.6 μm. Applied Physics Letters, 1973, 23 (11), 598.
106. van Driel, H.M., Sipe, J.E. and Young, J.F. Laser-induced periodic surface structure on solids: A universal phenomena. Physical Review Letters, 1982, 49 (26), 1955-1958.
107. Keilmann, F. and Bai, Y.H. Periodic Surface Structures Frozen into CO2 Laser-Melted Quartz. Applied Physics A, 1982, 29 (1), 9-18.
108. Sipe, J.E., Young, J.F., Preston, J.S. and van Driel, H.M. Laser-induced periodic surface structure. I. Theory. Physical Review B, 1983, 27 (2), 1141-1154.
109. Young, J.F., Preston, J.S., van Driel, H.M. and Sipe, J.E. Laser induced periodic surface structures. II. experiments on Ge, Si, Al, and brass. Physical Review B, 1983, 27 (2), 1155-1172.
110. Clark, S.E., Kerr, N.C. and Emmony, D.C. Anomalous laser-induced periodic surface structures. Journal of Physics D: Applied Physics, 1989, 22, 527-534.
111. Bonse, J., Rosenfeld, A. and Krüger, J. On the role of surface plasmon polaritons in the formation of laser-induced periodic surface structures upon irradiation of silicon by femtosecond-laser pulses. Journal of Applied Physics, 2009, 106 (10), 104910.

References

112. Reif, J., Varlamova, O., Varlamov, S. and Bestehorn, M. The role of asymmetric excitation in self-organized nanostructure formation upon femtosecond laser ablation. Applied Physics A, 2011, 104 (3), 969-973.
113. Crawford, T.H.R. and Haugen, H.K. Sub-wavelength surface structures on silicon irradiated by femtosecond laser pulses at 1300 and 2100 nm wavelengths. Applied Surface Science, 2007, 253 (11), 4970-4977.
114. Vorobyev, A.Y. and Guo, C. Femtosecond laser structuring of titanium implants. Applied Surface Science, 2007, 253 (17), 7272-7280.
115. Zheng, H.Y., Wang, X.C. and Zhou, W. Some current research in femtosecond laser-induced surface ripple structures. International Journal of Surface Science and Engineering, 2009, 3 (1/2), 114-124.
116. Reif, J., Costache, F., Henyk, M. and Pandelov, S.V. Ripples revisited: non-classical morphology at the bottom of femtosecond laser ablation craters in transparent dielectrics. Applied Surface Science, 2002, 197-198, 891-895.
117. Costache, F., Kouteva-Arguirova, S. and Reif, J. Sub-damage-threshold femtosecond laser ablation from crystalline Si: surface nanostructures and phase transformation. Applied Physics A, 2004, 79 (4-6), 1429-1432.
118. Erlebacher, J., Aziz, M.J., Chason, E., Sinclair, M.B. and Floro, J.A. Spontaneous Pattern Formation on Ion Bombarded Si (001). Physical Review Letters, 1999, 82 (11), 2330-2333.
119. Sigmund, P. A mechanism of surface micro-roughening by ion bombardment. Journal of Materials Science, 1973, 8, 1545-1553.
120. Bonse, J., Munz, M. and Sturm, H. Structure formation on the surface of indium phosphide irradiated by femtosecond laser pulses. Journal of Applied Physics, 2005, 97 (1), 013538.
121. Wu, Q., Ma, Y., Fang, R., Liao, Y., Yu, Q., Chen, X. and Wang, K. Femtosecond laser-induced periodic surface structure on diamond film. Applied Physics Letters, 2003, 82 (11), 1703.
122. Skolski, J.Z.P., Romer, G.R.B.E., Huis in 't Veld, A.J., Mitko, V.S., Obona, J.V., Ocelik, V. and De Hosson, J.T.M. Modeling of Laser Induced Periodic Surface Structures. Journal of Laser Micro/Nanoengineering, 2010, 5 (3), 263-268.
123. Bush, J.R., Nayak, B.K., Nair, L.S., Gupta, M.C. and Laurencin, C.T. Improved bio-implant using ultrafast laser induced self-assembled nanotexture in titanium. Journal of biomedical materials research Part B, Applied biomaterials, 2011, 97 (2), 299-305.
124. Nayak, B.K., Gupta, M.C. and Kolasinski, K.W. Formation of nano-textured conical microstructures in titanium metal surface by femtosecond laser irradiation. Applied Physics A-Materials Science & Processing, 2008, 90 (3), 399-402.

References

125. Bo Wu, M.Z., Jian Li, Xia Ye, Gang Li, Lan Cai. Superhydrophobic surfaces fabricated by microstructuring of stainless steel using a femtosecond laser. Applied Surface Science, 2009, 256, 61-66.
126. Zorba, V., Stratakis, E., Barberoglou, M., Spanakis, E., Tzanetakis, P., Anastasiadis, S.H. and Fotakis, C. Biomimetic Artificial Surfaces Quantitatively Reproduce the Water Repellency of a Lotus Leaf. Advanced Materials, 2008, 20 (21), 4049-4054.
127. Dyer, P.E., Jenkins, S.D. and Sidhu, J. Development and origin of conical structures on XeCl laser ablated polyimide. Applied Physics Letters, 1986, 49, 453-455.
128. Oliveira, V., Vilar, R. and Conde, O. Excimer laser ablation of Al2O3-TiC ceramics: laser induced modifications of surface topography and structure. Applied Surface Science, 1998, 127-129, 831-836.
129. Sanchez, F., Morenza, J.L., Aguiar, R., Delgado, J.C. and Varela, M. Dynamics of the hydrodynamical growth of columns on silicon exposed to excimer-laser irradiation. Applied Physics A, 1998, 66 (1), 83-86.
130. Oliveira, V., Sivakumar, M. and Vilar, R. A mathematical description of surface texture development in laser-ablated dentin. Journal of Applied Physics, 2006, 100, 104701.
131. Zuhlke, C.A., Anderson, T.P. and Alexander, D.R. Formation of multiscale surface structures on nickel via above surface growth and below surface growth mechanisms using femtosecond laser pulses. Optics Express, 2013, 21 (7), 8460-8473.
132. Hwang, T.Y. and Guo, C. Polarization and angular effects of femtosecond laser-induced conical microstructures on Ni. Journal of Applied Physics, 2012, 111 (8), 083518
133. Ionin, A.A., Kudryashov, S.I., Makarov, S.V., Rudenko, A.A., Seleznev, L.V., Sinitsyn, D.V., Golosov, E.V., Kolobov, Y.R. and Ligachev, A.E. Beam spatial profile effect on femtosecond laser surface structuring of titanium in scanning regime. Applied Surface Science, 2013, 284, 634-637.
134. Quere, D. Wetting and roughness. Annual Review of Materials Research, 2008, 38, 71-99.
135. Vadillo-Rodriguez, V., Pacha-Olivenza, M.A., Gonzalez-Martin, M.L., Bruque, J.M. and Gallardo-Moreno, A.M. Adsorption behavior of human plasma fibronectin on hydrophobic and hydrophilic Ti6Al4V substrata and its influence on bacterial adhesion and detachment. Journal of Biomedical Materials Research Part A, 2013, 101 (5), 1397-1404.
136. Drelich, J. and Chibowski, E. Superhydrophilic and superwetting surfaces: definition and mechanisms of control. Langmuir, 2010, 26 (24), 18621-18623.
137. Kietzig, A.M., Hatzikiriakos, S.G. and Englezos, P. Patterned Superhydrophobic Metallic Surfaces. Langmuir, 2009, 25 (8), 4821-4827.
138. Yan, Y.Y., Gao, N. and Barthlott, W. Mimicking natural superhydrophobic surfaces and grasping the wetting process: A review on recent progress in preparing superhydrophobic surfaces. Advances in Colloid and Interface Science, 2011, 169 (2), 80-105.

References

139. Liu, K., Yao, X. and Jiang, L. Recent developments in bio-inspired special wettability. Chemical Society Reviews, 2010, 39 (8), 3240-3255.
140. Liu, K. and Jiang, L. Metallic surfaces with special wettability. Nanoscale, 2011, 3 (3), 825-838.
141. Yao, X., Song, Y. and Jiang, L. Applications of bio-inspired special wettable surfaces. Advanced Materials, 2011, 23 (6), 719-734.
142. Chen, F., Zhang, D., Yang, Q., Yong, J., Du, G., Si, J., Yun, F. and Hou, X. Bioinspired wetting surface via laser microfabrication. ACS Applied Materials & Interfaces, 2013, 5 (15), 6777-6792.
143. Baldacchini, T., Carey, J.E., Zhou, M. and Mazur, E. Superhydrophobic surfaces prepared by microstructuring of silicon using a femtosecond laser. Langmuir, 2006, 22 (11), 4917-4919.
144. Zorba, V., Persano, L., Pisignano, D., Athanassiou, A., Stratakis, E., Cingolani, R., Tzanetakis, P. and Fotakis, C. Making silicon hydrophobic: wettability control by two-lengthscale simultaneous patterning with femtosecond laser irradiation. Nanotechnology, 2006, 17 (13), 3234-3238.
145. Jagdheesh, R., Pathiraj, B., Karatay, E., Romer, G.R. and Huis in't Veld, A.J. Laser-induced nanoscale superhydrophobic structures on metal surfaces. Langmuir, 2011, 27 (13), 8464-8469.
146. Yan Zhao, Q.L., Mei Li, and Xin Li. Anisotropic wetting characteristics on submicrometer-scale periodic grooved surface. Langmuir, 2007, 23, 6212-6217.
147. Chen, F., Zhang, D., Yang, Q., Wang, X., Dai, B., Li, X., Hao, X., Ding, Y., Si, J. and Hou, X. Anisotropic wetting on microstrips surface fabricated by femtosecond laser. Langmuir, 2011, 27 (1), 359-365.
148. Vorobyev, A.Y. and Guo, C. Water sprints uphill on glass. Journal of Applied Physics, 2010, 108, 123512.
149. Vorobyev, A.Y. and Guo, C. Laser turns silicon superwicking. Optics Express 2010, 18 (7), 6455-6460.
150. A.Y., V. and Guo, C. Making human enameland dentin surfaces superwetting for enhanced adhesion. Applied Physics Letters, 2011, 99, 193703.
151. Nunes, B., Serro, A.P., Oliveira, V., Montemor, M.F., Alves, E., Saramago, B. and Colaço, R. Ageing effects on the wettability behavior of laser textured silicon. Applied Surface Science, 2011, 257 (7), 2604-2609.
152. Wang, Z.K., Zheng, H.Y., Lim, C.P. and Lam, Y.C. Polymer hydrophilicity and hydrophobicity induced by femtosecond laser direct irradiation. Applied Physics Letters, 2009, 95, 111110.

References

153. Jones, F.H. Teeth and bones: applications of surface science to dental materials and related biomaterials. Surface Science Reports, 2001, 42 (3-5), 79-205.
154. Rose, F.R. and Oreffo, R.O. Bone tissue engineering: hope vs hype. Biochemical and Biophysical Research Communications, 2002, 292 (1), 1-7.
155. Salgado, A.J., Coutinho, O.P. and Reis, R.L. Bone tissue engineering: state of the art and future trends. Macromolecular Bioscience, 2004, 4 (8), 743-765.
156. Liu, H. and Webster, T.J. Nanomedicine for implants: A review of studies and necessary experimental tools. Biomaterials, 2007, 28, 354-369.
157. Stein, G.S. and Lian, J.B. Molecular Mechanisms Mediating Proliferation/Differentiation Interrelationships During Progressive Development of the Osteoblast Phenotype. Endocrine Reviews, 1993, 14 (4), 424-442.
158. Giancotti, J.C. Integrin Signaling. Science, 1999, 285 (5430), 1028-1033.
159. Takada, Y., Ye, X. and Simon, S. The integrins. Genome Biology, 2007, 8 (5), 215.
160. Adams, J.C. Cell-matrix contact structures. Cellular and Molecular Sciences, 2001, 58 (3), 371-392.
161. Geiger, B., Spatz, J.P. and Bershadsky, A.D. Environmental sensing through focal adhesions. Nature Reviews Molecular Cell Biology, 2009, 10 (1), 21-33.
162. Nobes, C.D. and Hall, A. Rho, Rac, and Cdc42 GTPases Regulate the Assembly of Multimolecular Focal Complexes Associated with Actin Stress Fibers, Lamellipodia, and Filopodia. Cell, 1995, 81, 53-62.
163. Alexandrova, A.Y., Arnold, K., Schaub, S., Vasiliev, J.M., Meister, J.J., Bershadsky, A.D. and Verkhovsky, A.B. Comparative dynamics of retrograde actin flow and focal adhesions: formation of nascent adhesions triggers transition from fast to slow flow. PLoS One, 2008, 3 (9), e3234.
164. Choi, C.K., Vicente-Manzanares, M., Zareno, J., Whitmore, L.A., Mogilner, A. and Horwitz, A.R. Actin and alpha-actinin orchestrate the assembly and maturation of nascent adhesions in a myosin II motor-independent manner. Nature Cell Biology, 2008, 10 (9), 1039-1050.
165. Schwartz, M.A. Integrins and extracellular matrix in mechanotransduction. Cold Spring Harbor Perspectives in Biology, 2010, 2 (12), a005066.
166. Biggs, M.J. and Dalby, M.J. Focal adhesions in osteoneogenesis. Proceedings of the Institution of Mechanical Engineers, 2010, 224 (12), 1441-1453.
167. Zamir, E., Katz, M., Posen, Y., Erez, N., Yamada, K.M., Katz, B.-Z., Lin, S., Lin, D.C., Bershadsky, A., Kam, Z. and Geiger, B. Dynamics and segregation of cell-matrix adhesions in cultured fibroblasts. Nature Cell Biology, 2000, 2, 191-196.
168. Morgan, M.R., Humphries, M.J. and Bass, M.D. Synergistic control of cell adhesion by integrins and syndecans. Nature Reviews Molecular Cell Biology, 2007, 8 (12), 957-969.

References

169. Oakes, P.W., Beckham, Y., Stricker, J. and Gardel, M.L. Tension is required but not sufficient for focal adhesion maturation without a stress fiber template. The Journal of Cell Biology, 2012, 196 (3), 363-374.
170. Forgacs, G. On the possible role of cytoskeletal filamentous networks in intracellular signaling: an approach based on percolation. Journal of Cell Science, 1995, 108, 2131-2143.
171. Ingber, D.E. Tensegrity: the architectural basis of cellular mechanotransduction. Annual Review of Physiology, 1997, (59), 575-599.
172. Williams, A.R. and Hare, J.M. Mesenchymal stem cells: biology, pathophysiology, translational findings, and therapeutic implications for cardiac disease. Circulation Research, 2011, 109 (8), 923-940.
173. Friedenstein, A.J., Chailakhjan, R.K. and Lalykina, K.S. The development of fibroblast colonies in monolayer cultures of guinea-pig bone marrow and spleen cells. Cell and Tissue Kinetics, 1970, 3, 393–403.
174. Yamachika, E. and Iida, S. Bone regeneration from mesenchymal stem cells (MSCs) and compact bone-derived MSCs as an animal model. Japanese Dental Science Review, 2013, 49 (1), 35-44.
175. Petersen, B.E. Bone Marrow as a Potential Source of Hepatic Oval Cells. Science, 1999, 284 (5417), 1168-1170.
176. Wilson, A. and Trumpp, A. Bone-marrow haematopoietic-stem-cell niches. Nature Reviews Immunology, 2006, 6 (2), 93-106.
177. Bjornson, C.R. Turning Brain into Blood: A Hematopoietic Fate Adopted by Adult Neural Stem Cells in Vivo. Science, 1999, 283 (5401), 534-537.
178. Kennea, N.L. and Mehmet, H. Neural stem cells. The Journal of Pathology, 2002, 197 (4), 536-550.
179. Potten, C.S. and Morris, R.J. Epithelial stem cells in vivo. Journal of Cell Science. Supplement, 1988, 10, 45-62.
180. Marshman, E., Booth, C. and Potten, C.S. The intestinal epithelial stem cell. BioEssays, 2002, 24 (1), 91-98.
181. Tuan, R.S., Boland, G. and Tuli, R. Adult mesenchymal stem cells and cell-based tissue engineering. Arthritis Research and Therapy, 2003, 5 (1), 32-45.
182. Caplan, A.I. Adult Mesenchymal Stem Cells for Tissue Engineering Versus Regenerative Medicine. Journal of Cellular Physiology, 2007, 213, 341-347.
183. Thomson, J.A. Embryonic Stem Cell Lines Derived from Human Blastocysts. Science, 1998, 282 (5391), 1145-1147.
184. Shamblott, M.J., Axelman, J., Wang, S., Bugg, E.M., Littlefield, J.W., Donovan, P.J., Blumenthal, P.D., Huggins, G.R. and Gearhart, J.D. Derivation of pluripotent stem cells

from cultured human primordial germ cells. Proceedings of the National Academy of Science, 1998, 95, 13726-13731.

185. Reubinoff, B.E., Pera, M.F., Fong, C.-Y., Trounson, A. and Bongso, A. Embryonic stem cell lines from human blastocysts: somatic differentiation in vitro. Nature Biotechnology, 2000, 18, 399-404.
186. Dominici, M., Le Blanc, K., Mueller, I., Slaper-Cortenbach, I., Marini, F., Krause, D., Deans, R., Keating, A., Prockop, D. and Horwitz, E. Minimal criteria for defining multipotent mesenchymal stromal cells: the International Society for Cellular Therapy position statement. Cytotherapy, 2006, 8, 315-317.
187. Pittenger, M.F., Mackay, A.M., Beck, S.C., Jaiswal, R.K., Douglas, R., Mosca, J.D., Moorman, M.A., Simonetti, D.W., Craig, S. and Marshak, D.R. Multilineage potential of adult human mesenchymal stem cells. Science, 1999, 284, 143–147.
188. Zuk, P.A., Zhu, M., Mizuno, H., Huang, J., Futrell, J.W., Katz, A.J., Benhaim, P., Lorenz, H.P. and Hedrick, M.H. Multilineage cells from human adipose tissue: implications for cell-based therapies. Tissue Engineering, 2001, 7, 211-228.
189. De Bari, C., Dell'Accio, F., Tylzanowski, P. and Luyten, F.P. Multipotent mesenchymal stem cells from adult human synovial membrane. Arthritis & Rheumatology, 2001, 44 (8), 1928 -1942.
190. Sabatini, F., Petecchia, L., Tavian, M., Jodon de Villeroche, V., Rossi, G.A. and Brouty-Boye, D. Human bronchial fibroblasts exhibit a mesenchymal stem cell phenotype and multilineage differentiating potentialities. Laboratory Investigation-Nature, 2005, 85 (8), 962-971.
191. Erices, A., Conget, P. and Minguell, J.J. Mesenchymal progenitor cells in human umbilical cord blood. British Journal of Haematology, 2000, 109, 235-242.
192. Zvaifler, N.J., Marinova-Mutafchieva, L., Adams, G., Edwards, C.J., Moss, J., Burger, J.A. and Maini, R.N. Mesenchymal precursor cells in the blood of normal individuals. Arthritis Research & Therapy, 2000, 2, 477-488.
193. Baksh, D., Yao, R. and Tuan, R.S. Comparison of proliferative and multilineage differentiation potential of human mesenchymal stem cells derived from umbilical cord and bone marrow. Stem Cells, 2007, 25, 1384-1392.
194. Yin, T. and Li, L. The stem cell niches in bone. Journal of Clinical Investigation, 2006, 116 (5), 1195-1201.
195. Watt, F.M. Out of Eden: Stem Cells and Their Niches. Science, 2000, 287 (5457), 1427-1430.
196. Barry, F.P. and Murphy, J.M. Mesenchymal stem cells: clinical applications and biological characterization. The International Journal of Biochemistry & Cell Biology, 2004, 36 (4), 568-584.

References

197. Caplan, A.I. Mesenchymal Stem Cells: The Past, the Present, the Future. Cartilage, 2009, 1 (1), 6-9.
198. Minguell, J.J., Erices, A. and Conget, P. Mesenchymal Stem Cells. Experimental Biology and Medicine, 2001, 226, 507-520.
199. Chamberlain, G., Fox, J., Ashton, B. and Middleton, J. Concise review: Mesenchymal Stem Cells: Their phenotype, differentiation capacity, immunological features, and potential for homing. Stem Cells, 2007, 25, 2739-2749.
200. Deans, R.J. and Moseley, A.B. Mesenchymal Stem Cells: Biology and potential clinical uses. Experimental Hematology, 2000, 28 (8), 875-884.
201. Mackay, A.M., Beck, S.C., Murphy, J.M., Barry, F.P., Chichester, C.O. and Pittenger, M.F. Chondrogenic differentiation of cultured human mesenchymal stem cells from marrow. Tissue Engineering, 1998, 4, 415-428.
202. Saadatian-Elahi, M., Teyssou, R. and Vanhems, P. Staphylococcus aureus, the major pathogen in orthopaedic and cardiac surgical site infections: A literature review. International Journal of Surgical Pathology, 2008, 6 (3), 238-245.
203. Delgado-Rodriguez, M., Gomez-Ortega, A., Sillero-Arenas, M. and Llorca, J. Epidemiology of surgical-site infections diagnosed after hospital discharge: a prospective cohort study. Infection Control and Hospital Epidemiology, 2001, 22 (1), 24-30.
204. Astagneau, P., Rioux, C., Golliot, F. and Brucker, G. Morbidity and mortality associated with surgical site infections: results from the 1997-1999 INCISO surveillance. Journal of Hospital Infection, 2001, 48 (4), 267-274.
205. Török, M.E. and Day, N.P.J. Staphylococcal and streptococcal infections. Medicine, 2014, 42 (1), 1-7.
206. Otto, M. Staphylococcal Biofilms. Current Topics in Microbiology and Immunology, 2008, 322, 207-228.
207. Götz, F. Staphylococcus and biofilms. Molecular Microbiology, 2002, 43 (6), 1367-1378.
208. Arciola, C.R., Campoccia, D., Speziale, P., Montanaro, L. and Costerton, J.W. Biofilm formation in Staphylococcus implant infections. A review of molecular mechanisms and implications for biofilm-resistant materials. Biomaterials, 2012, 33 (26), 5967-5982.
209. Humphreys, H. Staphylococcus aureus: The enduring pathogen in surgery. Surgeon, 2012, 10 (6), 357-360.
210. Weiss, P. and Garber, B. Shape and Movement of Mesenchyme Cells as Functions of the Physical Structure of the Medium. Contributions to a Quantitative Morphology. Proceedings of the National Academy of Science USA, 1952, 38 (3), 264-280.
211. Chen, S.C. Geometric Control of Cell Life and Death. Science, 1997, 276 (5317), 1425-1428.

References

212. McBeath, R., Pirone, D.M., Nelson, C.M., Bhadriraju, K. and Chen, C.S. Cell Shape, Cytoskeleton Tension, and RhoA Regulate Stem Cell Lineage Commitment. Developmental Cell, 2004, 6, 483-495.
213. Kilian, K.A., Bugarija, B., Lahn, B.T. and Mrksich, M. Geometric cues for directing the differentiation of mesenchymal stem cells. Proceedings of the National Academy of Science USA, 2010, 107 (11), 4872-4877.
214. Balloni, S., Calvi, E.M., Damiani, F., Bistoni, G., Calvitti, M., Locci, P., Becchetti, E. and Marinucci, L. Effects of Titanium Surface Roughness on Mesenchymal Stem Cell Commitment and Differentiation Signaling. The International Journal of Oral & Maxillofacial Implants, 2009, 24 (4), 627-635.
215. Wilkinson, C.D.W., Riehle, M., Wood, M., Gallagher, J. and Curtis, A.S.G. The use of materials patterned on a nano- and micro-metric scale in cellular engineering. Materials Science and Engineering: C, 2002, 19, 263-269.
216. Yim, E.K., Darling, E.M., Kulangara, K., Guilak, F. and Leong, K.W. Nanotopography-induced changes in focal adhesions, cytoskeletal organization, and mechanical properties of human mesenchymal stem cells. Biomaterials, 2010, 31 (6), 1299-1306.
217. Yim, E.K., Pang, S.W. and Leong, K.W. Synthetic nanostructures inducing differentiation of human mesenchymal stem cells into neuronal lineage. Experimental Cell Research, 2007, 313 (9), 1820-1829.
218. Chen, J., Ulerich, J.P., Abelev, E., Fasasi, A., Arnold, C.B. and Soboyejo, W.O. An investigation of the initial attachment and orientation of osteoblast-like cells on laser grooved Ti-6Al-4V surfaces. Materials Science and Engineering C, 2009, 29 (4), 1442-1452.
219. Crouch, A.S., Miller, D., Luebke, K.J. and Hu, W. Correlation of anisotropic cell behaviors with topographic aspect ratio. Biomaterials, 2009, 30 (8), 1560-1567.
220. Dalby, M.J., Gadegaard, N., Tare, R., Andar, A., Riehle, M.O., Herzyk, P., Wilkinson, C.D. and Oreffo, R.O. The control of human mesenchymal cell differentiation using nanoscale symmetry and disorder. Nature Materials, 2007, 6 (12), 997-1003.
221. Huang, J., Grater, S.V., Corbellini, F., Rinck, S., Bock, E., Kemkemer, R., Kessler, H., Ding, J. and Spatz, J. Impact of order and disorder in RGD nanopatterns on cell adhesion. Nano Letters, 2009, 7 (6), 1111-1116.
222. Park, J., Bauer, S., von der Mark, K. and Schmuki, P. Nanosize and vitality: TiO2 nanotube diameter directs cell fate. Nano Letters, 2007, 7 (6), 1686-1691.
223. Oh, S., Brammer, K.S., Li, Y.S., Teng, D., Engler, A.J., Chien, S. and Jin, S. Stem cell fate dictated solely by altered nanotube dimension. Proceedings of the National Academy of Science U S A, 2009, 106 (7), 2130-2135.

References

224. Zhao, L., Mei, S., Wang, W., Chu, P.K., Zhang, Y. and Wu, Z. Suppressed primary osteoblast functions on nanoporous titania surface. Journal of Biomedical Materials Research Part A, 2011, 96 (1), 100-107.
225. Lee, J.H., Jung, H.W., Kang, I.-K. and Lee, H.B. Cell Behaviour on Polymer Surfaces with Different Functional Groups. Biomaterials, 1993, 15 (9), 705-711.
226. Ruoslahti, E. RGD and other recognition sequences for integrins. Annual Review of Cell and Developmental Biology, 1996, 12, 697-715.
227. Ruoslahti, E. and Pierschbacher, M.D. New Perspectives in Cell Adhesion: RGD and Integrins. Science, 1987, 238 (4826), 491-497.
228. Chollet, C., Chanseau, C., Remy, M., Guignandon, A., Bareille, R., Labrugère, C., Bordenave, L. and Durrieu, M.-C. The effect of RGD density on osteoblast and endothelial cell behavior on RGD-grafted polyethylene terephthalate surfaces. Biomaterials, 2009, 30 (5), 711-720.
229. Huang, H., Zhao, Y., Liu, Z., Zhang, Y., Zhang, H., Fu, T. and Ma, X. Enhanced Osteoblast Functions on RGD Immobilized Surface. Journal of Oral Implantology, 2003, 29 (2), 73-79.
230. Kantlehner, M., Schaffner, P., Finsinger, D., Meyer, J., Jonczyk, A., Diefenbach, B., Nies, B., Hölzemann, G., Goodman, S.L. and Kessler, H. Surface Coating with Cyclic RGD Peptides Stimulates Osteoblast Adhesion and Proliferation as well as Bone Formation. Chem Bio Chem, 2000, 1(2), 107-114.
231. Balasundaram, G. and Webster, T.J. Increased osteoblast adhesion on nanograined Ti modified with KRSR. Journal of Biomedical Materials Research Part A, 2007, 80 (3), 602-611.
232. Kim, J.W., Ki, C.S., Park, Y.H., Kim, H.J. and Um, I.C. Effect of RGDS and KRSR peptides immobilized on silk fibroin in nanofibrous mats for cell adhesion and proliferation. Macromolecular Research, 2010, 18 (5), 442-448.
233. Schuler, M., Hamilton, D.W., Kunzler, T.P., Sprecher, C.M., de Wild, M., Brunette, D.M., Textor, M. and Tosatti, S.G. Comparison of the response of cultured osteoblast and osteoblasts outgrown from rat calvarial bone chips to nonfouling KRSR and FHRRIKA-peptide modified rough titanium surfaces. Journal of Biomedical Materials Research Part B: Applied Biomaterials, 2009, 91 (2), 517-527.
234. Schmitt, J.M., Hwang, K., Winn, S.R., . and Hollinger, J.O. Bone Morphogenetic Proteins: An Update on Basic Biology and Clinical Relevance. Journal of Orthopaedic Research, 1999, 17, 269-278.
235. Yin, H., Yeh, L.C., Hinck, A.P. and Lee, J.C. Characterization of ligand-binding properties of the human BMP type II receptor extracellular domain. Journal of Molecular Biology, 2008, 378 (1), 191-203.

References

236. Zouani, O.F., Chollet, C., Guillotin, B. and Durrieu, M.C. Differentiation of pre-osteoblast cells on poly(ethyleneterephthalate) grafted with RGD and/or BMPs mimetic peptides. Biomaterials, 2010, 31 (32), 8245-8253.
237. Murakami, N., Saito, N., Horiuchi, H., Okada, T., Nozaki, K. and Takaoka, K. Repair of segmental defects in rabbit humeri with titanium fiber mesh cylinders containing recombinant human bone morphogenetic protein-2 (rhBMP-2) and a synthetic polymer. Journal of Biomedical Materials Research, 2002, 62 (2), 169-174.
238. Ploux, L., Anselme, K., Dirani, A., Ponche, A., Soppera, O. and Roucoules, V. Opposite responses of cells and bacteria to micro/nanopatterned surfaces prepared by pulsed plasma polymerization and UV-irradiation. Langmuir, 2009, 25 (14), 8161-8169.
239. Wu, Y., Zitelli, J.P., TenHuisen, K.S., Yu, X. and Libera, M.R. Differential response of Staphylococci and osteoblasts to varying titanium surface roughness. Biomaterials, 2011, 32 (4), 951-960.
240. Braem, A., Van Mellaert, L., Mattheys, T., Hofmans, D., De Waelheyns, E., Geris, L., Anne, J., Schrooten, J. and Vleugels, J. Staphylococcal biofilm growth on smooth and porous titanium coatings for biomedical applications. Journal of Biomedical Materials Research, Part A, 2014, 102A, 215-224.
241. Ivanova, E.P., Truong, V.K., Wang, J.Y., Berndt, C.C., Jones, R.T., Yusuf, II, Peake, I., Schmidt, H.W., Fluke, C., Barnes, D. and Crawford, R.J. Impact of nanoscale roughness of titanium thin film surfaces on bacterial retention. Langmuir, 2010, 26 (3), 1973-1982.
242. Ivanova, E.P., Hasan, J., Webb, H.K., Gervinskas, G., Juodkazis, S., Truong, V.K., Wu, A.H., Lamb, R.N., Baulin, V.A., Watson, G.S., Watson, J.A., Mainwaring, D.E. and Crawford, R.J. Bactericidal activity of black silicon. Nature Communications, 2013, 4, 2838.
243. Xu, L.C. and Siedlecki, C.A. Submicron-textured biomaterial surface reduces staphylococcal bacterial adhesion and biofilm formation. Acta Biomaterialia, 2012, 8 (1), 72-81.
244. Puckett, S.D., Taylor, E., Raimondo, T. and Webster, T.J. The relationship between the nanostructure of titanium surfaces and bacterial attachment. Biomaterials, 2010, 31 (4), 706-713.
245. Ercan, B., Kummer, K.M., Tarquinio, K.M. and Webster, T.J. Decreased Staphylococcus aureus biofilm growth on anodized nanotubular titanium and the effect of electrical stimulation. Acta Biomaterialia, 2011, 7 (7), 3003-3012.
246. Truong, V.K., Lapovok, R., Estrin, Y.S., Rundell, S., Wang, J.Y., Fluke, C.J., Crawford, R.J. and Ivanova, E.P. The influence of nano-scale surface roughness on bacterial adhesion to ultrafine-grained titanium. Biomaterials, 2010, 31 (13), 3674-3683.

References

247. Fadeeva, E., Truong, V.K., Stiesch, M., Chichkov, B.N., Crawford, R.J., Wang, J. and Ivanova, E.P. Bacterial Retention on Superhydrophobic Titanium Surfaces Fabricated by Femtosecond Laser Ablation. Langmuir, 2011, 27, 3012-3019.
248. Rizzello, L., Sorce, B., Sabella, S., Vecchio, G., Galeone, A., Brunetti, V., Cingolani, R. and Pompa, P.P. Impact of nanoscale topography on genomics and proteomics of adherent bacteria. ACS NANO, 2011, 5 (3), 1865-1876.
249. Bonse, J., Wrobel, J.M., Krüger, J. and Kautek, W. Ultrashort-pulse laser ablation of indium phosphide in air. Applied Physics A, 2001, 72 (1), 89-94.
250. Liu, J.M. Simple technique for measurements of pulsed Gaussian-beam spot sizes. Optics Letters, 1982, 7 (5), 196-198.
251. Naumkin, A.V., Kraut-Vass, A., Gaarenstroom, S.W. and Powell, C.J. NIST X-ray Photoelectron Spectroscopy Database, 2000.
252. Tanahashi, M., Yao, T., Kokubo, T., Minoda, M., Miyamoto, T., Nakamura, T. and Yamamuro, T. Apatite coated on organic polymers by biomimetic process: improvement in its adhesion to substrate by NaOH treatment. Journal of Applied Biomaterials, 1994, 5 (4), 339-347.
253. Serro, A.P. Biomineralização de materiais de implante: estudos de molhabilidade. Chemical Engineering Department, 2001, Instituto Superior Tecnico-University of Lisbon, Lisbon-Portugal.
254. Li, D. and Neumann, A.W. Contact angles on hydrophobic solid surfaces and their interpretation. Journal of Colloid and Interface Science, 1992, 148 (1), 190-200.
255. Cheng, P., Li, D., Boruvka, L., Rotenberg, Y. and Neumann, A.W. Automation of axisymmetric drop shape analysis for measurements of interfacial tensions and contact angles. Colloids and Surfaces, 1990, 43, 151-167.
256. Marmur, A. Equilibrium and spreading of liquids on solid surfaces. Advances in Colloid and Interface Science, 1983, 19, 75-102.
257. Lavi, B. and Marmur, A. The exponential power law: partial wetting kinetics and dynamic contact angles. Colloids and Surfaces A: Physicochemical and Engineering Aspects, 2004, 250 (1-3), 409-414.
258. Girifalco, L.A. and Good, R.J. A theory for the estimation of surface and interfacial energies. I. Derivation and application to interfacial tension. Journal of Physical Chemistry, 1957, 61 (7), 904-909.
259. Good, R.J. and Girifalco, L.A. A theory for estimation of surface and interfacial energies. III. Estimation of surface energies of solids from contact angle data. Journal of Physical Chemistry, 1960, 64, 561-565.
260. Owens, D.K. and Wendt, R.D. Estimation of the surface free energy of polymers. Journal of Applied Polymer Science, 1969, 13, 1741-1750.

References

261. Barry, F.P. and Murphy, J.M. Mesenchymal stem cells: clinical applications and biological characterization. The International Journal of Biochemistry & Cell Biology, 2004, 36 (4), 568-584.
262. Biggs, M.J., Richards, R.G., McFarlane, S., Wilkinson, C.D., Oreffo, R.O. and Dalby, M.J. Adhesion formation of primary human osteoblasts and the functional response of mesenchymal stem cells to 330 nm deep microgrooves. Journal of the Royal Society Interface, 2008, 5 (27), 1231-1242.
263. Hoefel, D., Grooby, W.L., Monis, P.T., Andrews, S. and Saint, C.P. A comparative study of carboxyfluorescein diacetate and carboxyfluorescein diacetate succinimidyl ester as indicators of bacterial activity. Journal of Microbiological Methods, 2003, 52 (3), 379-388.
264. Fuller, M.E., Streger, S.H., Rothmel, R.K., Mailloux, B.J., Hall, J.A., Onstott, T.C., Fredrickson, J.K., Balkwill, D.L. and DeFlaun, M.F. Development of a vital fluorescent staining method for monitoring bacterial transport in subsurface environments. Applied and Environmental Microbiology, 2000, 66 (10), 4486-4496.
265. Stepanovic, S., Cirkovic, I., Ranin, L. and Svabic-Vlahovic, M. Biofilm formation by Salmonella spp. and Listeria monocytogenes on plastic surface. Letters in Applied Microbiology, 2004, 38 (5), 428-432.
266. Wagner, C.D., Davis, L.E. and Riggs, W.M. The Energy Dependence of the Electron Mean Free Path. Surface and Interface Analysis, 1980, 2 (2), 53-55.
267. De Chiffre, L., Lonardo, P., Trumpold, H., Lucca, D.A., Goch, G., Brown, C.A., Raja, J. and Hansen, H.N. Quantitative Characterisation of Surface Texture. CIRP Annals - Manufacturing Technology, 2000, 49 (2), 635-652.
268. Giavaresi, G., Finia, M., Cigada, A., Chiesa, R., Rondelli, G., Rimondini, L., Torricelli, P., Aldini, N.N. and Giardino, R. Mechanical and histomorphometric evaluations of titanium implants with different surface treatments inserted in sheep cortical bone. Biomaterials, 2003, 24, 1583-1594.
269. Lamolle, S.F., Monjo, M., Lyngstadaas, S.P., Ellingsen, J.E. and Haugen, H.J. Titanium implant surface modification by cathodic reduction in hydrofluoric acid: surface characterization and in vivo performance. Journal of Biomedical Materials Research Part A, 2009, 88 (3), 581-588.
270. Porto, S.P.S., Fleury, P.A. and Damen, T.C. Raman Spectra of TiO2, MgF2, ZnF2, FeF2, and MnF2. Physical Review B, 1967, 154 (2), 522-526.
271. Ocana, M., Garcia-Ramos, J.V. and Serna, C.J. Low-Temperature Nucleation of Rutile Observed by Raman Spectroscopy during Crystallization of TiO2. Journal of the American Ceramic Society, (1992), 75 (7), 2010-2012.

References

272. Alfonsetti, R., De Simone, G., Lozzi, L., Passacantando, M., Picozzi, P. and Santucci, S. SiOx Surface Stoichiometry by XPS: a Comparison of Various Methods. Surface and Interface Analysis, 1994, 22 (1-12), 89-92.
273. Baltrusaitis, J., Jayaweera, P.M. and Grassian, V.H. XPS study of nitrogen dioxide adsorption on metal oxide particle surfaces under different environmental conditions. Physical Chemmistry Chemical Physics, 2009, 11 (37), 8295-8305.
274. Branemark, P.-I. Osteointegration and its experimental background. The Journal of Prosthetic Dentistry, 1983, 50 (3), 399-410.
275. Reif, J., Costache, F. and Bestehorn, M. Recent Advances in Laser Processing of Materials, 2006, Elsevier.
276. Bäuerle, D. Laser Processing and Chemistry, 3rd edition, 2000, Berlim, Springer Verlag.
277. Muddu ganghadar, B.C., Armanath, G.S., Tripathi, S., Dikshit, S. and Divya, M.S. Biomaterials for Dental Implants: An Overview. International Journal of Oral Implantology and Clinical Research, 2011, 2 (1), 13-24.
278. Sul, Y.-T., Johansson, C.B., Petronis, S., Krozer, A., Jeonge, Y., Wennerberg, A. and Albrektsson, T. Characteristics of the surface oxides on turned and electrochemically oxidized pure titanium implants up to dielectric breakdown: the oxide thickness, micropore configurations, surface roughness, crystal structure and chemical composition. Biomaterials, 2002, 23, 491-501.
279. Lausmaa, J., Kasemo, B. and Mattsson, H. Surface Spectroscopy Characterization of Titanium Implant Materials. Applied Surface Science, 1990, 44, 133-146.
280. Betsch, R.J., Park, H.L. and White, W.B. Raman Spectra of Stoichiometric and Defect Rutile. Materials Research Bulletin, 1991, 26 (7), 613-622.
281. Yakovlev, V.V., Scarel, G., Aita, C.R. and Mochizuki, S. Short-range order in ultrathin film titanium dioxide studied by Raman spectroscopy. Applied Physics Letters, 2000, 76 (9), 1107.
282. Porto, S.P.S. and Krishnan, R.S. Raman Effect of Corundum. The Journal of Chemical Physics, 1967, 47 (3), 1009.
283. Misra, A., Bist, H.D., Navati, M.S., Thareja, R.K. and Narayan, J. Thin film of aluminum oxide through pulsed laser deposition: a micro-Raman study. Materials Science and Engineering B, 2001, 79, 49-54.
284. Han, I., Vagaska, B., Joo Park, B., Lee, M.H., Jin Lee, S. and Park, J.-C. Selective fibronectin adsorption against albumin and enhanced stem cell attachment on helium atmospheric pressure glow discharge treated titanium. Journal of Applied Physics, 2011, 109 (12), 124701.

References

285. Arima, Y. and Iwata, H. Effect of wettability and surface functional groups on protein adsorption and cell adhesion using well-defined mixed self-assembled monolayers. Biomaterials, 2007, 28 (20), 3074-3082.
286. Serro, A.P. and Saramago, B. Influence of sterilization on the mineralization of titanium implants induced by incubation in various biological model fluids. Biomaterials, 2003, 24 (26), 4749-4760.
287. Chung, J.Y., Youngblood, J.P. and Stafford, C.M. Anisotropic wetting on tunable micro-wrinkled surfaces. Soft Matter, 2007, 3, 1163-1169.
288. Marques, P.A.A.P., Serro, A.P., Saramago, B.J., Fernandes, A.C., Magalhães, M.C.F. and Correia, R.N. Mineralisation of two calcium phosphate ceramics in biological model fluids. Journal of Materials Chemistry, 2003, 13, 1484-1490.
289. Gumbiner, B.M. Cell adhesion: The Molecular Basis of Tissue Architecture and Morphogenesis. Cell, 1996, 84, 345-357.
290. Hidalgo-Bastida, L.A. and Cartmell, S.H. Mesenchymal stem cells, osteoblasts and extracellular matrix proteins: enhancing cell adhesion and differentiation for bone tissue engineering. Tissue Engineering Part B Reviews, 2010, 16 (4), 405-412.
291. Curtis, A.S., Dalby, M.J. and Gadegaard, N. Nanoprinting onto cells. Journal of Royal Society Interface, 2006, 3 (8), 393-398.
292. Dalby, M.J. Cellular response to low adhesion nanotopographies. International Journal of Nanomedicine, 2007, 2 (3), 373-381.
293. Pesskova, V., Kubies, D., Hulejova, H. and Himmlova, L. The influence of implant surface properties on cell adhesion and proliferation. Journal of Materials Science: Materials in Medicine, 2007, 18 (3), 465-473.
294. Biggs, M.J., Richards, R.G. and Dalby, M.J. Nanotopographical modification: a regulator of cellular function through focal adhesions. Nanomedicine, 2010, 6 (5), 619-633.
295. Martinez, E., Engel, E., Planell, J.A. and Samitier, J. Effects of artificial micro- and nano-structured surfaces on cell behaviour. Annals of anatomy, 2009, 191 (1), 126-135.
296. Sjostrom, T., Dalby, M.J., Hart, A., Tare, R., Oreffo, R.O. and Su, B. Fabrication of pillar-like titania nanostructures on titanium and their interactions with human skeletal stem cells. Acta Biomaterialia, 2009, 5 (5), 1433-1441.
297. Im, B.J., Lee, S.W., Oh, N., Lee, M.H., Kang, J.H., Leesungbok, R., Lee, S.C., Ahn, S.J. and Park, J.S. Texture direction of combined microgrooves and submicroscale topographies of titanium substrata influence adhesion, proliferation, and differentiation in human primary cells. Archives of Oral Biology, 2012, 57 (7), 898-905.
298. Wang, J.H.-C., Grood, E.S., Florer, J. and Wenstrup, R. Alignment and proliferation of MC3T3-E1 osteoblasts in microgrooved silicone substrata subjected to cyclic stretching. Journal of Biomechanics, 2000, 33, 729-735.

References

299. Soboyejo, W.O., Nemetski, B., Allameh, S., Marcantonio, N., Mercer, C. and Ricci, J. Interactions between MC3T3-E1 cells and textured Ti6Al4V surfaces. Journal of Biomedical Materials Research Part A, 2002, 62, 56-72.
300. Loesberg, W.A., te Riet, J., van Delft, F.C., Schon, P., Figdor, C.G., Speller, S., van Loon, J.J., Walboomers, X.F. and Jansen, J.A. The threshold at which substrate nanogroove dimensions may influence fibroblast alignment and adhesion. Biomaterials, 2007, 28 (27), 3944-3951.
301. Hu, W., Yim, E.K., Reano, R.M., Leong, K.W. and Pang, S.W. Effects of nanoimprinted patterns in tissue-culture polystyrene on cell behavior. Journal of vacuum science & technology, 2005, 23 (6), 2984-2989.
302. Fraser, S.A., Ting, Y.H., Mallon, K.S., Wendt, A.E., Murphy, C.J. and Nealey, P.F. Sub-micron and nanoscale feature depth modulates alignment of stromal fibroblasts and corneal epithelial cells in serum-rich and serum-free media. Journal of Biomedical Materials Research Part A, 2008, 86 (3), 725-735.
303. Uttayarat, P., Toworfe, G.K., Dietrich, F., Lelkes, P.I. and Composto, R.J. Topographic guidance of endothelial cells on silicone surfaces with micro- to nanogrooves: orientation of actin filaments and focal adhesions. Journal of Biomedical Materials Research Part A, 2005, 75 (3), 668-680.
304. Ward, M.D. and Hammer, D.A. A theoretical analysis for the effect of focal contact formation on cell-substrate attachment strength. Byophysical Journal, 1993, 64, 936-959.
305. Cooper, G.M. The Cell: A Molecular Approach. Cell Proliferation in Development and Differentiation, 2nd edition, 2000, Sunderland, Sinauer Associates.
306. Mathieu, P.S. and Loboa, E.G. Cytoskeletal and focal adhesion influences on mesenchymal stem cell shape, mechanical properties, and differentiation down osteogenic, adipogenic, and chondrogenic pathways. Tissue engineering Part B, 2012, 18 (6), 436-444.
307. McBeath, R., Pirone, D.M., Nelson, C.M., Bhadriraju, K. and Chen , C.S. Cell shape Cytoskeletal Tension and RhoA Regulate Stem Cell Lineage Commitment. Developmental Cell, 2004, 6, 483-495.
308. Biggs, M.J.P. and Dalby, M.J. Focal adhesions in osteoneogenesis. Proc Inst Mech Eng H, 2010, 224 (12), 1441-1453.
309. Campoccia, D., Montanaro, L. and Arciola, C.R. A review of the clinical implications of anti-infective biomaterials and infection-resistant surfaces. Biomaterials, 2013, 34 (33), 8018-8029.
310. Gristina, A.G., Giridhar, G., Gabriel, B.L., Nauylor, P.T. and Myrvik, Q.N. Cell biology and molecular mechanisms in artificial device infections. The International Journal of Artificial Organs, 1993, 16 (11), 755-763.

References

311. Katsikogianni, M.G. and Missirlis, Y.F. Interactions of bacteria with specific biomaterial surface chemistries under flow conditions. Acta Biomaterialia, 2010, 6 (3), 1107-1118.
312. Whitehead, K.A. and Verran, J. The Effect of Surface Topography on the Retention of Microorganisms. Food and Bioproducts Processing, 2006, 84 (4), 253-259.
313. Garrett, T.R., Bhakoo, M. and Zhang, Z. Bacterial adhesion and biofilms on surfaces. Progress in Natural Science, 2008, 18 (9), 1049-1056.
314. Del Curto, B., Brunella, M.F., Giordano, C., Pedeferri, M.P., Valtulina, V., Visai, L. and Cigada, A. Decreased bacterial adhesion to surface-treated titanium. The International Journal of Artificial Organs, 2005, 28 (7), 718-730.
315. Yang, B., Uchida, M., Kim, H.-M., Zhang, X. and Kokubo, T. Preparation of bioactive titanium metal via anodic oxidation treatment. Biomaterials, 2004, 25 (6), 1003-1010.
316. Nanci, A., Wuest, J.D., Peru, L., Brunet, P., Sharma, V., Zalzal, S. and McKee, M.D. Chemical modification of titanium surfaces for covalent attachment of biological molecules. Journal of Biomedical Materials Research, 1998, 40, 324-335.
317. Porté-Durrieu, M.-C., Labrugère, C., Villars, F., Lefebvre, F., Dutoya, S., Guette, A. and Bordenave, L. Development of RGD peptides grafted onto silica surfaces: XPS characterization and human endothelial cell interactions. Journal of Biomedical Materials Research, 1999, 46, 368-375.
318. Chollet, C., Chanseau, C., Remy, M., Guignandon, A., Bareille, R., Labrugere, C., Bordenave, L. and Durrieu, M.-C. The effect of RGD density on osteoblast and endothelial cell behavior on RGD-grafted polyethylene terephthalate surfaces. Biomaterials, 2009, 30 (5), 711-720.
319. Pichavant, L., Amador, G., Jacqueline, C., Brouillaud, B., Heroguez, V. and Durrieu, M.C. pH-controlled delivery of gentamicin sulfate from orthopedic devices preventing nosocomial infections. Journal of Controlled Release, 2012, 162 (2), 373-381.
320. Cheng, Z.A., Zouani, O.F., Glinel, K., Jonas, A.M. and Durrieu, M.C. Bioactive chemical nanopatterns impact human mesenchymal stem cell fate. Nano Letters, 2013, 13 (8), 3923-3929.

Appendices

A.1. Comissão de Acompanhamento de Tese (CAT)

This is a partial requirement of the Doctoral program in Materials Engineering of the Instituto Superior Técnico-Universidade de Lisboa. The results achieved during the first year of the research project were presented to a jury in 10/18/2011. The jury concluded that the results were clearly and logically presented. Therefore, the PhD student received the approval to continue and conclude his thesis sucessfully.

A.2. IDS-FunMat Deliverables

A.2.1. Training Schools and Annual Reports

- First Training school during March 13th-18th, 2011, held in Sesimbra-Portugal.
- Second Training school during March 25th-31st, 2012, held in Anglet-France.
- Third Training School during March 17th-22nd, 2013, held in Annecy-France.
- Three annual reports containing the advances of the research project during the years 2010-2011, 2011-2012, and 2012-2013.

A.3. Scientific Communications

A.3.1. Publications

- Oliveira V., Cunha, A., Vilar, R. Multi-scaled femtosecond laser structuring of stationary titanium surfaces, Journal of Optoelectronics and Advanced Materials, 12 (3), 2010, 654-658.
- Cunha, A., Serro, A.P., Oliveira, V., Almeida, A., Vilar, R., Durrieu, M.-C. Wetting behaviour of femtosecond laser textured Ti-6Al-4V surfaces, Applied Surface Science, 265, 2013, 688-696.
- Cunha, A., Oliveira, V., Serro, A.P., Zouani, O.F., Almeida, A., Durrieu, M.-C., Vilar, R. Ultrafast laser texturing of Ti-6Al-4V surfaces for biomedical applications, Proceedings of the 32nd International Congress on Applications of Lasers & Electro-Optics (ICALEO), Nanomanufacturing Conference, Laser Institute of America (LIA), 106, 2013, 910-918.

A.3.2. Future Publications

- Cunha, A., Zouani, O.F., Plawinski, L., Rego, A.M.B., Almeida, A., Vilar, R., Durrieu, M-.C. Human mesenchymal stem cells behavior onto femtosecond laser textured Ti-6Al-4V surfaces, submitted to Nanomedicine.
- Cunha, A., Plawinski, L., Serro, A.P., Rego, A.M.B., Almeida, A., Urdaci, M.C., Durrieu, M-.C., Vilar, R. Femtosecond laser surface texturing of titanium as a method to reduce the adhesion of *Staphylococcus aureus* and biofilm formation, to be submitted.

A.3.3. Oral and Poster Presentations

- Cunha, A., Almeida, A., Zouani, O.F., Durrieu, M.-C., Vilar, R. Bio-inspired multiscale interfaces dental and skeletal reconstruction biomaterials, Fisrt IDS-FunMat Training School, March 13th-18th, 2011, Sesimbra, Portugal. Oral presentation.
- Cunha, A., Almeida, A., Zouani, O.F., Durrieu, M.-C., Vilar, R. Bio-inspired multiscale interfaces dental and skeletal reconstruction biomaterials, Second IDS-FunMat Training School, March 25th-31st, 2012, Anglet, France. Poster presentation.
- Cunha, A., Almeida, A., Zouani, O.F., Durrieu, M.-C., Vilar, R. Mesenchymal Stem Cells adhesion and differentiation onto laser-induced periodic surface structures on titanium, 9th World Biomaterials Congress, June 1st-5th, 2012, Chengdu, China. Oral presentation.
- Cunha, A., Almeida, A., Zouani, O.F., Durrieu, M.-C., Vilar, R. Bio-inspired multiscale interfaces dental and skeletal reconstruction biomaterials, Annual scientific meeting of the Institute of Chemistry & Biology of Membranes & Nanoobjects (CBMN), December 13rd-14th, 2012, Pessac, France. Flash talk and poster presentation.
- Cunha, A., Almeida, A., Zouani, O.F., Durrieu, M.-C., Vilar, R. Bio-inspired multiscale interfaces dental and skeletal reconstruction biomaterials, Third IDS-FunMat Training School, March 17th-22nd, 2013, Annecy, France. Poster presentation.

- Cunha, A., Almeida, A., Zouani, O.F., Durrieu, M.-C., Vilar, R. Mesenchymal Stem Cells behaviour onto femtosecond laser textured Ti alloys, Materiais 2013, March 25th-27th, 2013, Coimbra, Portugal. Oral presentation.
- Cunha, A., Oliveira, V., Serro, A.P., Zouani, O.F., Almeida, A., Durrieu, M.-C., Vilar, R. Ultrafast laser texturing of Ti-6Al-4V surfaces for biomedical applications, 32nd International Congress on Applications of Lasers & Electro-Optics (ICALEO), October 6th-10th, 2013, Miami, FL, USA. Oral presentation.
- Cunha, A., Plawinski, L., Almeida, A., Vilar, R., Durrieu, M.-C. Multiscale femtosecond laser surface texturing of titanium alloys for dental and orthopaedic implants, Workshop du Pôle de Médecine Régénératrice de Bordeaux, November 17th-18th, 2014, Université de Bordeaux, Haut Carré, Talence, France. Poster presentation.

A.4. Awards

- Best poster communication at the Annual scientific meeting of the Institute of Chemistry & Biology of Membranes & Nanoobjects (CBMN), December 13rd-14th, 2012, Pessac, France.